

University of Bath



PHD

Parallel folding with friction

Edmunds, Rorie

Award date:
2005

Awarding institution:
University of Bath

[Link to publication](#)

General rights

Copyright and moral rights for the publications made accessible in the public portal are retained by the authors and/or other copyright owners and it is a condition of accessing publications that users recognise and abide by the legal requirements associated with these rights.

- Users may download and print one copy of any publication from the public portal for the purpose of private study or research.
- You may not further distribute the material or use it for any profit-making activity or commercial gain
- You may freely distribute the URL identifying the publication in the public portal ?

Take down policy

If you believe that this document breaches copyright please contact us providing details, and we will remove access to the work immediately and investigate your claim.

Download date: 22. May. 2019

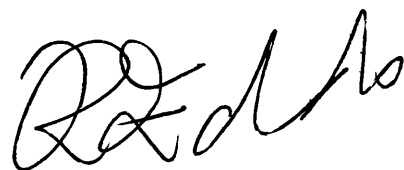
PARALLEL FOLDING WITH FRICTION

Submitted by Rorie Edmunds
for the degree of
Doctor of Philosophy
of the University of Bath
2005

COPYRIGHT

Attention is drawn to the fact that copyright of this thesis rests with its author. This copy of the thesis has been supplied on condition that anyone who consults it is understood to recognise that its copyright rests with its author and no information derived from it may be published without the prior written consent of the author.

This thesis may be made available for consultation within the University library and may be photocopied or lent to other libraries for the purposes of consultation.

A handwritten signature in black ink, appearing to read 'R. Edmunds', is located in the bottom right corner of the page.

UMI Number: U601793

All rights reserved

INFORMATION TO ALL USERS

The quality of this reproduction is dependent upon the quality of the copy submitted.

In the unlikely event that the author did not send a complete manuscript and there are missing pages, these will be noted. Also, if material had to be removed, a note will indicate the deletion.



UMI U601793

Published by ProQuest LLC 2013. Copyright in the Dissertation held by the Author.
Microform Edition © ProQuest LLC.

All rights reserved. This work is protected against
unauthorized copying under Title 17, United States Code.



ProQuest LLC
789 East Eisenhower Parkway
P.O. Box 1346
Ann Arbor, MI 48106-1346

UNIVERSITY OF BATH
LIBRARY
65 27 APR 2003
Ph.D

Abstract

A basic model is presented for parallel folding of two flexible layers under compression, obliged by the presence of overburden pressure to remain in contact along their length. The nonlinear effect of friction is fully explored via a quasi-energy formulation, using a simple Galerkin approximation obtained from experimental analysis. The calculus of variations leads to a representation of the model as an ordinary differential equation. The outcomes of both theoretical and numerical modelling are compared with the Galerkin approximation. The significance of friction-induced jamming is explored. Comparisons between the linearized differential equation under the nonlinear boundary conditions, and the full nonlinear formulation, indicate that the linearization captures most of the significant behaviour.

To embrace serial buckling behaviour, cubic B-splines are introduced into the linearized two-layer model. The stationary solutions of the quasi-energy formulation are then shown to correspond to the equilibrium states of practical interest, under conditions of both controlled load and controlled end-shortening. Consistent with Morse theory, under experimentally viable loading, non-periodic saddle points describing localized solutions are found to converge with unstable maxima representing periodic behaviour, until at a critical stage in the evolution only periodic solutions exist. This shift from localized to two-hump periodic behaviour is seen as a primitive exposition of the more general theme of serial or sequential fold formation.

Extending the two-layer model to a full multilayer formulation for n identical layers, the general behaviour of the multilayer is again characterized using a sinusoidal Galerkin approximation. When substituted into the linearized potential energy function, equations for the wavelength and critical load are found and

the limitations of the model are highlighted. Comparisons with experiments conducted on layers of paper constrained between two sheets of foam rubber show that the trend of the load-amplitude plots is in good agreement with that predicted. Excellent correlation is also achieved between the wavelengths calculated by the linearized buckling analysis and those seen experimentally.

Acknowledgements

Having spent eight years at the University of Bath there are many people that have helped my progress down the years, the culmination of this thesis could not have happened without them and so I acknowledge them here.

First and foremost I need to thank Professor Christopher Budd. I have known Chris since I started at the University of Bath to embark on my mathematics undergraduate degree. As my personal tutor—not always an easy task—Chris has put up with the trials and tribulations of my life throughout my undergraduate and postgraduate degrees. Chris' enthusiasm as a lecturer and for applying mathematics to physical situations has been a great inspiration and has rubbed off on me. I am also very grateful to Chris for introducing to my co-supervisor Professor Giles Hunt.

Giles is fairly unique in realizing the importance of interaction between different disciplines and the rewards that can be gained from such links. Giles gave me a genuinely interesting structural geology problem to study for my Ph. D. ; this was despite the fact that for a mathematician coming into engineering, it would involve huge amounts of effort on his part to get me up to speed. The first year and a half of my research was particularly difficult, but Giles has been a patient and supportive supervisor throughout my Ph. D. and I have the upmost appreciation for all that he has taught me.

I would also like to thank Dr. Ahmer Wadee for his contribution to this work. In offering me a research position in the Civil Engineering Department of Imperial College London at the end of my funding, Ahmer introduced me to academic life outside of the University of Bath. Since then Ahmer has become a good friend and I am especially grateful to him for allowing me to use the custom made rig

in the Structures laboratory (built and maintained by Ron Millward) to conduct my own experiments and to write up whilst under his employ—Chapter 6 of this thesis would not exist otherwise.

Other people who have contributed to this work through useful discussions and suggestions are Dr. JF Williams and Dr. Mark Peletier. In particular, it is necessary to thank John McAlpine, who went out of his way to obtain most of the references cited in the section of Chapter 1 on “Friction Theory”. I also give my appreciation to Chris Budd’s secretary Mrs Ann Linfield, who has always been friendly and helpful.

People who deserve a mention are those that have made my day-to-day life within the office more bearable, especially: Matthew Liston, Jenny Wright, Wenli Liu, Deepa Ferdous and Thomas Hesselberg. I have made many friends during my time at Bath, I would like to express my gratitude to the following for improving my quality of life outside of work: Tony Durrant, Katie Stevens, Al Simons, Stephen Mitchell, Andrea Dowling, Alice Skurczynski, Miranda Skurczynski and Christopher Smith. I give particular praise to: David Branson, Nicola Braidwood and Mark Pinnick, who all had to put up with me for the final months leading up to my submission.

Eight years is a significant part of my life, during this time I have become an adult, and so I feel that the University of Bath has helped shape me into the person that I am. I therefore need to thank the University of Bath and everyone associated with it, for funding me through my Ph. D. , for giving me a grant to live on and a stipend for my resources.

Lastly, but in no way least, I would like to thank all of my family for everything they have done for me, not just during my time at university, but throughout my life. The support and encouragement especially of my parents Guy and Alison, my brothers Damon and Shaun and my grandparents Harold and Patricia Yeomans and Doris Edmunds, has meant that I have been able to get through even the hardest of times. I hope to make them proud of me in the future.

Contents

1	Introduction	23
1.1	The parallel fold	23
1.2	Outline of thesis	25
1.2.1	Technical terminology	25
1.2.2	Literature review	25
1.2.3	Two-layer parallel folding with friction	26
1.2.4	The nonlinear differential equation	27
1.2.5	Sequential buckling	27
1.2.6	Multilayer parallel folding and conclusions	28
1.3	Geology fundamentals	28
1.3.1	Geological definitions	29
1.3.2	Elasticity and viscosity	35
1.3.3	Pressure and friction	37

1.3.4	Synchronous and non-synchronous buckling	39
1.4	Bending theory and the elastic strut	40
1.4.1	Simple bending theory of a beam	41
1.4.2	The elastica	44
1.4.3	Solving the elastica	45
1.4.4	Imperfections	49
1.5	Adding a foundation	51
1.5.1	Foundation models	51
1.5.2	The strut on an elastic foundation	53
1.6	Mathematical and engineering technical definitions	54
1.6.1	Dynamical systems definitions	55
1.6.2	Localization and cellular buckling	60
1.7	Friction theory	62
1.7.1	Laws of friction	62
1.7.2	True contact area	64
1.7.3	Adhesion and deformation forces	66
1.7.4	High pressure	67
1.7.5	Lubrication	69
2	Literature review	70

2.1	Introduction	70
2.2	Elastic single layer solutions	71
2.3	The influence of Biot	78
2.3.1	Biot and Ramberg	78
2.3.2	Viscosity arguments	83
2.3.3	Importance of layering	84
2.3.4	Elasticity arguments	85
2.3.5	Serial buckling	90
2.3.6	Shear banding	93
2.4	Localization and buckling	94
2.4.1	Localization	95
2.4.2	Geological applications	97
2.4.3	Other interesting and connected areas	99
2.5	Concluding remarks	101
3	The two-layer frictional parallel folding model	103
3.1	Introduction	103
3.2	Pseudo potential energy	105
3.2.1	Nonlinear formulation	105
3.2.2	Potential energy function	109

3.3	A useful Galerkin approximation	111
3.3.1	The Fast Fourier Transform (FFT)	111
3.3.2	Bifurcation diagram	116
3.3.3	Critical loads and wavelength selection	117
3.3.4	Stability of the solution paths	118
3.3.5	Jamming	118
3.3.6	Initial imperfections	119
3.4	Concluding remarks	120
4	Numerical analysis for the general case	122
4.1	Introduction	122
4.2	Calculus of variations	123
4.3	An analysis of the linear equation	127
4.3.1	The solution for $k = 0$	127
4.3.2	Bifurcation diagrams for $k = 0$	130
4.3.3	The solution for $k \neq 0$	132
4.3.4	Wavelength selection	133
4.3.5	Poincaré's inequality	138
4.4	Numerical results	139
4.4.1	Numerical solutions: AUTO	139

4.4.2	Linear equation	141
4.4.3	Nonlinear equation	143
4.5	Concluding remarks	143
5	A primitive model for serial parallel folding using cubic B-splines	146
5.1	Introduction	146
5.2	Two-layer model	148
5.3	Modelling waveshapes using cubic B-splines	150
5.3.1	The cubic B-spline	150
5.3.2	Single B-spline formulation	151
5.4	Two B-spline formulation	153
5.4.1	Overlap	154
5.4.2	Galerkin model	155
5.4.3	Results	155
5.5	Morse theory for a surface	161
5.5.1	Primitive periodic solution ($Q_2 = -Q_1$)	163
5.5.2	Primitive localized solution ($Q_2 \neq -Q_1$)	170
5.6	Concluding remarks	171
6	Comparing the multilayer formulation with experiments	173

6.1	Introduction	173
6.2	Experimental procedure	174
6.3	Total potential energy	178
6.3.1	Single layer	178
6.3.2	Multilayer formulation	179
6.3.3	Radius of curvature versus multilayer thickness	182
6.3.4	Linearized potential energy functional	184
6.3.5	Calculus of variations	186
6.4	Comparison with experiments	188
6.4.1	Young's modulus and second moment of area	188
6.4.2	Overburden pressure and coefficient of friction	189
6.4.3	Foundation stiffness	190
6.4.4	Graphical comparisons	193
6.5	Concluding remarks	197
7	Conclusions and further work	199
7.1	Concluding remarks	199
7.2	Further work	201
	References	205

List of Figures

1.1	Parallel fold in Beekmantown limestone, Rheems Quarry, Pennsylvania. (After Donath & Parker 1964)	24
1.2	Profile of fold: h and i are hinge and inflection points; c and t denote the crests and troughs of the fold; the dashed line is the median surface; α is the interlimb angle and A and L are the amplitude and wavelength of the fold. (After Price & Cosgrove 1990)	30
1.3	Construction of dip isogons. (After Price & Cosgrove 1990)	32
1.4	Classification based on dip isogon patterns: 1(a) Strongly convergent, 1(b) Parallel, 1(c) Weakly convergent, 2 Similar and 3 Divergent. (After Ramsey 1967)	32
1.5	Strain distribution of flexural flow/slip. (After Ramsey 1967) . . .	34
1.6	Serial buckling of a viscous multilayer. (After Blay <i>et al.</i> 1977) . .	40
1.7	Pure bending of a single layer.	41
1.8	Curvature over a small angle.	42
1.9	A pin-ended Euler strut. (After Thompsom & Hunt 1973)	44
1.10	The bifurcation diagram for the (a) Linear and (b) Nonlinear perfect strut, where Q is the maximum amplitude of the deflection. .	49

1.11 Families of imperfect systems for the (a) Stable symmetric and (b) Unstable symmetric bifurcation. (After Thompson & Hunt 1973)	50
1.12 An elastic strut on a Winkler foundation under loading.	52
1.13 Foundation behaviour in compression at cell level. (After Hunt & Wadee 1998)	53
1.14 (a) The homoclinic bifurcation (After Glendinning 1994), (b) Top: An homoclinic wave-profile and Bottom: A wavepacket. (After Thompson & Virgin 1988)	55
1.15 (a) An heteroclinic connection and (b) An heteroclinic wave-profile.	56
1.16 (a) Stable supercritical, (b) Stable subcritical, (c) Unstable subcritical and (d) Unstable supercritical pitchfork bifurcation. (After Glendinning 1994)	57
1.17 Finding the Maxwell displacement. (After Hunt <i>et al.</i> 2000) . . .	59
1.18 Phase-plane portraits of an Hamiltonian Hopf bifurcation. (After Thompson & Virgin 1988)	61
1.19 (a) A mass subjected to a frictional force F and normal load W , (b) How the friction force alters with sliding velocity.	63
1.20 Interaction of wedge shaped surface roughness. The coefficient of sliding friction $\mu_s = \tan \gamma$ is calculated using energy considerations.	64
1.21 (a) Orowan's and (b) Shaw <i>et al.</i> frictional model. (After Wanheim & Bay 1978)	67
1.22 A plot showing how α changes with W . (After Wanheim & Bay 1978)	68
1.23 A plot showing how F changes with W . (After Wanheim & Bay 1978)	68

2.1	(a) Parallel folds and (b) Similar folds. (After Van Hise 1894) . . .	72
2.2	Sketches showing the results of experiments by Kuenen & de Sitter (After de Sitter 1964); (a) Folded rubber plate, (b) Thickened and folded paraffin cake floating on water, (c) Folded pack of paper sheets and (d) Folded unstratified clay cake.	75
2.3	Similar folding of the <i>first</i> and <i>second</i> kind. (After Biot 1965b) .	80
2.4	(a) Continuous and (b) Discontinuous flow. (After Donath 1962) .	85
2.5	Concentric folding by flexural slip. (After Donath 1962)	86
2.6	(a) Three competent layers with wide spacing and (b) With close spacing. (c) A sequence with identical layering. (After Currie <i>et al.</i> 1962)	88
2.7	Experimental elastic multilayer deformation. (After Johnson & Honea 1975a)	89
2.8	The transition of folding from sinusoidal-to-concentric-to-chevron. (After Johnson and Honea 1975a)	91
3.1	(a) Parallel folding in layers of paper. For visual clarity, approximately every tenth layer has been edged in black. (b) Kink banding in layers of paper. (After Wadee & Edmunds 2005)	104
3.2	Slip between incompressible layers constrained to remain in contact.	106
3.3	Two layers bent through a small angle $d\theta$	108
3.4	Slip directions for $\chi = +1$. Top: Q positive. Bottom: Q negative.	110
3.5	Fitting points along deformed experimental layers.	113
3.6	(a) How the magnitude of c_1 alters throughout the multilayer and (b) Comparing $ c_2 $ to $ c_1 $ throughout the multilayer.	115

3.7	Bifurcation diagram indicating jammed region for constant μ . . .	116
3.8	Jamming in the presence of a positive initial imperfection ϵ : (a) $0 < \epsilon < \epsilon_{th}$, (b) $\epsilon > \epsilon_{th}$	120
4.1	Plot of load P against amplitude Q , for $k = 0, EI = 0.5, L = 1$ and $\mu qt = 0.1$	130
4.2	Phase plane trajectories plotted for $k = 0, EI = 0.5, L = 1$ and $\mu qt = 0.1$	131
4.3	Variation of P^C with L for different values of k	134
4.4	Difference in wavelength prediction between equations (4.31) and (4.42), plotted for $EI = 0.5, k = 1, \alpha = 1$ and $\mu qt = 0.1$	137
4.5	Bifurcation plot for the linear differential equation (4.9) plotted for $EI = 0.5, k = 1, \mu qt = 0.1$ and $L = \pi$	141
4.6	Waveshapes and corresponding phase portraits for the case of Fig. 4.5 at $Q = -0.082$	142
4.7	Waveshapes and corresponding phase portraits for the case of Fig. 4.5 at $Q = -0.42$	142
4.8	Bifurcation plot for the nonlinear differential equation (4.8) plotted for $EI = 0.5, k = 1, \mu qt = 0.1$ and $L = \pi$	143
4.9	Waveshapes and corresponding phase portraits for the case of Fig. 4.8 at $Q = -0.082$	144
4.10	Waveshapes and corresponding phase portraits for the case of Fig. 4.8 at $Q = -0.42$	144
4.11	Comparisons of linear and nonlinear solutions (a) $\mu qt = 0.1$ and (b) $\mu qt = 1$	145

5.1	Parallel folding in layers of paper, showing the serial buckling behaviour.	147
5.2	Bifurcation diagram indicating jammed region for constant μ . . .	149
5.3	The cubic B-spline.	150
5.4	Bifurcation diagram for one-spline model, linear foundation. . . .	152
5.5	Wave-profiles for one-spline model, nonlinear foundation.	153
5.6	Bifurcation diagram for the nonlinear one-spline model when $P > P^C$, for differing C values.	154
5.7	Schematic representation of primitive modeshapes from the two B-spline model: (a) homoclinic ($Q_1 \neq -Q_2$); (b) periodic ($Q_1 = -Q_2$).154	
5.8	Changes in preferred modeshape as the load drops and the end-shortening increases.	156
5.9	Energy, V , and end-shortening, \mathcal{E} , contour plot for $Q_1 - Q_2$ space when $P = 8$	158
5.10	Energy, V , and end-shortening, \mathcal{E} , contour plot for $Q_1 - Q_2$ space when $P = 6.1265$	159
5.11	Energy, V , and end-shortening, \mathcal{E} , contour plot for $Q_1 - Q_2$ space when $P = 4.6$	160
5.12	Schematic showing the evolution of the topology of V as the load drops, the extrema are denoted by crosses.	162
5.13	Energy contour plot in $Q_1 - \Omega$ space when $Q_2 = -Q_1$ for $P = 8$. .	164
5.14	Energy contour plot in $Q_1 - \Omega$ space when $Q_2 = -Q_1$ for $P = 6.1265$.165	
5.15	Energy contour plot in $Q_1 - \Omega$ space when $Q_2 = -Q_1$ for $P = 4.6$. 166	

5.16	Energy profile when $Q_2 = -Q_1$ for $P = 8, P = 6.1265$ and $P = 4.6$.	167
5.17	Schematic representation of transformation from $V(Q_1, \Omega)$ to F_Ω .	168
5.18	Variations of amplitude Q_1 , overlap Ω , and end-shortening \mathcal{E} , with load P , for the $Q_2 = -Q_1$ solution.	169
5.19	Variations of amplitudes Q_1 and Q_2 , and maximum and minimum displacements w_{\max} and w_{\min} , with P , for the $Q_2 \neq -Q_1$ solution.	170
5.20	Comparative variations of total energy V , and end-shortening \mathcal{E} , with P for both the $Q_2 = -Q_1$, and the $Q_2 \neq -Q_1$ solutions, noting the coalescence of these curves at $P \approx 6.1$	171
6.1	Experimental test rig.	175
6.2	Schematic of loading an experimental sample.	176
6.3	Output of axial and transverse compressive forces, plotted against axial end-shortening.	177
6.4	Parallel folding of 120 sheets of paper.	177
6.5	An experimental photograph, reduced to a schematic, to emphasize the concentricity of the folds.	183
6.6	(a) Transverse load (P_T) versus displacement (Δ) response for Experiment 2, where X marks the load at the first instability (see Fig. 6.9(a)). (b) Curve-fit in the neighbourhood of the point X. (Note that the curve is rescaled to start at the origin).	190
6.7	Diagram of the interaction of two springs acting either side of the layers when: (a) & (b) the pre-compression is added causing displacement Δ_0 in each spring, and (c) the axial load forces one spring to compress and the other to release by an amount δ	191

6.8	Schematic of the $P_T - \Delta$ plot when increasing and releasing the pre-compression.	192
6.9	Axial and transverse loads (P and P_T), plotted against end-shortening \mathcal{E} for the three further experiments (in addition to that of Fig. 6.3).194	
6.10	Comparison of model and experiment showing axial loads, plotted against end-shortening \mathcal{E}	195
6.11	Experiment 4: Foundation caught in the folds increasing the foundation stiffness and wavelength of the fold.	197
7.1	(a) Tracing envelopes of constant thickness of a sinewave, (b) Crumpling at the base of a fold. (After Goguel 1962)	202
7.2	Chevron folds obtained from kink bands. (After Hunt <i>et al.</i> 2000b)	204

List of Tables

1.1	After de Sitter (1964), the elastic modulus E of different rocks at low and high overburden pressures Pr	37
1.2	Various values of friction cited for differing situations.	38
6.1	Experimental configurations.	188
6.2	Experimental values compared against model predictions.	196

Nomenclature

Coordinates, dimensions and angles

x	Arclength of central interface
x_i	Arclength of layer i
$\xi = \frac{x}{L}$	Horizontal coordinate rescaled over $[0, 1]$
w	Vertical deflection of central interface
t	Thickness of individual layer
a_1	Width of the layers
a_2	Length of the layers
n	Number of layers
$T = nt$	Thickness of single thick layer/Total thickness of layers
θ	Angle layers bent through
R	Radius of curvature of central interface
R_i	Radius of curvature of layer i
$\bar{R}_{i,i+1}$	Average of radius of curvature between layers $i - 1$ and i

Material Properties

E	Young's modulus of layers
E_{foam}	Young's modulus of the foam
I	Second moment of area of individual layer
\hat{I}	Second moment of area of layer with thickness T
k	Transverse stiffness per unit length of foundation
C	Nonlinear foundation stiffness
μ	Coefficient of friction
q	Overburden pressure
k_{layers}	In-line stiffness of the paper multilayer
k_{foam}	In-line stiffness of the foam
k_{total}	Total in-line stiffness of the sample

Energy

U_B	Bending energy
U_F	Foundation Energy
\mathcal{E}	End-shortening
Δ	Transverse displacement
U_μ	Work done against friction
F	Total potential energy per unit length
V	Total potential energy
F_f	Foundation force

Loads, amplitudes and wavelengths

P	External lateral load
P^C	Critical buckling load
P_T	External transverse load
$P_{max} = \frac{8\pi^2 EI}{L^2}$	Upper value of P to ensure monotonicity
P_{min}	Minimum load level attained by the initial hump
Q	Maximum deflection of the central interface
L	Half wavelength
L_{opt}	Optimum buckle length for single cubic B-spline
L^C	Wavelength at critical load for single cubic B-spline
L_{expt}	Experimental half wavelength

Numerics

x_l	Horizontal distance along a layer (2π -periodic)
w_l	Vertical deflection of a layer
c_m	Fourier coefficient of index m
N	Number of points taken for the <i>fft</i> algorithm
W	Vector of vertical displacements needed for <i>fft</i> algorithm
C	Vector of Fourier coefficients
$\omega_N = e^{(-2\pi i)/N}$	N th root of unity
\mathbf{f}	Vector defining system of first order differential equations
\mathbf{u}	Vector of variables
p	One or more free parameters for parameter continuation
Γ	Free parameter for pseudo-arclength continuation

Miscellaneous

s	Cumulative interlayer slip
$s_{i:i+1}$	Slip between layers $i - 1$ and i
χ	Friction indicator
α	Slope of $w(x)$
ϵ	Imperfection in the sense of Q
$\epsilon_{\text{th}} = 2\chi\mu qt $	Threshold value of imperfection ϵ
Ω	Overlap variable
γ	Incline slip angle

Chapter 1

Introduction

“...the theoretical analyses already discussed place a disproportionate emphasis upon the viscous models. As will have become apparent to the reader, this emphasis merely reflects the dominance of such analyses in the literature. It is the authors’ current conviction that they do not correctly model rock behaviour during fold initiation. Other aspects relating to buckling tend to be ignored or neglected, especially for those folds in the upper levels of the crust. For example, major folds are ramified by fractures, some of which certainly developed while the fold was developing and may supply evidence of how finite folds develop.”
Price & Cosgrove (1990)

1.1 The parallel fold

Definition 1 *Parallel fold*

A *parallel fold* (also sometimes known a concentric fold) is a geological phenomenon that occurs when a *multilayered* structure composed of a stiff (more competent) material is embedded in a soft foundation (less competent matrix) and is buckled by a load parallel to the layering. The resulting wave pattern has the property that the thickness of the layers orthogonal to the orientation of the layers remains constant throughout. Examples are seen in many geological

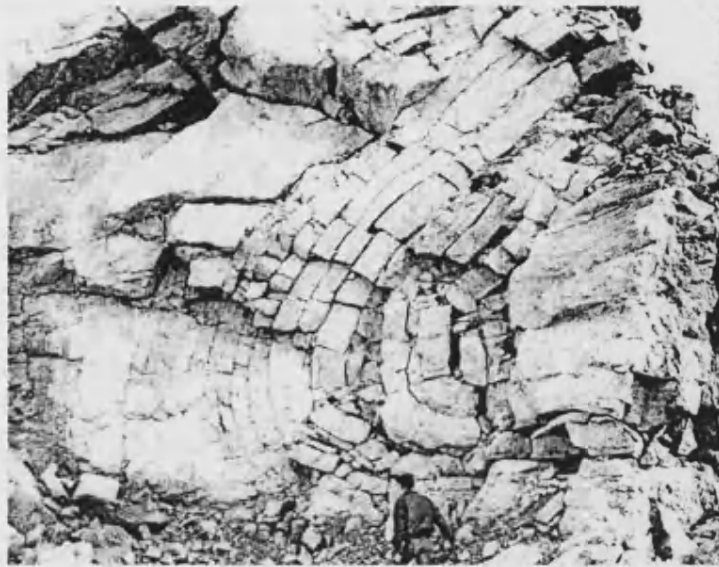


Figure 1.1: Parallel fold in Beekmantown limestone, Rheems Quarry, Pennsylvania. (After Donath & Parker 1964)

outcrops (Donath & Parker, 1964; Ramsey, 1967; Hobbs *et al.*, 1976; Price & Cosgrove, 1990), see Fig. 1.1.

The name *parallel fold* was given by Van Hise (1894) who originally described it, noting that each layer takes a different form to those above and below it and that the folding eventually dies out. Mistakenly assuming that the more closely folded layers are in a position where friction gives less resisting power, Van Hise did realize that the difference in the curvature of each layer could be attributed to friction.

Friction is inherent to the process, as rocks often deform at depths in the Earth's crust where the pressures are large—of the order of 1–5 kbars (Price, 1970)—and the slip planes are areas of natural weakness (Donath, 1962; Donath & Parker, 1964). Layer slippage under large overburden pressures has led us to believe that an elastic, frictional model for parallel folding, where buckling is cellular rather than synchronous, would accurately follow the real situation.

However, multilayer buckling, and more specifically parallel folding, has been studied in several different ways: theoretically, including elastically (Currie *et al.*, 1962; Johnson & Honea, 1975a) and viscously (Biot, 1961; Biot, 1965b; Ramberg, 1961; Ramberg & Strömberg, 1971); or through simple experiments (Kuenen &

de Sitter, 1938; Blay *et al.*, 1977). To simplify the modelling, much of this work concentrates on perfectly adhered to or freely sliding layers or even ignores the layering altogether and uses shearing as the deformation process.

As well as a purely academic interest, understanding parallel folding has a commercial use to mining companies. If the deformation process is understood then it is possible to find large amounts of minerals quickly and easily in outcrops by recognizing where any voids, cracks, gaps or faults are likely to be created as these are likely to be filled with mineral deposits (Hunt *et al.*, 1997). Also, although mainly found in geology, as is shown by experiments later, parallel folding may also occur in other layered structures. This type of deformation could be found in composites, especially if they have a combination of stiff and soft material. The concept of parallel folding is also of use to anyone interested in delamination, as from energy considerations, under conditions of high pressure, delamination or the appearance of voids between layers is unlikely.

1.2 Outline of thesis

With the concept of parallel folding introduced together with some of the ideas surrounding it in a geological context, we give here a summary of the content that is contained in the remainder of the thesis.

1.2.1 Technical terminology

Firstly, the rest of this chapter is dedicated to giving a more technical introduction to mathematical, engineering and geological terms and theory required for the rest of the thesis.

1.2.2 Literature review

Chapter 2 looks at the literature relevant to the subject area. The hope is to prove that an elastic, frictional model for parallel folding is not only valid, but

also that such work has not been undertaken before. The history of geological folding and buckling theory breaks down nicely into three sections. The first section concentrates on the early ideas of geological folding. This predominately involves the buckling of a single elastic layer, although does stretch to some theory and experimentation into multilayer concentric waves. The second part describes the revolution to geology caused by Biot, who threw out the notion of elasticity, proclaiming that viscosity dominated the deformation of rocks and introduced concepts taken from thermodynamics to model strata. This section also shows the beginnings of non-synchronous buckling theory that would negate some of the major assumptions of Biot's work. The final part leads up to this thesis by showing the development by structural engineers, particularly Michael Thompson and his contemporaries, of a general theory of buckling leading eventually to localization and cellular theories. This would subsequently be used by Giles Hunt and collaborators to look at geological phenomena.

1.2.3 Two-layer parallel folding with friction

Chapter 3, starts the main body of the thesis. We begin by introducing the most simple case, that of just two elastic layers confined in a matrix and subjected to axial loading. The behaviour of this system is studied using the total potential energy which consists of strain energy of bending, foundation energy, work done by load and most importantly the work done by friction included as a quasi-energy contribution. This model is influenced by the notion that in nature, energy will often be minimized and in a layered material, under large overburden pressure, the frictional resistance as strata slip relative to one another to stop voids, becomes non-trivial. Using Fourier analysis, a sinusoidal single degree-of-freedom Galerkin approximation is shown to be a justified first estimate. Hence the stationary values of the total potential are explored, giving expressions for both the critical load and wavelength. The bifurcation diagram has the appearance of the symmetric imperfect strut, and thus the effects of adding an extra small bias are easily assessed, more importantly it presents us with the visualization of a *jammed region*.

1.2.4 The nonlinear differential equation

Chapter 4 follows on from the previous chapter by finding the stationary solutions of the potential energy over all monotone admissible functions from the calculus of variations. This results in a fourth order ordinary differential equation for the response of the two-layer system and boundary conditions in the third derivative represent a step-change in the shear force. Initially removing the foundation, the differences (and similarities) between the linearized differential system and the Galerkin model are explored. A phase plane representation highlights the effect of the third derivative, which changes direction as the jammed region is traversed allowing further deflection of the buckle. Re-introducing the foundation stiffness leads to a critical load that agrees with the Galerkin analysis of Chapter 3 and to two methods of wavelength selection. The chapter finishes with a description of the numerical continuation code AUTO (Doedel *et al.*, 1997), which when used to find solutions to the linearized and full nonlinear model shows that, over much of the post-buckle range, the discrepancies between the two are slight. The work from Chapters 3 and 4 has been published in the 2003 paper (Budd *et al.*, 2003).

1.2.5 Sequential buckling

Cubic B-splines have continuous derivatives up to second-order, but allow discontinuities of third derivative. In much the same vein as the Galerkin approximation, in Chapter 5 cubic B-splines are introduced into the two-layer potential energy functional developed in Chapter 3. With inherent destabilization already present in the formulation, a restabilizing nonlinearity is added to the foundation; this has the effect of making the wavelength dependent on both the load and the amplitude. The single spline (one hump) model is very similar to the Galerkin; however, the two-spline model allows for serial folding as the two humps can have different amplitudes. Thus, we obtain *primitive* localized and periodic solutions. By studying the stationary values of the superposition and of the potential energy, it is possible to follow the development of a single hump through to a second, with increasing end-shortening. The work described in Chapter 5 has been submitted to the *Journal of Structural Geology* (Hunt *et al.*, 2005).

1.2.6 Multilayer parallel folding and conclusions

Chapter 6 completes the main body of work of the thesis by finding the full elastic, frictional, multilayer energy function. When compared with the first instability of experimental load-deflection plots gathered from paper multilayers embedded in a foam matrix, constrained laterally and compressed axially, there is very good agreement. The chapter begins with an explanation of the test procedure and an analysis of the data obtained from experiments. The multilayer model is formulated in terms of a single thick layer, which is divided into an even number of identical substrata and follows closely the method shown in the third chapter. As in Chapter 5 a restabilizing nonlinearity is added to the foundation. The constraints of the model encourage linearization and the previous Galerkin analysis gives the potential energy and wavelength explicitly. After Chapter 4, the linear ordinary differential equation and boundary conditions are obtained via the calculus of variations and again the physicality of the system is explored. Lastly, the multilayer model is compared with experimental results; a fairly detailed discussion as to how the relevant parameters are extracted from the results, shows that friction, overburden, and compressive load are simple to obtain. However, the foundation stiffness, which has an influence on the post-buckle response and wavelength is more difficult. This work has recently been submitted for publication in the *Journal of the Mechanics and Physics of Solids* (Edmunds *et al.*, 2005)

Finally, Chapter 7 brings the thesis to a close, by summarizing the conclusions to be drawn from the research and remarking on possible further work that could be undertaken as a result of the findings.

1.3 Geology fundamentals

In order to bring together the physicality of the real situation and the modelling theories that are applicable, we start by introducing the different subject areas separately, concentrating on the terminology and ideas that will prove useful in building up this body of work.

As parallel folding is predominantly found in geological outcrops—it is what

first brought this form of buckling to the author's attention—we shall take the studies in this direction. Hence, to this end, the following section begins by listing popular definitions used by geologists to describe the common natural phenomena they encounter. This is then followed by a brief look at the arguments as to the make-up of the Earth's crust and how and where geological folding might occur. Some of this discussion will be expanded on in Chapter 2, where a more comprehensive review of the literature is given.

1.3.1 Geological definitions

The following are fairly precise geological descriptions that are fundamental to the more technical geological concepts mentioned throughout this thesis. Unless otherwise stated, many of these definitions are adapted from the textbook "Analysis of Geological Structures" (Price & Cosgrove, 1990).

Definition 2 *Folds*

Folds are a commonly occurring structure in deformed rock; they are formed when planar features or linear features are deflected into curvilinear or curvilinear structures. They develop on interfaces, single layers, *multilayers* and rock fabrics and come in a wide variety of geometries and sizes. A common feature is that they show marked periodicity and a number of folds occurring together form a *train* of folds. The two surfaces that enclose a fold are called the *enveloping surfaces*.

Definition 3 *Bending*

Bending is the term used to describe the flexuring of a layer induced by compression acting at an high angle to the layering.

Definition 4 *Layers*

Layers are two adjacent surfaces. A single layer is usually a vein in a massive host. However, if adjacent competent layers in a sedimentary sequence develop different wavelengths and amplitudes, this is termed *disharmonic* folding and the layers are still isolated.

Definition 5 *Multilayer*

Multilayers are sedimentary sequences and are encountered more often than single layers. Despite differences in thickness and mechanical properties, if all layers buckle with the same wavelength and amplitude, this is termed *harmonic folding* with the layers behaving mechanically as a multilayer. This occurs if the strains associated with each competent layer developed in the matrix during buckling, called the *zone of contact strain*, are compatible and overlap. Ramsey (1967) determined that this zone is at less than one percent of its original value by a single wavelength away. Experiments and fieldwork support this notion and layers very close together act effectively as a single anisotropic layer, the geometry of which is decidedly rounded.

Definition 6 *Fold profile*

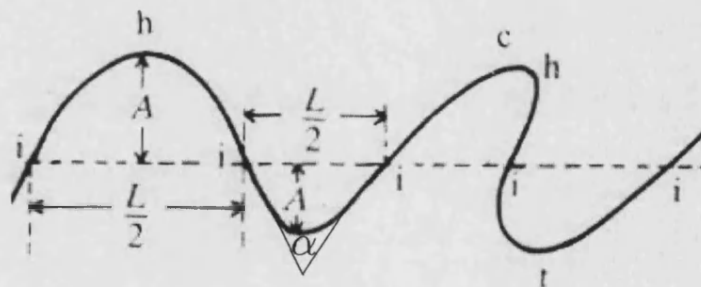


Figure 1.2: Profile of fold: h and i are hinge and inflection points; c and t denote the crests and troughs of the fold; the dashed line is the median surface; α is the interlimb angle and A and L are the amplitude and wavelength of the fold. (After Price & Cosgrove 1990)

The intersection of the folded surface on a plane normal to the fold axis is known as the *fold profile*. The geometrical features of a fold profile are shown in Fig. 1.2. Goguel (1962) highlighted the importance of choosing the fold profile when classifying folds, by pointing out that parallel folds cut at an oblique look like *similar folds* (see Definition 10 below and §2.2).

Definition 7 *Hinge and Inflection points*

The *hinge* points are those of maximum curvature and *inflection* points occur where the curvature is zero (Fig. 1.2). The *crest* and *trough* are the highest and lowest points of the fold respectively (Fig. 1.2). It is generally considered that two adjacent inflection points mark the limits of the fold, which is divided into a *hinge zone* and *fold limbs*. These are defined by Ramsey (1967) respectively as the areas with curvature greater than, and less than, the circular arc drawn with i_1i_2 as the diameter. Of course this definition is unhelpful if the curvatures are equal or small. The surface joining the inflection points is called the *median surface* (Fig. 1.2).

Definition 8 *Interlimb angle*

The *interlimb angle* is the minimum angle between the limbs in profile (Fig. 1.2).

Definition 9 *Amplitude and Wavelength*

The *amplitude* is the perpendicular distance between the median surface and fold hinge and the *wavelength* is the distance between alternating inflection points or twice the distance between adjacent ones (Fig. 1.2).

Definition 10 *Dip isogons*

The orientation of a fold's axial plane can be defined by a *dip* and *strike* value. These are the angle of the plane with respect to the horizontal, and the horizontal direction at right angles to the dip, respectively. By joining points of equal dip value on a profile section, we obtain the method of *dip isogons* which can be used to classify folds. To construct for a fold profile, a series of tangents are drawn to each folded surface, and the dip isogons are then formed by connecting the points of equal dip on adjacent surfaces (Fig. 1.3).

Ramsey (1967) gave a classification of folds based on the curvature of the arcs and the convergence of the dip isogons. The folds are divided into five classes on

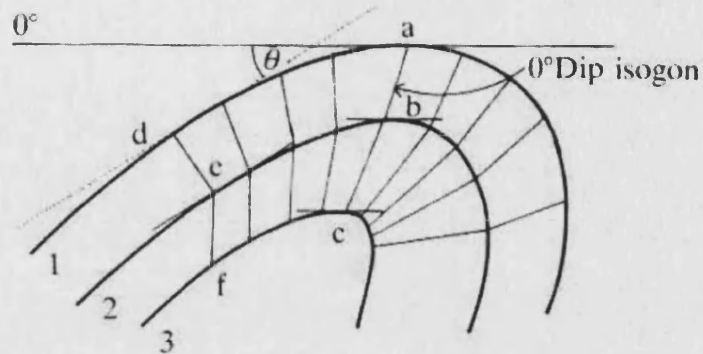


Figure 1.3: Construction of dip isogons. (After Price & Cosgrove 1990)

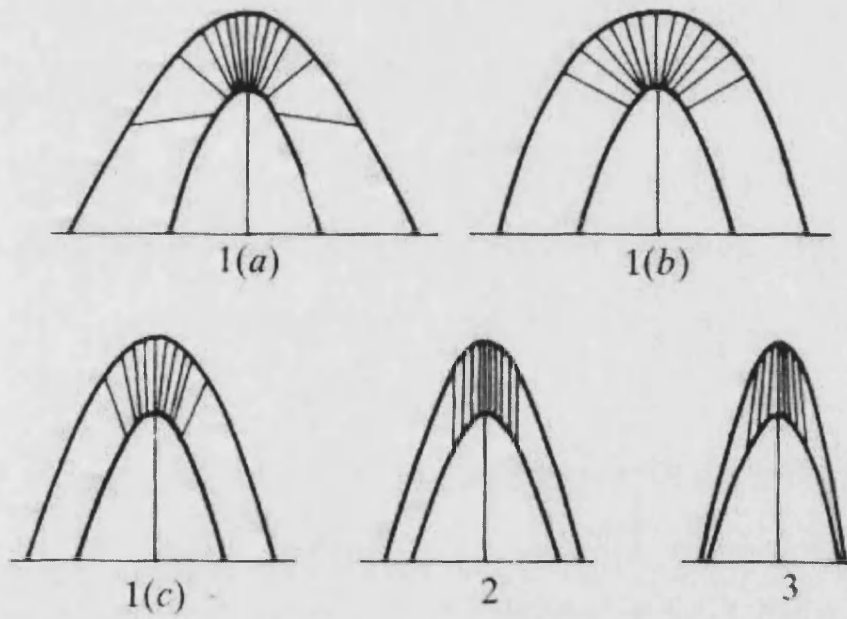


Figure 1.4: Classification based on dip isogon patterns: 1(a) Strongly convergent, 1(b) Parallel, 1(c) Weakly convergent, 2 Similar and 3 Divergent. (After Ramsey 1967)

the basis of the dip isogon patterns (Fig. 1.4). For Class 1 folds, the dip isogons converge from the outer to inner arc. Hence, Class 1 folds have deformed by bending only with no shearing. There are three types of Class 1 fold: 1(a) and 1(c) have strongly and weakly converging patterns respectively. The parallel fold is given a specific class of 1(b) where the isogons are normal to the boundary surface. Ramsey stated that competent folds are usually of Class 1, closely approximating a parallel fold. Class 2 are *similar folds*, where the isogons are parallel to each other and Class 3 are diverging. For the latter two categories shear deformation becomes the prevalent folding process and can be compared to the buckling at the core of a loaded sandwich panel (Hunt & Wade, 1998; Wade, 1998; Wade, 2000). The power of this technique is that often folds change type throughout a multilayer and hence each layer can be classified separately.

Definition 11 *Flexural flow/slip folds*

Many sedimentary strata have a well-developed plane parallel stratification, and this inherent weakness in the rocks controls the type of internal buckling. The individual rock layers are flexed and the outermost layers slip over the inner layers toward the fold hinge zones. The folds developed in this way have a true parallel form and are sometimes known as *flexural folds*. Ramsey (1967).

From the above definition *flexural folds* develop in layers with high anisotropy; for example, they can be produced by compressing a pack of paper parallel to the layering. As the pack buckles, sheets slide over each other, with the maximum slip on the limbs at the inflection points and decreasing towards the hinges where it is zero. The maximum strain is found at the inflection points, with no strain on the hinges (Fig. 1.5). Another important feature of flexural folds is that the layers maintain their initial thickness (Hobbs *et al.*, 1976).

If the slip planes are close together, layer-parallel shear is uniformly distributed across the folded layer on a granular scale, this is a true *flexural flow fold*. If more widely spaced then layer-parallel shear is not uniformly distributed, but concentrated on the bedding planes and is thus discrete, these are *flexural slip folds*.

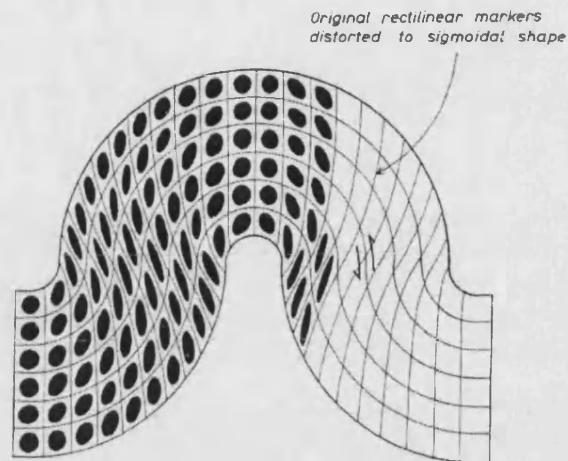


Figure 1.5: Strain distribution of flexural flow/slip. (After Ramsey 1967)

Definition 12 *Tangential longitudinal strain*

Tangential longitudinal strain is the strain pattern that develops when an homogeneous, isotropic layer is buckled; it has maximum strain at the hinges and none at the inflection points. The outer arc (the *extrados*) of the hinge is in extension and the maximum principal extension is parallel to the layer boundary. The inner arc is compressed and the minimum principal extension is also parallel to the layer boundary. These two states are separated by a line with no strain—the *neutral axis* and strain increases normal to the neutral plane. If the extrados fractures, the neutral axis moves downwards, as the effective thickness of the layer is altered (Price & Cosgrove, 1990).

Some of the more pertinent features of tangential longitudinal strain were mentioned by Hobbs *et al.* (1976), the most important being that whilst the neutral surface maintains its initial area and the layer maintains its initial thickness, there is extension on the outer arc where the area is increased and shortening on inner arc where the area decreases. This corresponds to engineering bending theory.

Real folds often show features of both flexural slip and tangential longitudinal strain and Ramsey (1967) stated that in nature both tangential longitudinal strain and flexural slip generally proceed together.

Definition 13 *Décollement (detachment along a basal shearing plane)*

Décollement is the detachment of the upper cover from its substratum (i. e. delamination), both of which may then deform independently and, in fact, the latter may not be deformed at all (de Sitter, 1964). This process is not restricted to any particular surface; there could be several possible places for detachment, but it does depend on the competency contrast of the cover. Basal detachment is very common in parallel folding as concentricity cannot be sustained below a certain point (often where the material forms a cusp), here incompressibility means that the layers crumple or fault.

1.3.2 Elasticity and viscosity

Rocks often deform through either elastic bending or through shearing, which can be elastic or viscous in nature. The elastic properties of rocks is a subject studied in greater detail in Chapter 2, where evidence from previous literature will be highlighted in order to validate the modelling ideas used throughout the remainder of the thesis. However, before proceeding to a discussion on elastic buckling theory, it is useful here to have some elucidation as to why this theory might be applicable. Except where referenced otherwise, much of the following has been influenced by Price & Cosgrove (1990). It is clear from reading their textbook that although there has been much debate in geological circles as to the deformation mode of folds, viscosity advocates have tended to dominate the field, to the point where even when evidence points to the contrary, viscous modelling techniques have been used.

Definition 14 *Elastic*

A body is *perfectly elastic* if when the stress is removed deformation completely and instantly disappears. The limit of the distortion, by bending or stretching, that a body can undergo and still return to its original form is called the *elastic limit*. Usually elasticity is a linear response described by Hooke's law and so within the elastic limit the strain ϵ is directly proportional to the stress σ producing it, i. e.

$$E = \frac{\sigma}{\epsilon}. \quad (1.1)$$

Here E is the *Young's modulus* (also know as the *modulus of elasticity* or *elastic modulus*), which is a measure of the stiffness of the material and characterizes its (tensile) strength.

If an elastic body is undergoing deformation by shearing or twisting, then the *shear strength* of the material is given by the *shear modulus* (or *rigidity modulus*) G . G is defined as the ratio of the shear stress τ and (engineering) shear strain γ

$$G = \frac{\tau}{\gamma}, \quad (1.2)$$

i. e. the shear modulus is the initial linear elastic slope of the shear stress-strain curve.

Definition 15 *Newtonian fluids and Viscosity*

For many liquids the relationship between shear stress τ and shear strain rate $d\gamma/dt$ is linear

$$\eta = \frac{\tau}{d\gamma/dt}. \quad (1.3)$$

Liquids obeying this are *Newtonian* and if the relationship is nonlinear, the liquid is *non-Newtonian*. The *viscosity* η is analogous to the elastic shear modulus G .

Although the stress-strain relationship of rocks is not always linear, the deviation is usually so small that a single value is given for the elastic modulus E . Strong rocks (i. e. those with an higher yield point) tend to exhibit high values of elastic modulus and a three-fold increase in strength is accompanied by a ten-fold increase in E . Experimental values of E for different rocks when subjected to low and high overburden pressure are shown in Table 1.1 (de Sitter, 1964). As can be seen from Table 1.1, the limits of the elastic rigidity are rather small and Biot (1961) argued that because the range of the coefficient of viscosity of rocks is much larger, this must account for the large number of fold types seen.

Biot implied that deformation occurs at such large depths and pressures that rock are likely to liquefy and hence viscosity is the primary influence on the deformation mode. This is contentious as often folds, particularly parallel folds, develop in the uppermost levels of the crust (de Sitter, 1964), and at these levels

Rock type	E (GPa)	
	$P_r = 0.1$ GPa	$P_r = 400$ GPa
Granite	0.24–0.61	0.45–0.84
Diabase	1.02–1.07	1.14
Schist	0.71	-
Sandstone	0.64	0.96
Limestone	0.58–0.63	0.63
Dolomite	0.71	-

Table 1.1: After de Sitter (1964), the elastic modulus E of different rocks at low and high overburden pressures P_r .

the layers will be solid and competent. The deformation of the beds is thus most likely to be elastic or elastic-plastic (Van Hise, 1894; Goguel, 1962; de Sitter, 1964; Price & Cosgrove, 1990). Price & Cosgrove (1990) stated that folding tends to be more rounded if a material has elastic-plastic behaviour and strain hardening.

There is no denying that pressure has an influence on the elastic modulus, as shown in Table 1.1, and hence plays a role in deformation. Below a limiting pressure rocks often break before they permanently deform, although, under high confining pressure the same material deforms smoothly (Hobbs *et al.*, 1976). Hence, the solid does not rupture, but flow and the pressure raises the elastic limit and changes the competency (de Sitter, 1964). Such changes even suggest that the rich variety of folds, that Biot feels are not feasible using elastic considerations, are possible, especially when localization and spatial chaos theories are introduced (see §1.6.1, 1.6.2 and 2.4).

1.3.3 Pressure and friction

The importance of overburden pressure to the deformation of rock has already been mentioned above, but it also has a secondary role in the folding process. Under pressure an elastic sedimentary sequence subjected to axial compression implies that frictional sliding will cause shear stresses parallel to the layering and strain results from the frictional resistance to slip (Price & Cosgrove, 1990). Hence the conclusion that rocks are elastic solids, under reasonable pressure, means that friction becomes of vital importance to the folding mechanism.

A reasonable estimate for the confining pressure is given by simply looking at the *lithostatic pressure*—the hydrostatic pressure generated at a depth due to the weight of the rocks (Price, 1970; Hobbs *et al.*, 1976)

$$\sigma_z = \rho_b g z, \quad (1.4)$$

where ρ_b is the bulk density, g acceleration due to gravity and z the depth. Reasonable values for the bulk density and depth are $\approx 2.5\text{kg/m}^3$ (Price & Cosgrove, 1990) and $\approx 10\text{km}$ (Van Hise, 1894) respectively, using these values we find that the lithostatic pressure is ≈ 2.5 kbars.

Values for the coefficient of friction of rock sliding on rock are stated by various sources and shown in Table 1.2. In practically all cases (Price & Cosgrove, 1990;

Source	μ	Situation/Rock type
Price & Cosgrove	0.577	Sandstone
	0.75	Frictional sliding on faults
	0.5–1.0	Shear induced pseudotachylite
	0.27	Clay
Rudnicki & Rice	0.4–0.9	Shear banding
Price	0.42–0.84	Fault movement
McClintock & Walsh	0.9–1.0	Marble
	0.7–0.8	Berea sandstone and shale

Table 1.2: Various values of friction cited for differing situations.

Rudnicki & Rice, 1975; Price, 1970; McClintock & Walsh, 1962) it can be seen that the value for the coefficient of friction is in the range $0.4 \leq \mu \leq 1$, and the consistency of the values means it is safe to assume that they are realistic. The exception to the above range is clay, which has a much lower friction coefficient as a result of its incompetency.

In many cases friction is measured in cold, dry rocks in a near surface environment. However, the crust is a porous solid, and hence liquid is present throughout. The liquid at each point has a different pressure, which varies with depth and pressure losses occur as the liquid moves through the rock from areas of high to low pressure (Goguel, 1962). The fluid and more specifically *fluid pressure* has an effect on the friction coefficient.

Bayly (1992) calculates how the friction is altered by introducing the *effective coefficient of friction*. After a dry material has failed, if slip occurs on a single

fracture plane

$$\text{Shear stress for slip} = \mu(\text{normal stress on fracture plane}) \quad (1.5)$$

where μ , the coefficient of friction, is constant over a wide range of normal stresses. If the material carries pore fluid then

$$\begin{aligned} \text{Shear stress} &= \mu(\text{normal stress} - \text{fluid pressure}) \\ &= \mu(\text{effective stress}) \\ &= \mu'(\text{normal stress}) \end{aligned} \quad (1.6)$$

where μ' is the effective coefficient of friction.

Hence as the fluid pressure is increased the effective coefficient of friction gets smaller and the values given in Table 1.2 might be considered to be slightly high in real geological folding.

1.3.4 Synchronous and non-synchronous buckling

A further fact used to suggest that viscous deformation dominates is that the time scales involved in geological folding are huge. This is based on the notion that all folds are formed at the same time. Hence it is necessary to give consideration as to how periodic folding patterns are formed: either simultaneously in a wavetrain or by some non-synchronous process whether random or sequential.

The latter, where each wave forms one after the other in sequence (Fig. 1.6) is known by several names: sequential amplification (Price & Cosgrove, 1990) and serial folding (Blay *et al.*, 1977) are both popular in the geology field, whereas cellular buckling (Hunt *et al.*, 2000b) is the usual terminology in structural engineering.

Whichever term is adopted, the important underlying point is that serial buckling is a phenomenologically different process to that of the wavetrain. If we consider that folds are initiated individually, then a single fold is formed in a significantly shorter period than the few million years usually stated (Price, 1975); this adds weight to the argument that folding is elastic in nature. Also, from a structural

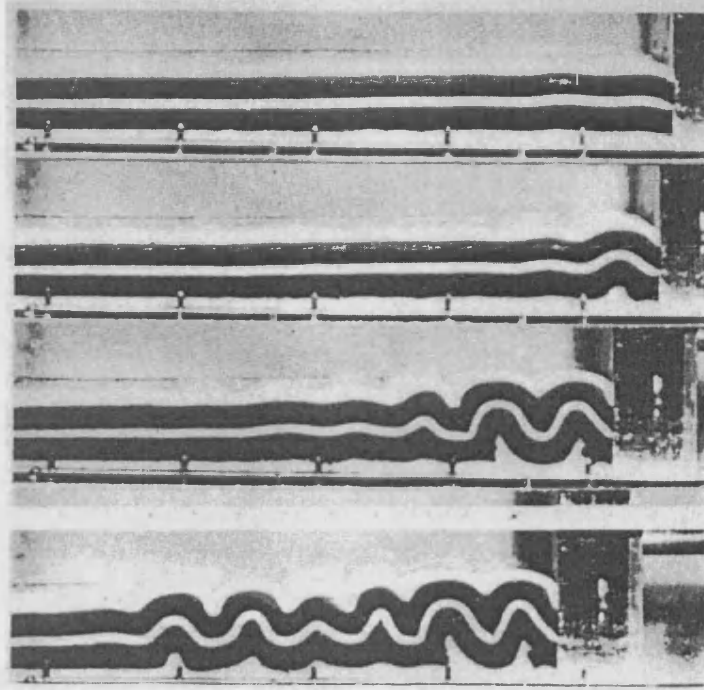


Figure 1.6: Serial buckling of a viscous multilayer. (After Blay *et al.* 1977)

viewpoint, as will be shown later, the wavelengths of the two types of folding are very different (Budd & Peletier, 2000).

1.4 Bending theory and the elastic strut

We now turn our attention to the bending of a beam. The theory developed to find the deflection of an axially loaded strut will prove to be at the core of the techniques we need to model a sequence of elastic strata. In general the equations governing the behaviour of a beam will need little adaptation to be extended to extra layers as the friction on the bedding planes adds only one additional term to the potential energy formulation described in this section. In fact in linearization of the problem to small deflections, it will be shown that the friction only affects the boundary conditions; however, this still changes the response of the system to a remarkable degree.

In this section we slowly build up the solution of a buckled beam, beginning with the fundamentals of simple bending theory. Under small deflections this

simplifies the problem of finding the curvature, as it can be assumed that the horizontal distance and the distance around an arc are the same. Moving on to more exact theory under large deflections, we can then find the curvature for the *elastica* and, using the total potential energy and stability arguments, follow Euler's method of solution for modelling the wave-profile of the axially loaded strut. We finish by mentioning how imperfections might affect the system.

1.4.1 Simple bending theory of a beam

Pure bending

Consider a portion of a beam of rectangular cross-section, in *pure bending* (i. e. with no shear). Bending is to a *circular shape* over this region. For a symmetric cross-section, the middle layer or *Neutral Axis* (N. A.) is unstressed, the top is in compression and the bottom is in tension. Consider a longitudinal fibre, depth y from the Neutral Axis (Fig. 1.7). As the length is proportional to the radius

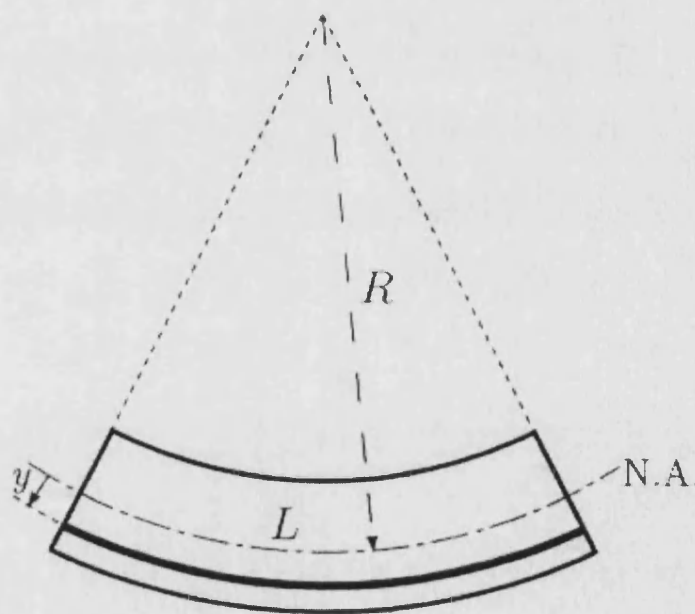


Figure 1.7: Pure bending of a single layer.

$$\frac{R}{R+y} = \frac{L}{L+\delta L} \quad (1.7)$$

Curvature

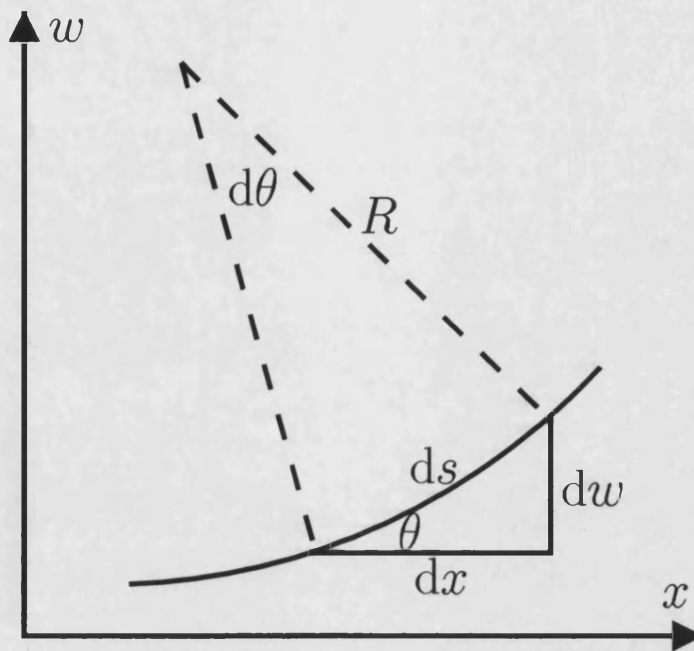


Figure 1.8: Curvature over a small angle.

Definition 16 *Curvature*

For a curve C , the *curvature* κ is defined as

$$\kappa = \frac{d\theta}{ds}, \quad (1.8)$$

where $\theta(s)$ denotes the angle which C makes with some fixed reference axis as a function of the path length s along the curve.

Under *small deformations*, the curvature at a point can be given in terms of orthogonal naturally scaled coordinates (x, w) (as shown in Fig. 1.8). We have that

$$\tan \theta = \frac{dw}{dx}. \quad (1.9)$$

If the x -axis is tangent to C at the point, then $\tan \theta \rightarrow \theta$ as $dx \rightarrow ds$, hence the curvature can be equivalently defined in terms of x and w as

$$\kappa = \frac{d^2w}{dx^2}. \quad (1.10)$$

The sign convention for curvature is dependent on the coordinate axes direction (Timoshenko & Gere, 1973) and using Fig. 1.8, the curvature of the beam axis is positive when bent concave upwards. The sign convention also says that positive moment M produces compression on the top of the beam and hence positive M implies that the curvature is also positive

$$\kappa = \frac{M}{EI}, \quad (1.11)$$

where E is the *Young's modulus* of the beam and I is the second moment of area. Hence EI is the bending stiffness of the beam.

Thus, using (1.10), if we assume small deflections

$$\kappa = \frac{d^2w}{dx^2} = \frac{M}{EI}. \quad (1.12)$$

(1.12) is the basic differential equation for the deflection curve and is only valid when Hooke's law applies, the deformation is small and is by pure bending.

From Fig. 1.8, with *large deformations*, we have that

$$\sin \theta = \frac{dw}{ds}, \quad (1.13)$$

and also that

$$\frac{1}{R} = \frac{d\theta}{ds}. \quad (1.14)$$

Using the chain-rule, from the the expression (1.13), we get that

$$\cos \theta \frac{d\theta}{ds} = \frac{d^2w}{ds^2}. \quad (1.15)$$

Hence, using simple trigonometry,

$$[1 - \sin^2 \theta]^{1/2} \frac{d\theta}{ds} = \frac{d^2 w}{ds^2}, \quad (1.16)$$

and substituting (1.13) back into this and rearranging, we obtain an equation for the curvature over large slopes

$$\frac{d\theta}{ds} = \kappa = \frac{w''}{[1 - (w')^2]^{1/2}}, \quad (1.17)$$

where ' denotes differentiation with respect to the arclength s .

1.4.2 The elastica

The exact differential equation describing the shape of an elastic curve (*elastica*) will now be formulated. It was first solved by Euler (1744), using his now famous *calculus of variations*.

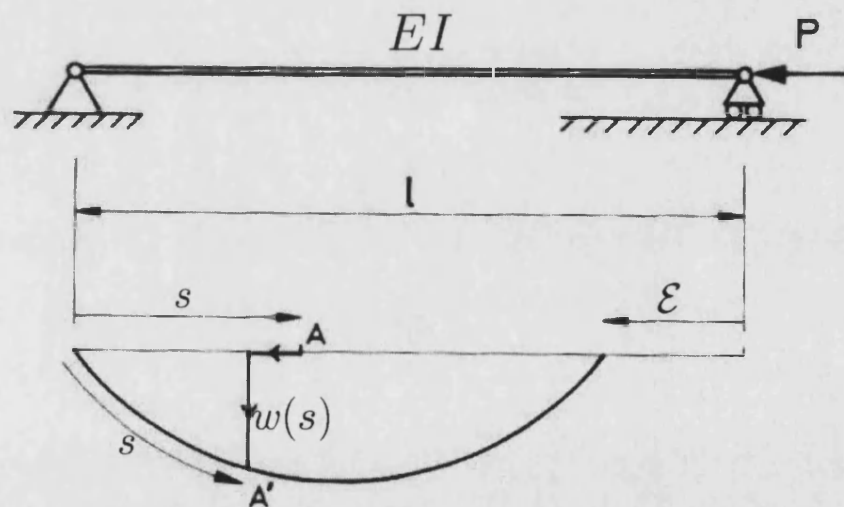


Figure 1.9: A pin-ended Euler strut. (After Thompson & Hunt 1973)

After Thompson & Hunt (1973), to set up this problem consider a pin-ended strut of length l and bending stiffness EI , simply supported and subjected to a load P acting in the axial direction (Fig. 1.9). The strut is assumed axially inextensible; thus the change in length of the column due to compression (i. e. pure squash) is neglected. Point A of the strut, originally a distance s from the left-hand side,

is displaced to A' with vertical component w . The centreline of the inextensible arclength is equal to s and the strut is specified by a function $w(s)$, $0 \leq s \leq l$.

There exists a load at which the beam starts to deflect; we call this the *critical load* and denote it P^C . If the load exceeds the critical value, $P > P^C$, then a large deflection is produced. If the arclength s is measured from the origin along the strut, we can find an exact solution for the curvature $d\theta/ds$ from (1.17). The bending moment of the bar equals the flexural rigidity multiplied by the curvature, hence

$$M = EI \frac{d\theta}{ds}. \quad (1.18)$$

1.4.3 Solving the elastica

To find the exact differential equation in order to solve the elastica, we follow Euler (1744) by considering the stationary solutions of the potential energy using the calculus of variations.

Potential energy function

The potential energy V of the loaded elastic beam is defined as:

$$\text{Total potential energy} = \text{Strain energy stored} - \text{Potential lost by loads},$$

hence

$$V = U - P\mathcal{E}, \quad (1.19)$$

where \mathcal{E} is the end-shortening.

If the moment M is constant, the beam is bent into a circular arc of curvature M/EI , and the angle subtended is $\theta = Ml/EI$. The maximum strain energy U

stored in the beam is (Timoshenko & Gere, 1973)

$$U = \frac{M\theta}{2} = \frac{EI\theta^2}{2l}. \quad (1.20)$$

If M varies along the length of the beam, then U is obtained by considering an element of length ds and integrating. With the curvature given as in (1.17), the strain energy functional is therefore

$$\begin{aligned} U &= \frac{EI}{2} \int_0^l \kappa^2 ds \\ &= \frac{EI}{2} \int_0^l (w''^2 + w''^2 w'^2 + w''^2 w'^4 + \dots) ds. \end{aligned} \quad (1.21)$$

The deflection of P is

$$\begin{aligned} \mathcal{E} &= 1 - \int_0^l (1 - w'^2)^{1/2} ds \\ &= \int_0^l (1/2w'^2 + 1/8w'^4 + 1/16w'^6 + \dots) ds. \end{aligned} \quad (1.22)$$

Hence we have the total potential energy $V = U - P\mathcal{E}$ to which we apply the calculus of variations.

The calculus of variations

The potential energy has the form $V = \int_0^l F(w'', w') ds$, and we can apply the calculus of variations by taking a small increment of V

$$\delta V = \int_0^l \left(\frac{\partial F}{\partial w''} \delta w'' + \frac{\partial F}{\partial w'} \delta w' \right) ds. \quad (1.23)$$

Integration by parts yields

$$\begin{aligned} \delta V &= \left[\frac{\partial F}{\partial w'} \delta w \right]_0^l + \left[\frac{\partial F}{\partial w''} \delta w' \right]_0^l - \left[\frac{d}{ds} \frac{\partial F}{\partial w''} \delta w \right]_0^l \\ &+ \int_0^l \left(\frac{d^2}{ds^2} \frac{\partial F}{\partial w''} - \frac{d}{ds} \frac{\partial F}{\partial w'} \right) \delta w ds. \end{aligned} \quad (1.24)$$

When $\delta V = 0$ for all δw , the last term is zero. The brackets are then eliminated by appropriate boundary conditions as follows: the first and third brackets vanish as $w(0) = w(l) = 0$ and as the second bending moment is zero at both ends,

$w''(0) = w''(l) = 0$, hence the second bracket also vanishes. Thus the analysis has found the *Euler equation* for a pin-ended strut and justified the boundary conditions. Performing the differentiations the equation becomes

$$w''''(1 - w'^2)^{-1} + 4w'''w''w'(1 - w'^2)^{-2} + w''^3(1 - 3w'^2)(1 - w'^2)^{-3} + P/EIw''(1 - w'^2)^{-3/2} = 0. \quad (1.25)$$

Under suitable rescaling of parameters, when linearized (1.25) is the same as the Swift-Hohenberg equation (Bensimon *et al.*, 1988; Nepomnyashchy *et al.*, 1994).

Solution and stability

We are interested in the initial post-buckling solution. To study this we use the potential energy to look at the stability of the static equilibrium paths. More specifically, there is a loss of stability of the pre-buckling state bifurcating to a buckled configuration. Static equilibrium here is as defined by Liapunov (Thompson & Hunt, 1973): an equilibrium is stable if and only if all motions of the system close to the equilibrium state remain close for all time.

A simple way to think about stability is given by Timoshenko & Gere (1961) who consider a ball in a potential well. A ball:

- (a) On a concave surface is in *stable equilibrium*;
- (b) On a convex surface is in *unstable equilibrium*;
- (c) On an horizontal plane is in *neutral equilibrium*.

For (a), displacement of the ball will raise its centre of gravity, work is needed to produce this displacement and the potential energy increases. For (b), displacement of the ball will lower its centre of gravity and the potential energy decreases. Thus for stable equilibrium the energy is a *minimum* and for unstable equilibrium it is a *maximum*.

The above follows directly from the two basic axioms of stability which say that stationary values of the potential energy with respect to each parameter is necessary and sufficient for equilibrium and also that if the stationary value is a relative

minimum, then this is necessary and sufficient for stability (Thompson & Hunt, 1973). These ideas are used in what Timoshenko & Gere call the *energy method* (Timoshenko & Gere, 1961): a small lateral deflection of the system, means an increase in the strain energy ΔU ; also the load P moves a small distance to do work, ΔT . The system is stable if $\Delta U > \Delta T$, unstable if $\Delta U < \Delta T$ and the *critical value* P^C is found when they are equal.

A method of solution of the elastica, that will prove useful later, is by harmonic analysis. This involves assuming the shape of the resulting wave-profile and substituting this shape into the potential energy. Following the energy method, the closer the assumed curve is to the exact one, the better the approximation of the true critical load.

For harmonic analysis, the change in deflection from the fundamental path is written as

$$w = \sum_{n=0}^{\infty} Q_n \sin \frac{n\pi s}{l}. \quad (1.26)$$

The Fourier harmonics represent the buckling modes of the strut and by varying Q_n various shapes of the curve are obtained, with more terms meaning a better solution. ΔU , ΔT and hence P are thus functions of Q_n and to find P^C , we need

$$\frac{\partial P}{\partial Q_n} = 0 \quad \forall n, \quad (1.27)$$

which defines the shape of the curve by giving Q_n .

Thus to first order the harmonic analysis yields that the resulting waveshape is sinusoidal and hence the critical load P^C is just the Euler buckling load

$$P^C = \frac{EI\pi^2}{l^2}. \quad (1.28)$$

This is correct for small deviations of a perfect strut, free to deflect with no disturbances and if the load-amplitude bifurcation diagram is studied, Fig. 1.10(a), under static equilibrium the strut is stable until P^C is reached when the equilibrium becomes unstable and the strut deflects left or right in an half-wave. Such buckling only begins to stabilize at large amplitudes, Fig. 1.10(b), and this is always the case unless imperfections or a foundation are added.

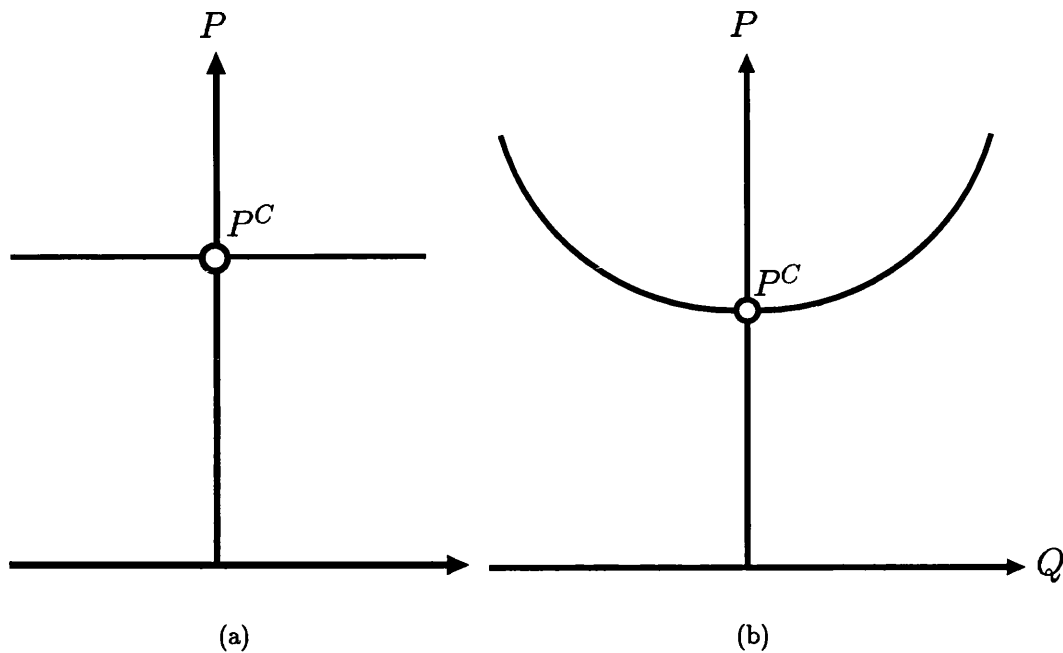


Figure 1.10: The bifurcation diagram for the (a) Linear and (b) Nonlinear perfect strut, where Q is the maximum amplitude of the deflection.

1.4.4 Imperfections

Manufacture of structural systems is never precise and inherent geometrical and material defects, mean that inevitable imperfections usually exist which can drastically alter the response. If there is a loss of stability of the imperfect system, this can lead to catastrophic consequences. By introducing a perturbation or imperfection parameter $\epsilon \neq 0$ into the potential energy function $V(\epsilon)$, we create a family of imperfect systems. When $\epsilon = 0$ we have the perfect system.

For different types of bifurcation, an imperfection will cause a different response. For the problem of a buckling strut the bifurcations are usually symmetric, unless a particularly large bias is introduced; thus we look more closely at the stable and unstable symmetric bifurcation point (Thompson & Hunt, 1973).

With a *stable symmetric bifurcation point*, Fig. 1.11(a), imperfections play no significant role, with $\epsilon > 0$ and $\epsilon < 0$ the equilibrium paths are continuously stable and rising. There is no failure load and the buckling is rapid as the critical load P^C is approached.

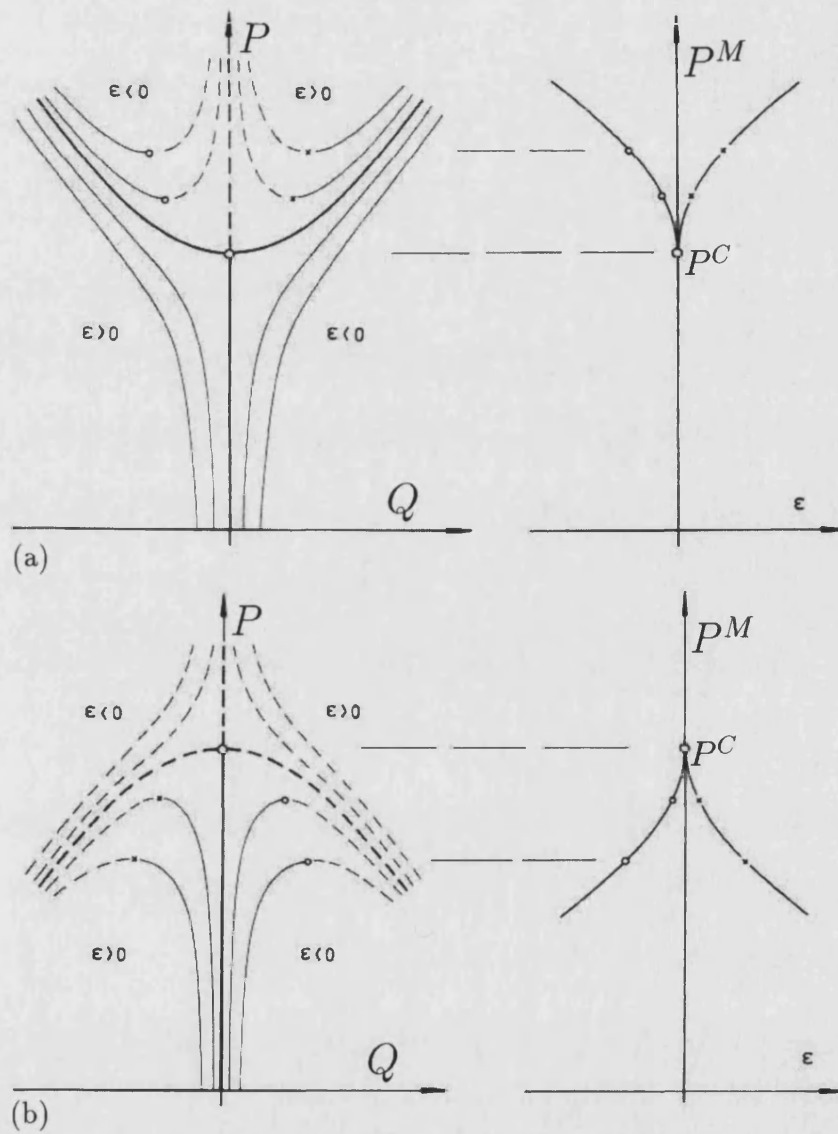


Figure 1.11: Families of imperfect systems for the (a) Stable symmetric and (b) Unstable symmetric bifurcation. (After Thompson & Hunt 1973)

In contrast, for the *unstable symmetric bifurcation point*, Fig. 1.11(b), whether the imperfection ϵ is positive or negative, failure occurs at the limit point with a reduced value of the load. The path plotting how the maximum load P^M changes with ϵ follows a two-thirds power law which yields a cusp.

1.5 Adding a foundation

Sedimentary sequences of competent layers are often embedded in a matrix of less competent (less stiff) material. In parallel folding, such a foundation is vital to the mode of deformation as it demarcates the limit of the folding, where the layers cusp, and also allows some lateral movement. The foundation may also take up some of the overburden pressure, allowing the folds to be more rounded.

The buckling of an elastic strut on a foundation is a subject that has been studied extensively in structural engineering and in order to attain the correct response from the foundation, many different models have been suggested. Although we, at least initially, choose a simple elastic foundation, for completeness it is useful to highlight the properties of those available. The section is concluded by briefly mentioning the energy formulation when an elastic matrix is added.

1.5.1 Foundation models

A good review of some of the various elastic and viscous foundation models is given by Kerr (1964). The simplest is the *Winkler* foundation consisting of closely spaced independent linear springs (Fig. 1.12). However, this model is often considered unrealistic as outside of the loaded region there is no displacement. To get around this the more complicated semi-infinite elastic continuum is an alternative. But as Kerr points out, many materials do not behave like either of the above and so models tend to proceed in one of two ways. Either it is assumed that there is interaction between the springs of the Winkler foundation; or assumptions are made as regards displacements and stresses of the continuum foundation.

Remarkably, Kerr stated that all extensions to the foundations mentioned turn

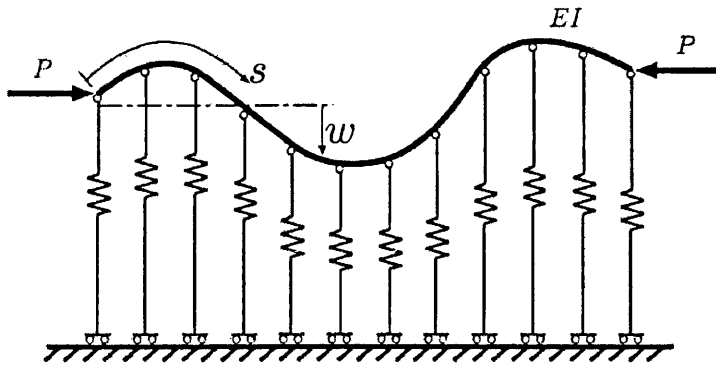


Figure 1.12: An elastic strut on a Winkler foundation under loading.

out to be essentially the same model, the *Pasternak* foundation. The Pasternak foundation assumes shear interactions between the springs, by connecting the ends of the springs to an incompressible beam. If dashpots and parallel dashpot-springs are added to the Pasternak foundation visco-elastic foundations can also be modelled.

From the above, the Winkler foundation is a linearized simplification of an elastic foundation; it provides resistance against lateral deflection, but not shear. Apart from the initial stiffness, the linearization removes much of the characteristics of the foundation and these need to be reintroduced. This is done by adding a nonlinear component that can either soften, stiffen or a combination of both (Hunt, 2005). Real foundations usually have a natural destiffening effect for small deflections followed by a strong restiffening for large deformations, especially as often the material is squashed by bends which exerts a large force in the opposite direction (Peletier, 2001b).

This is shown to be the case in Hunt & Wade (1998) which importantly talks about the material properties of a sandwich structure core. This is similar in nature to foam rubber which will later be used to represent the foundation in experiments (Chapter 6). It is found experimentally that the foam behaves *nonlinear* elastically when compressed, resulting from the cells making up the material at microscopic level. From Fig. 1.13, at first the foam is linearly elastic, then the cell walls buckle elastically causing loss of stiffness (which can even be negative); finally the opposite walls come into contact and the stiffness rises to close to the linear elastic value.

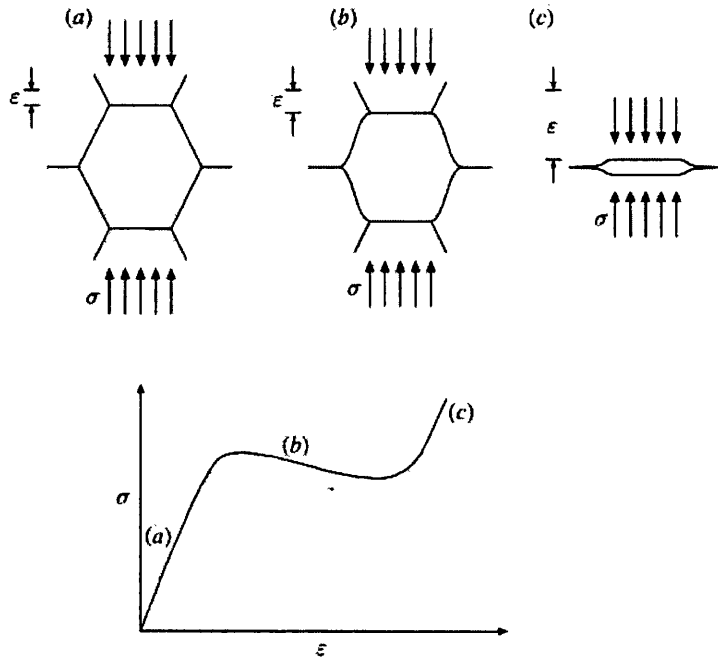


Figure 1.13: Foundation behaviour in compression at cell level. (After Hunt & Wadde 1998)

1.5.2 The strut on an elastic foundation

The situation is as shown in Fig. 1.9 and described in §1.4.2, with the inclusion that the strut rests on an elastic foundation of stiffness k per unit length. The foundation consists of a large number of springs tied to the strut and anchored at infinity, so that they remain perpendicular to the centre-line. The strain energy stored is (Thompson & Hunt, 1973)

$$U_F = \frac{k}{2} \int_0^l w^2 ds. \quad (1.29)$$

Using the harmonic analysis of §1.4.3, by substituting in (1.26), the same methodology is followed, adding that

$$\Delta U_F = \frac{kl}{4} \sum_{n=1}^{\infty} Q_n^2. \quad (1.30)$$

In finding P^C , we set all coefficients to zero except one Q_m , and hence the deflection and critical loads are (Timoshenko & Gere, 1961)

$$w = Q_m \sin \frac{m\pi s}{l} \quad \text{and} \quad P^C = \frac{\pi^2 EI}{l^2} \left(m^2 + \frac{kl^4}{m^2 \pi^4 EI} \right), \quad (1.31)$$

respectively, where m is the number of half-sinewaves in which the beam buckles. To first order

$$P^C = \frac{EI\pi^2}{l^2} + \frac{kl^2}{\pi^2}, \quad (1.32)$$

and finding the stationary value of the critical load with respect to the wavelength l , we find that l is given by

$$l = \pi \sqrt[4]{\frac{EI}{k}}. \quad (1.33)$$

1.6 Mathematical and engineering technical definitions

The following descriptions are of a mathematical nature and are predominantly from the dynamical systems field. Important to many nonlinear structural engineering problems, as will be shown at the end of the section, they are necessary for an understanding of the post-buckling solutions resulting from fourth order ordinary differential equations. Such equations were formulated in the last section when using potential energy methods to model the deflection of an elastic strut. In both the previous material on related subjects presented in Chapter 2, and the rest of the thesis, the Euler strut will prove to be a very helpful paradigm.

Unless otherwise cited, the definitions are amalgamated from a combination of sources: “Nonlinear Ordinary Differential Equations” (Jordan & Smith, 1977), “Nonlinear Dynamics and Chaos” (Strogatz, 1994), “Nonlinear Dynamics and Chaos” (Thompson & Stewart, 1986) and “Stability, Instability and Chaos: An Introduction to the Theory of Nonlinear Differential Equations” (Glendinning, 1994).

1.6.1 Dynamical systems definitions

Definition 17 *Manifold*

The *stable manifold* or *inset* of a fixed point is a set such that the first returns from points in the set approach the point as time tends to infinity.

The *unstable manifold* or *outset* of a fixed point is a set from which the first returns approach the point when time is reversed, i. e. time tend to minus infinity.

Definition 18 *Homoclinic*

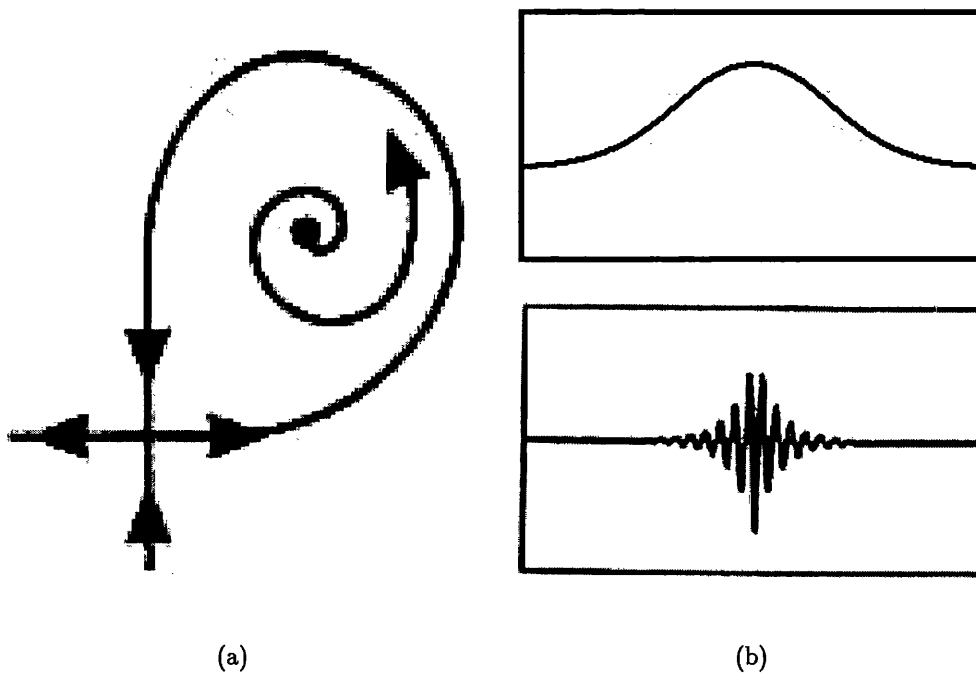


Figure 1.14: (a) The homoclinic bifurcation (After Glendinning 1994), (b) Top: An homoclinic wave-profile and Bottom: A wavepacket. (After Thompson & Virgin 1988)

An *homoclinic orbit* or *homoclinic connection* is a trajectory that approaches the same equilibrium (a saddle) as time tends to minus infinity and infinity. In other words a branch of the unstable manifold coincides with the stable manifold of the saddle. The behaviour of solutions near the homoclinic are dominated by the

behaviour near the stationary point and solutions slow down in a neighbourhood of this point. Hence an homoclinic connection may be thought of as a limit cycle of infinite period; by increasing the controlling variable, the attracting limit cycle oscillation has slowed down and ceased to oscillate.

A *saddle loop* or *homoclinic bifurcation* is an infinite period bifurcation that occurs when part of a limit cycle moves closer and closer to a saddle point. At the bifurcation the cycle touches the saddle point and becomes an homoclinic orbit, (Fig. 1.14(a)). This is structurally unstable; any perturbation will mean that the homoclinic does not exist, and reducing the controlling variable, the connection is broken and the periodic orbit disappears.

The resulting waveshape is shown in the top figure of Fig. 1.14(b). Often in geological folding we study localized periodic solutions. These take the form of an homoclinic orbit modulated by a sine function and are called homoclinic wavepackets (bottom figure of Fig. 1.14(b)).

Definition 19 *Heteroclinic orbit*

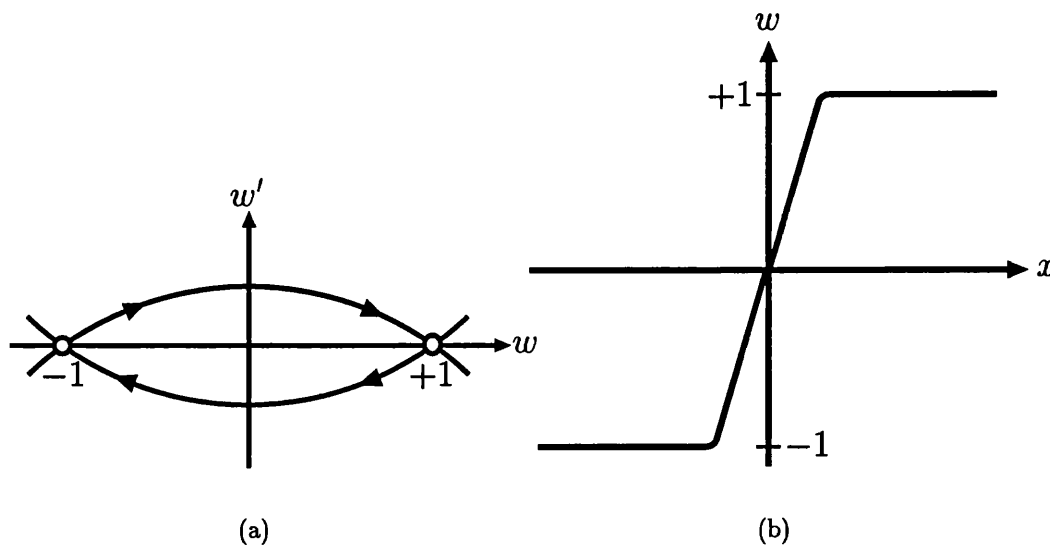


Figure 1.15: (a) An heteroclinic connection and (b) An heteroclinic wave-profile.

Twin saddle points joined by a pair of trajectories are called *heteroclinic trajectories* or *saddle connections* (Fig. 1.15(a)). Heteroclinics are often found in reversible or conservative systems where they take the solution from the flat

state to a periodic solution. The waveshape of an heteroclinic orbit is shown in Fig. 1.15(b).

Definition 20 *Pitchfork bifurcation*

The *pitchfork bifurcation* involves only stationary points and is found in systems equivariant under the transformation $x \rightarrow -x$ (i. e. with the system $\dot{x} = G(x, \mu)$, $-G(x, \mu) = G(-x, \mu)$). The system must satisfy the following conditions: $G(0, \mu)$, $G_\mu(0, \mu)$ and $G_{xx}(0, \mu)$ are zero for all μ , and G_{xxx} and $G_{x\mu}$ are always non-zero. A simple example is $G(x, \mu) = \mu x - x^3$.

The bifurcation is *supercritical* if the pair of stationary points is stable (Figs 1.16(a) and (d)), otherwise it is *subcritical* (Figs 1.16(b) and (c)).

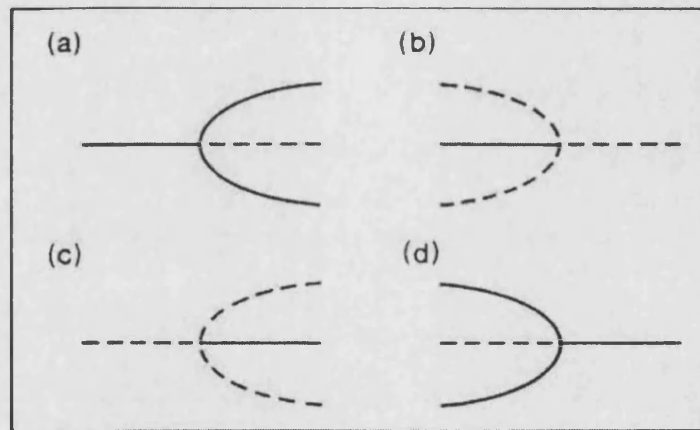


Figure 1.16: (a) Stable supercritical, (b) Stable subcritical, (c) Unstable subcritical and (d) Unstable supercritical pitchfork bifurcation. (After Glendinning 1994)

The pitchfork occurs in two distinct forms, stable (Figs 1.16(a) and (b)) and unstable (Figs 1.16(c) and (d)). The stable bifurcation is the cusp in which a stable equilibrium at the origin becomes a saddle and in the supercritical form two symmetric attractors. The catastrophic bifurcation is subcritical where two saddles shrink to a single stable saddle at the origin, i. e. the attractors and saddles are interchanged in the stable form.

Definition 21 *Lagrangian mechanics*

The *Lagrangian* $L(\mathbf{q}(t), \dot{\mathbf{q}}(t), t)$; where $\mathbf{q}(t)$ and $\dot{\mathbf{q}}(t)$ are the position and velocity at instant t , is given by

$$L = T - V. \quad (1.34)$$

T is the kinetic energy and V is the potential energy of the system. Conservation of energy in terms of L , comes when L does not depend explicitly on t ; the position and the velocity of the system determines the same value of L , whatever the time.

Definition 22 *Hamiltonian system*

Hamiltonian systems are differential equations for $\mathbf{p} \in \mathfrak{R}^n$, $\mathbf{q} \in \mathfrak{R}^n$ which (canonically) take the form

$$\frac{d\mathbf{q}}{dt} = \frac{\partial H}{\partial \mathbf{p}} \quad \frac{d\mathbf{p}}{dt} = -\frac{\partial H}{\partial \mathbf{q}}, \quad (1.35)$$

for the Hamiltonian function, $H(\mathbf{p}, \mathbf{q}, t)$. This has zero divergence and so an Hamiltonian system preserves volume and is non-dissipative; hence (1.35) is associated with reversible, frictionless systems. If when calculated (1.35) has a divergence less than zero then the system is dissipative.

The system arises from the general form of Newton's laws of motion, where \mathbf{p} is the general momentum and \mathbf{q} is the general coordinate of a mechanical system with n degrees-of-freedom. H is usually the sum of the kinetic and potential energies. If the system is stationary, then H is constant. As H is often the total energy of the system, this implies conservation of energy.

Definition 23 *Snap-back*

When an initial instability appears as a jump phenomenon under controlled end-displacement, it is so unstable that so-called *snap-back* behaviour is observed. The load can drop significantly as the system moves suddenly from a flat undeformed state to that of large localized displacement (Hunt *et al.*, 2000a).

Definition 24 *The Maxwell load*

The *Maxwell load* P_M , is the load at which the energy levels in the unbuckled and periodic post-buckled states are the same. No localized solutions exist below P_M and hence the Maxwell load marks the limit of appearance of localized solution (Hunt, 2005). For a linear elastic beam on a nonlinear foundation which stabilizes, destabilizes then restabilizes, propagation begins at the Maxwell load (Chater *et al.*, 1983).

Definition 25 *The Maxwell criterion*

When a system has an infinite critical load, the slightest disturbance can trigger snap-back. In this highly unstable situation the *Maxwell stability criterion* is sometimes adopted, where stability rests with global minimum of potential energy. This is commonly used in thermodynamics for modelling phase transitions (Hunt *et al.*, 2000a).

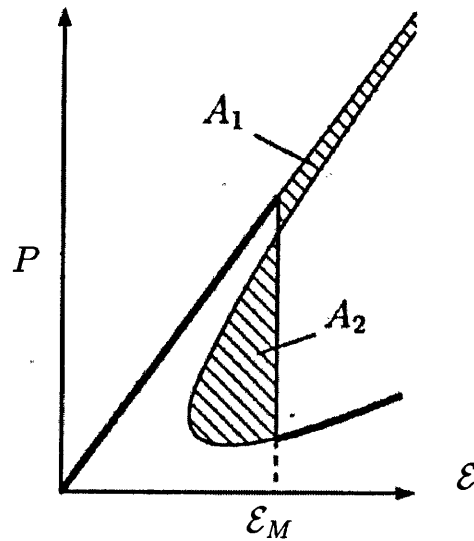


Figure 1.17: Finding the Maxwell displacement. (After Hunt *et al.* 2000)

The criterion gives the lower bound, with respect to the control parameter, at which the physical system has the potential to jump from a stable equilibrium state with higher load, to another different stable state at a lower load. Stability rests only with the lower energy state and if the end-displacement ϵ is controlled, when $(\epsilon = \epsilon_M)$, the *Maxwell displacement*, the minimum swaps at the same value of end-displacement (Wadee & Edmunds, 2005).

Referring to Fig. 1.17, to calculate \mathcal{E}_M the energies of interest are represented by areas A_1 —the energy to be overcome for the jump to occur—and A_2 —the released energy once the jump occurs—which need to be equal. The predictive power of the criterion depends on level of external disturbances (initial imperfections) being sufficient to cause the jump.

1.6.2 Localization and cellular buckling

Structures often buckle in a *localized* manner, where the buckle is confined to a specific region, rather than with the periodic form associated with the critical load. By considering static-dynamic analogies (replacing time with space), the definitions given in §1.6.1 can be used to show spatial chaos and localization. For example, if the critical load of an elastic strut on a foundation is studied using such analogies, it shows that the system is Hamiltonian. Spatial equations like the strut are reversible (although reversibility says there is no spatial analogy to damping), x can be replaced with $-x$ without changing the equation or solution and hence the Hamiltonian is conserved as x is varied (Hunt, 2005). The corresponding Lagrangian, represents the local contribution in x to the total potential energy of structure.

Adding a softening nonlinearity, the localized buckle pattern is seen as an homoclinic orbit when the critical load is approached (Thompson & Virgin, 1988). Looking at the two-dimensional portraits of an inverted stable cusp, the secondary path of which is the periodic solutions, below the critical load spatial localization corresponds to an homoclinic leaving and return to the phase-space origin (Fig. 1.18).

Thus, for a strut on a destabilizing-restabilizing foundation, far away from the critical load the solution has an homoclinic waveshape; but as the end-shortening increases and the load drops towards the critical load, we see a lengthening homoclinic connection from the fundamental equilibrium state to itself. In the limit this leads to heteroclinic connection from the unbuckled to post-buckled state and the solution changes to a periodic waveshape. Specifically this happens as the load approaches the Maxwell load (Budd *et al.*, 2001) and it has been argued that it is the minimum energy density periodic solution, picked out at Maxwell load, that governs the final buckle pattern (Hunt, 2005).

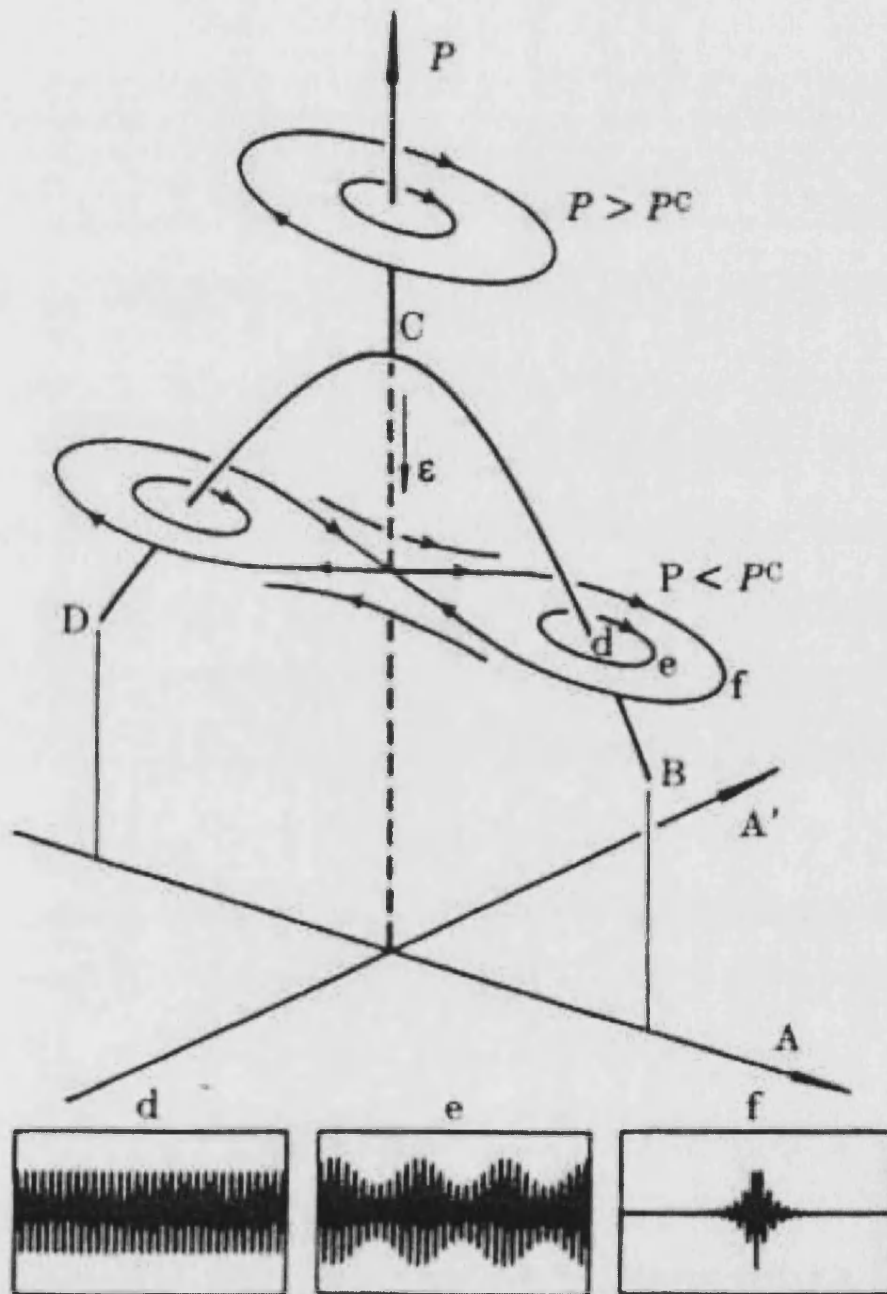


Figure 1.18: Phase-plane portraits of an Hamiltonian Hopf bifurcation. (After Thompson & Virgin 1988)

1.7 Friction theory

In concluding this introductory chapter, we make a study of friction theory. This includes the effects of high pressure and lubrication, both of which have relevance to the geological situations examined here. Although throughout the remainder of the thesis, the parallel folding model developed uses basic Coulomb friction, it is worth being aware of the wider body of research that surrounds this area. This is not only to validate the assumptions that we make, but also to be informed as to the possible pitfalls and limitations that such simplifications might make. This allows in the future, the possibility of adding more complicated and, in theory, more accurate frictional models to the system.

1.7.1 Laws of friction

Friction is defined as the resistance encountered by one body moving (sliding or rolling) over another (Fig. 1.19(a)). There are two basic laws of friction, which are often called *Amonton's laws*; however they were discovered much earlier by da Vinci (Bay, 1976). The basic laws of friction are described as follows:

- (i) The friction force F is proportional to the normal load W ;
- (ii) The friction force between two solids is independent of the apparent area of contact.

Sometimes added to these is a third law by Coulomb:

- (iii) If the velocity is non-zero, the friction force is independent of the sliding velocity (as shown in Fig. 1.19(b)).

Both sliding and rolling require a tangential force F to move the upper body over the lower, and the Amonton's 1st law says that the ratio of this and the normal load W is constant, i. e.

$$\mu = F/W. \tag{1.36}$$

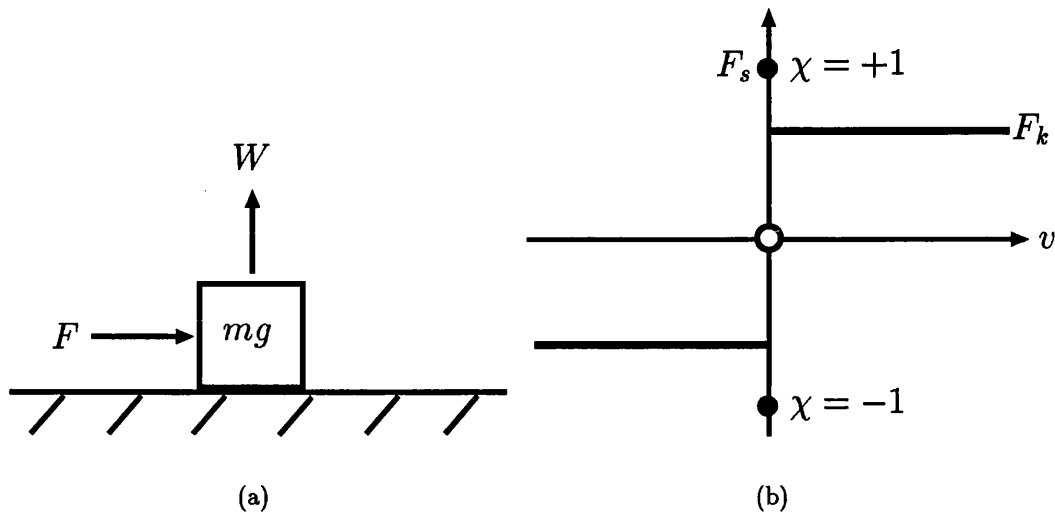


Figure 1.19: (a) A mass subjected to a frictional force F and normal load W , (b) How the friction force alters with sliding velocity.

The constant of proportionality μ is known as the *coefficient of friction* and it should be noted that μ is typical of *two* materials, similar or dissimilar under given surface and environmental conditions (Arnell *et al.*, 1991). For most materials sliding in air $0.1 \leq \mu \leq 1$ and although Amonton's laws were originally formulated under low normal pressure it has been shown that the coefficient of friction is often constant even when the load is varied by a factor of 10^6 .

It is usually seen that the static friction force F_s —the force to start a body moving—is a lot higher than the kinetic friction force F_k —the force to keep it moving (Fig. 1.19(b)). Both of these situations have corresponding coefficients of friction μ_s and μ_k respectively; from (1.36) it is apparent that $\mu_s > \mu_k$ in general (Bowden & Tabor, 1973). However, once sliding has started, the latter is independent of sliding velocity over a large range and hence, although not strictly valid in all situations, justifies the inclusion of the 3rd basic law.

In summary, from (1.36), we have that, if $v = 0$ then

$$\frac{F}{W} \in [-\mu_s, \mu_s], \quad (1.37)$$

which is equivalent to

$$\frac{F}{W} = \chi \mu_s \quad \chi \in [-1, 1]. \quad (1.38)$$

It is this latter notation (1.38) that we will later use to describe the direction-dependant friction in the parallel folding model. Between $\chi = -1$ and $\chi = 1$ a body is static and will sit in equilibrium, in this situation we will say that the system is “jammed”.

If $v > 0$ then

$$\frac{F}{W} = \mu_k, \quad (1.39)$$

and if the coefficient of friction is just stated, it is usually taken to mean μ_k (Arnell *et al.*, 1991).

1.7.2 True contact area

Early investigators decided that the major contribution to the frictional force was from the mechanical interaction between rigid surface roughnesses. Coulomb in particular, felt friction was due to the work done in dragging one surface up the wedge-shaped surface roughness of the other. In the Coulomb model, the lower surface consists of a single roughness making an angle γ to the horizontal and the upper surface resting on it carries load W , the horizontal force F needed to pull the upper surface up the slope is then calculated in terms of work (Bowden & Tabor, 1973) (Fig. 1.20).

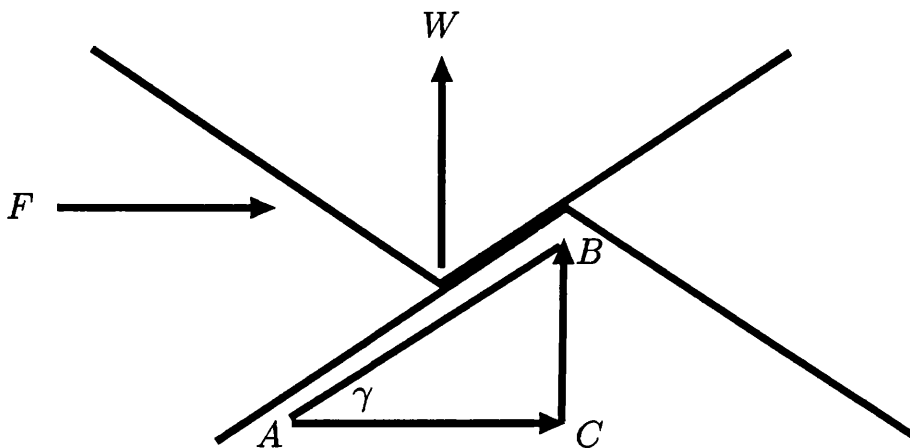


Figure 1.20: Interaction of wedge shaped surface roughness. The coefficient of sliding friction $\mu_s = \tan \gamma$ is calculated using energy considerations.

There are two principles involved:

- (i) Work done is equal to the force multiplied by the distance the object moved. Using Fig. 1.20, if, in moving from point A to B , the top body moves an horizontal distance AC then the work done by the force F is $F.AC$. At the same time the load W moves from C to B and the work done in overcoming gravity is $W.BC$.
- (ii) When energy is not lost, the work done is independent of the path. Therefore $F.AC = W.BC$ implying that $F = WBC/AC = W \tan \gamma$. Hence

$$F/W = \mu = \tan \gamma, \quad (1.40)$$

and thus we have the famous incline plane test for finding μ_s (Arnell *et al.*, 1991).

The problem with the above is that the surfaces move apart as they slide; the normal load then does work on the system and with the downward and upward slopes averaging zero, the potential energy is recovered i. e. there is *no* energy dissipation.

At the microscopic level surfaces are always rough and hence two surfaces will only touch at the highest points; these discrete points are known as *asperities*. Over the rest of the apparent area there are gaps of 100 Å or more and as atomic forces act over only a few atomic diameters the gaps completely separate the surfaces at these points (Bowden & Tabor, 1973). Thus the *real (or true) area of contact* is much smaller than the apparent, especially at low load. However, individual asperities deform according to elastic and plastic deformation laws, and with increasing load the real area of contact approaches the apparent in order to carry the load (Bay, 1976). Thus the true area of contact depends on both the geometry and the way that the asperities are deformed.

In fact the real area of contact A does not depend on the size, shape or number of asperities (Nellemann *et al.*, 1977), but is a material property proportional to the normal load W

$$A = qW, \quad (1.41)$$

where q is the constant of proportionality and is comparable to the indentation hardness of the material (Arnell *et al.*, 1991). This is only justified if the surfaces contain both elastic and plastic contacts and (near-)Gaussian topographies. As this is true in most cases the law is taken to be valid.

1.7.3 Adhesion and deformation forces

From the work of Bowden & Tabor (1973) the friction force has two sources:

- (i) An adhesion force developed at asperity junctions from attractive forces;
- (ii) A deformation force to plough the harder surface through the softer.

Although not strictly independent, they are usually assumed so and hence the force is the sum of the two contributions.

The first stems from the surfaces being in close proximity at the asperities and thus within the range of strong attractive forces. To separate the surfaces, these forces must be overcome and the junctions formed at the real contact areas need to be sheared for sliding to occur. Hence, there is friction, and the contribution from the adhesive forces is

$$\mu_{\text{adh}} = \frac{F_{\text{adh}}}{W} \approx \frac{s}{H}, \quad (1.42)$$

where s is the shear strength of the junctions (approximately the shear strength of the weaker material) and H is the indentation hardness of the softer material.

Secondly, if one surface is much harder, it may plough a groove (or a number of fine grooves) into the softer material. This adds an additional grooving or ploughing term to the friction. In some cases the attachment is so strong that small fragments of the softer material are plucked out. In most cases this is small compared to the force required to shear junctions and may be ignored; thus a low value of μ generally means poor adhesion and vice-versa (although the latter can be due to surface contamination and the release of elastic stresses). It is obvious that other effects are also likely to be involved, for example work-hardening (which will raise s) and junction growth.

1.7.4 High pressure

At low normal pressure the deformation zones of asperities are isolated; however, at high normal pressures the deformation zones interact (Bay, 1976).

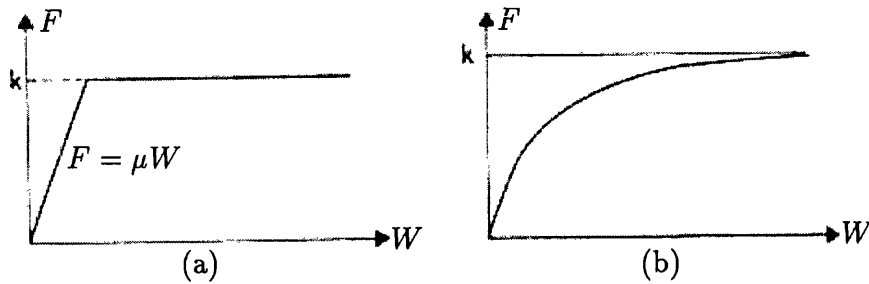


Figure 1.21: (a) Orowan's and (b) Shaw *et al.* frictional model. (After Wanheim & Bay 1978)

This added complication has meant that friction at low pressure has been studied extensively whereas the latter less so. Two early models for friction at high pressure were by Orowan and Shaw *et al.* (Wanheim & Bay, 1978). The former suggested that at low pressures friction stress and normal pressure are proportional and at high pressures the friction stress is equal to the yield stress k in pure shear (Fig. 1.21(a)). The latter was more precise and stated that with increasing pressure the ratio between the real and apparent areas of contact increases approaching the yield stress asymptotically (Fig. 1.21(b)).

If the relationship between the normal pressure W and the ratio of the real and apparent areas of contact α for static contact is examined, proportionality exists for low pressures whereas for high pressures it becomes more difficult to flatten the surface due to the asperity interaction; $\alpha = 1$ is thus approached asymptotically (Bay, 1976). This is shown graphically in Fig. 1.22 for metallic friction between a smooth tool and a workpiece, where m is the ratio between the friction force and shear yield stress.

Also, from Fig. 1.23, at low pressures, friction F and normal stresses W are proportional and hence Amonton's law is valid, but at high pressures the friction stress approaches a constant as the pressure increases and the coefficient of friction becomes pressure dependent. The maximum coefficient of friction is given by

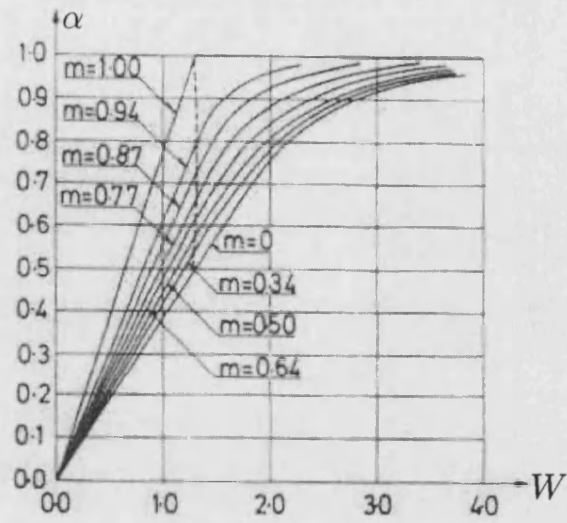


Figure 1.22: A plot showing how α changes with W . (After Wanheim & Bay 1978)

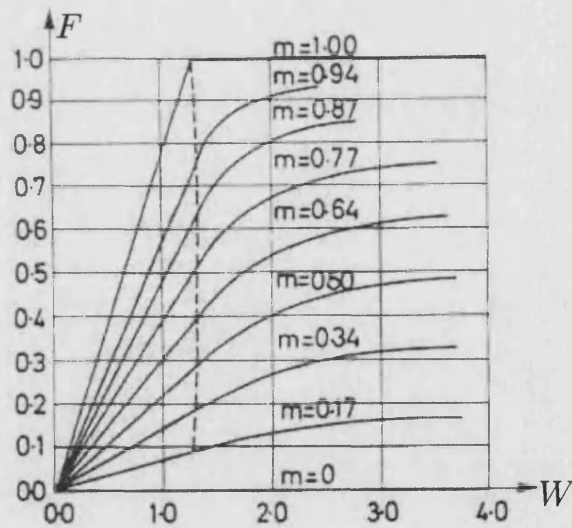


Figure 1.23: A plot showing how F changes with W . (After Wanheim & Bay 1978)

(Wanheim & Bay, 1978)

$$\mu_{\max} = \frac{k}{W}. \quad (1.43)$$

1.7.5 Lubrication

A trapped lubricant results in a superimposed hydrostatic pressure acting on the valleys of the asperities (Wanheim & Bay, 1978); it implies an increase p_f of the normal pressure necessary to obtain the same contact area as when no lubricant is present (Nellemann *et al.*, 1977)

$$W = p_f + W_{\text{dry}}, \quad (1.44)$$

where W_{dry} is the pressure necessary to obtain the same α without lubrication.

If the normal load is supported by the pressure within a thick film of fluid separating the surfaces, where the pressure exists due to viscous forces resulting from the relative motion between the surfaces, then this is called *hydrodynamic* lubrication. However, under very high contact pressures or at very low sliding speeds, hydrodynamic forces are insufficient and direct contact between asperities occurs.

This last statement has particular importance when looking at fluid forced into the interfaces between rock strata. As both the above conditions hold, the presence of the fluid is likely to have very little effect on the interaction between adjacent surface and so frictional contact can be assumed to exist.

Chapter 2

Literature review

2.1 Introduction

This chapter gives an historical overview of the literature on geological folding and also includes many works on the buckling of beams which are relevant to the problem. There has been very little written on the specific subject of parallel folding, but after an extensive search, the major contributors are hopefully represented.

From a timeline viewpoint, the work breaks down nicely into three sections:

Section 2.2: Immediately after the discovery of parallel folds in multilayers, only experiments and speculation based on field observations as to the involved processes were performed, there was little actual modelling. Elastic single layer models were considered, however, mainly using Euler beam theory, and this is the real birth of the subject of geological folding.

Section 2.3: Geological models in the 1960's and 70's were heavily influenced by the work of Biot, developed from thermodynamics concepts and mathematical tools for the deformation of elastic and viscous materials embedded in matrices. This work was then applied to geological situations, with Biot coming to the conclusion that rock deformation, in the main, is driven by viscosity and that exponential growth of waves leads to a *dominant wavelength*.

Whilst many embraced these ideas and added to the body of work, others chose to disregard it and stick to elastic assumptions or realized that certain aspects, such as the importance of layering, were missing. Later, however, from experimental evidence and strain rate analysis, certain geologists came to accept that periodic wavetrains, so typical of Biot's work, are less common in nature than localized serial buckling.

Section 2.4: At about this time, completely independently, structural engineers were primarily concerned with elastic stability theory. The development of this area, often using elastic struts on different foundations as a model, led to the concept of *localization*. Amongst others, the theory was progressed by Thompson, Hunt and their subsequent students and collaborators, using ideas of dynamic phase space analogies. The subsequent realization that these techniques could be applied to geological situations, leads to the work investigated in this thesis.

From the work contained in these sections, the hope is to demonstrate:

- (i) That elasticity is a viable model for the behaviour of rocks;
- (ii) The importance of the layers as regards folding;
- (iii) That friction has largely been ignored and certainly not studied in parallel folding;
- (iv) That often rocks fold sequentially, making the wealth of localization theory useful in the study of such problems.

2.2 Elastic single layer solutions

If a given bed in the centre of a rock formation be plicated and the layers above and below be folded in a strictly parallel manner, in passing away from the central bed in either direction those on either side are less closely folded, and finally the crenulations become slight.

Van Hise (1894)

Above is the definition that in 1894 Van Hise gave to the *parallel fold* (Fig. 2.1(a)),

the first of two forms of folding found to be prevalent in his study of geological formations and of enough importance to be given specific terminology. The second, the *similar fold* (Fig. 2.1(b)), folds in such a way that all of the layers are required to do the same thing and so material must be redistributed from the limbs to the hinges.

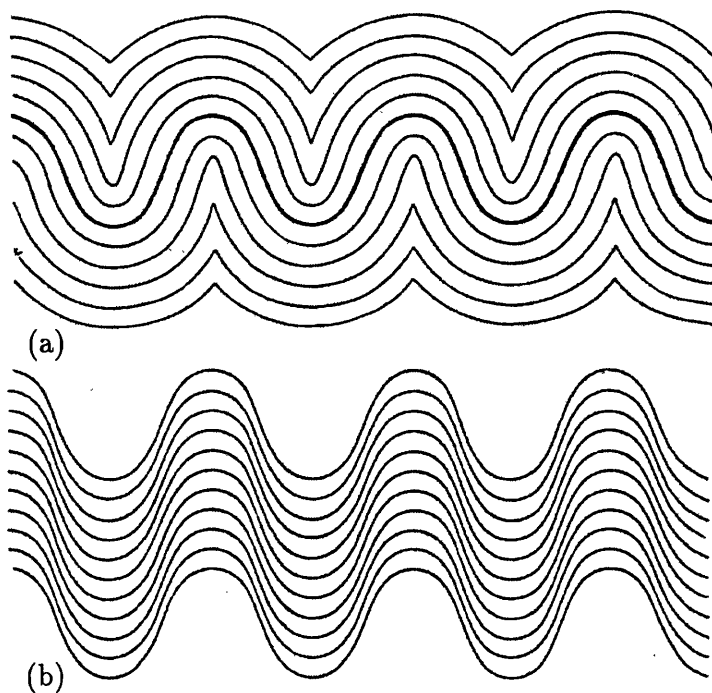


Figure 2.1: (a) Parallel folds and (b) Similar folds. (After Van Hise 1894)

Whilst realizing that these were very idealized forms of what could be seen in the field—in fact many geologists had drawn sections that were somewhere between the two forms—and although very much a field geologist, Van Hise felt that a lot could be learnt by understanding the mechanisms through which they occurred. Although no qualitative attempts were made to do this, Van Hise did make observations as to the processes involved in parallel folding and the conditions needed for folding in general. Firstly, he stated that rocks buried at a depth such that they are in a zone of plasticity and flowage, are most likely to fold. When forces are applied, these rocks obey hydrostatics laws and approach equilibrium. At the depths at which this happens, the pressure is high enough (it is claimed that at 10km, under gravity alone, the pressure is 2550 kg/cm^2) that it may turn rocks crystalline. This would presumably increase the friction between layers.

It is suggested that to bend without fracture, parallel folding is by *tangential longitudinal strain*. Differential movement is needed as all of the layers are originally the same length and this movement is at a maximum at the mid-limbs and minimized at the crests and troughs.

A mechanism for serial buckling was even mentioned by Van Hise. This is summarized as follows:

The first fold forms where the differential thrust is greatest, eventually the increased thickness of the material resists deformation and stress is transmitted to the thinner strata in advance, hence the second fold then forms.

Perceptively, it was revealed that it is not necessary for one fold to be completely formed before others develop. The thickening is found to be favourable for forward transmission of the stress.

Whilst Van Hise hinted that rocks behave in an elastic manner and that friction plays an important role in multilayer buckling, the first attempt at mathematically modelling the folding of rocks negated friction by concentrating on a single layer. In 1909 Smoluchowski closely followed Euler beam theory (Euler, 1744) by looking at a single layer buckling elastically, where a resistive force is given by the weight of the layer, i. e. the lithostatic pressure (§1.3.3). Using Kirchoff's equation for thin disks, when linearized, the (familiar) governing fourth order equation was found (Smoluchowski, 1909)

$$EI\ddot{w} + P\ddot{w} + \rho gw = 0. \quad (2.1)$$

By looking for exponential solutions, Smoluchowski showed that the characteristic equation leads to a critical value of P . Below P^C , with simply supported boundary conditions, the solution decayed whereas above P^C the solution was sinusoidal. By setting the waveshape as $\sin(k\pi/l)$, the critical load is

$$P^C = EI \left(\frac{k\pi}{l} \right)^2 + \rho g \left(\frac{l}{k\pi} \right)^2. \quad (2.2)$$

Smoluchowski then considered the stability of approximately sinewave solutions

by searching for an energy minimum of the potential energy, $U + V - W$, where

$$\begin{aligned} U &= \frac{EI}{2} \int_0^l \ddot{w}^2 dx \\ V &= \frac{\rho g}{2} \int_0^l w^2 dx \\ W &= \frac{P}{2} \int_0^l \dot{w}^2 dx. \end{aligned} \quad (2.3)$$

A purely sinusoidal half-wave gave equation (2.2) with $k = 1$, otherwise $P < P^C$ and the stable length was found to be

$$l = \pi \sqrt[4]{\frac{4EI}{\rho g}}. \quad (2.4)$$

When extended to k half-waves equivalent results were found.

In 1926, Goldstein repeated to a large extent the calculations made by Smoluchowski. The stability of a strut when the deflection is resisted linearly was explored; however, added to this was the difference between clamped and pinned end conditions (Goldstein, 1926). For both there was a critical load below which the strut is always stable, and above this value the beam length determined the load at which instability first occurred. By assuming either symmetric or asymmetric sinusoidal behaviour, the auxiliary equation was used to predict the wavelength and number of nodes. From this analysis, it was shown that a pinned strut buckles before a clamped strut of the same length.

Single layer elastic buckling, was again the subject of a 1937 paper by Gunn to model the Earth's crust. Gunn used the idea of isostatic equilibrium, i. e. that small deformations are unstable and will tend towards equilibrium. In describing the crust several important points were mentioned (Gunn, 1937); the first was that evidence leads to the conclusion that the crust is composed of individual unbonded layers, and the second was that at very low depths there is only faulting or fracture and at large depths there is only plastic flow. Gunn also thought about energy considerations in the context of mountain building; the calculations were approximate as Gunn points out there would be a lot of work overcoming friction. Whilst this contribution was not estimated, a "factor" was added to say that the compressing energy must be greater than that given and the reader is assured that this static calculation is consistent with those based on dynamics.

The buckling of a section of the crust was modelled using a beam of thickness T under compressional stress S . The weight of the material below the layer provided a resistive force as well as the sediment deposited above it. The equilibrium equations admitted a similar fourth order equation to Smoluchowski and again when solutions were in the form of linear combinations of exponentials, there was a critical value of the stress. Strangely, below this value the profile was quasi-periodic and according to the researcher “represents an upward or downward fold in the crust which is believed to be of considerable geological importance”, the actual shape and importance were not actually alluded to. Above the critical stress, the solution was periodic and again rather oddly, by making some assumptions as to the typical values of the quantities Gunn concluded that the periodic solution cannot exist.

In 1938, over forty years after Van Hise looked at natural geological examples of multilayers and first defined parallel folding, the topic was revisited by Kuenen & de Sitter. Having studied many geological structures de Sitter decided that in most simple cases folding was approximately concentric; unable to get a mathematical solution, the mechanisms involved were instead investigated. The end product was an experimental paper, the first to show the two ways that parallel folding can occur: *flexural folding* (slip and flow) and *tangential longitudinal strain* (Kuenen & de Sitter, 1938).

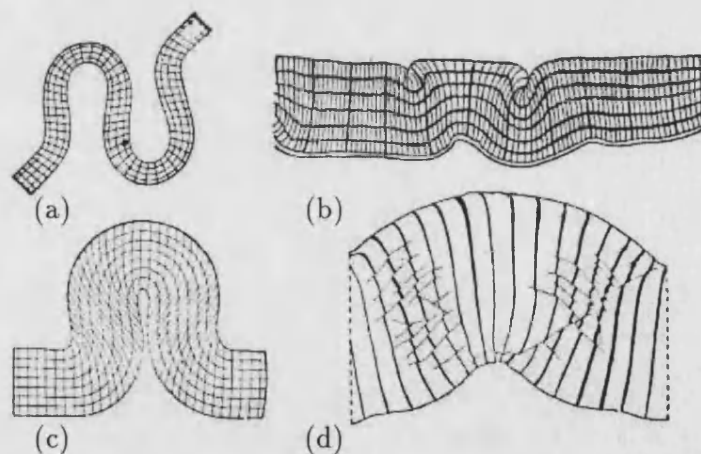


Figure 2.2: Sketches showing the results of experiments by Kuenen & de Sitter (After de Sitter 1964); (a) Folded rubber plate, (b) Thickened and folded paraffin cake floating on water, (c) Folded pack of paper sheets and (d) Folded unstratified clay cake.

Folding by tangential longitudinal strain was shown by homogeneous single layers of both rubber (Fig. 2.2(a)), exhibiting a purely elastic deformation, and the plastic buckling of a paraffin-vaseline-mineral oil mixture. The latter was very dependent on the horizontal load speed. In representing stratification planes, an elastic multilayer—a block of thin sheets of paper (Fig. 2.2(c)), glued at the ends to stop slipping—and a plastic multilayer—a layered paraffin cake (Fig. 2.2(b))—also showed tangential longitudinal strain as the fold mechanism. Although it was not mentioned, the experimental photographs suggest that the plastic multilayer buckled in a serial manner. Whilst expecting simple shear, Kuenen & de Sitter found that deformation was usually governed by internal friction, and so concluded that both are methods for real geological folding.

Lastly an unstratified cake consisting of very wet clay was tested and showed folding by flexural slip (Fig. 2.2(d)). Concentric shearing planes had formed almost exactly with the same frequency and movement as in the paper experiment. This showed that a solid material can develop zones of slip equivalent to a multilayered structure, where the spacing of the layers and the amount of slip appear to have remarkable similarities.

... nearly all the deformations in which we are interested lie in a zone between the plastic and elastic fields ... *de Sitter* (1964)

De Sitter indicated more about the elastic properties of rocks in the 1964 book “Structural Geology”, stating that even though rocks have permanent deformation, it is possible to apply a modified elasticity theory by assuming that deforming rocks are partially in elastic strain, becoming permanent with changing shape (de Sitter, 1964). De Sitter supported this by saying that deformation experiments have shown that not only are elastic properties maintained, but also that it is impossible to detect whether the deformation in rock is elastic or viscous. Evidence of the elastic properties of rock even at large depth is shown by purely elastic shockwaves, which are still present at 700km below the crust. The proof of elasticity is vital as de Sitter went on to say that the elastic stresses in the folded competent rocks govern deformation; the incompetent layers follow the shape of the competent layers passively. The conclusion from this was that the foundation will have different stress conditions from the layers in general.

Finally, as shown previously from his work with Kuenen (Kuenen & de Sitter,

1938), parallel folding is a common natural phenomenon and hence de Sitter studied the subject in some detail in "Structural Geology". Points of note are (de Sitter, 1964):

- (i) Competency and elasticity concepts are highly relevant to parallel folding as they commonly appear in the competent layers of bilaminates and that "concentric folding ... is typical of the smallest possible excess of stress over the elastic limit";
- (ii) As the last experiment in Kuenen & de Sitter (1938) shows, the elastic stresses inside a layer folded parallel to the surface can result in shear planes dividing the sheet into two. Further folding repeats the process and the elastic state of the rock is preserved allowing continuous bending without an increase in stress.

Unfortunately the author's knowledge of French is not up to the standard where justice can be done to the work of Goguel (1943); however, it is clear that a section was dedicated to the idea of elastic folding in rocks. Goguel performed calculations for similar folding, but suggested that thickness variations are not often seen and it is more usual to find that layers have preserved their thickness and folded in a parallel manner. Folding of this nature was said to be especially important for a limited body of layers, sliding at a foundation, and that the amount of sliding between two layers was equal to the product of the average thickness and the angle through which they have rotated. For a very large body it was stated that it is very difficult to do a complete geometric analysis as on the concave side the layers become very angular and may break and dislocate in various manners.

In his 1952 book on plate tectonics (translated into English in 1962), Goguel maintained that rocks have elastic or visco-elastic properties as they often break before permanently deforming (Goguel, 1962). It was stated that as speeds are slow (inversely proportional to the log of time), potential energy is very small; hence the type of deformation is dependent on the least amount of effective work being absorbed. Effective work was defined as the sum of the resistant work of deformation (pressures and friction) and the work of gravity. As such work was minimized through bending, rather than thickness variations, Goguel claimed that parallel folding is a common geological phenomenon.

2.3 The influence of Biot

2.3.1 Biot and Ramberg

... in the mechanism of folding, the viscous properties of the rock will tend to overshadow the effect of elasticity. *Biot* (1961)

Our study of Biot's work starts in the late 1930's with two papers extending classical elasticity theory. In the first (Biot, 1937), Biot stated that bending an infinite beam on an elastic continuum under lateral load was more realistic than on a Winkler foundation. By applying a sinusoidal load to the continuum, this causes a sinusoidal deflection and the load is dependent on the amplitude and wavelength. For a sine-like concentrated load, the bending moment and deflection close to the load were found to agree well with a Winkler foundation having the same maximum bending moment. In the second paper (Biot, 1938), large displacements and rotations were included for an elastic body under two-dimensional strain and the stability of a buckling plate was then considered; here a sinusoidal solution was obtained together with a critical stress equal to the Euler load.

In 1961, with a deep understanding of the deformation of elastic and viscous materials, Biot changed geologists' thinking by writing a seminal paper (Biot, 1961). Based on earlier work (Biot, 1957)—where the buckling instability of a single (elastic, plastic and viscous) layer in an infinite medium was studied using ideas taken from non-equilibrium thermodynamics—Biot presented the notion of the *dominant wavelength* and bandwidth selection for visco-elastic media, concluding that viscosity is the primary driving force in tectonic folding. Arguing that elastic rigidities of rock are too similar to explain folding and that deformation happens over a very long time frame, Biot surmized that in most cases viscosity will predominate. The theory is applicable to elastic and non-elastic media, if the viscosity coefficient is replaced by the rigidity modulus, through the *correspondence principle*.

To prove this, Biot studied elastic and viscous layers embedded in a viscous matrix with initial imperfections. The rate of growth was highly dependent on the wavelength of the folds and Biot contends that the fastest growing wavelength,

the so-called “dominant” wavelength, is that eventually seen as sinusoidal waves. The viscous plate differed to the elastic plate in that for the former the dominant wavelength is independent of the load and all wavelengths were amplified. Biot also stated that for well-defined folding the viscosity of the layer needs to be 100 times that of the matrix.

Adding gravity effects to the viscous layer, the dominant wavelength L_d became dependent on the compressive load P

$$L_d = \pi h \sqrt{\frac{2P}{\rho_1 g h}}, \quad (2.5)$$

where h is the thickness of the layer, g is the acceleration due to gravity and ρ_1 is the density of the matrix.

Biot also extended the work to multilayers; for n equal viscous layers with perfect lubrication, the dominant wavelength was given by

$$L_d = 2\pi h \sqrt[3]{\frac{n\nu}{6\nu_1}}, \quad (2.6)$$

where h is the thickness of an individual layer and ν and ν_1 are the viscosities of the layers and matrix respectively. A similar elastic multilayer was said to be equivalent to a single layer in a medium of viscosity ν_1/n ; in doing this the wavelength was unchanged, but the rate of deformation was increased.

Biot admitted that, by assuming perfect slip, this treatment was approximate, but that bilaminate viscous materials or buckling under hydraulic lifting are comparable to this situation. It was also claimed that if friction was added to the viscous case, then the wavelength falls to somewhere between (2.6) and that of a single layer of thickness nh .

In concluding, it was remarked that as the modelling is linear, it only represents the initial stages of buckling and limits the geometry. Nonlinearity is needed to account for the very regular folding seen in reality, but the theory is extendable to nonlinear media.

In later publications, Biot extended the ideas presented in the 1961 paper to the following:

- (i) Internal buckling. Firstly for an homogeneous, incompressible, elastic, infinite or rigid bound medium under hydrostatic pressure and horizontal load (Biot, 1963a), and then for a viscous, perfect-slip, bilaminate multilayer confined vertically and subjected to horizontal compression, (Biot, 1964). The incompetent layers were said to act as a lubricant and have little effect on the dominant wavelength. Biot declared that friction can be included and that the methods encompassed all situations with no restrictions placed on the layers.
- (ii) Multilayer stability. Biot used previous results to study the stability of an incompressible, elastic multilayer under initial strain, where the layers were orthotropic, isotropic or anisotropic (Biot, 1963c). When embedded in an infinite or semi-infinite medium, the stresses parallel and perpendicular were examined under conditions of perfect adherence and perfect slip. Later visco-elastic and gravity effects were added (Biot, 1963b).

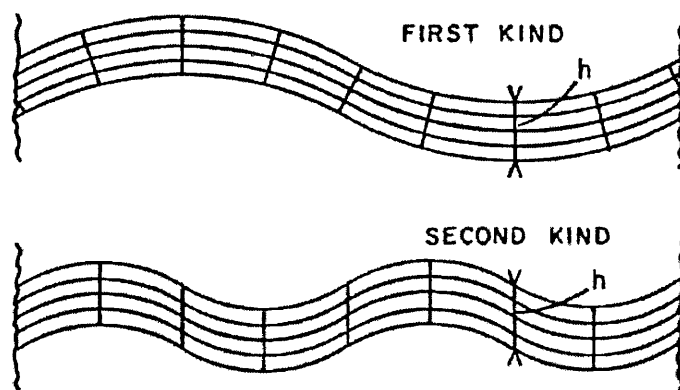


Figure 2.3: Similar folding of the *first* and *second* kind. (After Biot 1965b)

- (iii) Similar folding of the first and second kind. In 1965 a more relevant and interesting use of Biot's theory was given, where similar folding of the first kind is equivalent to parallel folding (Biot, 1965b). The model used a bilaminate multilayer, subjected to a lateral load (overburden pressure) by a surrounding soft foundation and having potentially large deformations. With layers of approximately the same viscosity, the wavelengths were large, the cross-sectional planes were normal to the layers and behaved almost as a single layer would in the same situation. Biot called this *similar folding of the first kind* (parallel folding) and although not mentioned the folding was by tangential longitudinal strain (Fig. 2.3). Through the correspon-

dence principle, Biot asserted that everything was the same for the elastic situation.

Biot's work culminated in 1965, by bring together all of his ideas into the book "Mechanics of Incremental Deformation" (Biot, 1965a).

There is no denying the contribution that Biot made to the field of geology; the influence of his work was far reaching and still initiates much debate today. However, there are several problems with Biot's research, some of which this thesis hopes to address. The largest problem is that, probably to simplify analysis (and the lack of high speed computers), all of Biot's work is linear, and hence only involves sinusoidal, small-amplitude, deflections. This periodic analysis only then really applies to wavetrains, which, as we will see shortly are not necessarily the normal method of buckling.

The viscous nature of rocks is not convincing; whilst deformation may not be strictly elastic, permanent deformation is more likely to be plastic rather than through the fluidity of the layers. The use of such ideas seems especially strange when Biot points out that rocks are initially elastic before viscosity dominates and that his studies are only relevant for infinitesimal amplitudes. The author finds the dominant wavelength notion difficult to believe, especially as it will be shown to be dubious in §2.4. There is also a feeling that the method overly complicates fairly trivial situations and whilst the correspondence principle may be correct, it produces long and involved equations.

Ramberg was more of an experimentalist than Biot, but had similar ideas, considering rocks to be viscous and insisting that the ideas can be transferred to the elastic case. Starting with theory and experiments in 1959 and 1960 on the buckling instability of a single viscous layer, Ramberg developed models close to those of Biot (Ramberg, 1959; Ramberg, 1960).

Seeing that, more commonly, folding is found in multilayers, where the competent layers interfere, Ramberg then looked at contact zones of competent layers and the corresponding wavelengths (Ramberg, 1961). Free and embedded bilaminate multilayers with no-slip conditions were considered and Ramberg pointed out that although rare to find a number of thin, identical, evenly spaced competent layers, the problem was still of interest. Strangely although all of the theory was

expressed in terms of viscosity, the experiments used to confirm the features were elastic, as they used layers of rubber.

For a single layer, by looking at the resistive forces and finding the stationary solution with respect to the wavelength, the wavelength λ was given by

$$\lambda = 4\pi h_0 \sqrt[3]{\frac{1}{6} \frac{\mu_1}{\mu_2}}, \quad (2.7)$$

where $2h_0$ is the layer thickness and μ_1 and μ_2 are the viscosities of the layers and medium respectively.

Like Biot, it was predicted that the fastest growing wavelength is the one seen in reality and (2.7) agrees with a similar formulation by Biot (1957). In fact, Biot stated that Ramberg's theories do not depart from work already undertaken by himself and also that by separating the rigid boundaries with a softer material, as Ramberg does, a dominant wavelength would not exist (Biot, 1964).

To study how the critical load and wavelength of the bilaminate multilayer was affected by altering the spacing of the competent layers, Ramberg introduced the ratio of the thickness of incompetent to competent layers $n = h/h_0$. For both elastic and viscous materials, with $n > 12$ a minimum wavelength existed dependant on n . Ramberg also proved, using elastic experiments, that, under no-slip, an embedded bilaminate multilayer buckles with a larger wavelength-thickness ratio than a similar single layer, in agreement with his developed theory. With small spacing between the competent layers, the wavelength is determined by the surrounding medium.

In 1971, to validate Ramberg's Newtonian visco-elastic modelling and to prove the possibility of more than one dominant wavelength, Ramberg and Strömgård tested multilayers of alternating competencies and differing thickness (Ramberg & Strömgård, 1971). From Ramberg's theory the layers are welded together and bounded by infinite half-spaces, rigid walls or free flexible surfaces. As before (Ramberg, 1961), the experiments were elastic, using layers made of gelatine and rubber, the outer layers of gelatine being significantly larger than the wavelengths, and hence could be regarded as infinite.

Whilst the experiments and theory had wavelengths and amplitudes in agreement,

there is no proof that the dominant wavelength methodology is correct. With increased deformation, the contact zones interfered, and the thin layers were forced to have the same wavelength as the thicker ones, proving that the theory is only correct for relatively small amplitudes.

2.3.2 Viscosity arguments

Whilst being an advocate of Biot's as regards the behaviour of rock, Chapple (1968), was one of those to point out the limitations of Biot's infinitesimal treatment. Chapple stated that linear approximations stop the analysis being useful beyond limb-dips of 5° and that the multilayer case gave unclear results. Justifying viscous behaviour, by saying that rocks usually have a threshold stress, Chapple then used elastic strain energy variational principles, stating the mathematical equivalence of a slow moving linearly viscous fluid and the deformation of an incompressible elastic body.

By numerically modelling a single linearly viscous layer embedded in a less viscous medium, Chapple extended Biot's analysis to finite amplitude folds, with limb-dips of up to 15° . For dips greater than 15° , the deviation from the theory is "explained" using nonlinear stress-strain relations, which lower the viscosity. It is claimed that this is why the dominant wavelength, which should be the most common, is not seen in reality. As with Biot and Ramberg, it is assumed that the layer buckled into a symmetric wavetrain.

Like Chapple, Bayly (1974), also studied Newtonian viscous finite buckling. But unlike Chapple, the research was of bilaminate multilayers, looking at the energy-consumption for different wave-profiles, to discover if there is a relationship between the profile geometry and mechanical properties. By finding the roundness of folds for known properties and reverse engineering the hope was to predict limits on the attributes of observed lithologies.

The folds considered were *similar*, with straight limbs and arched hinges and Bayly used the hinge/wavelength ratio as the parameter for determining the properties. It was assumed that the limbs and hinges of the layers adapt, such that they are in the least energy configuration, with the most energy consumed in changing of curvature of the hinges of the competent layers. Unfortunately, when

the layers have similar competences the analysis fails to hold and for parallel folding, where the hinge fraction is 0.6 or more, the changing profile and quick cusping stop the theory being valid.

Again no elasticity was involved in work by Smith in 1975 , who tried to tie up several types of deformation into one model using a single layer of Newtonian fluid embedded in a matrix of different viscosity (either higher or lower) (Smith, 1975). The layer is unstable and depending on whether the load is horizontal or vertical either folding or pinch and swell phenomena is observed. Hence the same mechanism caused four distinct cases. Like Biot, only the initial stages of the deformation were explored and even though the results correspond exactly to Biot, Smith cited Biot's work and that of Chapple to outline the limitations of many Euler beam based models. The primary objections were: only long wavelengths and large viscosity ratios are applicable; the initial instabilities are not really considered and that phenomena such as boudinage is not predicted.

In a later paper (Smith, 1977), Smith used non-Newtonian fluids to try and correct the discrepancies between the theory in his previous work (Smith, 1975) and reality. Smith turned to non-Newtonian flow after allowing slip between the layer and matrix and thus introducing an interface friction coefficient, did not overcome the shortcomings of his model.

2.3.3 Importance of layering

The importance of layering to fold development was discussed in two papers by Donath, the first in 1962, and then jointly with Parker in 1964. Donath stated that geologists were too interested in the geometry of folds and not the mechanisms that created them. To rectify this, layered rock deformation by brittle fracture and ductile flow was researched as well as the conditions that affected these states (Donath, 1962; Donath & Parker, 1964).

The assertion was that all folding occurs by either continuous or discontinuous flow (Fig. 2.4) and that anisotropy controls the geometry of the deformation. Discontinuous flow, called *slip*, is a gradation between shear fracture and flow. The ductility of the rock alters the influence of the layering, but if flow or slip is restricted to the (less cohesive) layer interfaces, the layers bend producing either

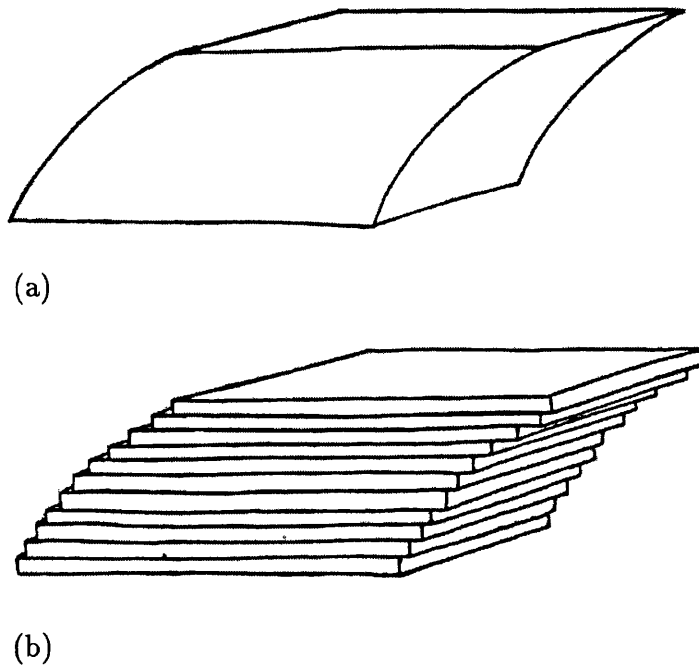


Figure 2.4: (a) Continuous and (b) Discontinuous flow. (After Donath 1962)

flexural slip or *flexural flow* folds. Although these are sometimes called flexural slip of the competent and incompetent layers respectively, Donath felt the use of the word “competent” is unclear as it can have several meanings from strength to ductility to the elasticity of the rocks.

Donath proclaimed that geometrically, flexural slip folds (Fig. 2.5) are parallel or concentric folds. They are found in moderately brittle to moderately ductile layered rocks—i. e. at low to medium pressures and low temperatures—occurring when shear stresses exceed the friction on the layer boundaries. By introducing the term *mean ductility*, defined to represent the behaviour of the most abundant rock type, Donath showed that low mean ductility suggests that flexural slip will occur.

2.3.4 Elasticity arguments

Not everyone followed the viscous or elasto-viscous line that was so heralded by Biot and Ramberg. In 1962 Currie *et al.* presented a mathematical model for stratified rock based on multilayered elastic behaviour. This strongly followed

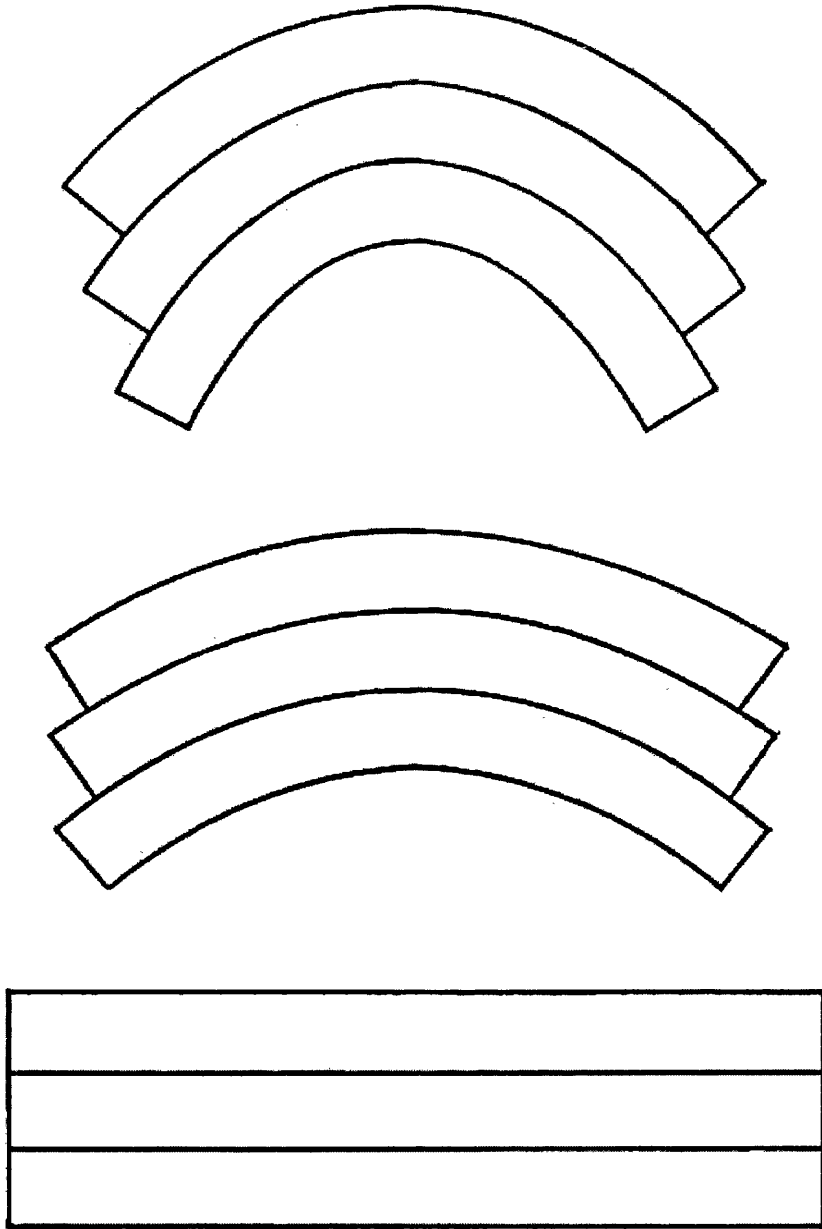


Figure 2.5: Concentric folding by flexural slip. (After Donath 1962)

Euler beam theory and builds up to the multilayered model in stages, firstly considering the elastic stability of an unconstrained beam with hinged ends (Currie *et al.*, 1962). In contrast to most elastic studies, they did, however, introduce the *critical wavelength-thickness ratio*

$$\frac{l}{T} = \sqrt{\frac{\pi^2 E}{12\sigma_p}}, \quad (2.8)$$

where E is the Young's modulus of the beam and σ_p is the proportional limit of compressive stress. Elastic sinusoidal buckling up to large curvatures is reported to be seen above this value and below it the beam buckles non-elastically or crushes.

To represent a medium or lithostatic weight, the elastic continuum used by Biot (1937) was added. Via the *correspondence principle* one can see that this gave formulations for the critical load and wavelength of the same structure as Biot's analysis for the dominant wave of a viscous beam embedded in a viscous foundation. Similarly, for elastic instability to occur it was concluded that $E \approx 100E_0$, where E_0 is the elastic modulus of the foundation. It was also stated that, in agreement with Ramberg (1961), if the height of the medium at least equals the wavelength in magnitude, then an infinite foundation is a very good approximation.

The multilayer formulation was obtained by replacing the single layer of thickness T by n layers of thickness t ($T = nt$). The boundaries were *frictionless*, and the energy found by simply summing the bending energy contributions. With a sinusoidal deflection, the critical load and wavelength were given by

$$P^C = \frac{n\pi^2 Et^3}{3L^2} + \frac{E_0 L}{2\pi}; \quad L = 2\pi t \sqrt[3]{\frac{nE}{6E_0}}. \quad (2.9)$$

To compare the models with reality Currie *et al.* undertook two studies, the first experimental using gum rubber strips embedded in gelatine, and the second using natural examples. For the latter, a log-log graph of dominant layer thickness and wavelength, showed remarkable agreement with the theory. However, the test results—examples of which are shown in Fig. 2.6—emphasized several flaws in the modelling: primarily that after limb-dips of just 5° , the outside competent layers cannot be considered sinusoidal and also that only at high curvature was the neutral axis near the centre of the layers; before this the layers were mostly

in compression.

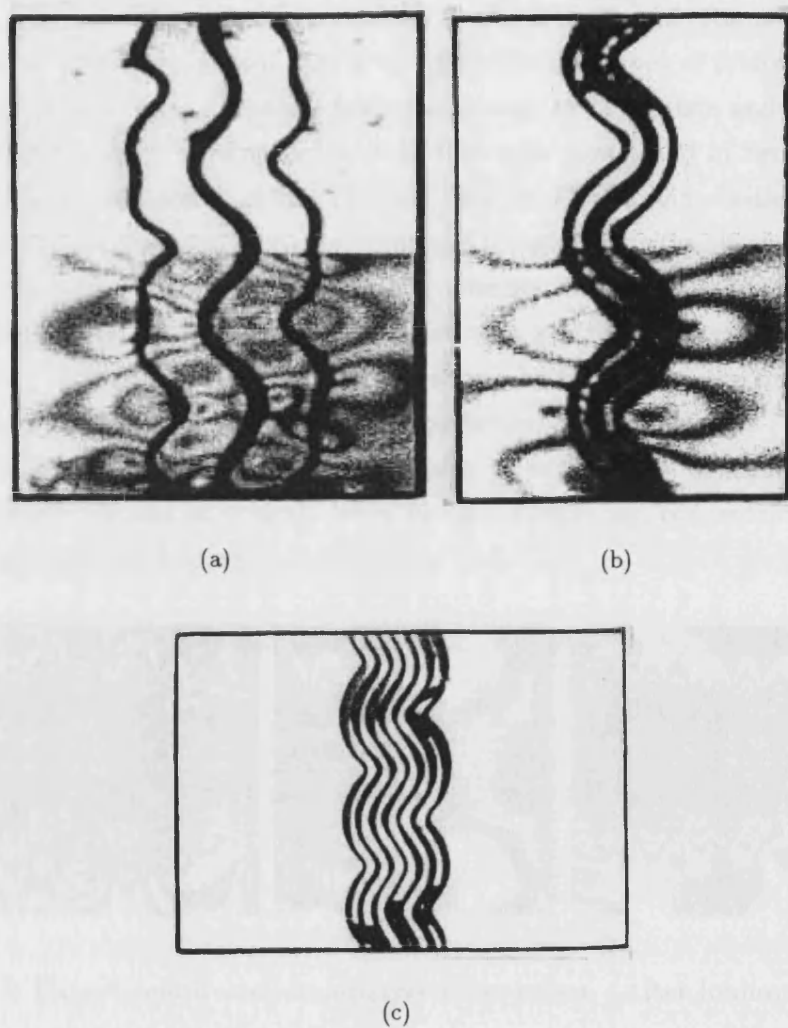


Figure 2.6: (a) Three competent layers with wide spacing and (b) With close spacing. (c) A sequence with identical layering. (After Currie *et al.* 1962)

A set of seven papers by Johnson attempted to put to rest arguments on how different fold shapes occur by using elastic theory. The four of interest here are: Johnson & Ellen (1974), Johnson & Honea (1975b; 1975a) and Honea & Johnson (1976). Some of the the ideas conveyed in these papers are repeated in the book “Styles of Folding” (Johnson, 1977). The justification for using elastic theory, was that rock theory generally assumes small strains linearly related to stresses; it is only later that these become permanent. Also the belief that rocks fold high-up in the Earth’s crust and so behave more elastic(-plastic) contributed to

the argument.

The first paper gave a general introduction to the subject area (Johnson & Ellen, 1974), showing examples from nature and the different types of folding that can occur: small-amplitude sinusoidal folds giving way to concentric and eventually chevron folds. Kink banding is the only fold-type mentioned in terms of frictional contact. Johnson & Honea (1975b) then developed, via elasticity theory, linearized equilibrium equations for compressible elastic materials and found sinusoidal solutions, which are then used by Johnson & Honea (1975a) and Honea & Johnson (1976) to describe the transition of a multilayer from sinusoidal-to-concentric-to-chevron folding. It was also shown how changing the properties of the layers can lead to kink banding. For the former, the premise was (Johnson & Honea, 1975a) that as sinewaves are unstable in multilayers, concentric folding is the stable form and so typical. With further shortening, concentric folding is replaced by chevron folding.

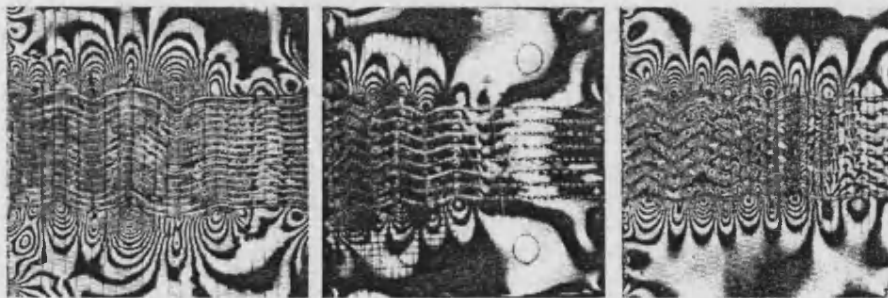


Figure 2.7: Experimental elastic multilayer deformation. (After Johnson & Honea 1975a)

Surprisingly, a large proportion of Johnson & Honea (1975a) is dedicated to showing that the linearized elastic theory developed by Johnson & Honea (1975b) over-complicated matters. The wavelengths resulting from their modelling, for several different situations, when compared to those from more simple methods requiring much less calculation, are in excellent agreement. It is even remarked by the researchers that there is little point in using their elastic theory.

When conducting the same elastic experiments used by Ramberg & Strömberg (1971) to prove viscous arguments (Fig. 2.7), it is suggested that if confined by rigid media, Biot's wavelength would be found; in the author's opinion in such a situation the layers would not deform sinusoidally. One thing of note is that the

more intense folding seen in Fig. 2.7 at one end of the multilayer appears to be serial buckling.

Lastly the transition from sine-to-concentric-to-chevron folding at the crux of this work is summarized below (Johnson & Honea, 1975a):

Imagine a bilaminate multilayer embedded in a confining medium is subjected to axial compression. The layers shorten until the critical load is reached, when the straight layers become unstable producing a sinusoidal wavetrain of Biot wavelength. Sinewave growth results in higher order effects which change the wavelength of the stiff layers due to normal stresses, decreasing in the core and increasing in the crests. The sinusoid is unstable as it grows and becomes concentric. With thick layers, the multilayer is more sinusoidal throughout; thin layers means more concentric looking folds. The layers eventually undergo elastic yielding resulting in chevron folding (Fig. 2.8).

There are several problems with the above, the main one being that concentric folding was explained by none of the theory given in these works, as it is a “higher order effect”. The linearized theory does not give reasons for the changing wavelengths within the multilayer that characterize the folds. The notion of an unconfined medium and layers going from straight to buckled are unrealistic. Honea & Johnson (1976) rectified the last point by having rigid boundaries and almost frictionless layers which have initial, low amplitude perturbations approximated by a Fourier series.

2.3.5 Serial buckling

One may often observe in model experiments relating to the development of fold series that the folds develop serially and in packets rather than simultaneously throughout the folded unit. If it assumed that this mode of fold development is followed in nature (and I cannot envisage how the many thousands of folds in a fold belt could have developed simultaneously), then this probable mode of fold development ... *Price* (1970)

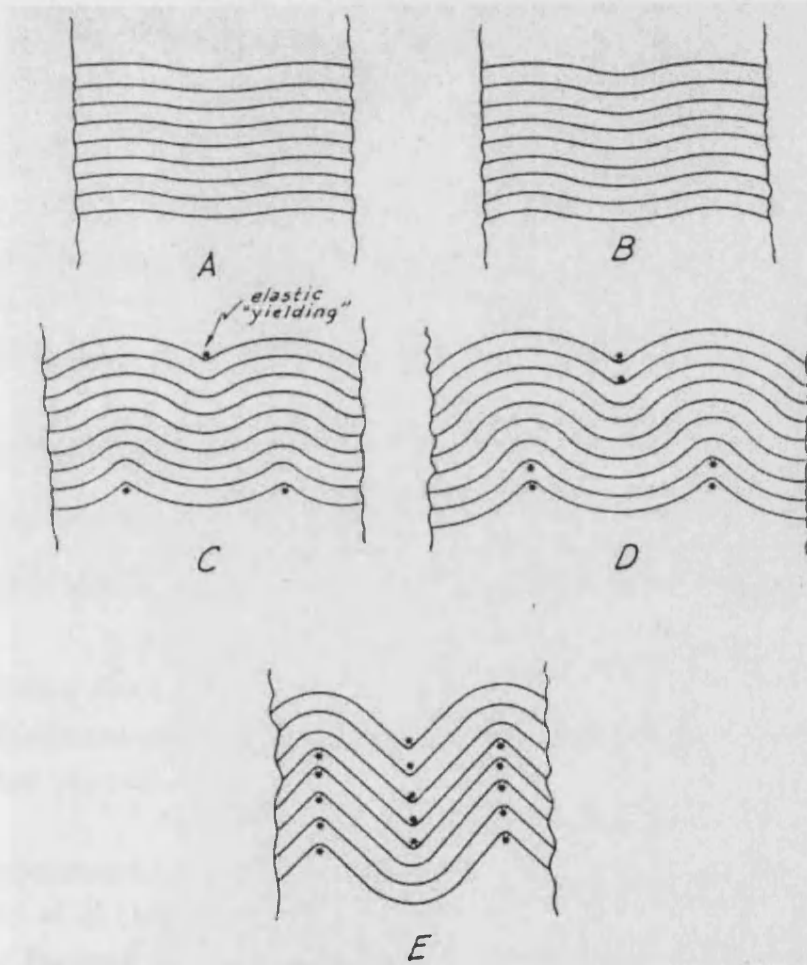


Figure 2.8: The transition of folding from sinusoidal-to-concentric-to-chevron.
 (After Johnson and Honea 1975a)

In 1970, for the first time since Van Hise, Price (1970) entertained the notion that folds form in a sequential manner rather than all at once in a wavetrain, contradicting much of the previous theory on folding, especially Biot. Price also stated that rocks are solid when deforming, coming from solid time-strain analysis fitting every rock type Price had tried; this was also justified given that rock near the Earth's crust has the ability to store residual stresses for very large times. Evidence of elastic deformation was shown from experimental cyclic loading, where several samples behaved in an elastic manner. An interesting point is made that a layer of material is often under horizontal compression even though no tectonic compression has taken place, purely through the geometry of the Earth, which is not flat in section as is usually drawn, but curved.

A later discussion of geological deformation rates by Price (1975) repeated several of these points and the reader is told that the three phases of fold development for a layer in the upper crust are:

- (i) Initial elastic deformation;
- (ii) Inelastic deformation, once the elastic limit is reached;
- (iii) Fold locking and flattening.

By thinking about the strain rates for this process and considering serial rather than instantaneous buckling, it was seen that folding can occur at a far faster rate than was normally quoted in geological literature up to that point.

The experimental evidence of serial buckling mentioned by Price was highlighted by Blay *et al.* (1977), when looking to model fold development in sedimentary strata. Focusing at the base of a gravity glide, horizontal layers of visco-elastic gelatine, able to support large elastic strains, were compressed axially using a motorized slow moving piston. Whilst occasionally the folding was in the form of uniform sinusoidal buckle trains, it was stated that more common was *non-synchronous* fold development, with amplification of individual folds at different times. This was either in a sequential manner, once the multilayer was fully axially loaded as shown in Fig. 1.6, or by isolated fold growth where arresting of the stress front allowed localized concentric folding.

Cobbold (1975), also tried to show that serial buckling does occur, firstly dis-

cussing metamorphic natural examples with homoclinic profiles and then conducting single layer experiments with “similar rheological properties”. Sedimentary inclusions were said to be the imperfection mechanism initiating geological folding which were modelled by introducing central deflections of varying magnitude. When buckled, a single fold was initiated, sequentially propagating, leading to a wavepacket and eventually periodic waveshape. The layers deformed by tangential longitudinal strain and hence there was no change in the orthogonal thickness. This last point is at odds with the usually held geological theory that modulated homoclinic profiles are the result of thickness changes within the layer.

2.3.6 Shear banding

In determining the structure of the Earth’s crust and hence whether elastic or viscous modelling is appropriate, it is useful to recognize phenomena particular to different areas of the strata. Higher up in the lithosphere, it is generally accepted that rocks are solid, behaving in a brittle manner, and so frictional considerations are usually more common. Shear bands, zones of localized deformation, are abundant in brittle rocks that have failed under compression and it is worth mentioning a couple of the more famous publications from this area.

Rudnicki and Rice (1975), produced a quasi-static formulation of the localization conditions and proposed a constitutive model. Here the compressed brittle rocks were seen as isotropic elastic bodies, with random fissures having frictional resistance to sliding. Localization occurs due to an instability in the constitutive description and inelastic strain arises from the sliding friction, making the relations pressure-sensitive.

For rocks close to the Earth’s surface, the mechanical behaviour is often described by elasto-plastic models. Maier & Hueckel (1979), showed however, that this is not totally adequate as rocks differ to metals and therefore characteristics need to be added or revised. To this end elasto-plastic constitutive laws were studied where the direction of the plastic strain rate vector does not depend on stress rates. In particular, it was shown that:

- (i) The plastic strain rate is not normal to the yield surface due to internal

friction;

- (ii) There is a coupling of elastic and plastic deformations;
- (iii) Yielding may be hardening, softening or not change at all.

2.4 Localization and buckling

Before starting this section, it is worth pointing out that there are several good reviews on elastic buckling, bifurcation, and cellular buckling theory when studying the elastic buckling literature post 1970. The first three mentioned below, in particular, give a good background of elastic stability research before 1970.

In 1970 Hutchinson & Koiter (1970), gave a review of postbuckling theory up to that point, with many references to previous work done on the subject. Whilst concentrating on the theory and applications for continuum thin-shell buckling, everything is applicable to the problems posed in this thesis. The bulk of the paper studied the loss of stability of a pre-buckling state, bifurcating to a buckled configuration, and also how load-deflection curves show the stability of a perfect and imperfect system.

Two articles by Hunt (1983; 1986) gave brief, but excellent, historical précis of bifurcation theory and conservative elastic buckling. The former also looked at the large deflection strut model, which was used to discuss an axially loaded plate and local and overall mode interaction of a stiffened plate.

As will be seen below, by 1989, *localization* had become a popular area of interest. Hunt *et al.* (1989), illustrated the buckling localization found in elastic structures, one of which was the strut on a nonlinear foundation, viewed from three perspectives including the *dynamic phase-space analogy*. Lastly, connected to this, Hunt *et al.* (2000a), used the strut on a nonlinear foundation, cylindrical shell, sandwich structure, geological folding and link models to look at destabilization-restabilization processes, localized buckles and sequential lockup.

2.4.1 Localization

Softening foundations

An early investigation into localization was conducted in 1980 by Tvergaard & Needleman (1980), who showed that a bifurcation at (or close to) the maximum load is vital for localization, using an axially loaded linear elastic column, with an initial imperfection, on a (piecewise linear) softening foundation. Similar localization behaviour was later found by Hunt & Bolt for an elastic link model, analogous to a strut on an elastic(-plastic) matrix, which was visualized in the form of a “hooking response” in the bifurcation diagram (Hunt & Bolt, 1986; Bolt, 1989).

Tvergaard & Needleman (1983) applied the same idea to several other static loading examples. For an elastic column on a softening foundation with both periodic, nonperiodic and mixed initial deflections and for thermal buckling of railway lines, identical localized behaviour were found. However, this was not the case for an elastic column under dynamic loading, considered to be on an elastic-plastic or bilinear softening foundation, and impact loaded by an infinite mass.

Potier-Ferry (1983), again obtained localized behaviour for a linear elastic beam on a softening foundation; but also proved that the localization involved nonlinear interactions between instability modes whose wavelengths were in a narrow band.

In 1988, the study of localization phenomena was advanced significantly in an article by Thompson & Virgin (1988), who used static-dynamic analogies to show spatial chaos and localization in a strut, by replacing time with space in nonlinear dynamical theory. Such ideas were taken further by Hunt & M. K. Wadee (1991), showing that the linear elastic strut on a softening foundation is a Hamiltonian system that follows Lagrange’s equations; by reworking the equations into fast and slow space, modulated and localized modes were possible. Importantly they proved that the upper and lower bounds of localized buckling are given by the critical and Maxwell loads respectively. Later, in conjunction with Shiacolas, similar results were shown for a nonlinear beam and linear foundation (Hunt *et al.*, 1993).

The slow-space variable was also used by Whiting (1997), who conducted Galerkin analysis to find localized buckle patterns for a strut on a softening foundation and determined the modes using perturbation analysis near the critical load.

Destabilizing-restabilizing foundations

By 2001, the literature had moved on to more realistic *destabilizing-restabilizing* foundations. Budd *et al.* (2001), showed that for an elastic strut on different Winkler foundations with such characteristics, the solution changes from an *homoclinic* (localized cellular post-buckle state) far away from the critical load to a periodic solution as the load approaches the Maxwell load via an *heteroclinic connection*. M. K. Wadee *et al.* (2002) looked more closely at how such wave patterns are seen, by modelling multi-packet localization solutions for a similar situation. As the localized solutions tend towards the periodic, two homoclinic wavepackets moving towards one another will meet and the solution then spreads outwards.

The year 2001 also saw Peletier publish an in-depth paper on the “localized buckling and spreading deformation of an axially loaded long elastic Euler strut on a destabilizing-restabilizing nonlinear elastic Winkler foundation” (Peletier, 2001b), recognizing the geological implications of such a model. The localization and delocalization were investigated using the “partially” linearized minimum strain energy profile for a particular end-shortening. After proving the existence of minimizers for the problem and the appearance of the periodic section, numerical solutions were obtained using finite elements. With global minimization difficult, Peletier used random sets of initial data, considering the stationary solution with the lowest value as the global minimizer. The solutions fall on the odd and even load-deflection curves of the ordinary differential equation, the jumps then being explained by equal energy arguments.

To prove the existence of bifurcation branches such that the Hamiltonian is zero along each solution on the branch, a more general fourth order, reversible Hamiltonian system was the subject in Beardmore *et al.* (2005). Depending on the form of the foundation term, the differential equation possessed periodic, homoclinic and heteroclinic solutions and is applicable to geology problems and buckling theory, especially *cellular buckling*.

2.4.2 Geological applications

One of the first papers to apply the localization theory and concepts given above to geological folding, and hence study such notions in a structural engineering context, was that published in 1997 by Hunt *et al.* (1997). Whilst stating that multilayer effects are important, they concentrated on a single (visco-)elastic layer in visco-elastic medium, and although they felt that a half-space is more realistic than a Winkler foundation, the latter was used as “it is good for finite depth supporting media”. Pointing out the flaws of Biot’s work, different types of nonlinearity were introduced to the foundation, including the hardening model—a realistic geological situation if it follows softening—and localized solutions sought.

The companion paper by Whiting & Hunt (1997) modelled the initiation and development of the folding of an elastic layer on a visco-elastic foundation, and highlighted the effects of the geometric and material nonlinear terms. Two models were used; the first included geometrically nonlinear terms and was capable of large deflections and the second used a linear beam on a nonlinear foundation, and was hence valid for small, finite deflections. Unlike Hunt *et al.* (1997) the foundation consisted of independent spring-dashpot elements with continuity due to the layer. The initial elastic deformation admitted localized buckling which during the evolution allowed nonperiodic waveforms ignored by linearity.

A slightly different problem was posed by Waltham (1997): how can the movement of the overburden initiate and affect buckling? Opposing the usual ideas of a medium as the overburden, here the overburden was modelled using an elastic plate on a viscous medium. Although familiar equations were formulated, the shear stress between layer and medium was also taken into account. Inserting values into the model, the wavelength λ is given by:

$$\lambda = 2\pi \left(\frac{D}{g(\rho_s - \rho_w)} \right)^{1/4}, \quad (2.10)$$

where D is the flexural rigidity of the plate, g is the acceleration due to gravity and ρ_s and ρ_w are the density of the salt and water respectively. This can be thought of as a strut embedded in two materials of different viscosity, which is an entirely reasonable proposition (de Sitter, 1964).

A pair of complementary papers by Budd & Peletier (1999; 2000), the former with

Hunt, looked at localized solutions of a single elastic layer embedded in both time dependent no-slip Winkler and viscous half-space foundations. Showing the evolution of folds from straight layers up to infinite time periods, they controlled this using constant and linearly increasing end-shortening. The solutions were shown to be approximately self-similar; hence they stay localized and are independent of the initial disturbances. The long-time behaviour was elasto-plastic or visco-elastic, even though the material is deformed past the plastic limit; this was justified by stating that wavelength selection is at the first increments of folding. Very importantly was shown that, as time increases, the wavelength alters proving that

no dominant wavelength is valid over all times,

the load tended towards Biot's load, but over excessively long time frames; hence Biot's analyses are not a good representation of reality.

So far all of the geological applications had been for a single layer. This changed when kink banding in multilayered structures was the subject of three papers by Hunt, Peletier & M. A. Wadee (Hunt *et al.*, 2000b; Hunt *et al.*, 2001; Wadee *et al.*, 2004). Two follow-up articles have been recently submitted by Wadee & Edmunds (Wadee & Edmunds, 2005; Edmunds & Wadee, 2005) extending the kink band model developed by Wadee *et al.* Kink banding, like parallel folding, has localization and sequential lockup behaviour, but differs in that it is a discrete process, with rigid boundaries, and that all of the layers have the same deformation. Initial imperfections and applied end-shortening mean that the system gives a nonlinear response, and by studying the total potential energy, the system seeks a stable global minimum. Using the *Maxwell stability criterion* the problem of having an infinite critical load is removed by saying that buckling has occurred once the compression is sufficient to overcome the internal friction. The later model (Wadee *et al.*, 2004) adds a Pasternak foundation, as opposed to a Winkler, and allows compressibility within the multilayer. When compared to experiments on sheets of paper, representing the stratified medium, there was remarkable agreement, proving that elastic, frictional energy models are able to imitate geological processes of this nature.

2.4.3 Other interesting and connected areas

When conducting an in-depth study of this type, it is inevitable that one finds literature that whilst relevant and interesting, is not directly associated with any of the larger bodies of work. For completeness these are included below.

Imperfections

There are many different types of imperfection that can exist within a system. Amazigo *et al.* (1970), concentrated on three types of initial displacement perturbations, using an infinitely long elastic strut on a softening foundation, and made an attempt to find asymptotics for a small imperfection in each case. The three chosen were: harmonic, dimple (localized and decaying exponentially) and random. Harmonic initial displacement was found to cause the greatest loss in buckling strength of the column, followed by random and finally dimple. For harmonic and dimple perturbations the analysis gave an asymptotically exact solution agreeing with the linearized solution. However, the multivariate Gaussian perturbation resulting from linearization of a random displacement, cannot be checked against a perturbation scheme and it was stated, that it is unlikely to be asymptotically exact. The dimple imperfections are also applied to cylinders in a follow-up paper (Amazigo & Fraser, 1971).

Elastic struts

Elastic struts, with and without foundations, have also been used in the following situations:

- (i) Thompson & Hunt (1983) modelled an arch as a simply supported beam with a central point load and analysed this using a sinusoidal Galerkin approximation;
- (ii) Sandwich structures: a single face and core can be modelled as strut on a foundation and the calculus of variations used to find the energy minimum (Hunt & Wadee, 1998; Wadee, 1998; Wadee, 1999; Wadee, 2000);

- (iii) The phenomenon of Arnold tongues was studied by Hunt & Everall (Hunt & Everall, 1999; Everall, 1999) using an elastic strut on a stiffening foundation;
- (iv) Domokos & Holmes looked at two situations with constrained Euler buckling. The first in 1997 with Royce, (Domokos *et al.*, 1997), investigated the elastic buckling of a beam, with mixed pin and clamped end displacements, laterally constrained by rigid, frictionless sidewalls. Formulated as a non-linear Euler strut and numerically analysed, the results were then compared to experiments. The second in 2000 with Hek (Holmes *et al.*, 2000) involved thin rods confined to the plane, where buckling resulted from a force field, linearly dependent on distance, distributed along the rod. Equilibrium equations derived from the Euler-Lagrange equations are Hamiltonian in nature, and although the bifurcation diagram is complicated in structure, it is composed of pitchfork bifurcations and thus equilibrium approaches homoclinic and heteroclinic connections at large loads (and large lengths).

Pipelines

In 1983, both Kryiakides & Babcock (1983) and Chater *et al.* (1983) looked at buckle propagation along a pipeline, the former in confined and unconfined pipelines due to external pressure. The latter used a laterally loaded beam on a foundation which stabilizes, destabilizes then restabilizes and hence there are three static equilibrium states: collapsed, uncollapsed and transitional. Propagation begins at the Maxwell load, but for a weak foundation, the load never reaches this and the buckling arrests.

Finally, an interesting buckling problem of an axially loaded cable in a blocked duct was studied by Rivierre *et al.* (2001). Dependent upon the load, the cable is straight or can take a sinusoidal or helical mode-shape. Included in the model are lockup and *friction*. Initially ignoring friction, using energy considerations, where the weight of the cable provided a resistive force, results from classical theory were found. However, including friction via Coulomb's law, the moving axial load for the sinusoidal case was presented as

$$\frac{dP(x)}{dx} = \mu \left(\delta_i \beta(\alpha(x)) w_e + \frac{rP^2}{8EI} \right), \quad (2.11)$$

where P , EI and μ are defined as usual, r is the clearance radius between the duct and the beam, w_e is the beam weight and α is an angular perturbation. The terms on the right correspond to the weight of the contact force and the sinusoidal configuration respectively and an increase in μ , increases the sinusoidal buckling load.

2.5 Concluding remarks

Having had an extensive look at the previous research connected to the ideas of geological folding, it has become obvious that the crust is usually made up of layers. The levels of the crust close to the Earth's surface are solid and brittle; permanent deformation is most likely to be by shear banding which under such conditions is a frictional process.

As we descend further down, the rocks become more ductile, the layer boundaries become indistinct, and eventually will deform very smoothly by flowage. At this point the orogenics could be thought of as having more liquid properties and viscosity enters into the scheme. However, at these sort of depths one does not see parallel folding.

Between these two extremes, somewhere in the upper regions of the crust, the strata are reasonably ductile, but still solid and elastic(-plastic); here folding is the dominant mode of deformation and because of the layered nature and the high pressures, friction is still involved in the process. Even with interlayering of less competent material or the pressure forcing fluid between the boundaries, friction would not be negated completely, just reduced, and the slipping planes would be more prominent.

Hence slippage between layers almost certainly occurs and is vital to the folding process; the seams are unlikely to be adhered and shearing is only of interest in very thick single layers folding in a parallel manner. Possibly due to the added complication in modelling, even though friction has been recognized in many articles as a probable phenomenon, its effects have not really been considered or investigated properly for more concentric-looking folding.

In some respects, it could be argued, that the fact as to whether layers are more solid or liquid during deformation seems fairly irrelevant, as all of the theories give similar values for wavelengths, thickness ratios etc. The simple elastic models give results comparable to much more complicated elastic and viscous models. If one is adding more complex behaviour, it seems foolish not to use the classic, although maybe more basic, techniques. This is especially true, if it is accepted that the layers often fold in a serial manner, as there is a whole host of theory and concepts dealing with localization, leading to periodicity, in the elastic buckling field.

Chapter 3

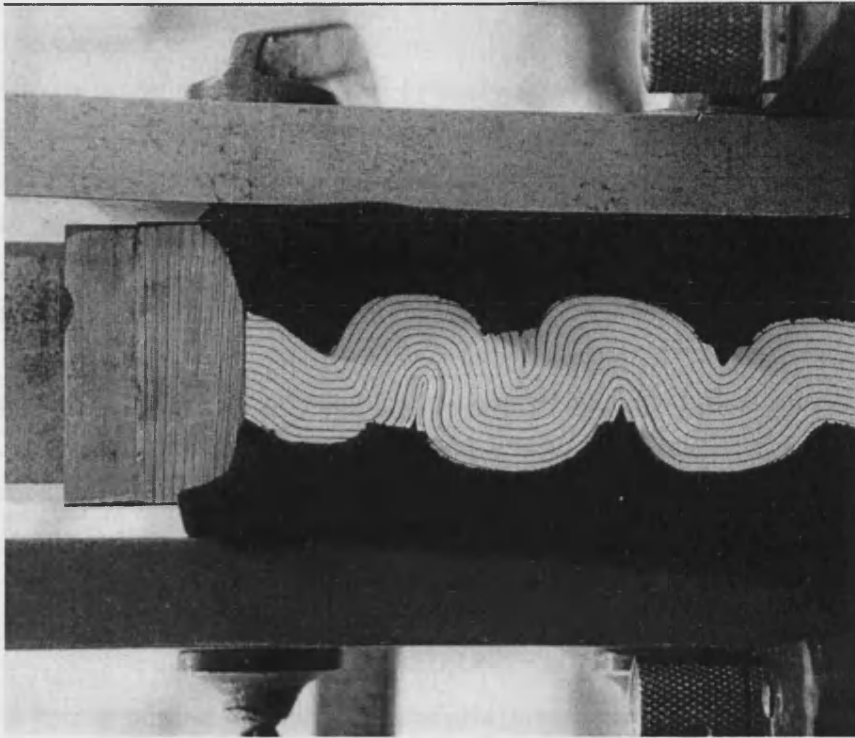
The two-layer frictional parallel folding model

3.1 Introduction

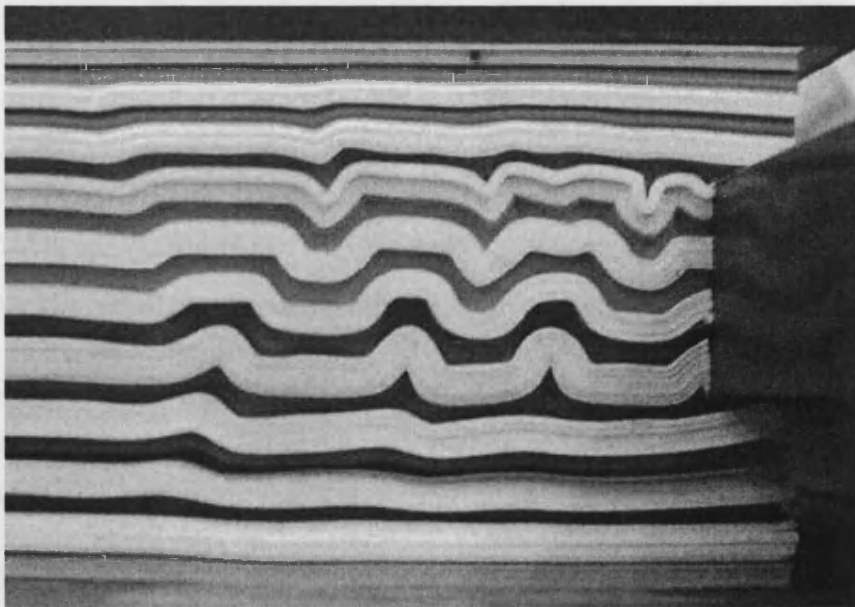
Geological folding due to tectonic compression is likely to occur under conditions of high overburden pressure (Price, 1970; Price & Cosgrove, 1990). In multi-layered structures as formed from sedimentary rocks, the appearance of voids between layers is then either denied, or at the very least subject to severe energy penalties.

If identical layers of finite thickness fold in identical fashion, without voids they can fit together only by choosing straight limbs and sharp corners; this leads to the phenomenon known as kink banding (Hunt *et al.*, 2000b; Hunt *et al.*, 2001; Wadee *et al.*, 2004). Alternatively, layers can bend with finite curvature about the same centre, implying that each layer differs from its neighbour and leading to *parallel folding*.

A simple compression test on layers of paper constrained by clamps between foam faces that deforms in such a way is shown in Fig. 3.1(a). Related experiments showed kink bands forming when the foam foundations were replaced with stiffer materials, and overburden pressures were elevated (Wadee *et al.*, 2004; Wadee & Edmunds, 2005) (Fig. 3.1(b)).



(a)



(b)

Figure 3.1: (a) Parallel folding in layers of paper. For visual clarity, approximately every tenth layer has been edged in black. (b) Kink banding in layers of paper. (After Wadee & Edmunds 2005)

Whether kink bands or parallel folds are formed, one key characteristic of folding in the absence of voids is that layers will slip relative to one another. The simultaneous presence of overburden pressure means that friction then becomes of primary importance. If the deflected shape is periodic, the direction of friction reverses as the slope changes sign, and this introduces a strongly nonlinear effect to what otherwise might be a linear model. Chapters 3 and 4 examine fully solutions of a simplified two-layer bending model in the presence of such a nonlinearity.

This chapter starts by introducing a two-layer, axially-rigid, flexural model and summing the contributing energy terms which comprise strain energy of bending, foundation energy and work done by load. Friction is also included as a quasi-energy contribution. The expected phenomenology is then explored using a single degree-of-freedom Galerkin approximation, obtained from a Fast Fourier Transform analysis of experimental samples, which allows description of the important *jammed region*. The effects of small imperfections are assessed, and similarities with the corresponding unfolding of a bifurcation point in the absence of friction are explored.

3.2 Pseudo potential energy

3.2.1 Nonlinear formulation

Consider two axially and transversely incompressible layers of thickness t , formed from a material of bending stiffness EI , embedded in a soft foundation of transverse stiffness k per unit length, and compressed longitudinally by a load P such that they remain in contact along their length, as shown in Fig. 3.2. The coordinate system for this model is taken as the arclength, x , and the vertical deflection, w .

To fit snugly (without voids), the layers must bend about the same centre of curvature. If centrelines are to remain unchanged in length, differential stretching at the interface generates slip, s , between the layers as illustrated. The work done against friction during slip will be taken into account as a quasi-energy

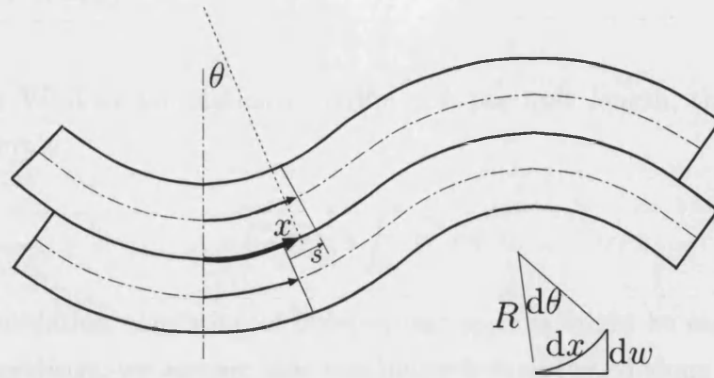


Figure 3.2: Slip between incompressible layers constrained to remain in contact.

contribution to the total potential energy.

Bending energy

If the interface bends to a radius of curvature R , the centreline of the inner layer must bend to a radius $R - t/2$ while that of the outer layer takes a radius of $R + t/2$. The bending energy from both layers dU_B over an incremental length dx is then,

$$dU_B = \frac{1}{2}EI \left(\frac{1}{(R - t/2)^2} + \frac{1}{(R + t/2)^2} \right) dx. \quad (3.1)$$

If $t^2 \ll 4R^2$ this can simply be rewritten as $dU_B = EI/R^2 dx$ and the total bending energy contribution over a length L , written in terms of deflection w becomes (Thompson & Hunt, 1973),

$$U_B = EI \int_0^L \left(\frac{\ddot{w}^2}{1 - \dot{w}^2} \right) dx, \quad (3.2)$$

where dots denote differentiation with respect to x . Subject to the above restriction on t , this expression holds over large deflections.

Foundation energy

For a linear Winkler foundation of stiffness k per unit length, the foundation energy is simply

$$U_F = \frac{1}{2}k \int_0^L w^2 dx. \quad (3.3)$$

Whilst a foundation consisting of independent springs might be considered geologically unrealistic, we assume that continuity is maintained along the length of the layers.

Work done by load

If the compressive load P moves inwards by the shortening of the interface, the corresponding deflection \mathcal{E} of the load P over large deflections is (Thompson & Hunt, 1973)

$$\begin{aligned} \mathcal{E} &= L - \int_0^L \sqrt{1 - \dot{w}^2} dx \\ &= \int_0^L (1 - \sqrt{1 - \dot{w}^2}) dx. \end{aligned} \quad (3.4)$$

Hence the work done by the load is

$$P\mathcal{E} = P \int_0^L (1 - \sqrt{1 - \dot{w}^2}) dx. \quad (3.5)$$

Work done against friction

Over the incremental length dx seen in the inset to Fig. 3.2, if the centreline of each layer is to remain unchanged in length, there must be a difference in length between the outermost fibre of the inner layer and the innermost fibre of the outer layer.

From simple bending theory, it follows that, over a small change in angle $d\theta$, this

difference is

$$ds = \left(\frac{R}{R - t/2} - \frac{R}{R + t/2} \right) dx = \frac{Rt}{R^2 - (t/2)^2} dx. \quad (3.6)$$

If, as for the bending energy, it is assumed that $t^2 \ll 4R^2$, this reduces to,

$$ds = \frac{t}{R} dx = t d\theta. \quad (3.7)$$

Alternatively, for two layers of thickness t , the amount of slip over a change in angle $d\theta$, is approximately the difference in length between the Neutral Axis (N. A.) of each layer (Fig. 3.3). From Fig. 3.3, R_{l_1} and R_{l_2} the radius of curvature

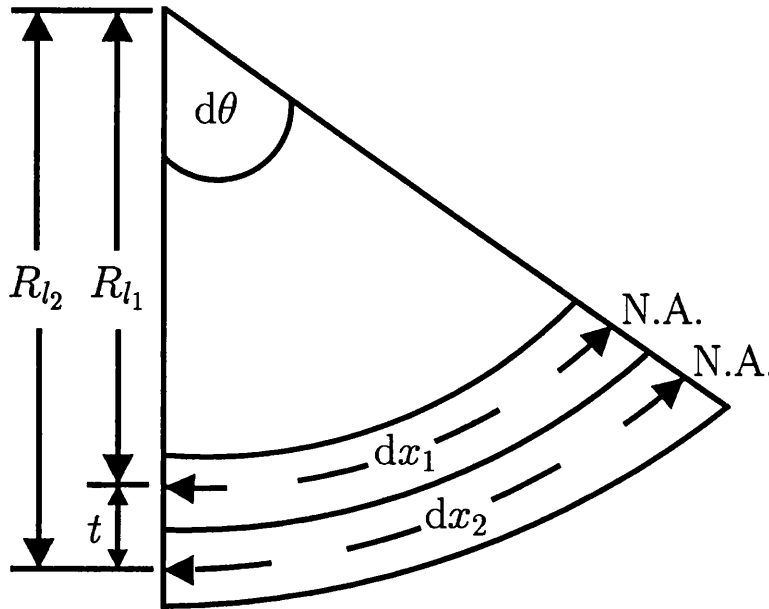


Figure 3.3: Two layers bent through a small angle $d\theta$.

for the first and second layer respectively; dx_1 and dx_2 are the corresponding arclengths. Basic trigonometry tells us that for small enough $d\theta$

$$d\theta = \frac{dx_1}{R_{l_1}} = \frac{dx_2}{R_{l_2}}. \quad (3.8)$$

Now $R_{l_1} = R_{l_2} - t$, hence

$$\frac{dx_2}{R_{l_2}} = \frac{dx_1}{R_{l_2} - t}, \quad (3.9)$$

which implies that

$$\begin{aligned}
dx_1 &= \frac{dx_2}{R_{l_2}}(R_{l_2} - t) \\
&= dx_2 - \frac{dx_2}{R_{l_2}}t \\
&= dx_2 - d\theta t.
\end{aligned}
\tag{3.10}$$

Thus the amount of slip between two adjacent layers is $d\theta t$, in agreement with (3.7).

As slip at position x is cumulative, the total slip s at x is given by,

$$s = \int_0^x ds = \int_0^\theta t|d\theta| = t|\theta|. \tag{3.11}$$

Here a modulus sign is included to ensure that for θ positive or negative the work done is maintained as positive. Integrating as before over the range $0 < x < L$ the total work done against friction is then,

$$U_\mu = \mu q t \int_0^L |\theta| dx = \mu q t \int_0^L |\sin^{-1} \dot{w}| dx, \tag{3.12}$$

where μ is the coefficient of friction and q is the overburden pressure. (3.12) uses the relationship $\theta = \sin^{-1} \dot{w}$, which can be seen from the inset in Fig. 3.2.

3.2.2 Potential energy function

The total potential energy function comprises the bending energy minus the work done by the load (Thompson & Hunt, 1973), together with the contribution from the work done against friction. The sign of this friction term can be either positive or negative, depending on whether the friction acts to resist the release of strain energy or in the opposite sense. To allow for all possibilities we therefore introduce a *friction indicator* (Brogliato, 1999) $\chi = \pm 1$ on the friction energy. Here: $\chi = +1$ implies that friction opposes the external force and gives a positive friction energy contribution; alternatively, $\chi = -1$ implies that friction acts in the same sense as the external force, giving a negative friction energy contribution (see Fig. 3.4). We can then write the total potential energy function, valid over

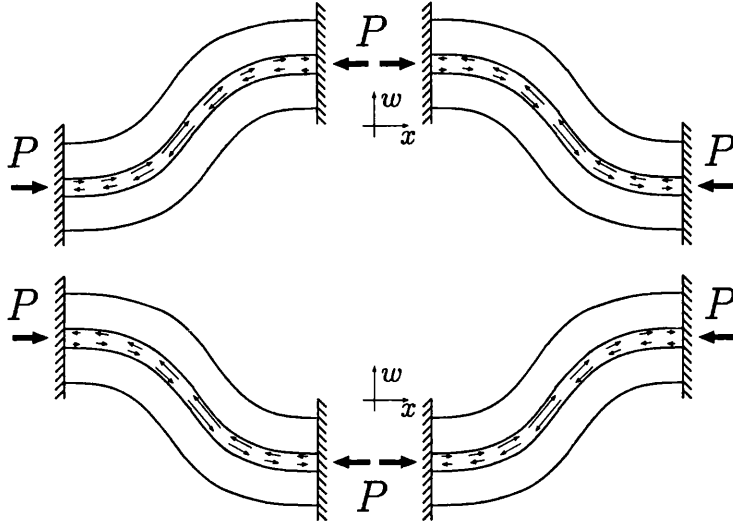


Figure 3.4: Slip directions for $\chi = +1$. Top: Q positive. Bottom: Q negative.

large deflections, as follows

$$\begin{aligned}
 V &= U_B + U_F - P\mathcal{E} + \chi U_\mu \\
 &= EI \int_0^L \left(\frac{\ddot{w}^2}{1 - \dot{w}^2} \right) dx + \frac{1}{2}k \int_0^L w^2 dx + P \int_0^L (1 - \sqrt{1 - \dot{w}^2}) dx \\
 &+ \chi \mu q t \int_0^L |\sin^{-1} \dot{w}| dx. \tag{3.13}
 \end{aligned}$$

The solutions of the system are then stationary points of this energy functional.

Small deflection potential energy function

If w is assumed to be small, then the first derivative \dot{w} is also small. This allows us to replace

$$\frac{\ddot{w}^2}{1 - \dot{w}^2} \quad \text{by} \quad \ddot{w}^2, \tag{3.14}$$

$$1 - \sqrt{1 - \dot{w}^2} \quad \text{by} \quad \frac{1}{2}\dot{w}^2, \tag{3.15}$$

and

$$\sin^{-1} \dot{w} \quad \text{by} \quad \dot{w}. \tag{3.16}$$

Thus, the energy function (3.13) reduces to,

$$V = \int_0^L \left(EI\ddot{w}^2 - P\frac{\dot{w}^2}{2} + k\frac{w^2}{2} + \chi\mu q t|\dot{w}| \right) dx. \quad (3.17)$$

3.3 A useful Galerkin approximation

The behaviour of the system can usefully be seen in the context of an unfolded bifurcation plot. To develop such a description, let us assume a deflected shape,

$$w(x) = Q \cos\left(\frac{\pi x}{L}\right), \quad (3.18)$$

so that $Q = ((w(0) - w(L))/2)$. The rationale behind such an assumption is explained next.

3.3.1 The Fast Fourier Transform (FFT)

We suppose that the waveshape of any layer making up part of a parallel fold is 2π -periodic and composed of a combination of sinewaves. We can then say that the vertical deflection w_l , written in terms of the horizontal distance along the layer x_l , is given by

$$w_l(x_l) = \sum_{m=-N}^N c_m e^{imx_l}, \quad (3.19)$$

where the coefficients c_m can take any complex value and the greater N is, the more accurate the resultant waveshape. Here $i^2 = -1$ as usual.

The coefficients c_m can be determined using the MATLAB function `fft` (The Math Works, 2001), which returns the Discrete Fourier Transform (DFT) of a vector (Solymar, 1988) computed using a Fast Fourier Transform (FFT) algorithm (Press *et al.*, 1986). Given a vector of vertical displacements W of length N , the function $C = \text{fft}(W)$ implements a one-dimensional Fast Fourier Transform

by

$$C_K = \sum_{m=1}^N W_m \omega_N^{(m-1)(K-1)}, \quad (3.20)$$

where

$$\omega_N = e^{(-2\pi i)/N}, \quad (3.21)$$

is an N th root of unity. If w_l is a real function then we have that $C_K = \bar{C}_{N-K+1}$.

From “Numerical Recipes: The Art of Scientific Computing” (Press *et al.*, 1986), Fast Fourier Transform algorithms tend to work using the following methodology. A DFT of length N can be written as the sum of two DFTs, each of length $N/2$, one formed from the even-numbered points and the other the odd-numbered points,

$$C_K = C_K^e + \omega_N^K C_K^o, \quad (3.22)$$

where C_K^e (C_K^o) is the K th component of the DFT with length $N/2$ formed from the even (odd) components of the function.

The idea is then used recursively, i. e. C_K^e is reduced to the transform of its $N/4$ even-numbered (C_K^{ee}) and odd-numbered (C_K^{eo}) data. It is easiest to do the above if N is an integer of power 2, if it is not then pad with zeros. The process is continued until C_K is subdivided into transforms of length 1, and then for every pattern of e 's and o 's there exists a single point transform that is just one of the input numbers' function.

Although this sounds complicated the practicalities are far more simple, we just need to supply the *fft* function with a vector of length N showing how the vertical deflection of a layer alters over a single wavelength. For reasons that are apparent from the description of the FFT above let $N = 32$. To get the points W_m , a rather basic, but effective, technique was employed using the spreadsheet package EXCEL. A photograph, cropped to a typical experimental wave, can be set as the background of an (x, w) -scatter plot in EXCEL; the points on the plot can then be moved to follow the curve of a particular layer (Fig. 3.5). W_m alter automatically and whilst the values themselves are irrelevant, the difference between them is of

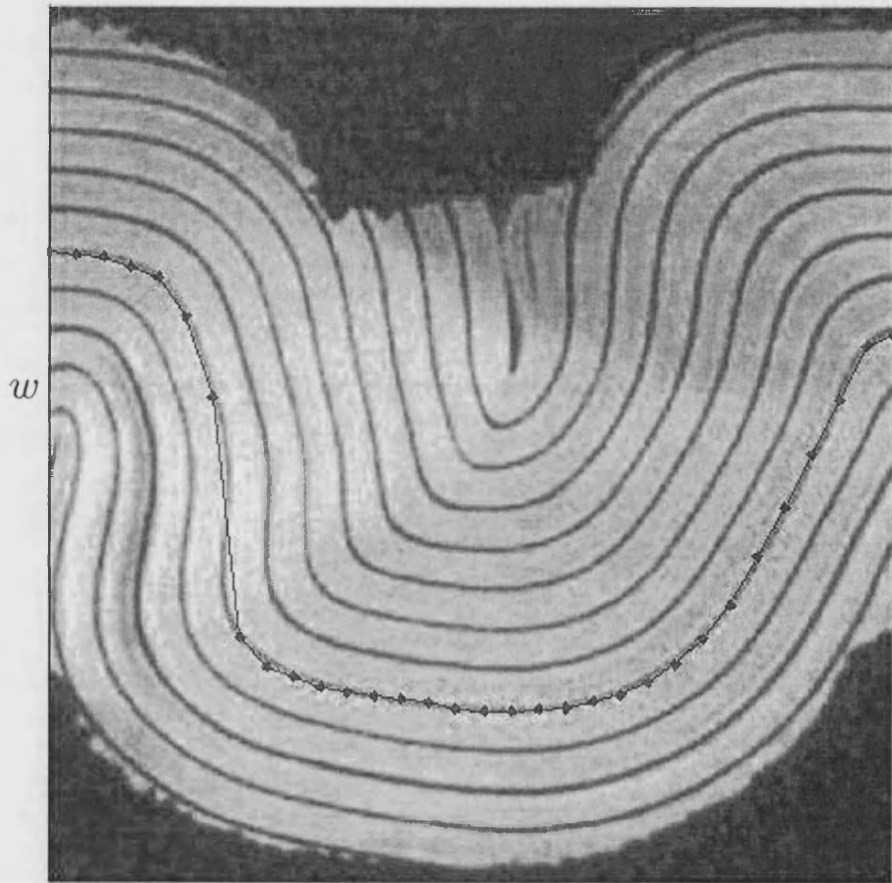


Figure 3.5: Fitting points along deformed experimental layers.

importance when tracing each path. W can then be exported to the `fft` command in MATLAB to obtain C .

As in Fig. 3.1, every tenth layer in Fig. 3.5 is blackened to highlight the deformation and the `fft` routine was performed on each of the visible black layers. Fig. 3.6(a) shows how the magnitude of the initial coefficient c_1 , associated with $\cos x_i$, changes throughout the multilayer. It is immediately obvious that towards the centre of the multilayer the layers become much more sinusoidal in shape. This result is made even stronger when studying the relative sizes of c_1 and c_2 ; it can be seen from Fig. 3.6(b) that in the central region of a parallel fold the first coefficient dominates the subsequent ones. It is worth noting that not only does Fig. 3.6(b) show the sinusoidal nature of the central layers, but also emphasizes the *non-sinusoidal* behaviour of the layers on the extremities.

Hence it is natural, as a first approximation, to assume that the central interface is a single cosine of the form given in (3.18). We then consider the energy $V(Q, L)$ of the solutions of this form and look for stationary solutions in this restricted class. In Chapter 4 we extend the analysis to the full class of solutions via the calculus of variations, but this simple analysis leads to considerable insights. The deflection is illustrated in Fig. 3.4 over the range $-L \leq x \leq L$, for Q positive at the top and Q negative at the bottom. When $Q > 0$ the function $w(x)$ is decreasing on the interval $[0, L]$ so on this interval we could write $|\dot{w}| = \alpha\dot{w}$ where $\alpha = -1$. Similarly when $Q < 0$, the function $w(x)$ is increasing on the interval $[0, L]$ so we could again write $|\dot{w}| = \alpha\dot{w}$ but with $\alpha = 1$. This alternative notation will prove useful when we look at the more general solutions by means of the calculus of variations in the next chapter.

When the ansatz (3.18) is substituted into the linearized potential (3.17) the resulting energy is given by

$$V = \frac{1}{2}EIL \left(\frac{\pi}{L}\right)^4 Q^2 - \frac{1}{4}PL \left(\frac{\pi}{L}\right)^2 Q^2 + \frac{1}{4}kLQ^2 + 2\chi\mu qt|Q|. \quad (3.23)$$

Here the modulus on \dot{w} , and hence on Q , ensures that for positive χ , the energy contributions from all four quadrants of Fig. 3.4 are always positive as illustrated.

3.3.2 Bifurcation Analysis

The characteristic equation (3.1) can be written as

$$\lambda^2 + (a_1 + a_2)\lambda + a_1 a_2 = 0 \quad (3.1)$$

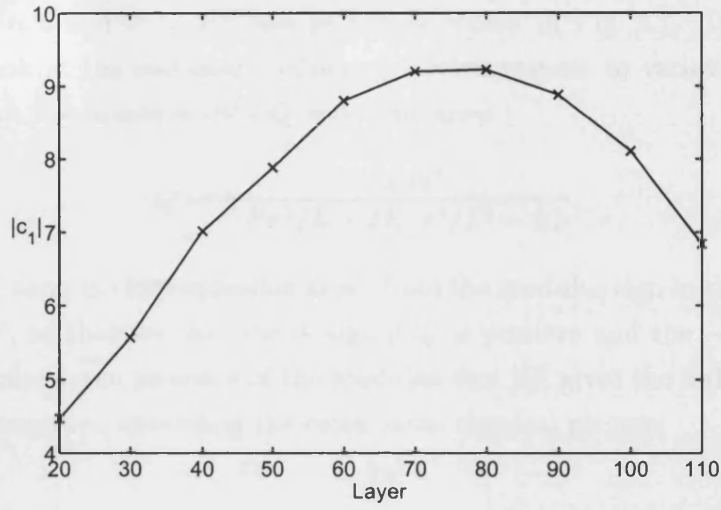
where λ is the eigenvalue. The characteristic equation (3.1) can be written as

$$\lambda^2 + (a_1 + a_2)\lambda + a_1 a_2 = 0 \quad (3.2)$$

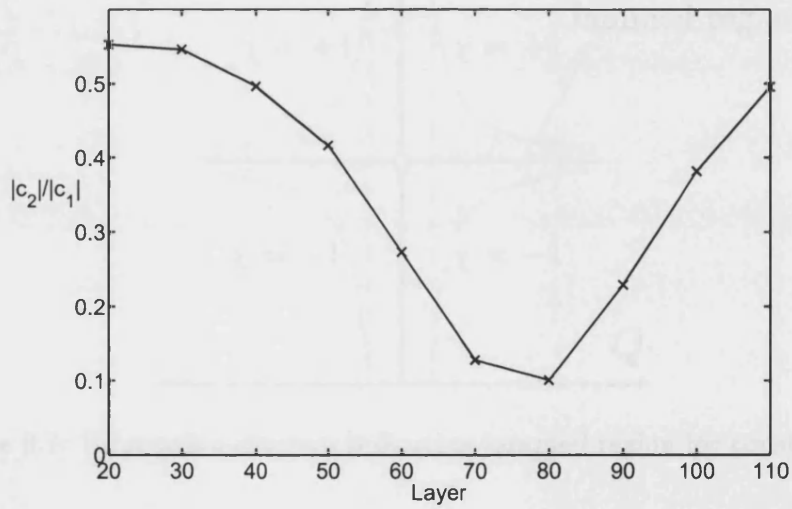
where the λ is the eigenvalue. The characteristic equation (3.2) can be written as

$$\lambda^2 + (a_1 + a_2)\lambda + a_1 a_2 = 0 \quad (3.3)$$

and the λ is the eigenvalue. The characteristic equation (3.3) can be written as



(a)



(b)

Figure 3.6: (a) How the magnitude of c_1 alters throughout the multilayer and (b) Comparing $|c_2|$ to $|c_1|$ throughout the multilayer.

3.3.2 Bifurcation diagram

The combination of the coefficient of friction μ and the friction indicator χ now can be seen in exactly the role of an imperfection, “unfolding” the bifurcation point at $Q = 0$ and $P = P^C$ (see §4.3.3) as shown in Fig. 3.7. To derive this figure we look at the stationary values of V with respect to variations in Q , so that we solve the equation $\partial V/\partial Q = 0$. This gives

$$Q = \pm \frac{4\chi\mu qt}{P\pi^2/L - 2EI\pi^4/L^3 - kL}, \quad (3.24)$$

where the \pm term in this expression arises from the modulus sign in the expression (3.23) for V , so that we take the $+$ sign if Q is positive and the $-$ sign if Q is negative. Indeed, the presence of the modulus sign $|Q|$ gives the unfolding a rich and novel structure, extending the more usual classical picture.

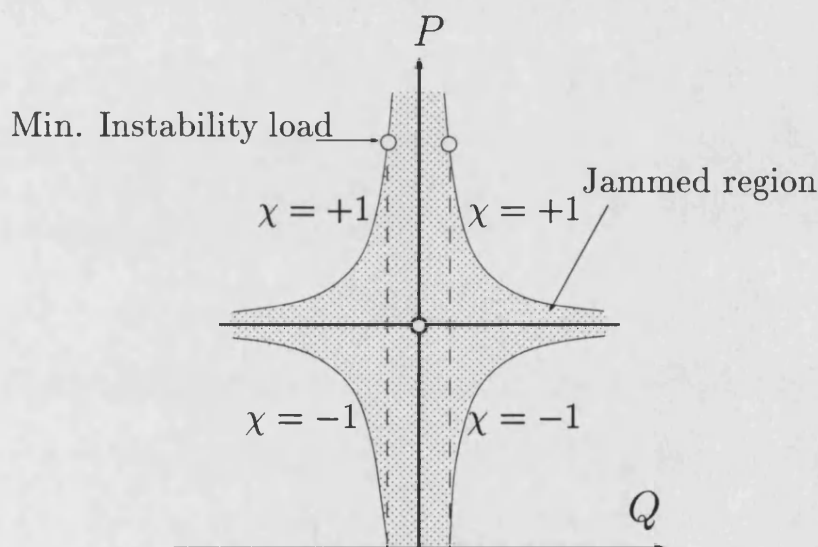


Figure 3.7: Bifurcation diagram indicating jammed region for constant μ .

3.3.3 Critical loads and wavelength selection

There is a critical value of $P = P^C$ at which $|Q| = \infty$. From (3.24) this is given by

$$P^C = \frac{2EI\pi^2}{L^2} + \frac{kL^2}{\pi^2}. \quad (3.25)$$

Conventionally, this is obtained by minimizing P^C over all possible values of L . It is easy to see that this occurs when

$$L = \pi \sqrt[4]{\frac{2EI}{k}}, \quad (3.26)$$

and

$$P^C = 2\sqrt{2EI k}. \quad (3.27)$$

This expression corresponds to the classical result for a strut on a linear elastic foundation of bending stiffness $2EI$ (Hunt *et al.*, 1989), and allows us to determine the critical wavelength at which we expect to see the unfolded bifurcation structure.

Alternatively, we may determine L from the condition that the energy per unit length should be stationary with respect to changes in L (Peletier, 2001a), so that

$$\partial(V/L)/\partial L = 0.$$

This leads to the condition

$$-2EI \left(\frac{\pi}{L}\right)^4 Q^2 + \frac{1}{2}P \left(\frac{\pi}{L}\right)^2 Q^2 - 2\chi\mu q t \frac{|Q|}{L} = 0. \quad (3.28)$$

Combining the expressions (3.24) and (3.28) it is easy to see that the critical wavelength is again given by (3.26). Thus the alternative conditions on L , for the minimum critical load and for the energy to be stationary with respect to changes in L , lead to identical values for the wavelength.

3.3.4 Stability of the solution paths

Stability of equilibrium under dead load is governed in the first instance by the second derivative (Thompson & Hunt, 1973),

$$\frac{d^2V}{dQ^2} = \frac{EI\pi^4}{L^3} - \frac{1}{2} \frac{P\pi^2}{L} + \frac{1}{2}kL. \quad (3.29)$$

If $d^2V/dQ^2 > 0$ there is a relative minimum of V and the solution is stable. Conversely, if $d^2V/dQ^2 < 0$ there is a relative maximum and it is unstable. Clearly, with P^C given by expression (3.25), if $P < P^C$ we have stability and if $P > P^C$ we have instability.

3.3.5 Jamming

At constant load P , points in the region between the two curves defined by $\chi = -1$ (or $+1$) are stationary positions where the system can be considered to be “trapped” or “jammed” between the two critical slip conditions with Q positive and negative and the frictional forces acting in opposite senses (as in the top and bottom of Fig. 3.4). Anywhere within the jammed region the system sits in equilibrium. The finite area of the region therefore replaces the infinitesimally thin equilibrium paths of a perfect (bifurcating) system without friction (Thompson & Hunt, 1973). Placed outside the jammed region, at constant load the system would move horizontally towards it until being brought to a halt at its boundary.

From Fig. 3.7, a typical sequence under changing load might then be as follows. At zero load, the system can rest in equilibrium anywhere along the Q -axis within the jammed region. To get to the intersection with a $\chi = -1$ line for example, a $|Q|$ value greater than that at the intersection can be input, whereupon the system will slip back to the boundary. This reverses the direction of the frictional arrows from those shown in Fig. 3.4. Application of positive load P then moves the system into the jammed region, following the dashed line, until the equivalent critical state for $\chi = +1$ is met. Instability then occurs, i. e. the system will suddenly deflect with $|Q|$ increasing, and continue to deflect. In the presence of a suitable nonlinearity there may be restabilization at some other larger value of

$|Q|$, but for the linear system this would never happen.

Note that symmetry of the curves about the value $P = P^C$ suggests that the minimum instability load is always at $P = 2P^C = 4\sqrt{2EI\bar{k}}$, independently of the value of μ ($\neq 0$). This suggests that, as μ vanishes, there would be a sudden drop in the load to cause instability, from $2P^C$ to P^C . The effect is lost with the introduction of a small imperfection, as described in the following section.

3.3.6 Initial imperfections

An imperfection ϵ in the sense of Q , implying that the system has a natural bias towards buckling in the positive Q direction, would be expected to appear in the energy function as a term in ϵQ with a negative coefficient (Thompson & Hunt, 1973). Hence from (3.23)

$$\begin{aligned} V_\epsilon &= \frac{1}{2}EIL\left(\frac{\pi}{L}\right)^4 Q^2 - \frac{1}{4}PL\left(\frac{\pi}{L}\right)^2 Q^2 + \frac{1}{4}kLQ^2 + 2\chi\mu qt|Q| - \epsilon Q \\ &\equiv (A - PB)Q^2 + 2\chi\mu qt|Q| - \epsilon Q. \end{aligned} \quad (3.30)$$

The imperfection has the effect of shifting the jammed region as shown in Fig. 3.8, which can be seen by minimising (3.30) over all Q . If $Q > 0$ then

$$\frac{\partial V_\epsilon}{\partial Q} = 2(A - PB)Q + (2\chi\mu qt - \epsilon) = 0,$$

giving

$$Q = \frac{-(2\chi\mu qt - \epsilon)}{2(A - PB)}. \quad (3.31)$$

If $Q < 0$ then

$$\frac{\partial V_\epsilon}{\partial Q} = 2(A - PB)Q - (2\chi\mu qt + \epsilon) = 0,$$

leading to

$$Q = \frac{2\chi\mu qt + \epsilon}{2(A - PB)}. \quad (3.32)$$

Let threshold value $\epsilon_{th} = |2\chi\mu qt|$. Then if $0 < \epsilon < \epsilon_{th}$ we get Fig. 3.8(a) and if $\epsilon > \epsilon_{th}$, Fig. 3.8(b). If the magnitude of ϵ is greater than that of ϵ_{th} , the bias

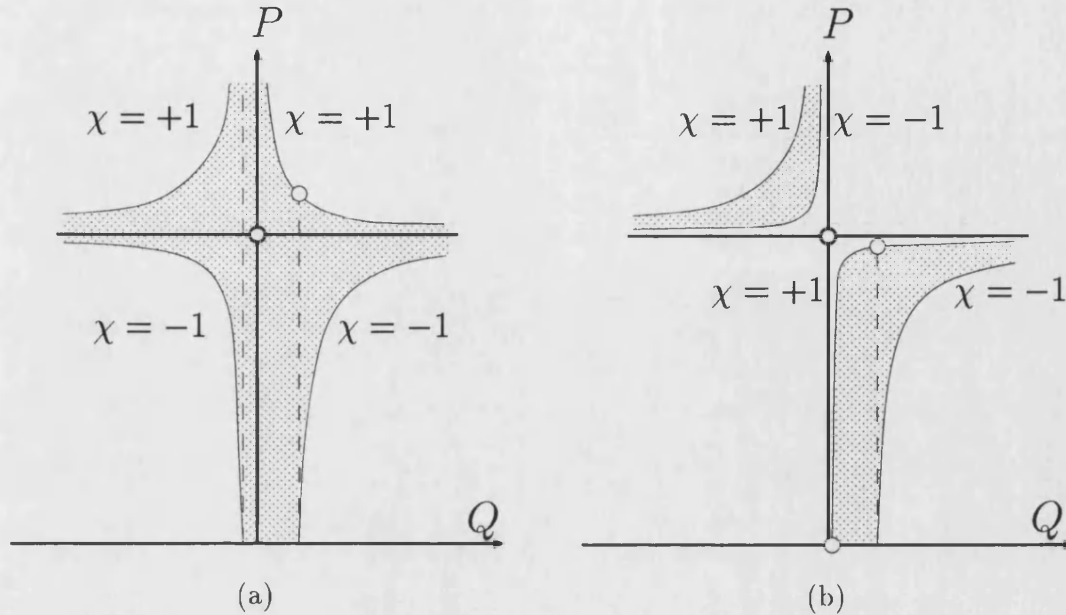


Figure 3.8: Jamming in the presence of a positive initial imperfection ϵ : (a) $0 < \epsilon < \epsilon_{th}$, (b) $\epsilon > \epsilon_{th}$.

is strong enough to push the critical slip curve for $\chi = +1$ and $Q > 0$ into the region where $P < P^C$, as shown in Fig. 3.8(b). The jammed region then divides into two and misses the bifurcation point altogether. As ϵ_{th} depends linearly on μ , $\epsilon_{th} \rightarrow 0$ as $\mu \rightarrow 0$. The sudden drop in minimum instability load described in the previous section is therefore destroyed by the presence of a vanishingly small imperfection.

3.4 Concluding remarks

This chapter presents a basic model for the concentric folding of two competent, elastic layers surrounded by a less competent medium, under layer parallel compression. The presence of overburden pressure obliges the layers to remain in contact along their length and suggests that frictional slip along the layer boundaries is the driving force behind the mode of deformation. This is in stark contrast to previous work in this field, which either concentrates on predominantly viscous effects or assumes perfect adherence or slip.

Simple bending theory allows us to formulate a quasi-energy formulation that includes the energy contribution of the frictional resistance to slippage, and in opposing the direction of sliding, the work done may be positive or negative. Using a simple Galerkin approximation, that is justified from experimental results, the nonlinear effect of friction is fully explored and shown to act like an imperfection. Equations for the critical load and wavelength are found to be consistent with classical results; however the existence of a “jammed” region means that the former is in most cases unobtainable.

The model given in this chapter forms the foundation for the rest of the thesis. It is remarkably powerful and with relatively little extension, all of the pertinent behaviour associated with parallel folding are shown to exist in the following chapters. The next chapter will compare the conclusions of this fundamental regime to the more general case using the calculus of variations. Linearization of the resulting differential equation, simplifies this analysis, allowing the distinctions between the models to be highlighted.

Chapter 4

Numerical analysis for the general case

4.1 Introduction

In the previous chapter we presented a two-layer parallel folding model, the inclusion of friction in this model being the fundamental difference to previous investigations into concentric geological buckling. A sinusoidal waveshape inserted into the quasi-energy formulation highlighted the effects of including the frictional force and allowed us to find equations for the critical load and wavelength.

In this chapter a nonlinear differential equation for the response of the two-layer model is developed from the calculus of variations. When the energy is linearized to simplify the analysis, we still have a nonlinear system, due to the direction-dependant friction term. Solutions of this differential equation are found in the absence of the foundation and the subtle differences between it and the Galerkin model are explored using a phase plane representation.

When the foundation is introduced, the solution technique is outlined and equations are found for the wavelength and critical load. The chapter finishes by giving a description of the numerical continuation code AUTO (Doedel *et al.*, 1997), which is then used to plot a few comparisons between the linearized and fully nonlinear model produced by consideration of the full set of possible geo-

metric effects. It is shown that the nonlinearity changes the behaviour very little for the majority of the range of feasible amplitudes.

4.2 Calculus of variations

The Galerkin analysis of the previous chapter has constructed a stationary solution of V over the class of cosine functions. We now extend this analysis to find the stationary solutions of V over the class of *all* admissible functions. We will continue to consider solutions which have a half wavelength of L so that they are monotone over the interval $[0, L]$ and

$$\dot{w}(0) = \dot{w}(L) = 0. \quad (4.1)$$

We initially assume that L is known. Later we consider two alternative mechanisms for finding L , either that the critical load P^C is minimised (equivalent to the calculation in (3.27)), or that V/L is stationary with respect to changes in the length scale. (Both mechanisms have been seen to be equivalent for the space of cosine functions).

Over a half-wave of length L , the total potential energy of the system has the form

$$V = \int_0^L F(\ddot{w}, \dot{w}, w) dx,$$

where F , the total potential energy per unit length, is given by

$$F = EI \frac{\ddot{w}^2}{1 - \dot{w}^2} - P(1 - \sqrt{1 - \dot{w}^2}) + k \frac{w^2}{2} + \alpha \chi \mu q t \sin^{-1}(\dot{w}), \quad (4.2)$$

where $\alpha = \pm 1$. As L is half a wavelength, \dot{w} does not change sign and thus α is fixed at either $+1$ or -1 and F is a smooth function of w , \dot{w} and \ddot{w} . Here, as in Chapter 3, $\alpha = +1$ if w is *increasing* over the half interval $[0, L]$ and $\alpha = -1$ if w is *decreasing* over the same half interval.

Applying the calculus of variations by taking a small increment δw of the function w , we have that the perturbation to the energy V is given to leading order by

the expression ((Thompson & Hunt, 1973))

$$\delta V = \int_0^L \left(\frac{\partial F}{\partial \ddot{w}} \delta \ddot{w} + \frac{\partial F}{\partial \dot{w}} \delta \dot{w} + \frac{\partial F}{\partial w} \delta w \right) dx. \quad (4.3)$$

The order of differentiation in this expression may be reversed, for example the second term may be written as

$$\int_0^L \frac{\partial F}{\partial \dot{w}} \delta \dot{w} dx = \int_0^L \frac{\partial F}{\partial \dot{w}} \frac{d}{dx} \delta w dx.$$

Hence integration by parts of the expression (4.3) yields

$$\begin{aligned} \delta V &= \left[\frac{\partial F}{\partial \dot{w}} \delta w \right]_0^L + \left[\frac{\partial F}{\partial \ddot{w}} \delta \dot{w} \right]_0^L - \left[\frac{d}{dx} \frac{\partial F}{\partial \ddot{w}} \delta w \right]_0^L \\ &+ \int_0^L \left(\frac{d^2}{dx^2} \frac{\partial F}{\partial \ddot{w}} - \frac{d}{dx} \frac{\partial F}{\partial \dot{w}} + \frac{\partial F}{\partial w} \right) \delta w dx. \end{aligned} \quad (4.4)$$

For $\delta V = 0$ for all δw we require that both the ordinary differential equation

$$\frac{d^2}{dx^2} \frac{\partial F}{\partial \ddot{w}} - \frac{d}{dx} \frac{\partial F}{\partial \dot{w}} + \frac{\partial F}{\partial w} = 0, \quad (4.5)$$

should be satisfied, and that each of the expressions in the square brackets should be zero. This leads to a new set of boundary conditions for the function w . The boundary conditions (4.1) force all admissible perturbations to satisfy

$$\delta \dot{w}(0) = \delta \dot{w}(L) = 0,$$

and hence terms in the second square bracket vanish identically. The first and third terms in the square brackets also vanish for all δw if, at $x = 0$ and L , we have

$$\frac{\partial F}{\partial \dot{w}} - \frac{d}{dx} \frac{\partial F}{\partial \ddot{w}} = 0. \quad (4.6)$$

Substituting from the explicit form (4.2) for F , and making use of the boundary conditions (4.1), this reduces to,

$$\alpha \chi \mu q t - 2EI \ddot{w} = 0,$$

at $x = 0$ and L . We thus find the additional boundary conditions

$$\ddot{w}(0) = \ddot{w}(L) = \frac{\alpha\chi\mu qt}{2EI}. \quad (4.7)$$

The new boundary conditions (4.7) represent a step change in the shear force at the boundaries, and requires some explanation. Frictional traction on a layer sums to a force of magnitude μqL , acting along an outermost fibre as shown in Fig. 3.4. Each is reacted at one end of the region in question by an equal and opposite force acting at the neutral axis of the layer. This sets up an out-of-balance moment in each layer, of magnitude $\mu qLt/2$, which in turn is resisted by a couple comprising lateral point loads at the ends of the region. It is these reactive point loads that appear as the boundary conditions (4.7).

Performing the necessary differentiations on the explicit form of F , from the Euler-Lagrange equation (4.5) we obtain the nonlinear differential equation

$$2EI[\dot{w}(1-w^2)^{-1} + \{4\dot{w}\ddot{w}\dot{w} + \ddot{w}^3\}(1-w^2)^{-2} + 4\dot{w}^3\dot{w}^2(1-w^2)^{-3}] + P\ddot{w}(1-w^2)^{-1/2}(1+w^2(1-w^2)^{-1}) - \chi\mu qt\dot{w}|\dot{w}|(1-w^2)^{-3/2} + kw = 0. \quad (4.8)$$

The associated linear differential equation for small displacements is given by

$$2EI\ddot{w} + P\ddot{w} + kw = 0, \quad (4.9)$$

with the same boundary conditions as before. This equation corresponds to taking the stationary values of the energy resulting from the 'linearized' energy density given by

$$F = EI\dot{w}^2 - P\frac{\dot{w}^2}{2} + k\frac{w^2}{2} + \chi\mu qt|\dot{w}|. \quad (4.10)$$

It is interesting that the only way that friction enters the linear differential equation (4.9) is as the boundary term (4.7). Although friction acts along the length, bending theory is based on the assumption that plane sections remain plane, and thus at first order is unable to account for a distributed shearing effect like that being imposed here. However, it is important to note that through the inclusion of (4.7), even though we have linearized the differential equation, the system is still inherently nonlinear. This is due to the friction being direction-dependent.

The linearity of (4.9) simplifies the analysis and allows us to deduce some results

immediately without solving the differential equation explicitly. In particular we have the following.

Lemma 1 *If $k > 0$ then*

$$\int_0^L w \, dx = 0. \quad (4.11)$$

Proof: From (4.9) it follows that

$$w = -\frac{1}{k}(2EI\ddot{w} + P\ddot{w}).$$

Thus

$$\int_a^b w(x) \, dx = -\frac{1}{k} \int_0^L (2EI\ddot{w} + P\ddot{w}) \, dx = -\frac{1}{k} [2EI\dot{w} + P\dot{w}]_0^L = 0,$$

using (4.1) and (4.7). For consistency, when $k = 0$, we insist that $\int_0^L w \, dx = 0$.

Lemma 2 *The function w depends linearly on the friction.*

Proof: Suppose that the function $u(x)$ satisfies the equation plus boundary conditions,

$$\begin{aligned} 2EI\ddot{u} + P\ddot{u} + ku &= 0, \\ \dot{u}(0) = \dot{u}(L) &= 0, \\ \ddot{u}(0) = \ddot{u}(L) &= \frac{\alpha\chi qt}{2EI}. \end{aligned}$$

Let $w = \mu u$, then

$$\frac{dw}{dx} = \frac{d(\mu u)}{dx} = \mu \frac{du}{dx},$$

etc. Substitution leads to an identical equation,

$$2EI\ddot{w} + P\ddot{w} + kw = 0,$$

with the boundary conditions,

$$\dot{w}(0) = \dot{w}(L) = 0,$$

and,

$$\ddot{w}(0) = \ddot{w}(L) = \frac{\alpha\chi\mu qt}{2EI}.$$

4.3 An analysis of the linear equation

The linearity of the differential equation (4.9) makes analysis straightforward, as seen in this and the next section. This analysis gives considerable insights into the non-classical role played by the modulus term representing the friction. A fuller numerical investigation of the nonlinear equation (4.8) is given later. The case of $k = 0$ is technically easier and is given first.

4.3.1 The solution for $k = 0$

When $k = 0$ the ordinary differential equation (4.9) becomes

$$\begin{aligned} 2EI\ddot{w} + P\dot{w} &= 0, \\ \dot{w}(0) = \dot{w}(L) &= 0, \\ \ddot{w}(0) = \ddot{w}(L) &= \frac{\alpha\chi\mu qt}{2EI}. \end{aligned} \quad (4.12)$$

Integrating once, and using the boundary conditions to determine the constants of integration we have

$$2EI\dot{w} + Pw = \frac{\alpha\chi\mu qt}{2EI}. \quad (4.13)$$

In the phase space describing (\dot{w}, w) the solutions of this equation give trajectories, which are piece-wise elliptical arcs centred on the point

$$(\dot{w}, w) = \left(\frac{\alpha\chi\mu qt}{P}, 0 \right).$$

Hence (4.13) has the solution

$$w(x) = \frac{\alpha\chi\mu qt}{P}x + A \cos\left(\sqrt{\frac{P}{2EI}}x\right) + B \sin\left(\sqrt{\frac{P}{2EI}}x\right) + C. \quad (4.14)$$

To find the constants A and B we apply the boundary conditions to give the solution

$$w = \frac{\alpha\chi\mu qt}{P}x + \frac{\sqrt{2EI}\alpha\chi\mu qt}{P^{\frac{3}{2}}} \left[\tan\left(\sqrt{\frac{P}{2EI}}\frac{L}{2}\right) \cos\left(\sqrt{\frac{P}{2EI}}x\right) - \sin\left(\sqrt{\frac{P}{2EI}}x\right) \right] + C. \quad (4.15)$$

(Note: (4.15) uses the relation

$$\tan\left(\sqrt{\frac{P}{2EI}}\frac{L}{2}\right) = \frac{1 - \cos(\sqrt{P/2EI}L)}{\sin(\sqrt{P/2EI}L)}, \quad (4.16)$$

which comes directly from the double angle formulae. The free constant of integration C can be fixed by insisting (following Lemma 1) that the mean of w should be identically zero.

Alternatively, the same result can be found by seeing that the auxiliary equation for the differential equation is

$$\phi^2 \left(\phi^2 + \frac{P}{2EI} \right) = 0. \quad (4.17)$$

The solutions of this equation are $\phi = 0$ (twice) and $\phi = \pm\sqrt{P/2EI}i$ and from the superposition theorem

$$w(x) = Dx + A \cos\left(\sqrt{\frac{P}{2EI}}x\right) + B \sin\left(\sqrt{\frac{P}{2EI}}x\right) + C. \quad (4.18)$$

As before, to find the constants D , A and B , we use the boundary conditions which leads to (4.15).

For the solution of (4.15) to be consistent with the earlier analysis, we require that $w(x)$ should be monotone over the interval $[0, L]$. This imposes a restriction on P and it is easy to see that for monotonicity we require that P should lie in the interval

$$P \in [0, P_{max}] \equiv \left[0, \frac{8\pi^2 EI}{L^2} \right]. \quad (4.19)$$

Here, P_{max} is the value at which

$$\ddot{w}(0) = \ddot{w}(L) = 0, \quad (4.20)$$

and we have that

$$\begin{aligned} \ddot{w}(0) &= -\frac{\alpha\chi\mu qt}{\sqrt{2EI}P} \tan\left(\sqrt{\frac{P}{2EI}}\frac{L}{2}\right) = 0, \\ \ddot{w}(L) &= \frac{\alpha\chi\mu qt}{\sqrt{2EI}P} \tan\left(\sqrt{\frac{P}{2EI}}\frac{L}{2}\right) = 0. \end{aligned} \quad (4.21)$$

Thus $\tan(\sqrt{P/2EI}L/2) = 0$, implying that either $\sqrt{P/2EI}L/2 = 0$ or $\sqrt{P/2EI}L/2 = \pi$ and yielding (4.19) above.

Consistent with the Galerkin analysis of Chapter 3, we define

$$Q = \frac{1}{2}(w(0) - w(L)),$$

so that, after some manipulation, we have

$$Q = \frac{\alpha\chi\mu qt}{2P} \left(-L + 2\sqrt{\frac{2EI}{P}} \left(\tan\left(\sqrt{\frac{P}{2EI}}\frac{L}{2}\right) \right) \right), \quad (4.22)$$

which is directly comparable with the expression (3.24).

We see from (4.22) that $|Q|$ becomes infinite when $\tan(\sqrt{P/2EI}L/2) = \infty$. This occurs when $\sqrt{P/2EI}L/2 = \pi/2$ and thus the critical value of the external load is given by

$$P^C = \frac{2\pi^2 EI}{L^2}. \quad (4.23)$$

This is precisely the value obtained by the Galerkin analysis given earlier in (3.25) when $k = 0$. However, a consequence of setting $k = 0$ is that L must be fixed a priori. As L increases, P^C drops, until for a two-layer specimen of infinite length, $P^C = 0$ and $L = \infty$. Hence whilst the above analysis gives insight into the form of the solutions of the problem, it highlights the importance of the foundation stiffness in selecting the value of L , and we return to this point presently.

4.3.2 Bifurcation diagrams for $k = 0$.

Using the expression (4.22) we may plot the (Q, P) bifurcation diagram and the resulting solutions described by (4.15). There are two cases to consider here.

Case 1: slipping

In this case the friction indicator is fixed at one of the two critical values of $\chi = \pm 1$. The value of Q for each value of P is then given by (4.22). There are four quadrants to the resulting figure, obtained by taking $\chi = \pm 1$ and $\alpha = \pm 1$, as shown in Fig. 4.1. This picture is very similar, both quantitatively and qualitatively, to that given in Fig. 3.7, although now the external load P is restricted to be less than P_{max} .

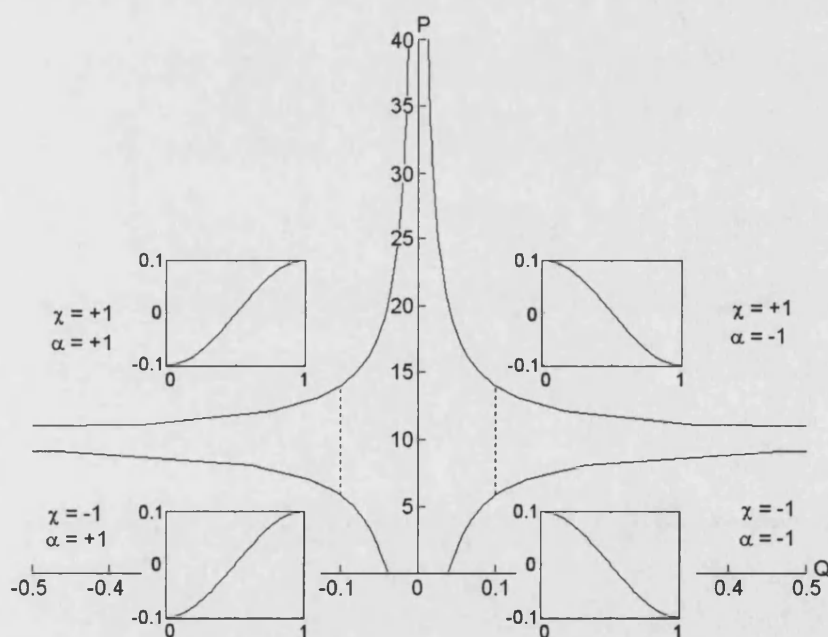


Figure 4.1: Plot of load P against amplitude Q , for $k = 0$, $EI = 0.5$, $L = 1$ and $\mu qt = 0.1$.

If $\chi = +1$ we have a positive energy contribution due to friction, which in this case acts like strain energy of bending in resisting the external load. If $\chi = -1$ we have a negative energy contribution due to friction which now acts in the opposite

sense, to resist the release of strain energy. Examples of these two extremes are given in the (\dot{w}, \ddot{w}) phase plane in Fig. 4.2, along with a third solution well within the equivalent of the jammed region of Fig. 3.7, at $\chi = 0.032$.

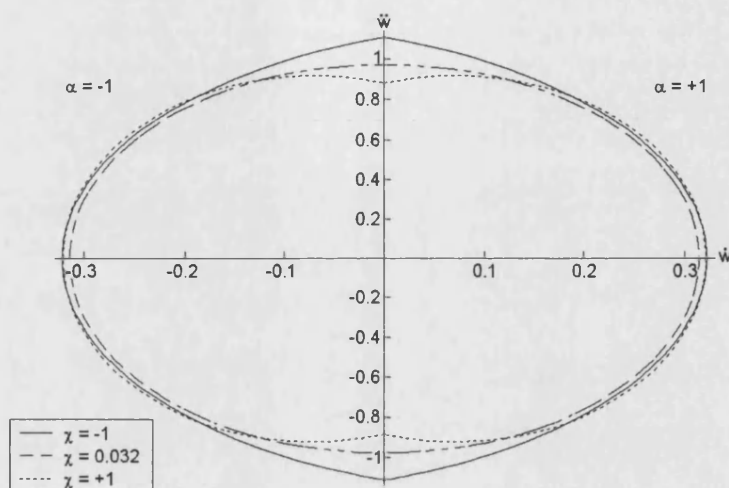


Figure 4.2: Phase plane trajectories plotted for $k = 0, EI = 0.5, L = 1$ and $\mu qt = 0.1$.

Over most of the trajectory these solutions appear very similar, with the only significant differences arising at the ends of the sample. This reflects the difference in \ddot{w} which comes about as the directions of the point load reactions reverse with the change in sign of χ .

Case 2: jamming

Some nonlinear work against friction is experienced in moving between the two solutions given by $\chi = -1$ and $\chi = +1$ through the equivalent of the jammed region of Fig. 3.7. However, in the linearized equation (4.9), the total work done against friction over one half wavelength is

$$\alpha \chi \mu q t \int_0^L \dot{w} dx = 2 \chi \mu q t |Q|. \quad (4.24)$$

Hence, there is no difference in the work done against friction *between any two solutions with the same Q* . A path of jammed solutions in the jamming region can then be described by fixing Q in the expression (4.22) and letting χ vary between -1 and $+1$. This in turn implicitly determines the value of P corresponding to each such value of χ . Note that if $\chi \rightarrow 0$ then we have $P \rightarrow P^C$ and the solution approaches the pure sinusoid function $w(x) = Q \cos(\pi x/L)$, as considered in the Galerkin analysis.

4.3.3 The solution for $k \neq 0$

The solution of (4.9) for $k > 0$ can be obtained along similar, although more complex, lines to that for $k = 0$. This analysis allows a value of L to be determined.

Seeking a solution of (4.9) of the form $w(x) = e^{i\varphi x}$ we obtain

$$2EI\varphi^4 - P\varphi^2 + k = 0. \quad (4.25)$$

This is a quadratic in φ^2 and hence

$$\varphi_{\pm}^2 = \frac{P}{4EI} \pm \frac{1}{4EI} \sqrt{P^2 - 8EI k}. \quad (4.26)$$

Observe that if φ is real, then the minimum value of P over all values of φ is given when

$$P = 2\sqrt{2EI k} \quad \text{and} \quad \varphi^2 = \frac{P}{4EI}. \quad (4.27)$$

Let $\omega_1^2 = \varphi_-^2$ and $\omega_2^2 = \varphi_+^2$, where φ_{\pm} are given in (4.26). Then,

$$w(x) = A_1 \cos(\omega_1 x) + B_1 \sin(\omega_1 x) + A_2 \cos(\omega_2 x) + B_2 \sin(\omega_2 x). \quad (4.28)$$

From the boundary conditions given in (4.1) and (4.7), at $x = 0$ we have

$$\begin{aligned} \omega_1 B_1 + \omega_2 B_2 &= 0, \\ -\omega_1^3 B_1 - \omega_2^3 B_2 &= \frac{\alpha \chi \mu q t}{2EI}, \end{aligned}$$

and hence,

$$B_1 = \frac{-\alpha\chi\mu qt}{2EI\omega_1(\omega_1^2 - \omega_2^2)} \quad \text{and} \quad B_2 = \frac{\alpha\chi\mu qt}{2EI\omega_2(\omega_1^2 - \omega_2^2)}.$$

At $x = L$ we have similarly that

$$\begin{aligned} -\omega_1 A_1 \sin(\omega_1 L) + \omega_1 B_1 \cos(\omega_1 L) - \omega_2 A_2 \sin(\omega_2 L) + \omega_2 B_2 \cos(\omega_2 L) &= 0, \\ \omega_1^3 A_1 \sin(\omega_1 L) - \omega_1^3 B_1 \cos(\omega_1 L) + \omega_2^3 A_2 \sin(\omega_2 L) - \omega_2^3 B_2 \cos(\omega_2 L) &= \frac{\alpha\chi\mu qt}{2EI}. \end{aligned}$$

Solving this simultaneous system, provided that

$$\omega_1\omega_2(\omega_1^2 - \omega_2^2) \sin(\omega_1 L) \sin(\omega_2 L) \neq 0, \quad (4.29)$$

A_1 and A_2 are obtained uniquely.

Loss of solvability occurs when either $\omega_1 L$ or $\omega_2 L$ is a multiple of π . The corresponding value of $P = P^C$ thus arises when φ_{\pm} from (4.26) equals π/L so that,

$$P^C = \frac{2EI\pi^2}{L^2} + \frac{kL^2}{\pi^2}. \quad (4.30)$$

This result corresponds with the value (3.25) given by the Galerkin analysis.

4.3.4 Wavelength selection

For a particular foundation stiffness k , the length of the half-wave will determine the value of the bifurcation point P^C . The question we now ask is: how is the wavelength and hence P^C selected?

As in the Galerkin analysis, we may choose L either to minimise the critical load P^C , or to seek the value of L such that $\partial(V/L)/\partial L = 0$. For the Galerkin approximation these two approaches give the same answer, but in this more general case the answers are different, although very similar.

Minimisation of the load

To find the half-wavelength associated with the minimum critical load we can minimise P^C over all values of L . Fig. 4.3 shows how P^C changes with L for various values of k . Differentiating (4.30) with respect to L and setting the result

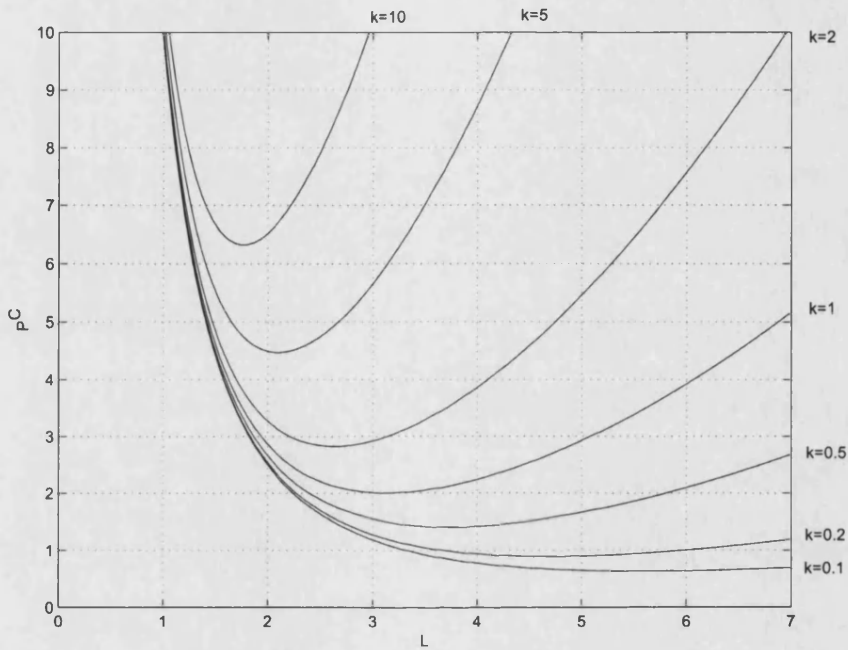


Figure 4.3: Variation of P^C with L for different values of k .

to zero leads to

$$L = \pi \sqrt[4]{\frac{2EI}{k}}, \quad (4.31)$$

corresponding to (3.26) of the Galerkin analysis. Substituting into (4.30) again gives the classical expression (3.27) for the minimum value of P^C for the strut on linear elastic foundation (Hunt *et al.*, 1989).

Let $y = k^{1/4}x$ and $\hat{P} = Pk^{-1/2}$. Then the linear differential equation (4.9) rescales to,

$$2EIw_{yyyy} + \hat{P}w_{yy} + w = 0. \quad (4.32)$$

Also, if we have L as given in (4.31), then w satisfies the boundary conditions,

$$w_y(0) = w_y(\pi\sqrt[4]{2EI}) = 0, \quad (4.33)$$

and

$$w_{yyy}(0) = w_{yyy}(\pi\sqrt[4]{2EI}) = \frac{\alpha\chi\mu qt}{2EI}k^{-3/4}. \quad (4.34)$$

Let $\mu k^{-3/4} = \hat{\mu}$. Then we have,

$$w_{yyy}(0) = w_{yyy}(\pi\sqrt[4]{2EI}) = \frac{\alpha\chi\hat{\mu}qt}{2EI}. \quad (4.35)$$

We deduce that all solutions of (4.9) for general k , with the boundary conditions satisfied when L is given by (4.31), are rescalings of the solution when $k = 1$.

Stationary values of energy density

Alternatively we may consider the problem of finding stationary values of the energy per unit length (Peletier, 2001a). To do this we set $x = L\xi$ and express all derivatives with respect to ξ . This allows us to rescale the linearized energy so that all calculations are over the length $[0, 1]$. We then have

$$V/L = \int_0^1 \left(L^{-4}EI(w'')^2 - L^{-2}\frac{P}{2}(w')^2 + \frac{k}{2}w^2 + L^{-1}\chi\mu qt|w'| \right) d\xi, \quad (4.36)$$

where primes refer to derivatives with respect to ξ .

Differentiation with respect to L gives,

$$\partial(V/L)/\partial L = - \int_0^1 (4L^{-5}EI(w'')^2 - L^{-3}P(w')^2 + L^{-2}\chi\mu qt|w'|) d\xi. \quad (4.37)$$

For a stationary solution, $\partial(V/L)/\partial L = 0$. Thus, after a rescaling of the above integral to be an expression in the original variables, it follows that for $\partial(V/L)/\partial L = 0$ we must augment the ordinary differential equation (4.9) plus the boundary

conditions (4.1, 4.7), with the integral condition

$$\int_0^L (4EI\ddot{w}^2 - P\dot{w}^2 + \chi\mu qt|\dot{w}|) dx = 0. \quad (4.38)$$

The equation (4.38) implicitly defines the length L .

Now, the linearized ordinary differential equation for w is given by

$$2EI\ddot{w} + P\dot{w} + kw = 0,$$

with $\dot{w}(0) = \dot{w}(L) = 0$ and $\ddot{w}(0) = \ddot{w}(L) = \alpha\chi\mu qt/2EI$. Multiplying by w , integrating by parts over $[0, L]$, and applying the boundary conditions, we have

$$[\alpha\chi\mu qt w]_0^L + \int_0^L (2EI\ddot{w}^2 - P\dot{w}^2 + kw^2) dx = 0. \quad (4.39)$$

But

$$[\alpha\chi\mu qt w]_0^L = \int_0^L \chi\mu qt|\dot{w}| dx,$$

so that

$$\int_0^L (2EI\ddot{w}^2 - P\dot{w}^2 + kw^2 + \chi\mu qt|\dot{w}|) dx = 0. \quad (4.40)$$

Combining the two equations (4.38) and (4.40) gives the following two results.

Lemma 3 *If w and L are such that $\delta V/\delta w = 0$ and $\partial(V/L)/\partial L = 0$ then*

$$2EI \int_0^L \ddot{w}^2 dx = k \int_0^L w^2 dx, \quad (4.41)$$

or, the strain energy of bending equals the energy stored in the foundation.

Lemma 4 *The critical value of L defined by Lemma 3 is independent of the friction μ .*

Note that if we approximate $w(x)$ by $Q \cos(\pi x/L)$ and $\dot{w}(x)$ by $-(\pi/L)^2 Q \cos(\pi x/L)$ then (4.41) gives that $L \approx \pi(2EI/k)^{1/4}$, which is precisely the expression obtained earlier. However, for $\mu \neq 0$, the result for L differs slightly from that of (4.31), as shown in Fig. 4.4.

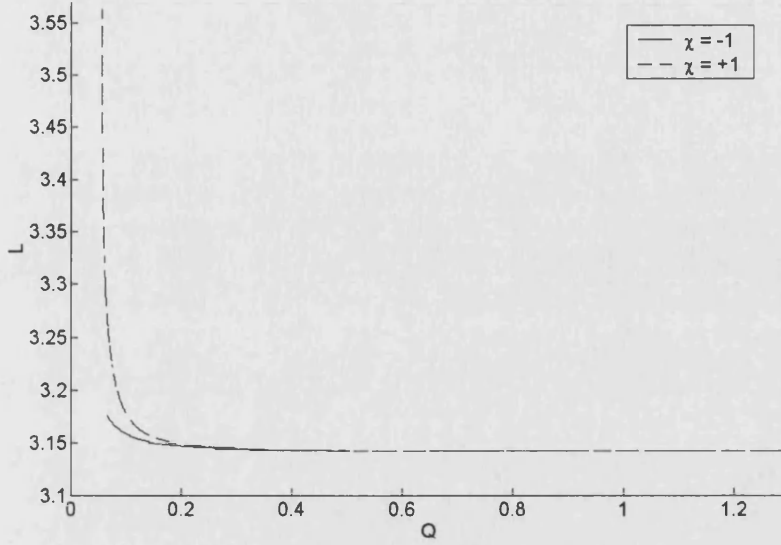


Figure 4.4: Difference in wavelength prediction between equations (4.31) and (4.42), plotted for $EI = 0.5, k = 1, \alpha = 1$ and $\mu qt = 0.1$.

If as before we rescale the identity (4.41) by setting $x = L\xi$ we have,

$$\frac{2EI}{L^4} \int_0^1 w''^2 d\xi = k \int_0^1 w^2 d\xi.$$

Thus

$$L^4 = \frac{2EI \int_0^1 w''^2 d\xi}{k \int_0^1 w^2 d\xi}. \quad (4.42)$$

But from Lemma 1, $\int_0^1 w d\xi = 0$, and also $w_\xi(0) = w_\xi(1) = 0$. It therefore follows from repeated applications of the Poincaré inequality (Smoller, 1983; Marti, 1986) that

$$\int_0^1 w''^2 d\xi \geq \pi^4 \int_0^1 w^2 d\xi. \quad (4.43)$$

Combining results we have that for all solutions

$$L \geq \pi^4 \sqrt{\frac{2EI}{k}}, \quad (4.44)$$

as seen in Fig. 4.4.

4.3.5 Poincaré's inequality

Before proceeding to the numerical solutions of the fourth order differential equation. A brief interlude is necessary, to give an overview of the Poincaré inequality and hence explain the result given in (4.43).

Suppose that, over the interval $[0, 1]$, we wish to minimize a system of the form

$$\frac{\int_0^1 w'^2 d\xi}{\int_0^1 w^2 d\xi}, \quad (4.45)$$

with either the boundary conditions,

$$w(0) = w(1) = 0, \quad (4.46)$$

or the integral condition that

$$\int_0^1 w d\xi = 0. \quad (4.47)$$

Then, the minimum is obtained if w satisfies the ordinary differential equation

$$w'' + \lambda w = 0, \quad (4.48)$$

and (4.45) takes the value of λ .

This implies that if (4.46) holds then $w = \sin(\pi\xi)$, or if (4.47) holds then $w = \cos(\pi\xi)$. In both cases w is sinusoidal and $\lambda = \pi^2$.

Proof: Follows from the fact that the minimum value of

$$\frac{\int_0^1 w'^2 d\xi}{\int_0^1 w^2 d\xi}, \quad (4.49)$$

over all functions w is (by scaling) the minimum of $\int_0^1 w'^2 d\xi$ over functions such that $\int_0^1 w^2 d\xi = 1$. Hence, if λ is a Lagrange multiplier, it is the minimizer of

$$\left[\int_0^1 w'^2 d\xi - \lambda \left(\int_0^1 w^2 d\xi - 1 \right) \right]. \quad (4.50)$$

Applying the calculus of variations to (4.50), the minimum is achieved when w satisfies the Euler-Lagrange equations so that

$$w'' + \lambda w = 0. \quad (4.51)$$

If $w(0) = w(1) = 0$ or $\int_0^1 w \, d\xi = 0$ then the only solution of this arises when $\lambda = \pi^2$ and depending on the conditions $w = \sin(\pi\xi)$ or $w = \cos(\pi\xi)$.

The Poincaré inequality effectively says that because the minimum of (4.45) is equal to π^2 , when w is sinusoidal, then for any other function where (4.46) or (4.47) holds

$$\frac{\int_0^1 w'^2 \, d\xi}{\int_0^1 w^2 \, d\xi} \geq \pi^2. \quad (4.52)$$

The closer that the function is to a sinewave, the closer that the ratio given by (4.45) approximates π^2 .

4.4 Numerical results

4.4.1 Numerical solutions: AUTO

Primarily AUTO is used to solve either algebraic systems

$$\mathbf{f}(\mathbf{u}, p) = 0, \quad (4.53)$$

or systems of ordinary differential equations (ODEs) of the form

$$\mathbf{u}' = \mathbf{f}(\mathbf{u}, p) = 0, \quad (4.54)$$

where \mathbf{f} and \mathbf{u} are n -dimensional vectors in real space and p denotes one or more free parameters used to see how the initial solution evolves through the numerical continuation process and are termed *continuation parameters*. The code discretizes problems using orthogonal collocation (de Boor & Swartz, 1973) and for each problem automatically adapts the mesh in such a way as to distribute the local discretization error evenly (Russell & Christiansen, 1978). Whilst AUTO

is designed for autonomous systems, non-autonomous systems can be solved by introducing an extra variable transforming an n -order non-autonomous system into an $(n + 1)$ -order autonomous system.

For boundary value problems (BVPs) on $[0, 1]$ —(4.54) expressed with boundary conditions—AUTO can compute solution curves subject to both general nonlinear boundary and integral conditions. The boundary conditions can be separated or non-separated—i. e. where both ends are involved in a single equation. Different types of critical point can be detected including: folds, bifurcation points, period-doubling bifurcations, torus bifurcations and Hopf bifurcations. In addition with the HOMCONT package, the detection of homoclinic and heteroclinic global bifurcations is possible.

The continuation routines use predictor-corrector methods, which, for starting values $\mathbf{u} = \mathbf{u}_0$ and $p = p_0$, find the next point along the solution path by first taking a prediction as to the values— $(\bar{\mathbf{u}}_1, \bar{p}_1)$. To correct this initial guess, a modified Newton-Raphson method is used by the code to iterate until it finds the actual solution— (\mathbf{u}_1, p_1) to a specified tolerance. However, correction by this method fails at limit points and folds; hence pseudo-arclength continuation is used in conjunction with Newton-Raphson (Riks, 1972), such that computations are performed past where a fold is encountered by p . Thus, a new parameter using the norm of \mathbf{u} , Γ , is introduced in combination with p where

$$\mathbf{f}(\mathbf{u}(\Gamma), p(\Gamma)) = 0 \quad \|\dot{\mathbf{u}}(\Gamma)\|^2 + \dot{p}(\Gamma)^2 = 1, \quad (4.55)$$

and a component of the norm of \mathbf{u} is given by

$$\|u\| = \sqrt{\int_0^1 u^2 dx}. \quad (4.56)$$

For BVPs, pseudo-arclength continuation is given by

$$\mathbf{f}(\mathbf{u}_1, p_1) = 0 \quad (\mathbf{u}_1 - \mathbf{u}_0)^T \dot{\mathbf{u}}_0 + (p_1 - p_0) \dot{p}_0 = \Delta\Gamma, \quad (4.57)$$

which is put into Newton's method, with \mathbf{u}_1 and p_1 found iteratively.

This procedure works well for fold detection, but poorly for bifurcation points.

To get around this, Crisfield and Wills (1986) discovered, that by examining the negative pivots of the tangential stiffness matrix, they could tell the difference between folds and bifurcation points in nonlinear finite element techniques such as the modified Newton-Raphson. Doedel (1997) outlines the details of the numerical algorithm used to detect bifurcation points in AUTO.

Numerical solutions to the governing differential equations (4.9) and (4.8) subject to boundary conditions (4.1, 4.7), have been obtained using the numerical continuation code AUTO (Doedel *et al.*, 1997). In accordance with the convention of this package, the output that follows is given over the rescaled length $\xi = [0, 1]$ discussed earlier.

4.4.2 Linear equation

Numerical solutions to the linear equation (4.9) are presented in Fig. 4.5. Corresponding wave shapes and phase portraits are given in Figs. 4.6 and 4.7, for the two different values of $Q = -0.082$ and $Q = -0.42$ respectively, at the two extremes of slip represented by $\chi = \pm 1$.

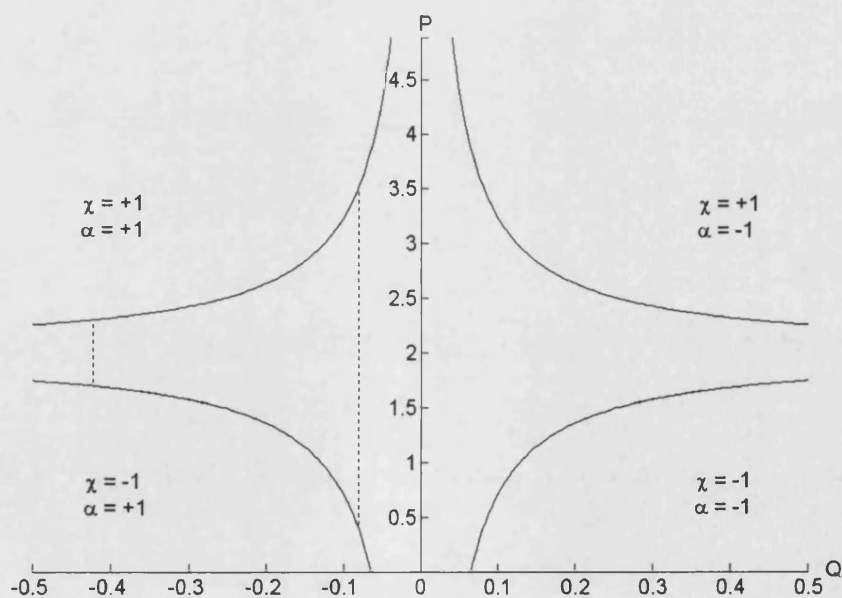


Figure 4.5: Bifurcation plot for the linear differential equation (4.9) plotted for $EI = 0.5$, $k = 1$, $\mu qt = 0.1$ and $L = \pi$.

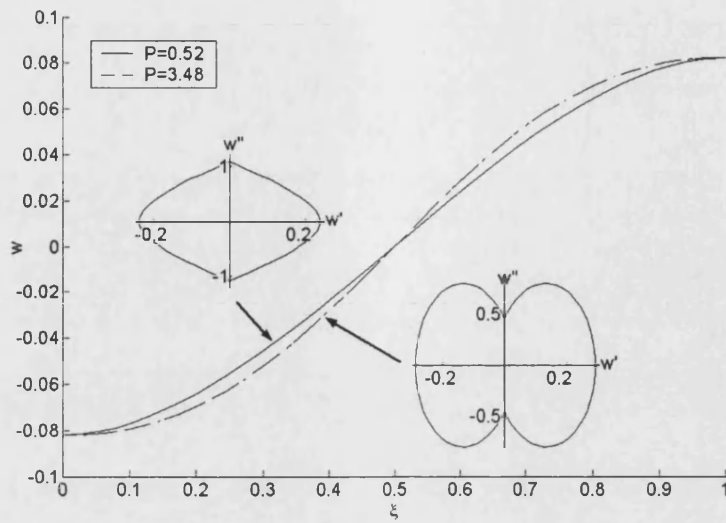


Figure 4.6: Waveshapes and corresponding phase portraits for the case of Fig. 4.5 at $Q = -0.082$.

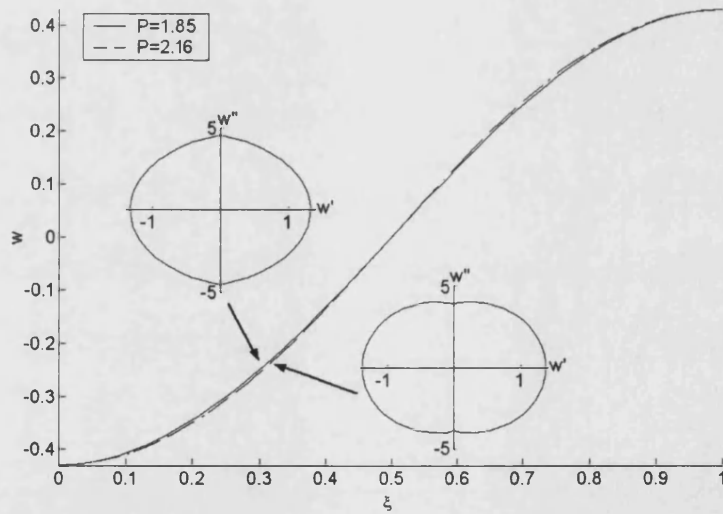


Figure 4.7: Waveshapes and corresponding phase portraits for the case of Fig. 4.5 at $Q = -0.42$.

4.4.3 Nonlinear equation

Numerical solution of the full nonlinear equation (4.8) for a typical set of parameter values is given in Fig. 4.8. Waveshapes and the corresponding phase portraits are given in Figs. 4.9 and 4.10, for the two different values of $Q = -0.082$ and $Q = -0.42$ respectively, at the two extremes of slip represented by $\chi = \pm 1$.

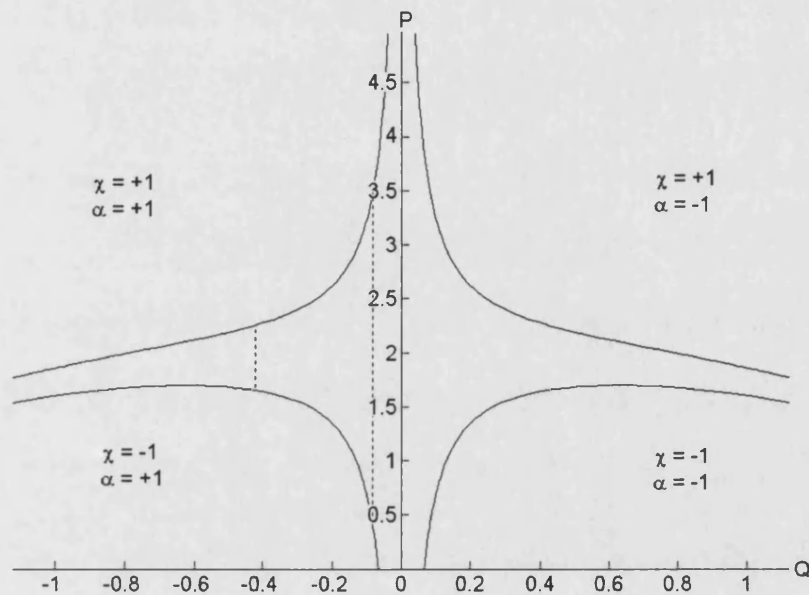


Figure 4.8: Bifurcation plot for the nonlinear differential equation (4.8) plotted for $EI = 0.5$, $k = 1$, $\mu qt = 0.1$ and $L = \pi$.

4.5 Concluding remarks

This chapter compares the outcomes of both theoretical and numerical modelling with the simple Galerkin approximation of Chapter 3 and the significance of friction-induced jamming is explored. Comparisons between the solutions of the linear and nonlinear equations are presented in Fig. 4.11 for two different values of μ , one small and one large. These, along with the plots of Figs. 4.5 to 4.10, demonstrate that little of phenomenological significance is added by including the full set of geometric nonlinearities.

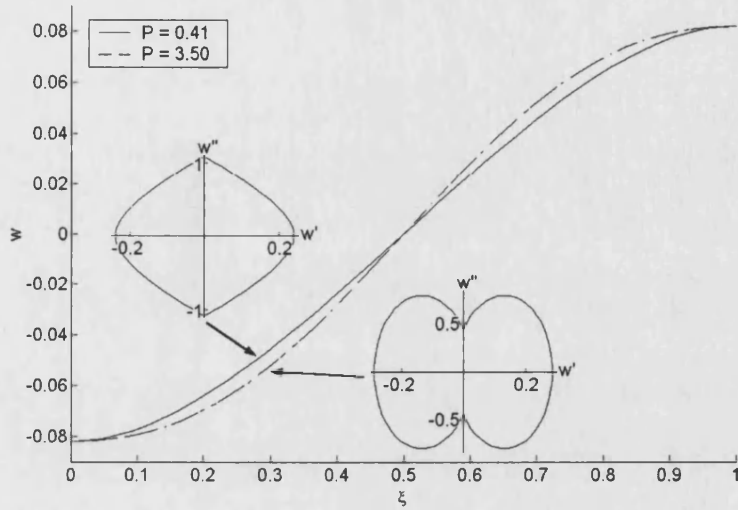


Figure 4.9: Waveshapes and corresponding phase portraits for the case of Fig. 4.8 at $Q = -0.082$.

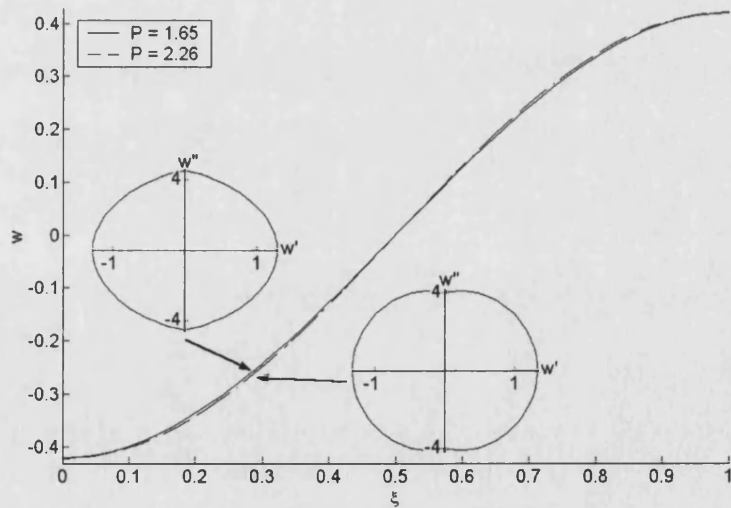


Figure 4.10: Waveshapes and corresponding phase portraits for the case of Fig. 4.8 at $Q = -0.42$.

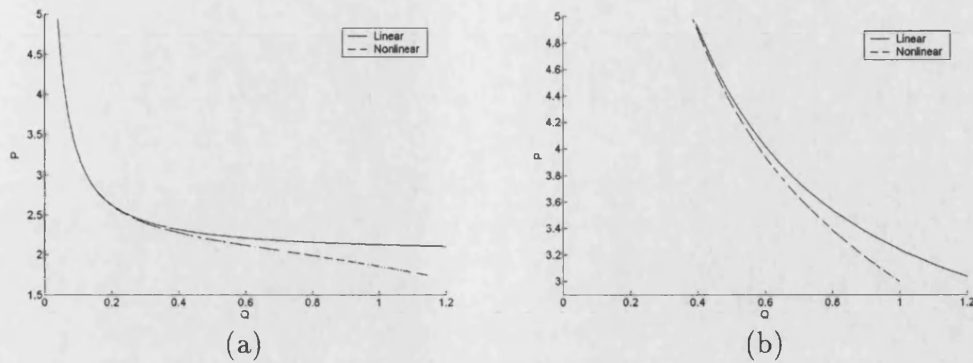


Figure 4.11: Comparisons of linear and nonlinear solutions (a) $\mu qt = 0.1$ and (b) $\mu qt = 1$.

Fig. 4.8 indicates a slight overall downwards curvature to the $\mu = 0$ response in contrast with the linear view of Fig. 4.5 for example, but the related $\mu \neq 0$ curves show little difference of consequence. By contraposition, the nonlinearity that is brought in by the modulus change at the boundaries has a profound phenomenological effect on the system, as demonstrated most clearly in the Galerkin plots of Figs. 3.7 and 3.8, found in Chapter 3.

Analysis throughout has concentrated on a single half-wave of buckling, no indication being given of how the pattern continues into further waves. The unstable nature of the final buckle (see Fig. 3.7) suggests that homoclinic (Budd *et al.*, 1999; Budd & Peletier, 2000) or localized behaviour is to be expected, which in this case might manifest itself as the formation of a single half-wave, with the remainder of the layers remaining jammed in the straight configuration. Then, if a tendency to restabilize is found over large deflections, a form of cellular buckling would be expected (Hunt *et al.*, 2000a), with half-waves forming and then locking-up in sequential fashion. In such circumstances, a heteroclinic orbit that connects the flat state to a periodic configuration defined by Maxwell considerations (Budd *et al.*, 2001), becomes the dominant characteristic. This is explored in the next chapter.

Chapter 5

A primitive model for serial parallel folding using cubic B-splines

5.1 Introduction

When a periodic folding pattern is observed in the field, the exact mechanism of formation is unlikely to be immediately apparent. Fig. 5.1 shows a recent series of experiments on layers of A4 size paper held together transversely under an applied overburden pressure, and compressed in the longitudinal direction to initiate a *serial buckling* sequence of parallel folds propagating from the loaded edge.

Serial folding differs in fundamental ways from its spontaneously-occurring counterpart (Hunt, 2005). For instance, the resulting wavelengths of these two generic forms of instability are likely to be quite different (Budd *et al.*, 2001). While that of the spontaneous buckle would be expected to be picked up at the classical critical load and remain with effectively the same wavelength until well into the post-buckling range, cellular buckling is liable to pick up the wavelength associated with an underlying periodic shape at the *Maxwell load* (Peletier, 2001a). Interest thereby is shifted from linear buckling studies to information obtained only from the advanced post-buckling regime.

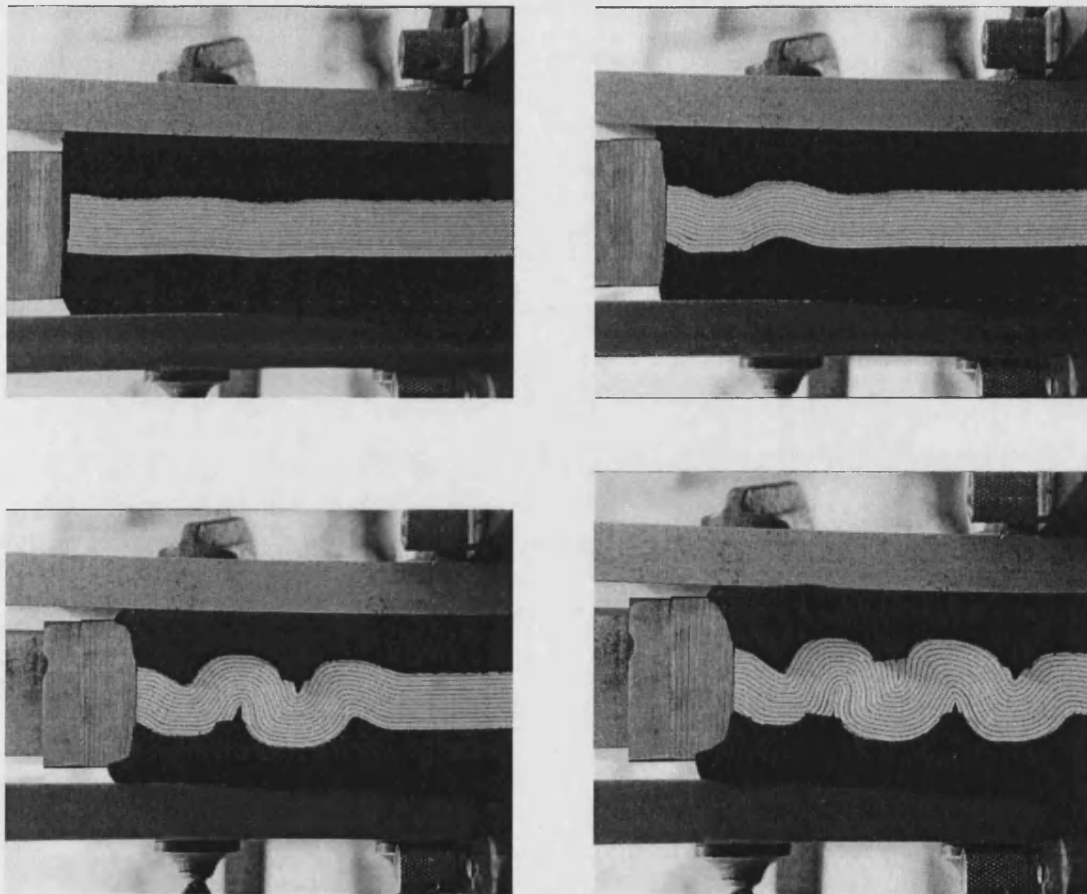


Figure 5.1: Parallel folding in layers of paper, showing the serial buckling behaviour.

In Chapters 3 and 4 an elementary two-layer model for parallel folding in the presence of friction was developed, with the aim of identifying the important governing parameters. A Galerkin sinewave representation of the interface between the layers compared well with the exact solution of the underlying differential equation. The formulation was based on a linear representation of the bending of the layers, with an additional nonlinearity linked to discontinuities in the third derivative (related to jumps in shear force) at points along the length where the frictional force switches direction.

The introduction of extra layers to the model will be described in Chapter 6 and is relatively straightforward; however, the need to accommodate amplitude modulation means the extension to serial folding is not. In this chapter we introduce a two-layer, two-hump, model of serial folding, employing the concept of cubic B-splines. These have continuous derivatives up to second-order, but allow discontinuities of third derivative as required. The representation allows for two successive humps of different amplitude, and thence provides a primitive form of a *homoclinic solution* (Champneys *et al.*, 1999) representing a localized buckle over only a part of the available spatial regime. Primitive *periodic solutions* are also found, where the amplitudes of the humps are the same. Tracking the development of serial folding with increasing end-shortening, we successfully mirror the sequence seen in Fig. 5.1, from buckling into a single hump through to the development of the two-hump “periodic” form.

5.2 Two-layer model

Consider the two-layer set-up described in Section 3.2.1. From §3.2.2 recall that the total potential energy function, over small vertical deflections w is

$$V = \int_0^L \left(EI\ddot{w}^2 - P\frac{\dot{w}^2}{2} + k\frac{w^2}{2} + \chi\mu qt|\dot{w}| \right) dx, \quad (5.1)$$

where dots denote differentiation with respect to the axial coordinate x .

Serial buckling implies that an unstable localized response is followed by restabilization and eventual lockup (Hunt *et al.*, 2000a), and hence in addition to the

terms in (5.1) a nonlinearity is included via the extra term,

$$\frac{1}{4}C \int_0^L w^4 dx, \quad (5.2)$$

where C adds a stiffening nonlinear component to the linear foundation stiffness k .

With this extra term, using the same Galerkin approximation as Chapter 3, the bifurcation diagram is shown in Fig. 5.2.

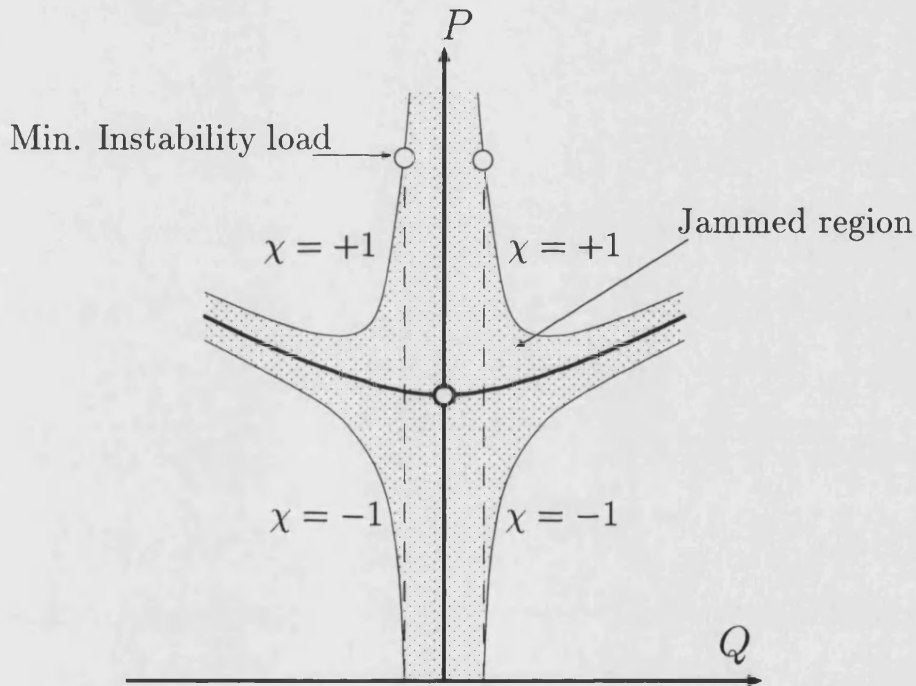


Figure 5.2: Bifurcation diagram indicating jammed region for constant μ .

The falling equilibrium paths in the upper two quadrants on the edge of the jammed region are likely to be stable under conditions of rigid loading (parametric variation in end-shortening), and restabilize anyway when the path starts to curve back up as $|Q|$ increases. Remember that with a linear foundation ($C = 0$) this restabilization never takes place, the paths simply approaching asymptotically a flat (horizontal) path that crosses the P -axis at the critical bifurcation load $P = P^C$ (see Chapter 3).

5.3 Modelling waveshapes using cubic B-splines

5.3.1 The cubic B-spline

To avoid discontinuities in slopes and bending moments, the shape function w should be continuous in both first and second derivatives. The cubic B-spline (Wait & Mitchell, 1985; Lancaster & Šalkausas, 1987), B_3 , (see Fig. 5.3) has this

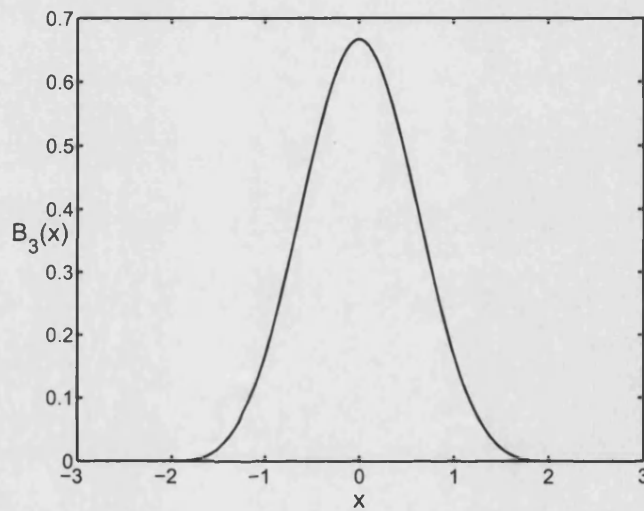


Figure 5.3: The cubic B-spline.

necessary property, but allows discontinuities in third derivative to give the step changes in shear force seen in Chapter 4. A single cubic spline $B_3(x)$ has the deflected shape

$$B_3(x) = \begin{cases} 0 & x \leq -2 \\ \frac{4}{3} + 2x + x^2 + \frac{x^3}{6} & -2 \leq x \leq -1 \\ \frac{2}{3} - x^2 - \frac{x^3}{2} & -1 \leq x \leq 0 \\ \frac{2}{3} - x^2 + \frac{x^3}{2} & 0 \leq x \leq 1 \\ \frac{4}{3} - 2x + x^2 - \frac{x^3}{6} & 1 \leq x \leq 2 \\ 0 & x \geq 2. \end{cases} \quad (5.3)$$

Note that, unlike the sinusoidal waveshape approximation used in Chapter 3, the deflection of the cubic B-spline together with its first and second derivatives are zero at both ends. Thus it can be smoothly matched to the flat (undeflected) state as in a classical homoclinic or localized solution (Champneys *et al.*, 1999).

5.3.2 Single B-spline formulation

Following the Galerkin approximation of Chapter 3, the deflection, w , can be modelled with a single cubic B-spline. To remain consistent with the earlier work, B_3 is rescaled to the range $0 \leq x \leq L$, and an amplitude variable, Q , is introduced on the waveshape.

$$w = Q \begin{cases} \frac{4}{3} + \frac{4(2x-L)}{L} + \frac{4(2x-L)^2}{L^2} + \frac{4(2x-L)^3}{3L^3} & 0 \leq x \leq \frac{L}{4} \\ \frac{2}{3} - \frac{4(2x-L)^2}{L^2} - \frac{4(2x-L)^3}{L^3} & \frac{L}{4} \leq x \leq \frac{L}{2} \\ \frac{2}{3} - \frac{4(2x-L)^2}{L^2} + \frac{4(2x-L)^3}{L^3} & \frac{L}{2} \leq x \leq \frac{3L}{4} \\ \frac{4}{3} - \frac{4(2x-L)}{L} + \frac{4(2x-L)^2}{L^2} - \frac{4(2x-L)^3}{3L^3} & \frac{3L}{4} \leq x \leq L. \end{cases} \quad (5.4)$$

If w is substituted into the nonlinear total potential energy function, V , this can then be written explicitly as

$$V(Q, L) = \frac{512EI}{3L^3}Q^2 - \frac{4P}{3L}Q^2 + \frac{151kL}{2520}Q^2 + \frac{4\chi\mu qt}{3}|Q| + \frac{40853}{4324320}CQ^4L. \quad (5.5)$$

The linearized solution ($C = 0$)

When $C = 0$ the nonlinearity in the foundation is absent and we can directly follow the Galerkin analysis of Chapter 3. The optimum buckle length is obtained by minimizing V with respect to L , giving

$$L_{\text{opt}} = \sqrt{\frac{48\sqrt{1225P^2 + 84560kEI} - 1680P}{151k}}. \quad (5.6)$$

Note that L_{opt} does not depend upon Q in this case.

Equilibrium states (which necessarily correspond to functions with w, \dot{w} and \ddot{w} all zero at the ends) are found by seeking stationary values of V with respect to Q ($\partial V/\partial Q = 0$) to give,

$$Q = \pm \frac{1680\chi\mu qtL^3}{3360PL^2 - 430080EI - 151kL^4}. \quad (5.7)$$

Combining these two results gives the equilibrium states of Fig. 5.4, which are very close in form to those in Chapter 3, but relate inherently to a single hump rather than periodic response.

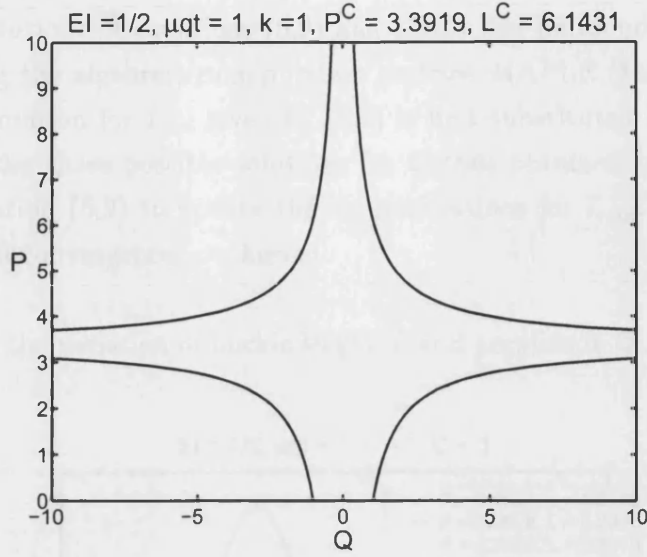


Figure 5.4: Bifurcation diagram for one-spline model, linear foundation.

The critical load P^C and related length L^C can be found by substituting L_{opt} into the second derivative of V with respect to Q and setting the result to zero ($\partial^2 V / \partial Q^2 = 0$) (Thompson & Hunt, 1973) to give

$$P^C = \sqrt{\frac{2416}{105} kEI}; \quad L^C = 8 \sqrt[4]{\frac{105 EI}{151 k}}. \quad (5.8)$$

The nonlinear solution ($C \neq 0$)

The same sequence of arguments can be applied to the case of $C \neq 0$, although the presence of the nonlinearity makes solution more difficult. First minimizing V with respect to L gives

$$L_{\text{opt}} = \sqrt{\frac{192 \sqrt{15015 (15015 P^2 + 1036464 EIk + 163412 EICQ^2)} - 2882880 P}{259116k + 40853CQ^2}}, \quad (5.9)$$

which we note is now a function of both P and Q . The equilibrium equation $\partial V / \partial Q = 0$ becomes,

$$\frac{\partial V}{\partial Q} = \frac{1024EI}{3L^3} Q - \frac{8P}{3L} Q + \frac{151kL}{1260} Q \pm \frac{4}{3} \chi \mu q t + \frac{40853CL}{1081080} Q^3 = 0. \quad (5.10)$$

For $P > P^C$ and each L , there are three possible solutions of equation (5.10) for Q . The solutions of equations (5.9) and (5.10) can be found by iteration of L and Q using the algebraic manipulation package MAPLE (Heck, 1996). The linear approximation for L_{opt} given by (5.6) is first substituted into (5.10), and then each of the three possible solutions for Q thus obtained is substituted in turn into equation (5.9) to update the approximations for L_{opt} . The process is continued until convergence is achieved.

Fig. 5.5 shows the variation of buckle length L and amplitude Q with load P , for

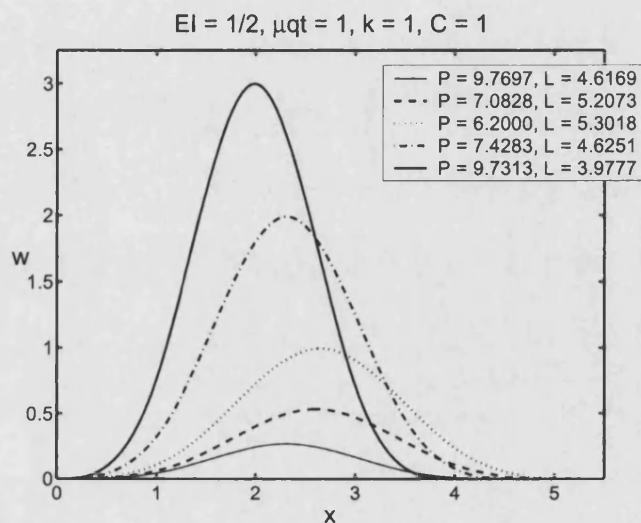


Figure 5.5: Wave-profiles for one-spline model, nonlinear foundation.

into the post-buckling range. Also, the upper right quadrant of the bifurcation diagram for several values of C is seen in Fig. 5.6, detailing how the restabilization is affected by the degree of nonlinearity.

5.4 Two B-spline formulation

In serial folding, humps are observed to form sequentially. To explore this multiple hump scenario in the simplest manner, we next consider a two-spline formulation allowing for two independent maxima/minima. We take values of $C > 0$ for loads above P^C , such that restabilization of the foundation and the consequent lockup in amplitude can successfully model the response of the experiments of Fig. 5.1.

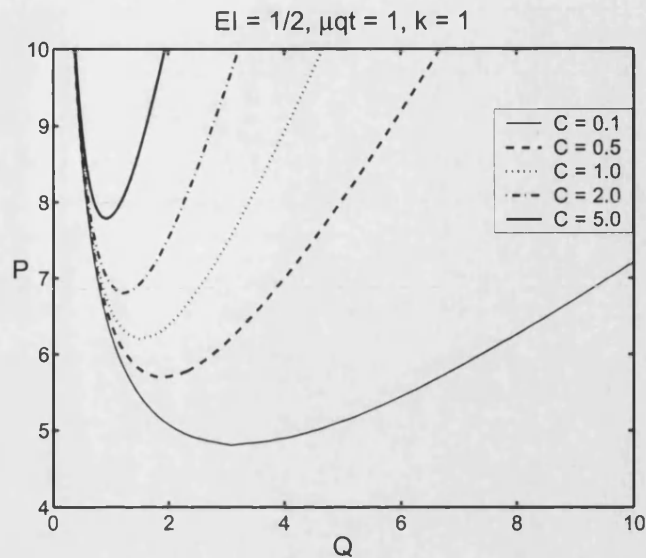


Figure 5.6: Bifurcation diagram for the nonlinear one-spline model when $P > P^C$, for differing C values.

The wave pattern is represented by two rescaled cubic B-splines w_1 and w_2 with amplitudes Q_1 and Q_2 and lengths L_1 and L_2 respectively. The full deflection w along the wave is then found by superposition of w_1 and w_2 . Both primitive periodic ($Q_2 = -Q_1$) and localized ($Q_2 \neq -Q_1$) solutions are found to co-exist (see Fig. 5.7).

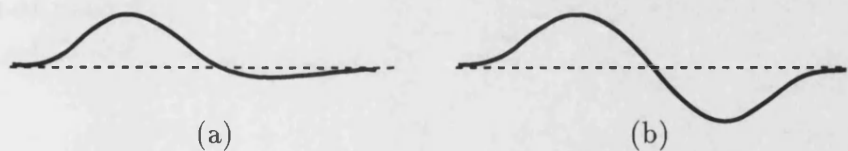


Figure 5.7: Schematic representation of primitive modeshapes from the two B-spline model: (a) homoclinic ($Q_1 \neq -Q_2$); (b) periodic ($Q_1 = -Q_2$).

5.4.1 Overlap

If the wave is modelled in this way, then it is necessary to consider how much w_1 and w_2 should interfere. To this end we introduce an overlap variable, $0 \leq \Omega \leq 1$, such that ΩL_1 represents the position along the first spline where the second spline

starts: $\Omega = 0$ thus implies complete overlap and $\Omega = 1$ implies no interference at all. For the intervals $0 \leq \Omega \leq 1/4$, $1/4 \leq \Omega \leq 1/2$, $1/2 \leq \Omega \leq 3/4$ and $3/4 \leq \Omega \leq 1$ different sections of w_1 are superposed with w_2 and the total length, $(\Omega L_1 + L_2)$, must be split up accordingly. Later we will minimize the maximum total potential energy with respect to Ω .

5.4.2 Galerkin model

The two-spline model has a total of five degrees-of-freedom, amplitudes Q_i ($i = 1, 2$), their corresponding lengths L_i , and overlap Ω . Ideally, energy minimization should be carried out with respect to each of these variables independently. However, the resulting process was considered unnecessarily cumbersome, and for the present descriptive purposes it was found more instructive to reduce the description to the two underlying variables Q_1 and Q_2 , such that the contour plots of the following section could be drawn.

This was done by minimizing only once at each load value with respect to Ω , under the periodic assumption $Q_1 = -Q_2$. Whilst noting that the localized solutions $Q_1 \neq -Q_2$ could possibly lead to slightly different overlap values if complete freedom were allowed, the two sets of results were not expected to differ to any great extent. In searching over $Q_1 - \Omega$ and $Q_1 - Q_2$ space, with P and Q_i known at each point, the spline lengths were taken directly from the nonlinear single spline result (5.9).

5.4.3 Results

Having reduced the potential energy to two degrees-of-freedom, the energy function at any particular load level can be visualized as a two-dimensional surface $V(Q_1, Q_2)$. The stationary values of this surface then correspond to states of equilibrium. Although it is possible for a system to get stuck in a local minimum, in the following it shall be assumed that equilibrium states with the lowest energy will provide the preferred modeshapes. Taking the parameter values $\chi\mu qt = 1$, $EI = 1/2$, $k = 1$ and $C = 1$, the equilibrium solutions can be found either by varying P or by varying the end-shortening \mathcal{E} . In Fig. 5.8 we present the

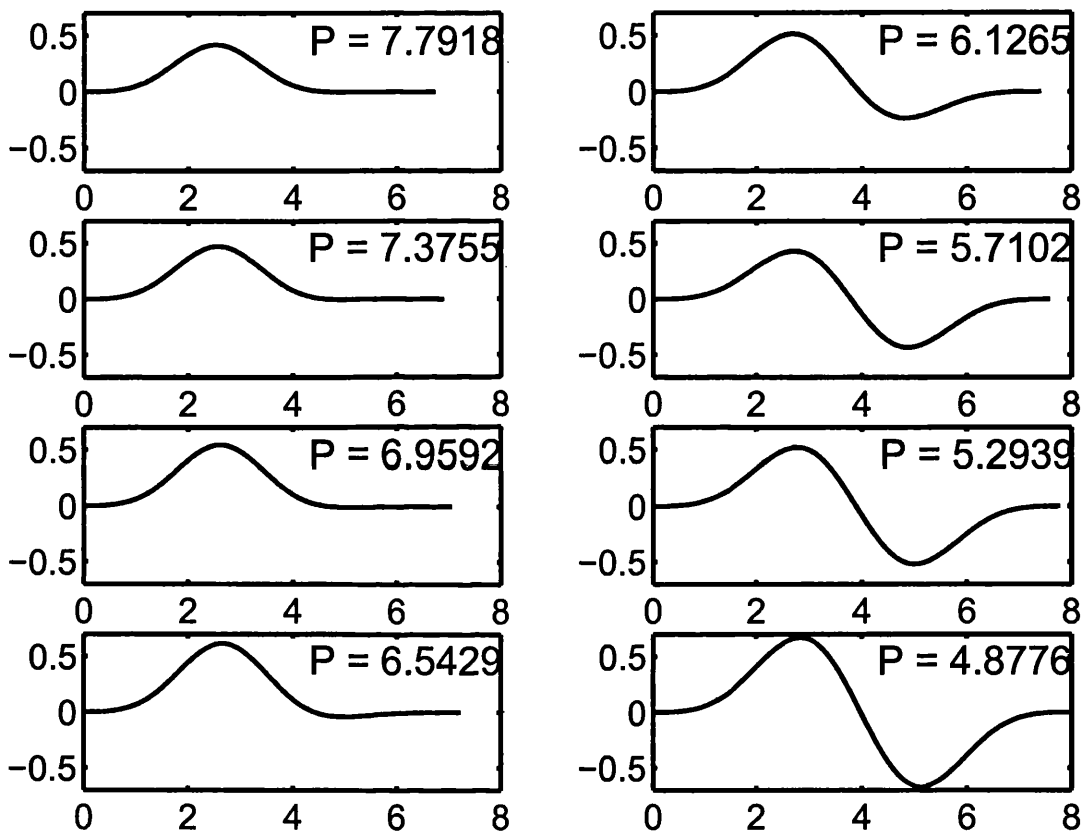


Figure 5.8: Changes in preferred modeshape as the load drops and the end-shortening increases.

results of a series of such calculations, taking an initially large load P and successively reducing it in value. This shows an interesting transition in the preferred modeshape.

For P greater than a value of $P \approx 6.5$ the preferred modeshape is a localized solution with effectively just one hump, whereas for P less than this value a second hump starts to develop. Localized solutions are found to be favoured at high load levels, much like the single spline solution, with a transition taking place to the periodic solutions as the load level falls. This therefore successfully models the early stages of the experimental sequence seen in Fig. 5.1.

We can understand the nature of this transition by studying the way that the contour surfaces of V change as P (or \mathcal{E}) is altered. For $P > 6.5$ the contour surface has four saddle points and two maxima, corresponding to co-existing periodic and localized solutions, of which the localized solutions have the lowest energy. At $P \approx 6.5$ these maxima and saddle points start to coalesce, so that for $P < 6.1$ only two saddle points remain, corresponding now to the existence of low energy periodic solutions.

Fig. 5.9 shows the energy contours for a high load level, $P = 8$. This shows both saddle points and maxima, all of which are stationary solutions. It can be observed that at this constant load, all non-trivial equilibrium states have the same value of end-shortening, $\mathcal{E} = 0.098$, illustrated by the thick elliptical line.

Apart from the apparent minimum of energy in the flat state $Q_1 = Q_2 = 0$, which lies within the jammed region of Fig. 5.2 and hence is of no practical significance, there are two equilibrium states of immediate interest. We have first the maximum of energy $V \approx 0.444$ lying in two positions on the $Q_1 = -Q_2$ line at $Q_1 \approx \pm 0.4$, representing the primitive periodic solution. Secondly there are the saddle-points at $V \approx 0.3915$ occurring in four positions at $Q_1 \approx \pm 0.6$ with Q_2 very small, and again with $Q_2 \approx \pm 0.6$ and Q_1 very small. These are the primitive homoclinic solutions.

Interestingly, as both the maxima and the saddle points appear on the same end-shortening contour, at this value of \mathcal{E} the release of strain energy suggested by the different energy levels takes place without any change in load.

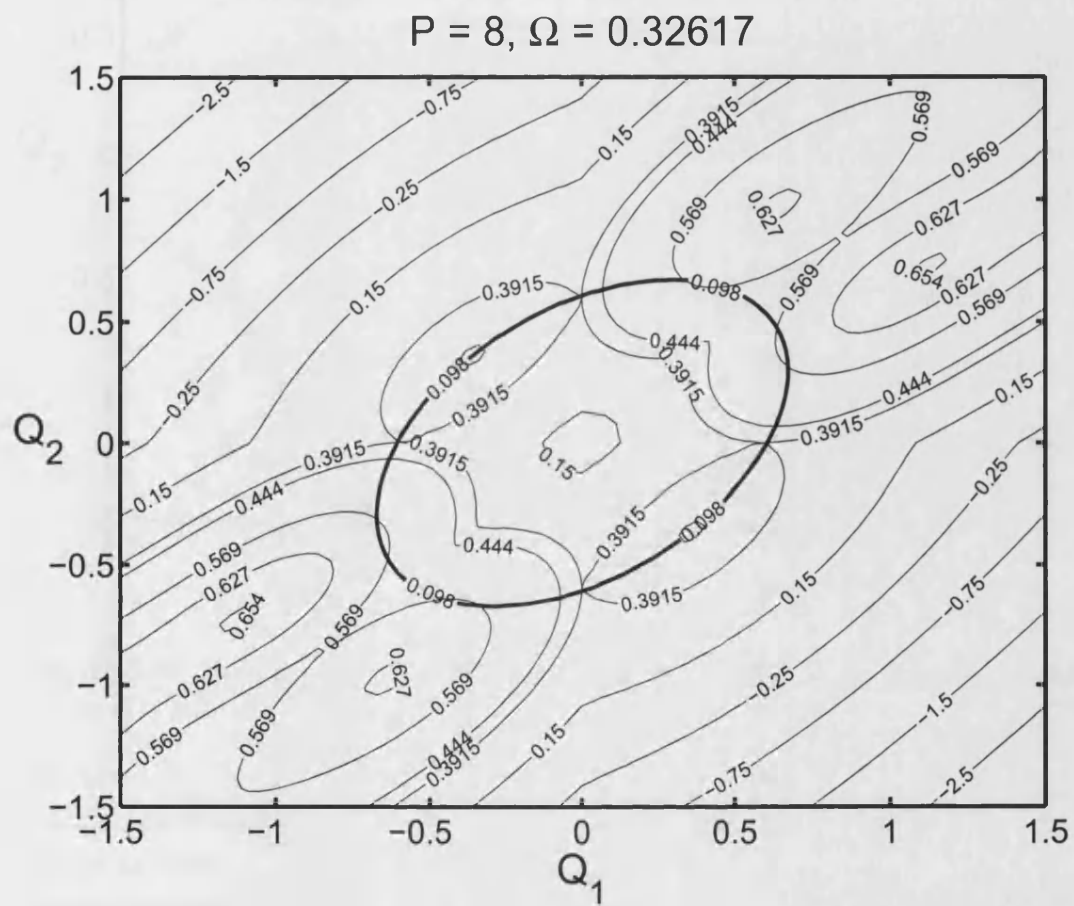


Figure 5.9: Energy, V , and end-shortening, \mathcal{E} , contour plot for $Q_1 - Q_2$ space when $P = 8$.

Fig. 5.10 shows the energy contours for $P = 6.1265$ and an end-shortening contour

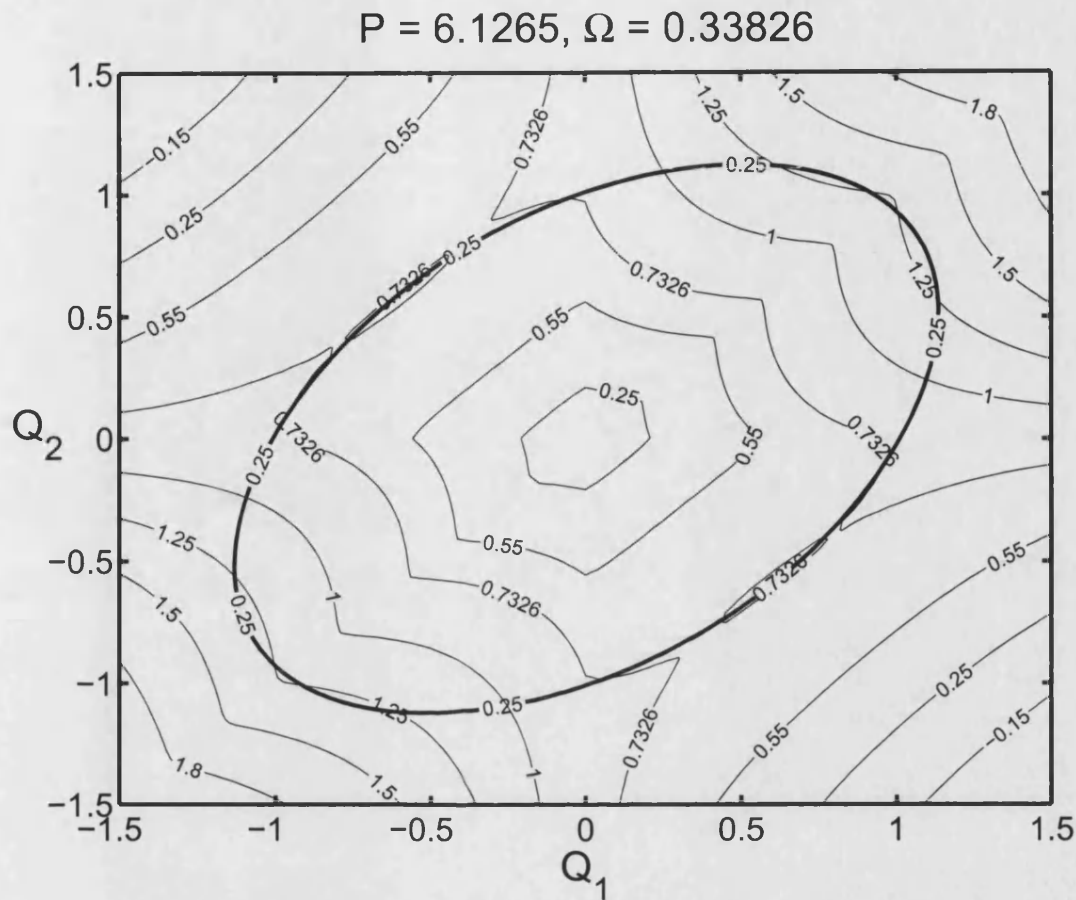


Figure 5.10: Energy, V , and end-shortening, \mathcal{E} , contour plot for $Q_1 - Q_2$ space when $P = 6.1265$.

for $\mathcal{E} = 0.25$. This has the same topological features as Fig. 5.9, except that two saddle points have converged on each maximum to the point where all three are about to become a single saddle on the $Q_1 = -Q_2$ line. Note that the three states now take slightly different values of \mathcal{E} at this load level, indicating that an instability would be accompanied by a drop in load.

The conjunction of the three states of equilibrium is seen to take place at just about the same load level as the single-spline model for $C = 1$ starts to restabilize (see Fig. 5.6). At this stage in the loading sequence, the system is starting to find it easier to take the periodic rather than the localized shape.

Fig. 5.11 is the plot when $P = 4.6$, close to the minimum possible load, or *nadir*, of the equilibrium path. Here the single remaining saddle point is in the process

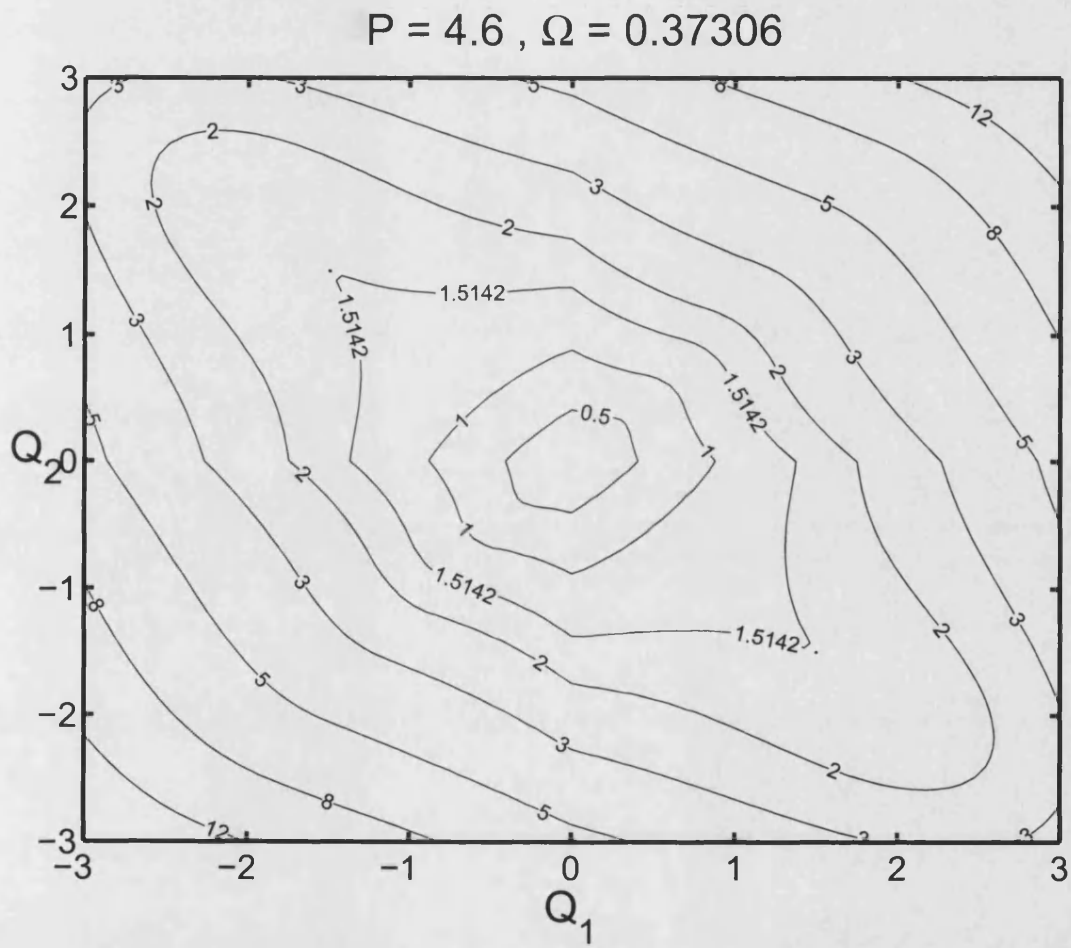


Figure 5.11: Energy, V , and end-shortening, \mathcal{E} , contour plot for $Q_1 - Q_2$ space when $P = 4.6$.

of converging with the minimum of V that represents the far-field restabilized periodic buckled state, appearing outside the illustrated range of the earlier two plots. The eventual restabilization for the periodic state thus takes place very much like that of Fig. 5.6 for the single spline, only at lower load levels.

The sequence described in the contour plots, taking place under falling load but increasing applied end-shortening, involves the preferred modeshape changing from localized to periodic as seen experimentally. This is further illustrated in the plots of Fig. 5.8 which shows this smoothly varying sequence over almost the complete range of the contour plots of Figs. 5.9 to 5.11. The sequence could clearly be extended to further humps of buckling with the inclusion of extra splines.

It must be noted that fixing the overlap Ω in this way, although making the problem more manageable, is bound to lead to errors. It can be seen that calculating the lengths of Q_1 and Q_2 for each point from (5.9), perfect symmetry is lost in the $Q_1 - Q_2$ contour plots. This is because away from the lines of (a)symmetry, where $\pm Q_1 = \pm Q_2$, $L_2 + (\Omega L_1) \neq L_1 + (\Omega L_2)$.

However, in general, especially for the regions of interest, the errors are very small and the total lengths are so close that they are virtually indistinguishable. Whilst there is a noticeable difference in Fig. 5.9 either side of the $Q_1 = Q_2$ line, this area of the plot takes no part in the analysis of this chapter. Here, the critical points vanish almost immediately as the load drops, leaving a topology that is—to all intensive purposes—symmetric.

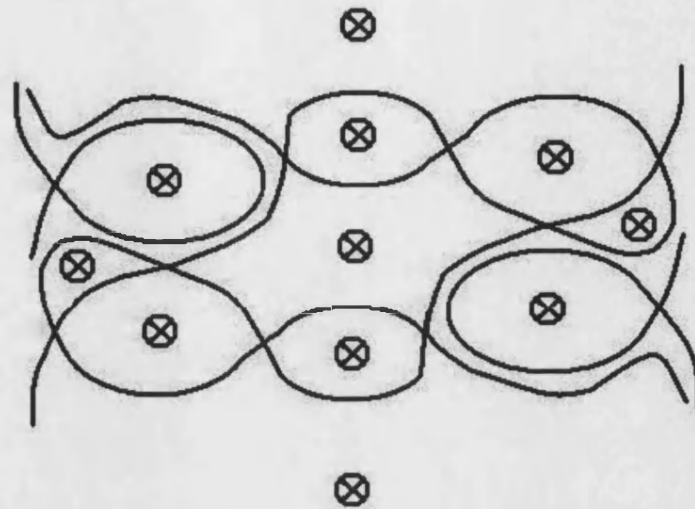
5.5 Morse theory for a surface

The *Euler number* χ_S of a mountainous landscape built on a closed surface S is given by

$$\chi_S = \text{Maxima} - \text{Saddles} + \text{Minima}, \quad (5.11)$$

and we therefore have family of smooth (differentiable) height functions on S . χ_S is a differential invariant—if the height of S is measured in different ways,

χ_S is always the same (Griffiths, 1981). (5.11) is sometimes referred to as the “mountaineer’s equation” and its influence in topology is due to Marston Morse.



(a) $P = 8$



(b) $P \approx 6.1$



(c) $P = 4.6$

Figure 5.12: Schematic showing the evolution of the topology of V as the load drops, the extrema are denoted by crosses.

Fig. 5.12 shows a schematic of the topology of the potential energy V at the three load levels in Figs. 5.9–5.11 of the previous section. Adding the number of maxima and minima in each case and then subtracting the number of saddle points, we find that in all cases the Euler number $\chi_S = 1$. This is what is predicted by *Morse theory*.

Morse theory is a general theory describing the topology of the level surfaces of a nonlinear function of two (or more) variables. When related to the surfaces shown in Fig. 5.12, resulting from an analysis of the potential energy, the theory says that as you vary the parameters smoothly then you see a conservation of index, where the index is defined to be the Euler number.

To ensure that χ_S is always constant for the surface, it is important to realize that if χ_S is non-zero, then there must be some critical points on S ; critical points cannot be destroyed without others (not necessarily of the same type) being created. However, Morse theory shows that saddles and extrema can combine in such a way that the Euler number is conserved. As is observed from Figs. 5.9–5.11 and Fig. 5.12, with falling load, at certain points there is coalescence of a saddle with two extrema to give a minimum.

A mathematically precise description of Morse theory is given by Nash & Sen (1983) and by Hirsch (1976), both of which discuss the *Morse inequalities*. These place restrictions on the number of non-degenerate critical points that a smooth real valued function f can have due to the topology of a closed differentiable surface S with dimension n .

5.5.1 Primitive periodic solution ($Q_2 = -Q_1$)

The primitive two-spline periodic solution, given by $Q_2 = -Q_1$, has been seen on the contour plots of Figs. 5.9 to 5.11. We next explore these particular solutions in more depth, starting with a description of the selection process for the value of Ω used in the plots.

Figs. 5.13 to 5.15 show contours of Q_1 against Ω for this solution, at the three load levels used earlier. For the highest two loads, a single saddle point in V , specifically a minimum with respect to Ω and a maximum with respect to $Q_1(-Q_2)$, is clearly visible. The final contour plot for $P = 4.6$, at the minimum possible post-buckling load, shows this saddle point in the process of combining with the minimum energy state from the restabilized path, and vanishing.

Fig. 5.16 plots the energy variation with respect to Q_1 across the saddle point, at the three load levels. This illustrates again the transition from an energy shape

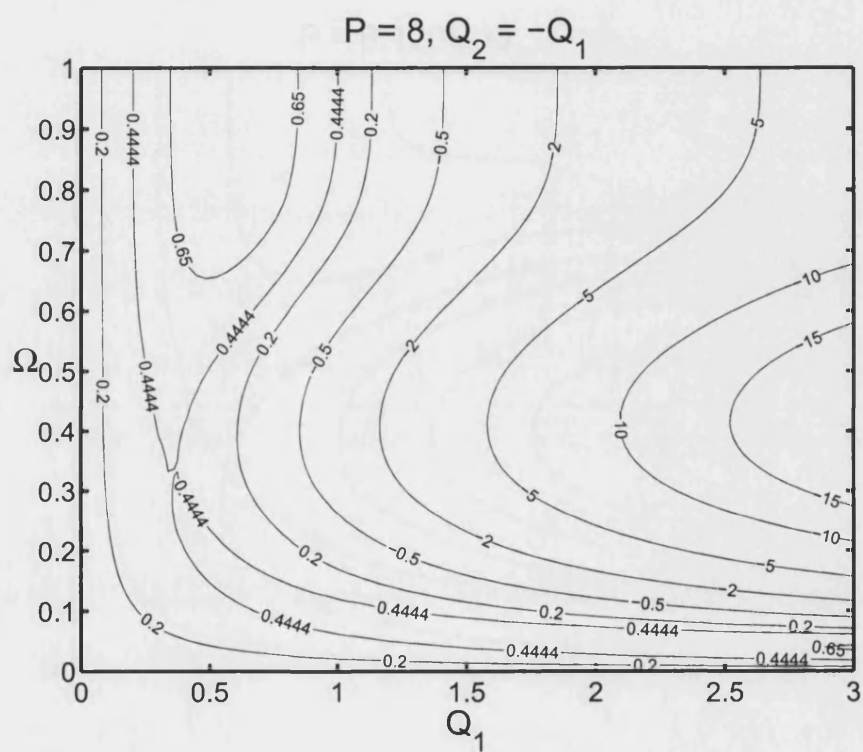


Figure 5.13: Energy contour plot in $Q_1 - \Omega$ space when $Q_2 = -Q_1$ for $P = 8$.

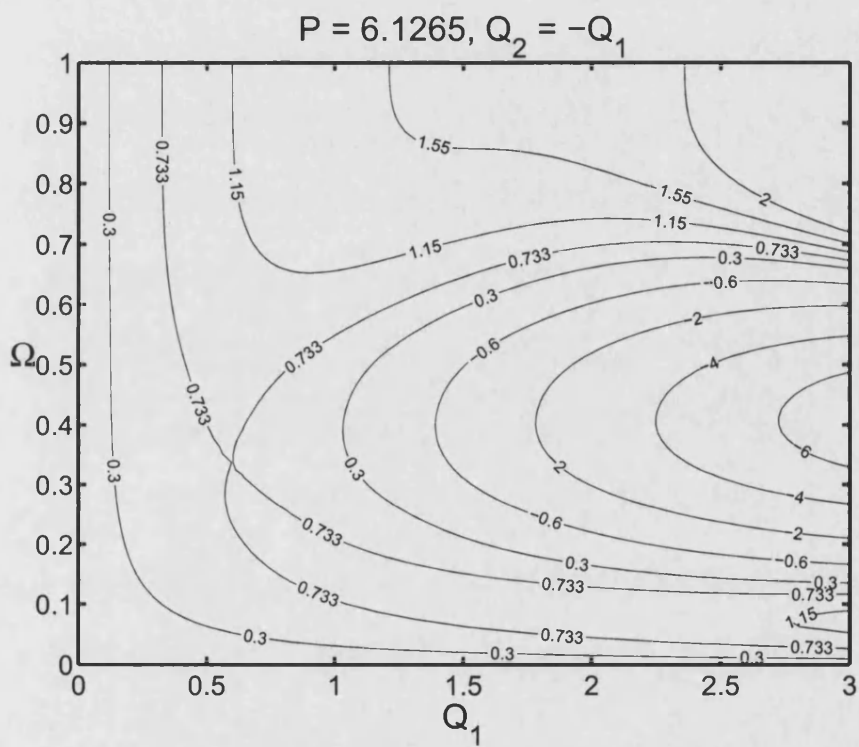


Figure 5.14: Energy contour plot in $Q_1 - \Omega$ space when $Q_2 = -Q_1$ for $P = 6.1265$.

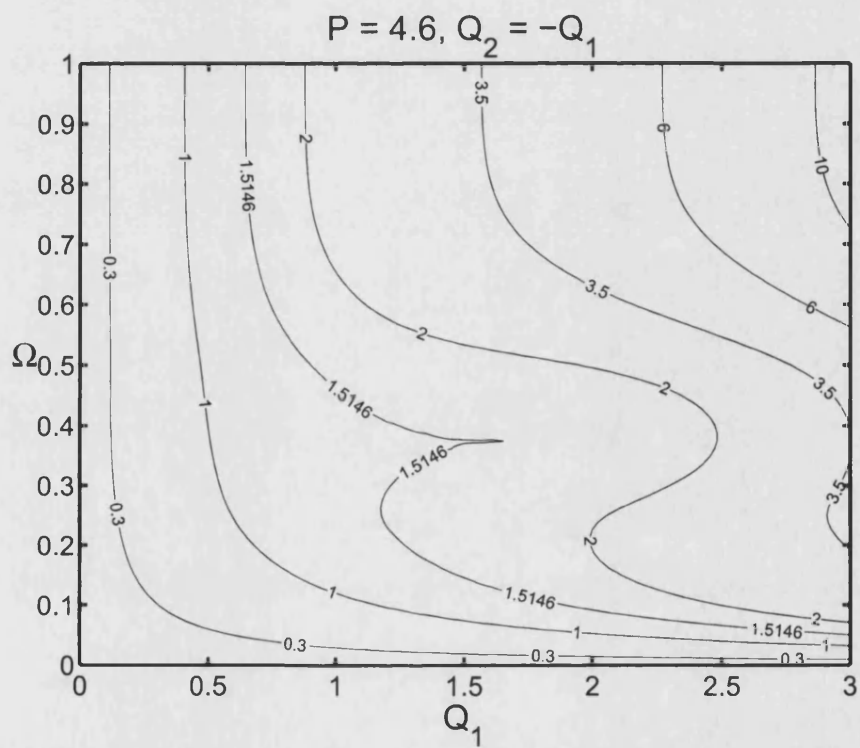


Figure 5.15: Energy contour plot in $Q_1 - \Omega$ space when $Q_2 = -Q_1$ for $P = 4.6$.

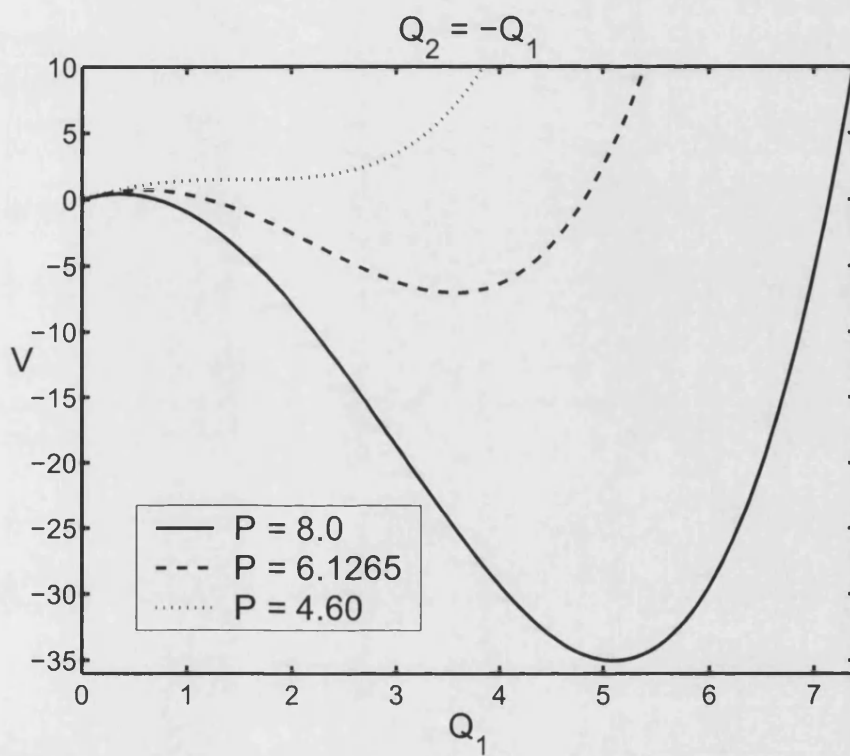


Figure 5.16: Energy profile when $Q_2 = -Q_1$ for $P = 8$, $P = 6.1265$ and $P = 4.6$.

with both a maximum and minimum, to one where there is no stationary point or equilibrium state.

The position of the saddle points can be determined numerically by transforming them into minima as follows. We start by reducing energy function $V = V(Q_1, \Omega)$ to just two degrees-of-freedom, by setting $Q_2 = -Q_1$ and the load to be constant. If we then define the function,

$$F_\Omega = \left(\frac{\partial V}{\partial Q_1} \right)^2 + \left(\frac{\partial V}{\partial \Omega} \right)^2, \quad (5.12)$$

it becomes a relatively simple exercise to demonstrate that saddles in V convert to minima in F_Ω (Hunt *et al.*, 2004), a schematic of which is shown in Fig. 5.17.

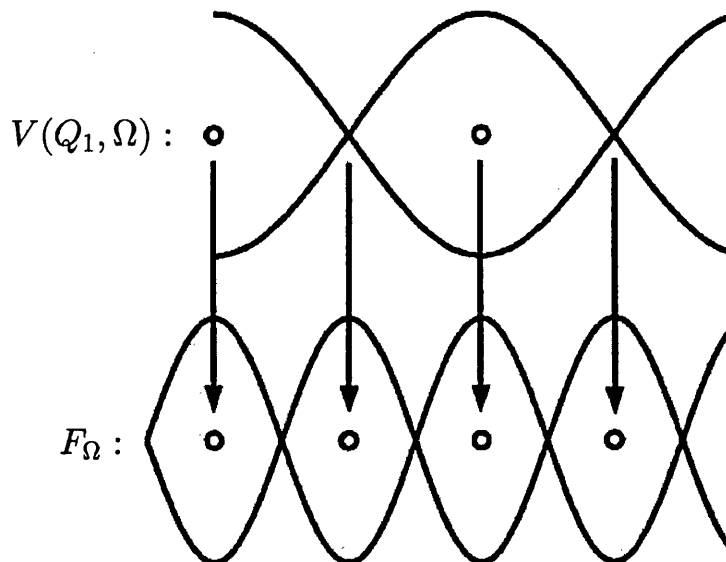


Figure 5.17: Schematic representation of transformation from $V(Q_1, \Omega)$ to F_Ω .

Using the MATLAB command *fminsearch*, which performs unconstrained non-linear optimization (The Math Works, 2001), with an educated initial guess for the values of Q_1 and Ω at $P = 8$ from Fig. 5.13, we can converge to the correct values at the saddle point. These can then be used for the initial guess at the next load level.

fminsearch (The Math Works, 2001) finds the local minimum x of a scalar function f of n real variables, starting at an initial estimate x_0 . The general syntax

is

$$x = \text{fminsearch}(f, x_0, \text{opt}_{\text{list}}, p), \quad (5.13)$$

where p is one or more function parameters and opt_{list} is a list of optimization parameters to alter values such as the termination tolerance etc. x_0 can be a scalar, vector, or matrix.

It uses the simplex search method. In n -dimensional space, a simplex has $n + 1$ distinct vectors that make up its vertices, e. g. in three-dimensional space, the simplex is a pyramid. At each search step, by comparing the function values at the vertices with a new point, in or close to the simplex; a new simplex is generated if the point replaces one of the vertices. This is repeated until the diameter of the simplex is less than the specified tolerance.

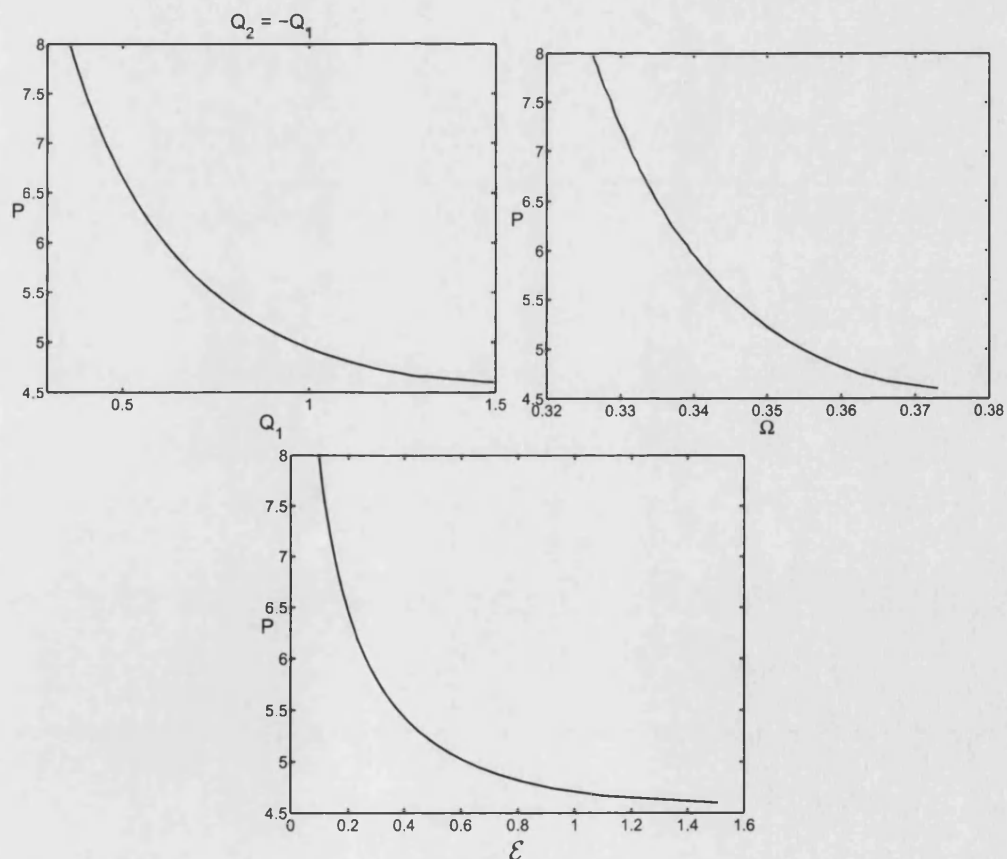


Figure 5.18: Variations of amplitude Q_1 , overlap Ω , and end-shortening \mathcal{E} , with load P , for the $Q_2 = -Q_1$ solution.

Fig. 5.18 shows variations of amplitude, overlap and end-shortening for the $Q_2 =$

$-Q_1$ solution, over the post-buckling regime where the load falls while the end-shortening increases; this is the regime of *negative overall stiffness*.

5.5.2 Primitive localized solution ($Q_2 \neq -Q_1$)

With Ω found at each load level, using Fig. 5.9, initial estimates for the values of Q_1 and Q_2 at the saddle points when $P = 8$ can be made. To locate the saddle points of $V = V(Q_1, Q_2)$, the same method used in the previous subsection to search $Q_1 - \Omega$ space is adopted, with the role of Ω replaced by Q_2 , i. e. we minimize

$$F_{Q_2} = \left(\frac{\partial V}{\partial Q_1} \right)^2 + \left(\frac{\partial V}{\partial Q_2} \right)^2. \quad (5.14)$$

Fig. 5.19 shows variations of the spline amplitudes Q_1 and Q_2 , and the maximum

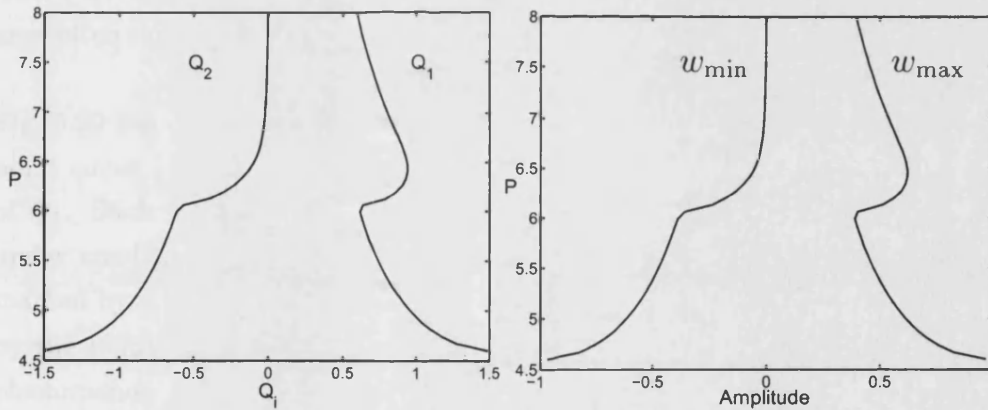


Figure 5.19: Variations of amplitudes Q_1 and Q_2 , and maximum and minimum displacements w_{\max} and w_{\min} , with P , for the $Q_2 \neq -Q_1$ solution.

and minimum displacements along the length (combinations of Q_1 and Q_2) over the same post-buckling load range as Fig. 5.18. Both plots show a fall in the greater of the two values accompanied by an increase in the smaller value, as the chosen equilibrium state changes from localized to periodic.

This process is examined further in Fig. 5.20, which compares the energy levels and the end-shortening values in the two possible equilibrium states. The comparative energy levels show that where the two curves differ, the localized

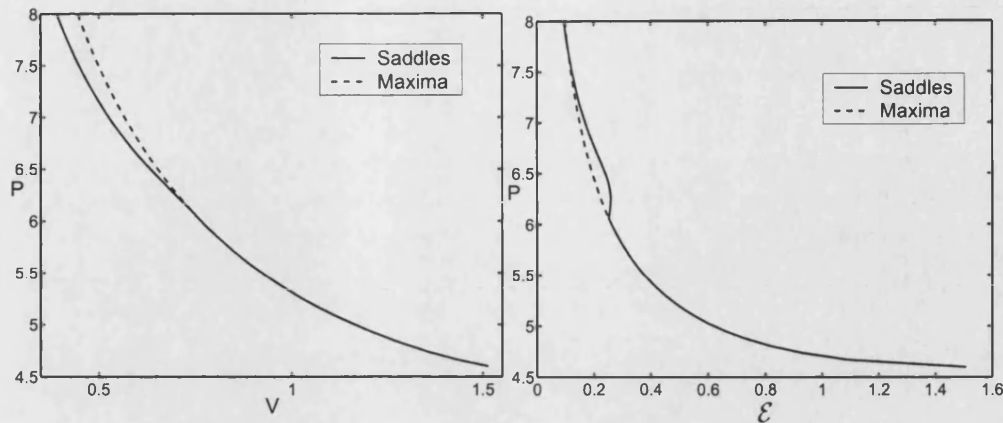


Figure 5.20: Comparative variations of total energy V , and end-shortening \mathcal{E} , with P for both the $Q_2 = -Q_1$, and the $Q_2 \neq -Q_1$ solutions, noting the coalescence of these curves at $P \approx 6.1$.

solution is clearly favoured. However, the stiffness of the localized solution, although negative, has a slightly higher numerical value than that of the periodic. This contrasts with other structural situations, where a lower post-buckling stiffness often indicates the preferred solution (Hunt, 1989).

Fig. 5.20 has one other distinctive feature. At $P \approx 6.4$, part of the falling saddle point curve apparently turns back on itself, accompanied by a drop in the value of Q_1 . Such behaviour would not normally be obtainable experimentally, even under conditions of controlled end-shortening. The actual response would be marked by a sudden downwards drop in load, at the constant value of \mathcal{E} marked by the point of vertical tangency of the load/end-shortening curve. This same phenomenon is familiar from a number of related structural problems, and has been termed *snap-back* behaviour. It is often, even in paper samples, marked by an audible bang (Wadee *et al.*, 2004) as significant strain energy is released.

5.6 Concluding remarks

The nonlinear model for two-layer parallel folding presented in the previous two chapters is extended to find a primitive form of serial buckling behaviour, using two cubic B-splines. Investigating the stationary solutions of the linearized total potential energy, the associated wave-profiles are shown to follow those seen in

real experimental situations. Controlled under loading or end-shortening, the saddle points corresponding to localized solutions converge with unstable maxima representing periodic behaviour. Eventually only periodic solutions exist, as described by Morse theory.

However, in earlier work detailing the transition from highly localized to periodic modeshapes, the formation of additional cells in sequence takes place through a snaking sequence of equilibrium behaviour, marked by the load periodically falling and rising (Hunt *et al.*, 2000a; Budd *et al.*, 2001; Wadee *et al.*, 2004). This contrasts with the present case, where localization is lost and (primitive) periodicity imposed while the load is still falling.

Of course, the present formulation of just two cells would clearly be inadequate to model the continuing sequence, and the increasing complexity of adding extra cells make this impractical. However, even with this extension, there are several properties of natural propagation that are unexplored, including the lockup process. We therefore forego such studies at the present time in preference to extending the two-layer frictional model for parallel folding to the more realistic case of a multilayer. This then allows comparison with experimental results to highlight the accuracies of the model and where further development may be necessary.

Chapter 6

Comparing the multilayer formulation with experiments

6.1 Introduction

Layer slippage under large overburden pressures has led to an elastic, frictional model for two-layer parallel folding (Chapters 3 and 4). Formulated using potential energy considerations, the assumption that the least energy configuration is that seen in nature negates the formation of voids and deformation is by primarily by buckling. Extension to a restabilizing nonlinear foundation, allows, using cubic B-splines, the possibility of localized homoclinic solutions which approach the periodic waveform as the load drops (Chapter 5).

In this chapter we extend the energy formulation of the model given in Chapter 3 to the deformation of a multilayer of n equal layers. Then, by finding values of the involved parameters from laboratory experiments on layers of paper, the load-displacement curves for the model and experiments are compared.

Following the work of Wadee *et al.* (2004) on kink banding in multilayered structures, laboratory experiments on layers of paper embedded in a less competent foam rubber medium are used to highlight the mechanisms involved. Parallel sheets are constrained transversely in a test rig to simulate overburden pressure, and then compressed in the layer parallel direction at a controlled (slow) rate

of displacement. The resulting load–displacement curves are then available for comparison with the multilayer model developed from the two-layer formulation. Measures of the Young’s modulus, friction coefficient and linear and nonlinear components of the foam bedding material, are evaluated independently of the test, whilst the overburden pressure and in-plane compressive load are measured directly by load cells. The first instability, associated with the formation of the first hump in each sequence of localized buckles, and subsequent lockup, are compared with the model formulation and excellent agreement is found.

The chapter starts by showing how the test rig was set up and gives an explanation of the typical data obtained from an experiment. Adding a nonlinearity to the foundation as in Chapter 5, the next section then uses a similar total potential energy procedure as Chapter 3 to formulate the multilayer model in terms of a single layer with the same total thickness. Linearization of the functional and substitution of a sinusoidal Galerkin approximation gives an explicit formulation for the potential energy and hence the expected wavelength. Finally, the predictions from the multilayer model are compared with the results from four separate experiments, along with an explanation as to how the relevant parameters are extracted from the results.

6.2 Experimental procedure

The experiments were conducted in the Department of Civil and Environmental Engineering at Imperial College London using the rig developed by Wadee *et al.* (2004) to study kink banding, a photograph of which is shown in Fig. 6.1. The rig allows application of both axial and transverse loading to an experimental sample, the first of these is applied using a motorized piston the direction and speed of which can be controlled; the latter is slightly more crude as it is applied manually. The piston face can be removed and replaced with one of different width, depending on the depth of the sample. However, for the tests carried out here, a depth of 20.2mm was sufficient in all cases. The magnitude of the parallel and lateral loads and displacements can be measured using 100kN load cells and in-plane transducers, respectively, at 1 second intervals. The values are monitored and recorded with a dedicated data logger connected to a stand-alone computer using the DALITE software package.

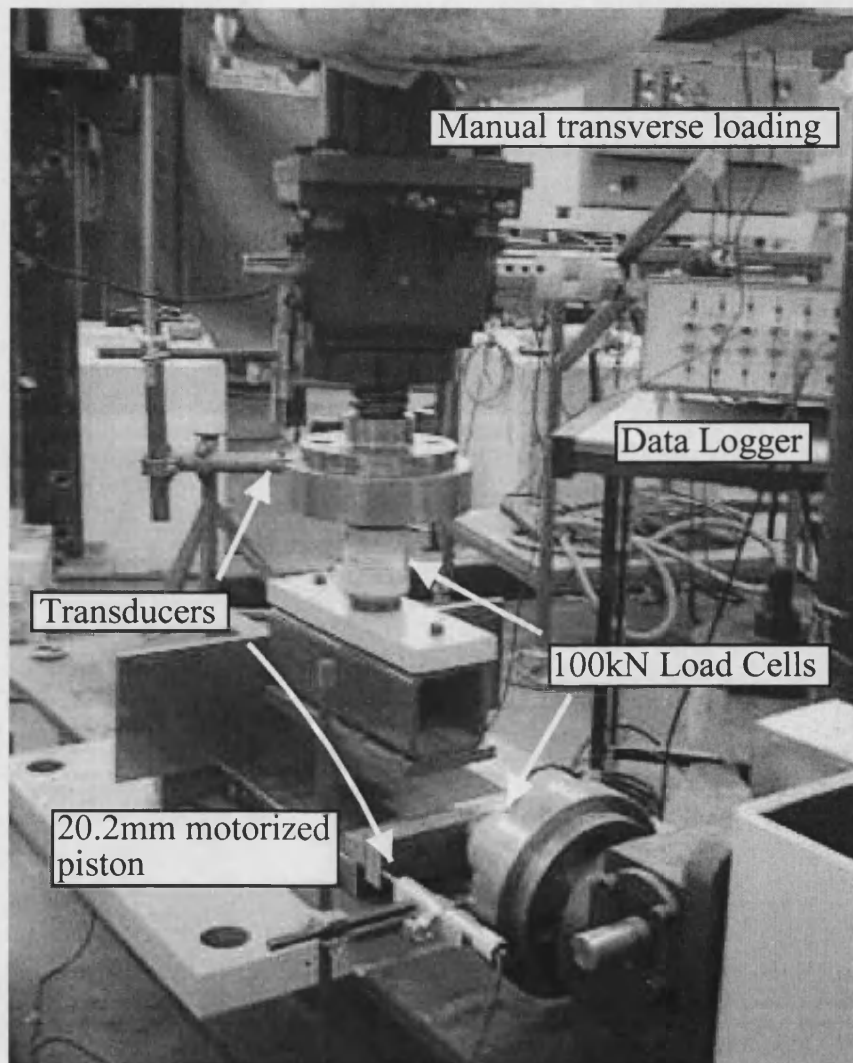


Figure 6.1: Experimental test rig.

To perform the investigation into parallel folding, layers of paper (105mm x 297mm) were used to represent the multilayer, each side of which was then placed a piece of foam ($\approx 110\text{mm} \times 298\text{mm} \times 25\text{mm}$). Hence the multilayer was embedded in an elastic foundation, held transversely under the rigid screw device and compressed in the layer-parallel direction by applying end-shortening at a constant rate over the layers and a proportion of foam. A schematic of this is shown in Fig. 6.2.

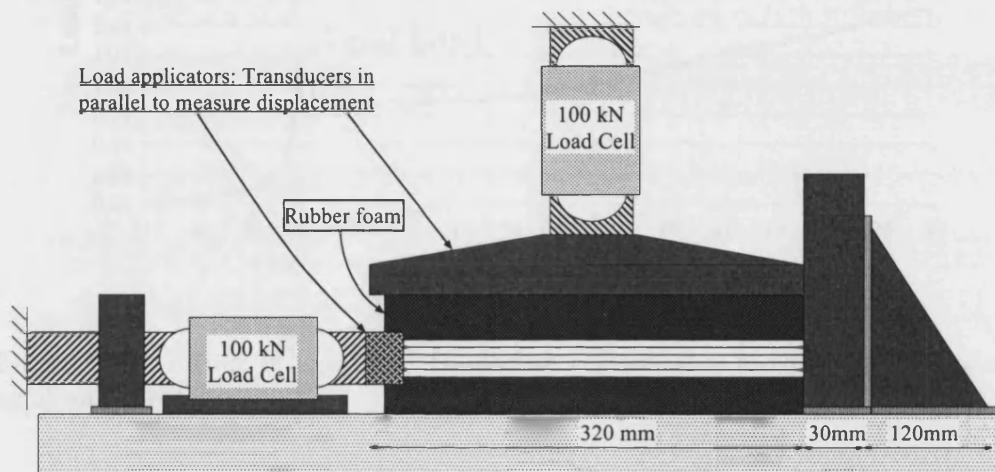


Figure 6.2: Schematic of loading an experimental sample.

There are several constraints as to the magnitude of the loads and displacements. Firstly, the parallel folding model is a static formulation; therefore it is necessary to ensure that the speed of the axial loading applicator is slow enough to reflect this in a quasi-static sense. Secondly, overburden pressures can only be moderate, otherwise the phenomenon of parallel folding could give way to kink banding. An associated consideration is that the rigid boundaries must not interfere with layers; hence it is unwise to have a large numbers of layers. In fact, previous work (Ramberg, 1961) has suggested that the thickness of the foundation should at least be of the same order as the wavelength of the layers. Finally, the foam must be allowed sufficient time to recover after each experiment, or else the elastic properties can change.

The output from a typical experiment is shown in Fig. 6.3, and a photograph of the deformation in Fig. 6.4. As Fig. 6.3 shows, the loading behaviour can be followed throughout an experiment. Initially the transverse overburden pressure is set and held rigid, after which the axial displacement is applied at a slow but

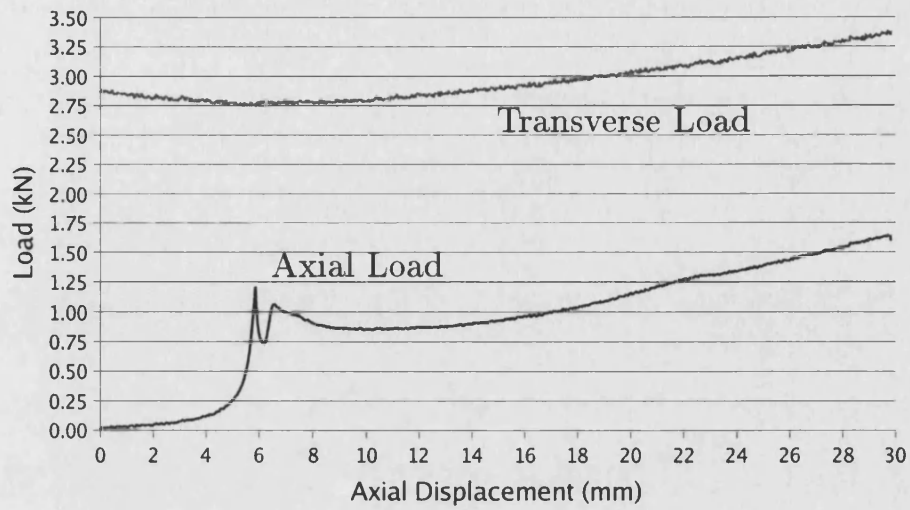


Figure 6.3: Output of axial and transverse compressive forces, plotted against axial end-shortening.

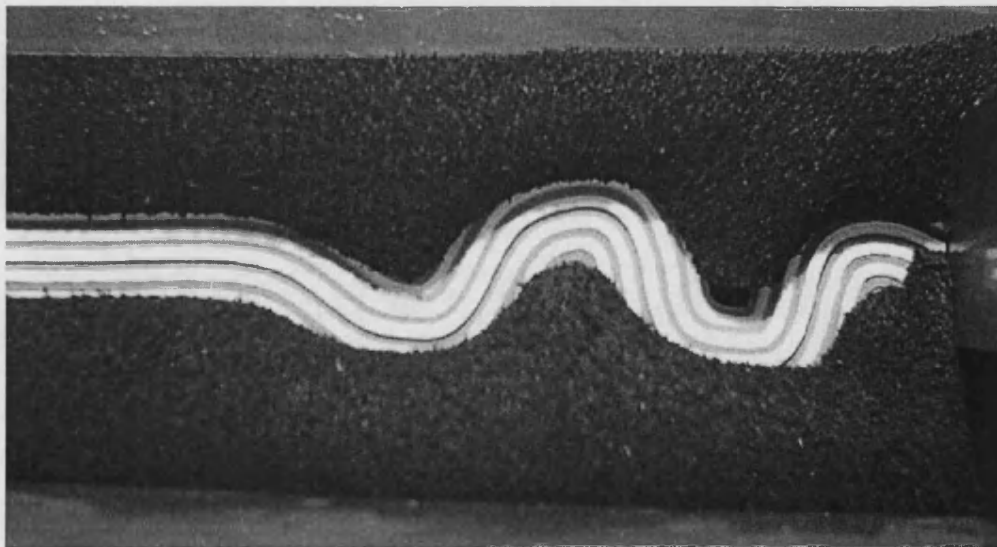


Figure 6.4: Parallel folding of 120 sheets of paper.

constant speed. After an initial phase during which both the layers and foundation are in the process of taking up the load, the in-plane load increases in a fairly linear fashion. During the axial displacement, before any instability, the transverse load stays moderately constant. Nearly always at the loaded end, an instability occurs and the first hump forms (sometimes two humps appear almost simultaneously) and the load drops smoothly, restabilizing and eventually increasing again as the hump locks-up (Hunt *et al.*, 2000a). Once the initial instability is triggered the transverse load begins to increase in a nonlinear fashion. As the next hump forms the load drops slightly, although the effect is considerably less pronounced than for the first hump. The sequence then continues in a similar way—stiffening followed by instability in sequence. Moreover, as the axial displacement continues to be applied, there is an overall restabilization of the system observed by the axial load showing an underlying tendency to rise.

6.3 Total potential energy

6.3.1 Single layer

In order to set up the multilayer model, let us first imagine a single layer of thickness T , with flexural rigidity $E\hat{I}$ and compressed axially by a load P . Following Chapter 5, we assume that the layer is embedded in a nonlinear hardening foundation with linear stiffness k per unit length and nonlinear hardening coefficient C . The coordinates for this system are the arclength x and the vertical deflection w .

Using the definition of \hat{I} , the second moment of area, we find that

$$E\hat{I} = \frac{Ea_1T^3}{12}, \quad (6.1)$$

where a_1 is the width of the sample and will be kept constant throughout the modelling.

The bending energy, U_B , is given by

$$U_B = \frac{E\hat{I}}{2} \int_0^L \frac{\ddot{w}^2}{1 - \dot{w}^2} dx, \quad (6.2)$$

where L , as in the two-layer model, is the length over which the resulting deflection is monotone, i. e. over the interval $[0, L]$, the wave is either increasing or decreasing.

The foundation energy, U_F , is

$$U_F = \frac{k}{2} \int_0^L w^2 dx + \frac{C}{4} \int_0^L w^4 dx, \quad (6.3)$$

and the work done by the load, $P\mathcal{E}$, is

$$P\mathcal{E} = P \int_0^L (1 - \sqrt{1 - \dot{w}^2}) dx. \quad (6.4)$$

6.3.2 Multilayer formulation

If we now have n layers where $n = 2m, m \in \mathbb{N}$, and the total thickness is T , then each layer has thickness $t = T/n$. Let the top layer be l_1 , the second $l_2 \dots$ and the bottom layer l_n . w is now the vertical deflection of the interface between l_m and l_{m+1} . Then following the procedure used in Chapter 3, the nonlinear pseudo-potential energy can be formulated.

Bending energy

If I is the second moment of area associated with each layer, then

$$EI = \frac{Ea_1 T^3}{12n^3} = \frac{E\hat{I}}{n^3}. \quad (6.5)$$

The central interface bends with radius of curvature R , hence each layer l_i has a radius of curvature R_{l_i} :

$$\text{The centreline of } l_1 \text{ has radius } R - \frac{(n-1)T}{2n};$$

The centreline of l_2 has radius $R - \frac{(n-3)T}{2n}$;

⋮

The centreline of l_m has radius $R - \frac{T}{2n}$;

The centreline of l_{m+1} has radius $R + \frac{T}{2n}$;

⋮

The centreline of l_{n-1} has radius $R + \frac{(n-3)T}{2n}$;

The centreline of l_n has radius $R + \frac{(n-1)T}{2n}$.

Hence

$$R_{l_i} = R - [n - (2i - 1)] \frac{T}{2n}. \quad (6.6)$$

Note that we assume here that R_{l_i} is *always* greater than zero.

Thus, the change in bending energy over a small change in x is

$$\begin{aligned} dU_B &= \frac{E\hat{I}}{2n^3} \left(\frac{1}{(R - (n-1)T/n^2)^2} + \frac{1}{(R - (n-3)T/n^2)^2} + \dots \right. \\ &\quad \left. \dots + \frac{1}{(R + (n-3)T/n^2)^2} + \frac{1}{(R + (n-1)T/n^2)^2} \right) dx, \end{aligned} \quad (6.7)$$

which is equivalent to

$$dU_B = \frac{E\hat{I}}{2n^3} \sum_{i=1}^n \frac{1}{R_{l_i}^2} dx. \quad (6.8)$$

If $T^2 \ll \frac{4n^2 R^2}{(n-1)^2}$ and the series is evaluated, (6.8) can be rewritten as

$$dU_B = \frac{E\hat{I}}{2n^2 R^2} dx. \quad (6.9)$$

The total bending energy over L written in terms of w is thus

$$U_B = \frac{E\hat{I}}{2n^2} \int_0^L \frac{\ddot{w}^2}{1 - \dot{w}^2} dx. \quad (6.10)$$

It should be noted that as the number of layers n becomes very large, the contribution of the bending energy U_B becomes small and in the limit as $n \rightarrow \infty$, $U_B \rightarrow 0$. This is predominantly to do with the scaling and, as will be shown in §6.3.5, when reformulated in terms of I , the bending energy remains finite in the differential equation. It does have a physical explanation though, as in this situation the system stops acting as a multilayer and behaves like a continuum. Folding then is by flexural flow, where shearing, rather than layer slippage, becomes the dominant deformation mechanism, smearing the solution throughout the body.

Foundation energy and work done by load

The foundation energy U_F and work done by load $P\mathcal{E}$ are the same as those in §6.3.1, (6.3) and (6.4) respectively.

Work done against friction

For the layers to remain unchanged in length, there must be differential stretching at the interfaces. From bending theory, over a small change in angle $d\theta$, the differences in length between the interfaces are

$$\begin{aligned} ds_{l_1 l_2} &= \frac{R_{l_1} + R_{l_2}}{2} \left(\frac{1}{(R - (n-1)T/n^2)^2} - \frac{1}{(R - (n-3)T/n^2)^2} \right) dx; \\ ds_{l_2 l_3} &= \frac{R_{l_2} + R_{l_3}}{2} \left(\frac{R}{(R - (n-3)T/n^2)^2} - \frac{R}{(R - (n-5)T/n^2)^2} \right) dx; \\ &\vdots \\ ds_{l_{n-1} l_n} &= \frac{R_{l_{n-1}} + R_{l_n}}{2} \left(\frac{R}{(R + (n-3)T/n^2)^2} - \frac{R}{(R + (n-1)T/n^2)^2} \right) dx. \end{aligned}$$

Hence

$$ds_{l_i l_{i+1}} = \bar{R}_{l_i l_{i+1}} \left(\frac{1}{R_{l_i}} - \frac{1}{R_{l_{i+1}}} \right) dx, \quad (6.11)$$

where

$$\begin{aligned} \bar{R}_{l_i l_{i+1}} &= \frac{1}{2}(R_{l_i} + R_{l_{i+1}}) \\ &= \frac{1}{2} \left(2R - [n-2i] \frac{T}{n} \right), \end{aligned} \quad (6.12)$$

is the average of the radii of curvature.

The total difference is the sum of these

$$\begin{aligned}
 ds &= \sum_{i=1}^{n-1} ds_{i,i+1} \\
 &= \left[\frac{RT}{n(R^2 - (n-1)^2 T^2 / 4n^2)} + \frac{2RT}{n} \sum_{j=1}^{\frac{n}{2}-1} \frac{1}{R^2 - (n - (2j-1))^2 T^2 / 4n^2} \right] dx.
 \end{aligned} \tag{6.13}$$

Again, if $T^2 \ll \frac{4n^2 R^2}{(n-1)^2}$, this reduces to

$$ds = \frac{(n-1)T}{nR} dx = \frac{(n-1)T}{n} d\theta. \tag{6.14}$$

The total cumulative slip s at x is given by

$$s = \frac{(n-1)T}{n} |\theta|, \tag{6.15}$$

and hence the total work done against friction is

$$U_\mu = \frac{(n-1)}{n} \mu q T \int_0^L |\sin^{-1} \dot{w}| dx. \tag{6.16}$$

6.3.3 Radius of curvature versus multilayer thickness

From the previous section we find that in order to simplify the bending energy U_B and the work done against friction U_μ , the following relationship between the radius of curvature of the central interface R , and the total thickness of the multilayer T , is assumed to hold

$$T^2 \ll \frac{4n^2 R^2}{(n-1)^2}. \tag{6.17}$$

As the number of layers within the multilayer n tends to infinity, we find that the fraction $n^2/(n-1)^2$ tends to unity and hence for large n the inequality reduces to

$$T^2 \ll 4R^2, \tag{6.18}$$

and it is fairly obvious that over large deflections this condition becomes less valid with increasing n .

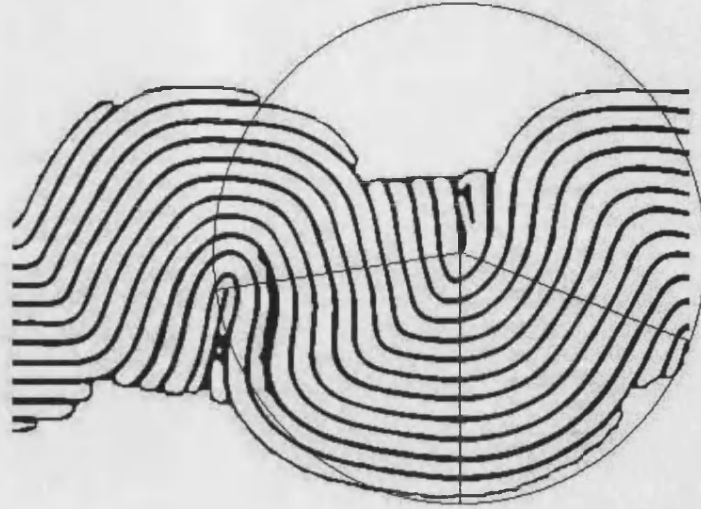


Figure 6.5: An experimental photograph, reduced to a schematic, to emphasize the concentricity of the folds.

Experimental results highlight this fact as is shown in Fig. 6.5. From this figure we can see that the folds have become almost concentric and that the centre of curvature is at the point of the cusp, meaning that the radius of curvature at the core of the multilayer is approximately half the thickness of the multilayer. Thus $R \approx T/2$ and equation (6.18) tells us that $T \ll T$. This would seem like a paradox, in reality it just highlights that the experiment has gone beyond our theoretical model. The singularity created at the cusp (Fig. 6.5) is not covered by the present model.

However, under small deflections, (6.17) is an acceptable assumption, even for large n . It was shown in Chapter 4 that linearization of the two-layer problem changes very little of the post-buckle response over the majority of the range of amplitudes Q . The same methodology will be adopted here for the case of the multilayer and hence, as a consequence, the approximation resulting from (6.17) is justified.

6.3.4 Linearized potential energy functional

It is interesting to note that the bending energy U_B and the work done against friction U_μ can also be obtained from the corresponding energy contributions of the central two layers l_m and l_{m+1} . For these two layers in the multilayer, the bending energy is given by

$$U_B(l_m, l_{m+1}) = \frac{E\hat{I}}{n^3} \int_0^L \left(\frac{\ddot{w}^2}{1 - \dot{w}^2} \right) dx. \quad (6.19)$$

If this is representative of the multilayer with n layers, then there are $n/2$ pairs of layers. Hence

$$\begin{aligned} U_B(l_1, \dots, l_n) &= \frac{n}{2} \frac{E\hat{I}}{n^3} \int_0^L \left(\frac{\ddot{w}^2}{1 - \dot{w}^2} \right) dx \\ &= \frac{E\hat{I}}{2n^2} \int_0^L \left(\frac{\ddot{w}^2}{1 - \dot{w}^2} \right) dx. \end{aligned} \quad (6.20)$$

Also, the work done against friction at the interface between l_m and l_{m+1} is

$$U_\mu(l_m, l_{m+1}) = \frac{1}{n} \mu q T \int_0^L |\sin^{-1} \dot{w}| dx. \quad (6.21)$$

Again, if this is representative of n layers, there are $n - 1$ such interfaces and

$$U_\mu(l_1, \dots, l_n) = \frac{(n-1)}{n} \mu q T \int_0^L |\sin^{-1} \dot{w}| dx. \quad (6.22)$$

Now, with Chapter 3 in mind, if w is assumed to be small, the geometrical nonlinearities become unimportant and the potential energy function becomes

$$V = \int_0^L \left(\frac{E\hat{I}}{2n^2} \ddot{w}^2 - \frac{P}{2} \dot{w}^2 + \frac{k}{2} w^2 + \frac{(n-1)\chi\mu q T}{n} |\dot{w}| \right) dx, \quad (6.23)$$

with $\chi = \pm 1$ as defined in Chapter 3.

At initiation, it is valid to assume a fold has a sinusoidal shape and if the layer is made up of independent sheets, then it is likely to become a concentric fold (Ramsey, 1967). Hence, assuming a sinusoidal deflected shape for the middle

interface as given in Chapter 3,

$$w(x) = Q \cos\left(\frac{\pi x}{L}\right), \quad (6.24)$$

this behaviour then is representative of the whole multilayer. Note that whilst using (6.24) as an approximation of the waveshape gives a somewhat “smeared” solution, it was shown in Chapter 5, using cubic B-splines as a more sophisticated curve-fitting technique, that a single hump analysis gives similar results.

A simple linear eigenvalue analysis yields the critical load thus

$$P^C = \frac{E\hat{I}\pi^2}{n^2L^2} + \frac{kL^2}{\pi^2}, \quad (6.25)$$

and minimizing the critical load, with respect to the length L ,

$$L = \pi \sqrt[4]{\frac{E\hat{I}}{n^2k}}. \quad (6.26)$$

We again recognize that as $n \rightarrow \infty$, $L \rightarrow 0$. As before, this is due to the scaling of the model and when reformulated does not turn out to be an issue of concern.

Unfortunately, linearization also removes the nonlinear characteristics of the foundation. As will be shown in §6.4.3 real foundations often have a strong natural restiffening under large transverse loading (Fig 6.6(a)). Hence we wish to retain the stiffening behaviour in our model and to this end, before we compare the theory with experimental output, we re-introduce the nonlinear energy contribution of the foundation to obtain the “partially” linearized potential energy function (Peletier, 2001b)

$$V = \int_0^L \left(\frac{E\hat{I}}{2n^2} \ddot{w}^2 - \frac{P}{2} \dot{w}^2 + \frac{k}{2} w^2 + \frac{C}{4} w^4 + \frac{(n-1)\chi\mu qT}{n} |\dot{w}| \right) dx. \quad (6.27)$$

Before leaving this section, we compare (6.25) and (6.26) with the equations given by Currie *et al.* (1962) for a multilayer of n equal layers each having thickness t , where the boundaries of the individual component members are *frictionless* (see §2.3.4). When recalculated using (6.24), to be consistent with the model

presented here, the critical load and wavelength become

$$P^C = \frac{\pi^2 E \hat{I}}{n^2 L^2} + kL\pi; \quad L = \pi \sqrt[3]{\frac{E \hat{I}}{n^2 k}}. \quad (6.28)$$

The latter agrees with the equation given by Biot (1961) for the *dominant wavelength* L_d of a viscous multilayer, with perfect lubrication, within a viscous matrix (via the *correspondence principle*). The discrepancies between the current formulation and those given by (6.28) lie with the foundation energy. Currie *et al.* (1962) calculate this term using the force required to deflect a plate a distance w at x in an *elastic continuum*, as stated by Biot (1937)

$$\mathcal{F} = w \frac{k\pi}{2L}, \quad (6.29)$$

and hence get that the foundation energy is

$$\begin{aligned} U_F &= \int_0^L \left(\frac{wk\pi}{L} \right) \frac{w}{2} dx \\ &= \frac{k\pi}{2L} \int_0^L w^2 dx. \end{aligned} \quad (6.30)$$

Note that (6.29) and (6.30) are again reformulated in order to make the comparisons easy.

6.3.5 Calculus of variations

Although the resulting linearized differential equation will not be analysed here, for completeness, we repeat the calculations undertaken for the two-layer model in Chapter 4 in order to get stationary solutions of V over all admissible functions. As mentioned in §6.3.1, the solutions are monotone over $[0, L]$ and hence the boundary conditions

$$\dot{w}(0) = \dot{w}(L) = 0, \quad (6.31)$$

hold as before.

We also re-introduce $\alpha = \pm 1$ to indicate whether w is increasing ($\alpha = +1$) or decreasing ($\alpha = -1$). Using this notation, the “partially” linearized energy

density—the total potential energy per unit length— F is given by

$$F = \frac{E\hat{I}}{2n^2}\ddot{w}^2 - \frac{P}{2}\dot{w}^2 + \frac{k}{2}w^2 + \frac{C}{4}w^4 + \frac{(n-1)\alpha\chi\mu qT}{n}\dot{w}. \quad (6.32)$$

F , and therefore, V , have the same form as in Chapter 4, hence performing the calculus of variations leads to the same expression for δV

$$\begin{aligned} \delta V &= \left[\frac{\partial F}{\partial \dot{w}} \delta w \right]_0^L + \left[\frac{\partial F}{\partial \ddot{w}} \delta \dot{w} \right]_0^L - \left[\frac{d}{dx} \frac{\partial F}{\partial \ddot{w}} \delta w \right]_0^L \\ &+ \int_0^L \left(\frac{d^2}{dx^2} \frac{\partial F}{\partial \ddot{w}} - \frac{d}{dx} \frac{\partial F}{\partial \dot{w}} + \frac{\partial F}{\partial w} \right) \delta w \, dx. \end{aligned} \quad (6.33)$$

Setting this equal to zero, the second bracket is automatically zero from the boundary conditions above and the Euler-Lagrange equation resulting from the integral yields

$$\frac{E\hat{I}}{n^2}\ddot{\ddot{w}} + P\ddot{w} + kw + Cw^3 = 0. \quad (6.34)$$

Substituting I , as defined in §6.3.2, into (6.34), we are able to compare the above with (4.9)

$$nEI\ddot{\ddot{w}} + P\ddot{w} + kw + Cw^3 = 0, \quad (6.35)$$

and we see that the term resulting from the bending energy dominates the differential equation.

Again, following Chapter 4, the first and third brackets vanish if, for all δw at $x = 0$ and L

$$\frac{\partial F}{\partial \dot{w}} - \frac{d}{dx} \frac{\partial F}{\partial \ddot{w}} = 0, \quad (6.36)$$

which leads to the boundary conditions

$$\ddot{\ddot{w}}(0) = \ddot{\ddot{w}}(L) = \frac{n(n-1)\alpha\chi\mu qT}{E\hat{I}} = \frac{(n-1)\alpha\chi\mu qT}{nEI}. \quad (6.37)$$

As above, when (6.37) are reformulated using the definition of I , comparison with the two-layer model becomes more obvious. As in Chapter 4, the boundary conditions are due to a step change in the shear force at the ends of the monotone section $[0, L]$. However, for the strata embedded within the multilayer,

the moments cancel at the boundary interfaces and an out of balance moment of magnitude $\mu qLt/2$ is only to be found on the first and last layers, i. e. those in contact with the foundation. This couple has a lever arm equal to $t(n-1)$, the distance between the neutral axes' of l_1 and l_n , and as before is resisted by lateral point loads at the limits. Even though (6.37) are related to the deflection of central interface, physically, the point loads would have an overall effect felt throughout the multilayer and hence the inclusion of the terms.

6.4 Comparison with experiments

Data for four separate experiments from the rig of Fig. 6.2 is given in Table 6.1. Here Experiment 1 is that with the response given in Fig. 6.3. Paper of grade 80 g/m^2 was used in each case. Direct comparison with the model requires independent estimates of E, q, μ, k and C , obtained in the following manner.

Quantity	Experiment			
	1	2	3	4
a_1 (mm)	105	105	105	105
a_2 (mm)	297	297	297	297
t (mm)	0.1	0.1	0.1	0.1
n	120	140	160	180
T (mm)	12	14	16	18
E (kN/mm ²)	1.56	1.42	1.55	1.26
\hat{I} (mm ⁴)	15120	24010	35840	51030
q (kN/mm)	0.0092	0.0096	0.012	0.013
k (kN/mm ²)	0.0063	0.0046	0.0070	0.0036
C (kN/mm ⁴)	0.0136	0.0084	0.0186	0.0149

Table 6.1: Experimental configurations.

6.4.1 Young's modulus and second moment of area

Given the stiffness k_{layers} of the paper, the in-plane Young's modulus is obtained from

$$E = \frac{k_{\text{layers}} a_2}{T a_1}, \quad (6.38)$$

where a_1 and a_2 are the width and length of the layers and T is the total thickness of the layered sample.

The in-line spring stiffness, for the layers plus a proportion of the foundation, is given by the initial slope of the $\mathcal{E} - P$ plot, as seen in Fig. 6.3. Whilst we recognize that the section of the sample under axial loading acts as three springs in parallel and hence

$$k_{\text{layers}} = k_{\text{total}} - 2k_{\text{foam}}, \quad (6.39)$$

the paper is inherently stiffer than the foam. Therefore we take k_{layers} to be equal to the gradient of the load versus end-shortening plot. Wadee (1999) stated that the Young's modulus of the foam is $E_{\text{foam}} = 0.0004 \text{ kN/mm}^2$, several orders of magnitude lower than the values given in Table 6.1, justifying this assumption.

As shown in (6.1) of §6.3.1, the second moment of area for the multilayer is simply

$$\hat{I} = \frac{a_1 T^3}{12}. \quad (6.40)$$

6.4.2 Overburden pressure and coefficient of friction

The overburden pressure q , per unit length of the multilayer is simply given by dividing the total transverse load at the first instability by the length a_2 .

As in Wadee *et al.* (2004), the experimental coefficient of friction is determined by the critical slope at which an inclined stack of the paper begins to slide. The coefficient of friction μ , is then given as (see §1.7.2)

$$\mu = \tan \gamma, \quad (6.41)$$

where γ is the angle at which the inclined paper slips. The value of $\mu = 0.57$ found by Wadee *et al.* (2004) is assumed in all cases as the same paper was used. This corresponds to a slip angle of $\gamma \approx \pi/6$ radians and is comparable to sandstone (Price & Cosgrove, 1990).

6.4.3 Foundation stiffness

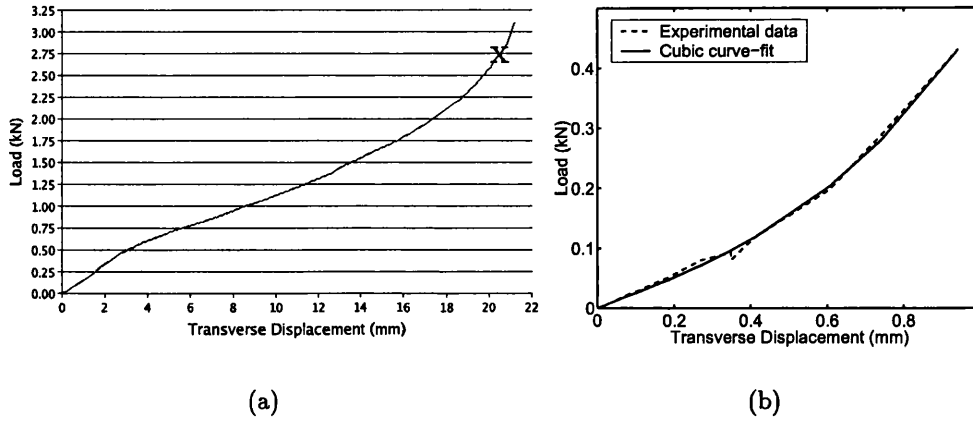


Figure 6.6: (a) Transverse load (P_T) versus displacement (Δ) response for Experiment 2, where X marks the load at the first instability (see Fig. 6.9(a)). (b) Curve-fit in the neighbourhood of the point X. (Note that the curve is rescaled to start at the origin).

The linear and nonlinear foundation stiffnesses, k and C respectively, are more difficult to obtain, but can be estimated from the pure transverse load versus displacement plot resulting from each experiment. Using Experiment 2 as an example, from Fig. 6.6(a), the loading response is seen to first soften, and then restiffen, when compared with its initial stiffness. For the foam used in the experiments, this is in agreement with Wadee (1999), who added a destiffening term to the foundation energy; an explanation for this behaviour is given by Hunt & Wadee (1998). However, for these tests, when the axial end-shortening is applied, the foundation has already been compressed until well into the stiffening region and the curve is replaced by a linear stiffness combined with a cubic stiffening coefficient.

To determine the linear and nonlinear constants from the pre-stressed—but otherwise undeformed—foundation, we study the $P_T - \Delta$ plot for each experiment at the appropriate load level, i. e. that associated with the first instability. We then use the MATLAB function *fminsearch* (The Math Works, 2001) (see Chapter 5) to find a curve-fit with both linear and cubic terms (Fig. 6.6(b)). This leads to an equation of the form

$$P_T = \mathcal{K}\Delta + \mathcal{C}\Delta^3, \quad (6.42)$$

where Δ is measured from the pre-compressed state.

The curve of Fig. 6.6 represents transverse load plotted against the corresponding displacement, and involves the paper sample as well as a layer of foam top and bottom. If we take the paper as much stiffer than the foam, the measured stiffness \mathcal{K} and nonlinear coefficient \mathcal{C} result from the two layers of foam acting in series. The stiffness of a single layer is therefore obtained by doubling the measured stiffness as

$$\frac{1}{\mathcal{K}} = \frac{2}{\mathcal{K}_{\text{spring}}}. \quad (6.43)$$

Moreover, as the paper starts to deflect into the foam, the combined effect of the two layers on the paper lying between them is as two springs acting in parallel, and again the measured stiffness must be doubled. To see this, imagine that the

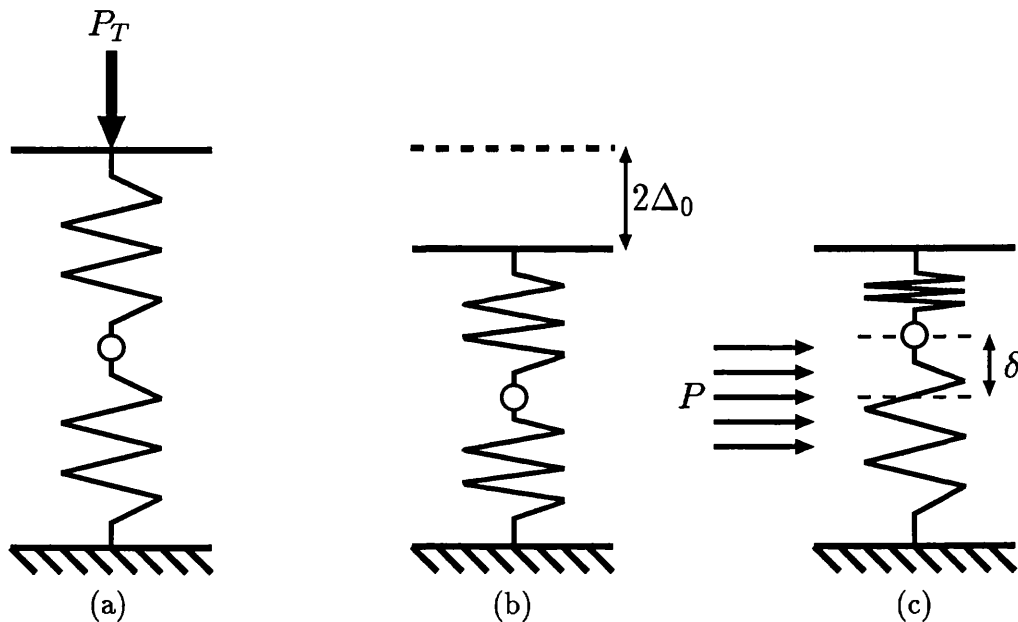


Figure 6.7: Diagram of the interaction of two springs acting either side of the layers when: (a) & (b) the pre-compression is added causing displacement Δ_0 in each spring, and (c) the axial load forces one spring to compress and the other to release by an amount δ .

foundation consists of just two springs and that under the transverse loading P_T (Fig. 6.7(a)) the springs have both compressed by a distance Δ_0 (Fig. 6.7(b)). With P applied parallel to the layering, when a fold forms at the first instability, the material moves further into one side of the matrix an amount δ whilst releasing the other side by the same amount (Fig. 6.7(c)).

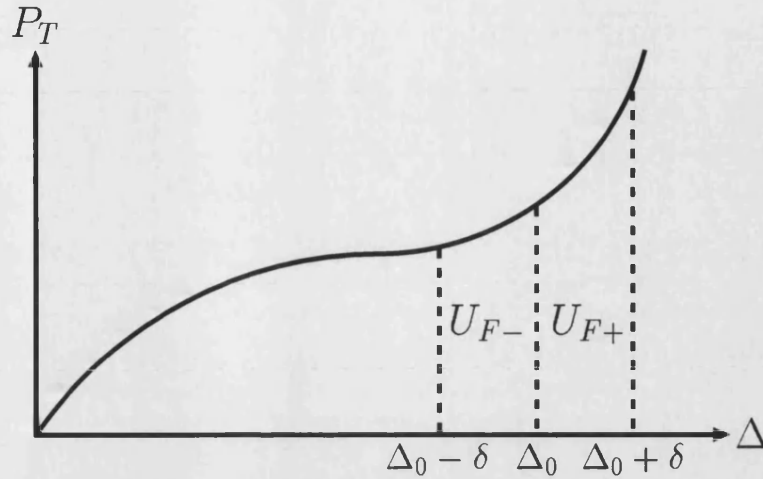


Figure 6.8: Schematic of the $P_T - \Delta$ plot when increasing and releasing the pre-compression.

When under extra compression δ , the first spring gives a positive energy contribution U_{F+} (Fig. 6.8), which is calculated as

$$\begin{aligned}
 U_{F+} &= \int_{\Delta_0}^{\Delta_0+\delta} (k\Delta + C\Delta^3) d\Delta \\
 &= \frac{k}{2} [(\Delta_0 + \delta)^2 - \Delta_0^2] + \frac{C}{4} [(\Delta_0 + \delta)^4 - \Delta_0^4] \\
 &= \frac{k}{2}(\delta^2 + 2\delta\Delta_0) + \frac{C}{4}(\delta^4 + 4\delta^3\Delta_0 + 6\delta^2\Delta_0^2 + 4\delta\Delta_0^3). \quad (6.44)
 \end{aligned}$$

The negative energy contribution U_{F-} , due to the second spring releasing some of its pre-compression by the amount δ , is given by (Fig. 6.8)

$$\begin{aligned}
 U_{F-} &= \int_{\Delta_0-\delta}^{\Delta_0} (k\Delta + C\Delta^3) d\Delta \\
 &= \frac{k}{2} [\Delta_0^2 - (\Delta_0 - \delta)^2] + \frac{C}{4} [\Delta_0^4 - (\Delta_0 - \delta)^4] \\
 &= \frac{k}{2}(2\delta\Delta_0 - \delta^2) + \frac{C}{4}(4\delta^3\Delta_0 - 6\delta^2\Delta_0^2 + 4\delta\Delta_0^3 - \delta^4). \quad (6.45)
 \end{aligned}$$

Thus the total foundation energy U_F for the two springs is found from the difference of (6.44) and (6.45)

$$\begin{aligned}
 U_F &= U_{F+} - U_{F-} \\
 &= k\delta^2 + \frac{C}{2}\delta^4 + 3C\delta^2\Delta_0^2. \quad (6.46)
 \end{aligned}$$

The latter term is an higher order effect and can be ignored as we are finding the curvature of a particular slope. The first two terms show that, under in-plane loading, when each hump is formed, the foundation acts as though the two

springs are in parallel, doubling the linear and nonlinear coefficients.

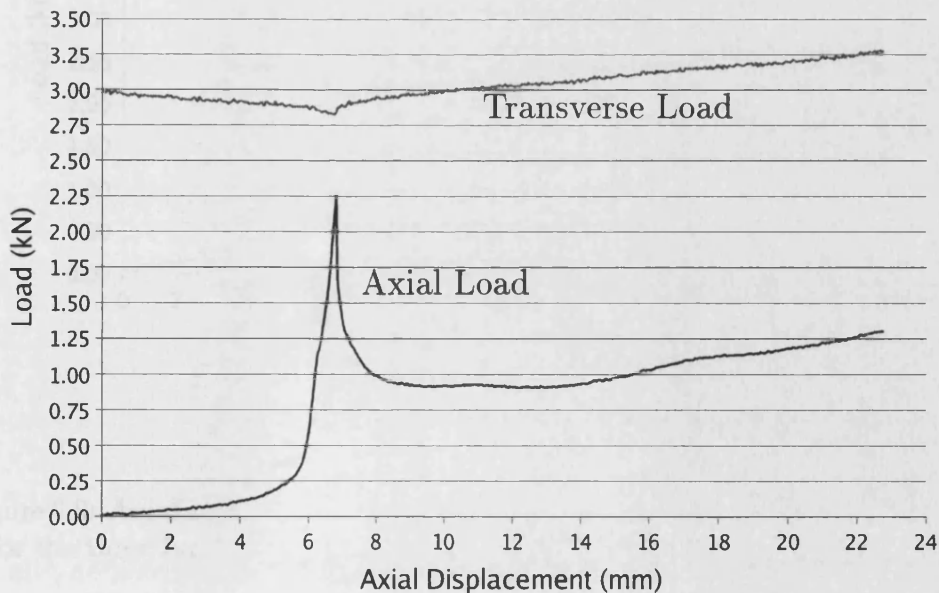
Therefore, from (6.43) and (6.46), to determine the stiffness per unit length of the foundation, the measured stiffness of Fig. 6.6 must first be multiplied by a factor of four, and then divided by the length a_2 . The same goes for the nonlinear coefficient C , and we can write,

$$k = \frac{4\mathcal{K}}{a_2}; \quad C = \frac{4\mathcal{C}}{a_2}. \quad (6.47)$$

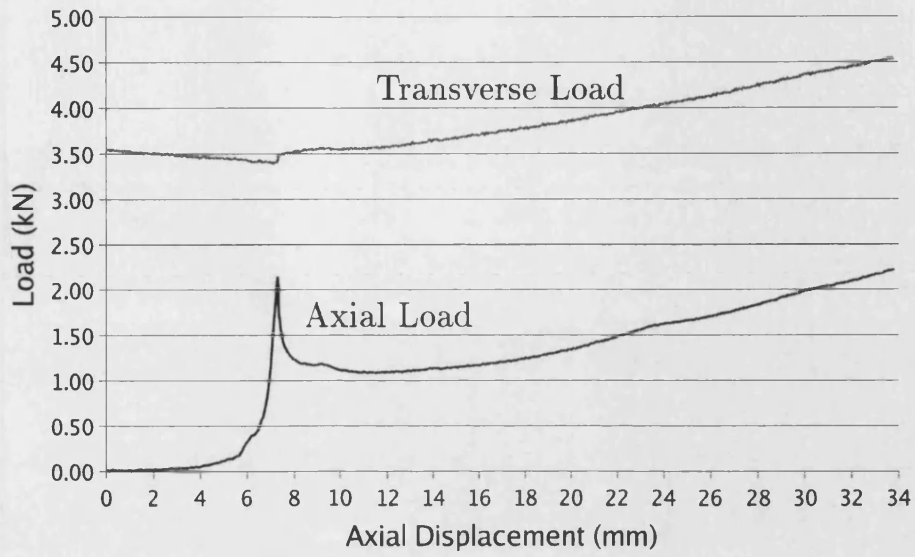
Results from this process are given in Table 6.1, where it is seen that the values of k found experimentally are of the same order of magnitude as that stated by Wadee (1999) for the linearly elastic compression of the foam.

6.4.4 Graphical comparisons

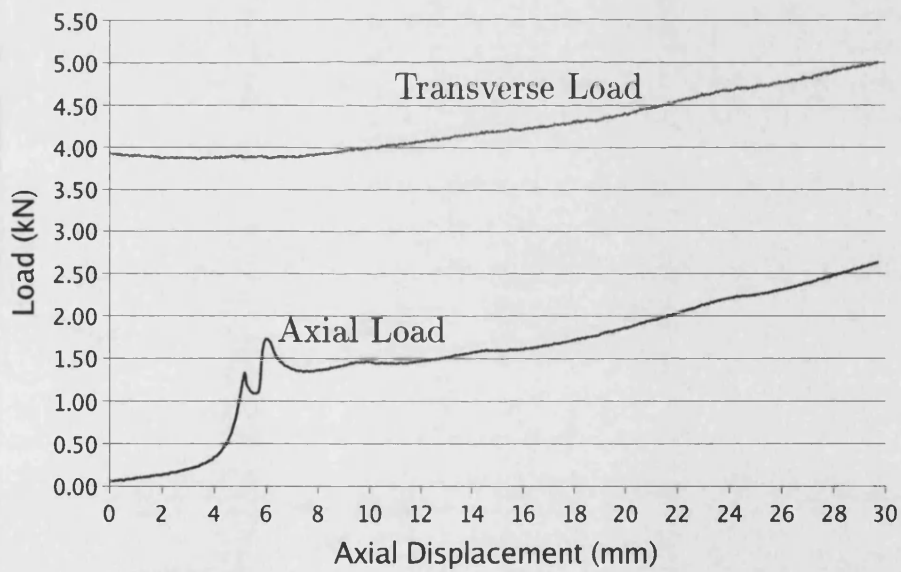
For the four experimental set-ups shown in Table 6.1, direct comparisons are now made between the results from these experiments and the solutions of model given in (6.23). This has been done using the algebraic manipulation package MAPLE (Heck, 1996).



(a) Experiment 2

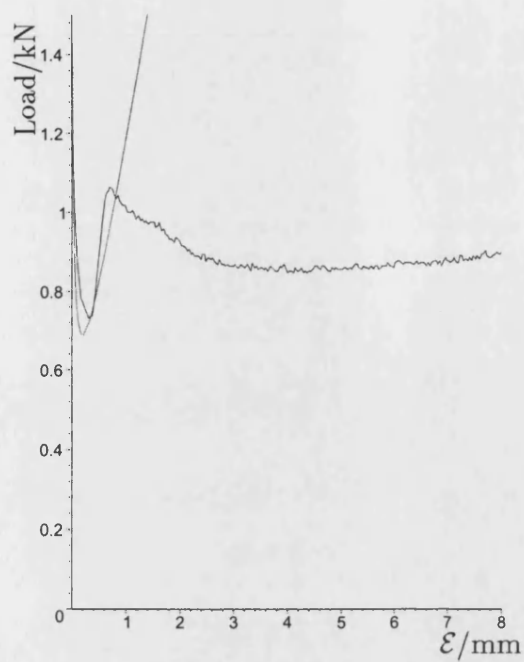


(b) Experiment 3

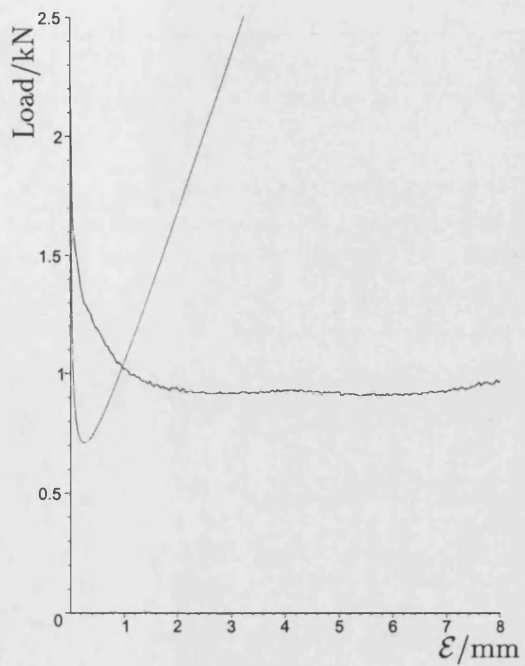


(c) Experiment 4

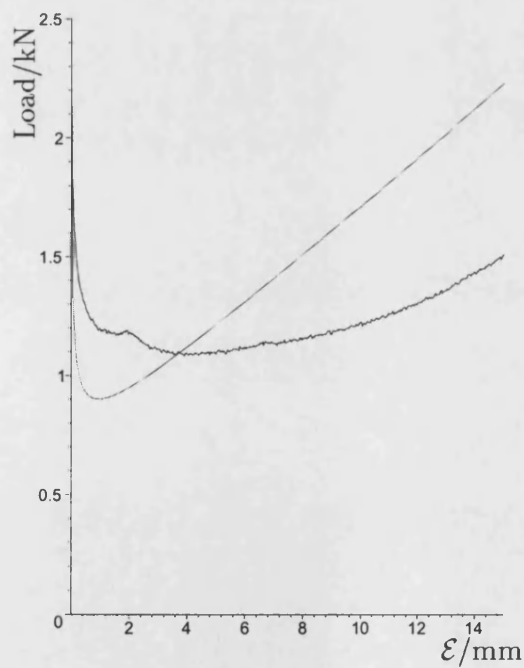
Figure 6.9: Axial and transverse loads (P and P_T), plotted against end-shortening \mathcal{E} for the three further experiments (in addition to that of Fig. 6.3).



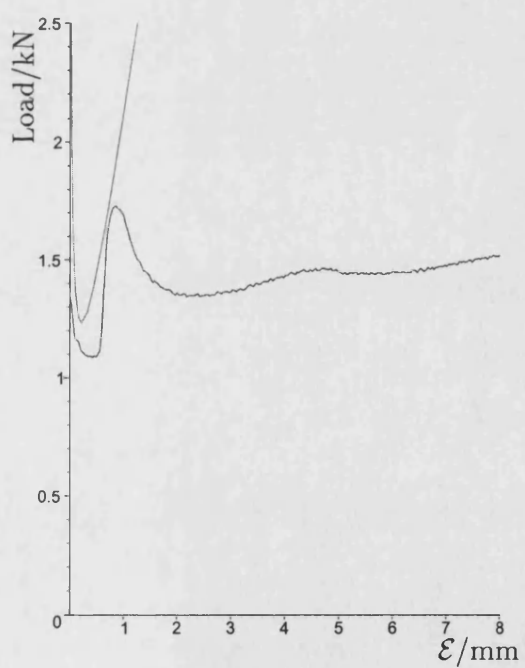
(a) Experiment 1



(b) Experiment 2



(c) Experiment 3



(d) Experiment 4

Figure 6.10: Comparison of model and experiment showing axial loads, plotted against end-shortening \mathcal{E} .

For Experiment 1, the raw data for the transverse and axial loads against end-displacement, were given in Fig. 6.3 to exemplify the loading sequence; similar output for the other three experiments is presented in Fig. 6.9. Fig. 6.10 shows plots of the experimental axial load versus displacement curves against the corresponding theoretical ones.

Table 6.2 contrasts the minimum post-fold load level P_{min} and the wavelength L ;

Expt	Theoretical values			Experimental values			% Difference	
	L (mm)	P_{min} (kN)	P^C (kN)	L (mm)	P_{min} (kN)	Q (mm)	L	P_{min}
1	12.61	0.6877	0.2036	11.45	0.7316	11.44	-9.2	6.4
2	13.84	0.7098	0.1790	13.45	0.8855	13.80	-2.8	24.8
3	13.19	1.0485	0.2468	11.99	1.0824	13.89	-9.1	3.2
4	15.24	1.2336	0.1681	15.31	1.0867	15.35	0.46	-11.9

Table 6.2: Experimental values compared against model predictions.

as well as stating the theoretical critical load P^C and experimental amplitude Q for completeness. As we are using a harmonic Galerkin approximation, for the theoretical curves, P_{min} is the minimum load associated with a periodic deflected shape. For the experiments, this is compared with the minimum load reached when the first hump forms. Note however that for experiments 2 and 3 the first two humps form simultaneously or nearly so. In this case therefore P_{min} is associated with the formation of the first two humps.

For the experiments, L was measured for the first full fold, as often the initial hump was irregular in shape and therefore difficult to determine. The experimental estimates of wavelength are in very good agreement with the theoretical predictions, to within 10% in all four cases. In two of the tests the correspondence is remarkable and, interestingly, where the wavelengths are well matched, the P_{min} comparisons are less so and vice-versa. However, no real conclusion can be drawn from these data as the sample size is so small.

What is clear from the graphical comparisons of Fig. 6.10 is that, where a single hump forms distinctly on its own, the theoretical and experimental curves are consistent over both the initial formation and restabilization (Experiments 1 and 4), whereas if two humps form simultaneously, or nearly so, the match is less good (Experiments 2 and 3). The reasons for this difference in response are presently unclear, although the presence of initial imperfections is expected to have some

bearing on the matter, as is the speed of the axial loading.

It is worth re-iterating that the theoretical wavelength calculated here is that found from minimization with respect to the critical load. Thus L is associated with a wavetrain and not buckling in sequence, where it is expected that the solution at the *Maxwell load* would pick out the wavelength (Budd *et al.*, 2001).

6.5 Concluding remarks

This chapter has taken the nonlinear model for parallel folding in two-layers formulated in Chapters 3 and 4 and extended it to a system of n layers, by dividing a single body into an even number of identical strata. The limitations of such a formulation are highlighted. The linearized potential energy admits expressions for the critical load and wavelength by characterizing the general behaviour using the Galerkin approximation of Chapter 3; these are found to be consistent with other such analyses. Applying the calculus of variations to the linearization, the differential equation and boundary conditions are found.

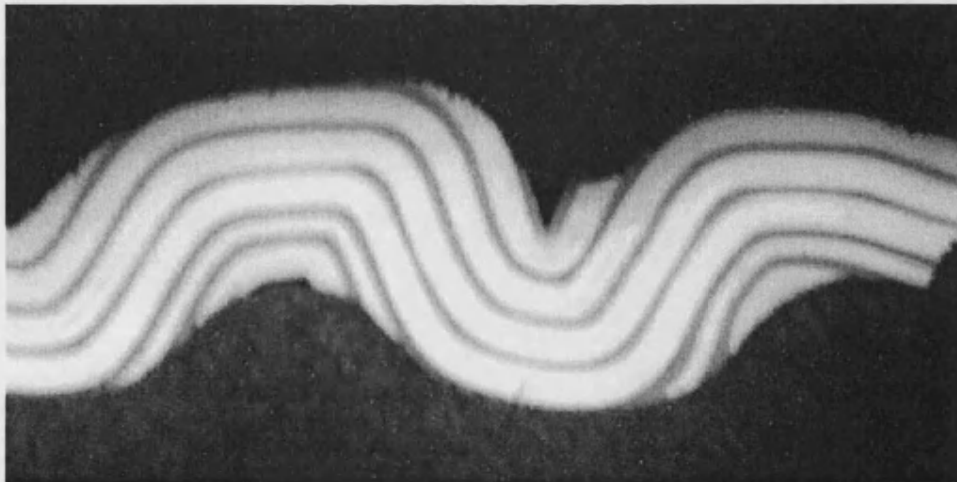


Figure 6.11: Experiment 4: Foundation caught in the folds increasing the foundation stiffness and wavelength of the fold.

The energy functional is validated with simple physical experiments conducted on layers of paper constrained between two sheets of foam rubber. Comparison emphasizes the non-triviality of finding the parameters, but shows that the trend of the load-displacement plots and the wavelengths are in very good agreement

with those predicted. However, unlike kink banding (Wadee *et al.*, 2004), the current model for parallel folding has no lockup criterion.

The fact that the lockup of the humps is not particularly marked on the experimental axial loading plots could be attributed to the foundation not acting as a true basal layer (de Sitter, 1964) and obstructing the folds (Fig. 6.11). The effect of the foundation becoming “trapped” in the cusps is to raise the foundation stiffnesses (Peletier, 2001b) at these points and hence stop the waves from closing. It can also be seen from flattening of the waves that the rigid interfaces of the rig are possibly interfering with the deformation. To reduce both of the above effects another set of experiments, using a thicker foundation, would be of interest.

Chapter 7

Conclusions and further work

7.1 Concluding remarks

This thesis has presented a nonlinear elastic model for multilayer parallel folding with the inclusion of friction at the bedding interfaces. Although taking a solid, elastic approach is in contrast with much of the previous work on multilayer buckling, it is the addition of the friction, that makes this research a novel study of geological concentric folding.

Concentrating the analysis on the buckling of a single half-wave of two layers, under high overburden pressure, energy considerations penalize delamination and lead to a formulation for the total potential energy using simple bending theory. The work done by the direction-dependent friction is found from the slip between the layers and a *friction indicator* is needed to show whether this contribution is positive or negative. A sinusoidal approximation gives a visualization of the bifurcation diagram similar to the classical plot for a strut on an elastic foundation with an imperfection (Fig. 3.7). Importantly, in the area between the stationary paths, expressed as the *jammed region*, the system sits in equilibrium. However, as the system passes through the region, the direction of the friction reverses until the layers are able to slip relative to one another.

Extension of the analysis to the class of all admissible monotone functions, results in a nonlinear differential equation and boundary conditions. The boundary

conditions in the third derivative represent the step change in shear force at the ends of the layers; these terms literally “fall out” of the calculus of variations and suggest that some of the physicality is captured by the model. In linearizing the differential equation, nonlinearity is not lost as friction enters the system via the boundary conditions. Phase space plots highlight the importance of this in subtly altering the system as it passes through the jammed region (Fig. 4.2). When the numerical continuation code AUTO (Doedel *et al.*, 1997) is used to compare the solutions of the linear and nonlinear equations, little of phenomenological significance is added by including the full set of geometric nonlinearities. Over much of the loading there is little deviation of the solution paths; thus analysis of the more simple linear system is used to extend the model.

There is nothing in the model up to this point to show how the pattern continues into further waves. Localized behaviour is suggested by the unstable nature of the buckling and with a nonlinearity added to the foundation such that the system restabilizes over large deflections, cellular buckling is predicted, with half-waves forming and then locking-up in sequential fashion. By adding a restabilizing term to the foundation and curve-fitting the wave-profiles using two cubic B-splines, such ideas were explored by studying the stationary solutions of the two-layer potential energy functional. As the splines may take different amplitudes we get the possibility of *primitive* serial folding. Surprisingly, following the development of a single hump through to a second, with increasing end-shortening, we find that localization is lost and (primitive) periodicity imposed while the load is still falling. This is in major contrast to earlier work (Hunt *et al.*, 2000b; Budd & Peletier, 2000; Wadee *et al.*, 2004), where the addition of another cell in the transition from a homoclinic to heteroclinic connection is seen by equilibrium behaviour where the load falls and rises periodically.

Finally, we see that extending the nonlinear two-layer model for parallel folding to a multilayer of n identical layers, is a relatively straightforward exercise. Several of the limitations of the model are brought to light in doing so and we find that as the number of layers increases, over large deflections, some of the simplifications begin to break down. However, when compared to the work of Currie *et al.* (1962), the critical load and wavelength are fairly consistent and the calculus of variations shows that again the boundary conditions are physically sound; both of these points lend some credibility to the methodology. The simplest comparison of the model with experiments comprising paper multilayers embedded in a foam

matrix, uses first order harmonic analysis of the linearized potential and shows a very good agreement between the theoretical and actual load-amplitude plots and wavelengths.

The fact that so-called serial buckling is inherent to the model, and that there is good comparison with an experimental investigation using layered structures, highlights the power of the applied techniques and makes us confident that the paradigm improves our understanding of the real physical situation. Moreover, using the techniques introduced in this thesis, the following extensions should be considered.

7.2 Further work

The research presented in this thesis only models the central interface of a multi-layer body undergoing parallel folding. Everything else is assumed to follow from the geometry of this bedding plane, through the definition that the orthogonal thickness of the layers must be maintained at all points. However, this is not as straightforward as it appears; the geometry eventually gets more complicated, due to the reduction of the radius of curvature. For example, let us assume that at the core of the fold the wave is sinusoidal. As Fig. 7.1(a) shows, if the envelope of constant normal thicknesses is followed from the sinewave the layers eventually fold through themselves.

Of course, in reality this does not occur; the multilayer usually dies out by forming a cusp and then the subsequent strata form a corner. In many geological outcrops, this situation is accompanied by faulting or zones of crumpling (crenulations), as shown in Fig. 7.1(b) (Goguel, 1962; de Sitter, 1964). Such behaviour needs more study and modelling by accurately tracing wavefronts.

Related to this is the idea of *lockup* and here we have no lockup criterion. As shown for kink banding, a lockup criterion would enable us to model the propagation of the fold and if successful allow more direct comparison with experimental results (Wadee & Edmunds, 2005). In an ideal situation the lockup is governed by the geometry of the layers cusping; therefore geometrical lockup happens when the extreme layers are in contact with themselves. In reality, as soon as it more

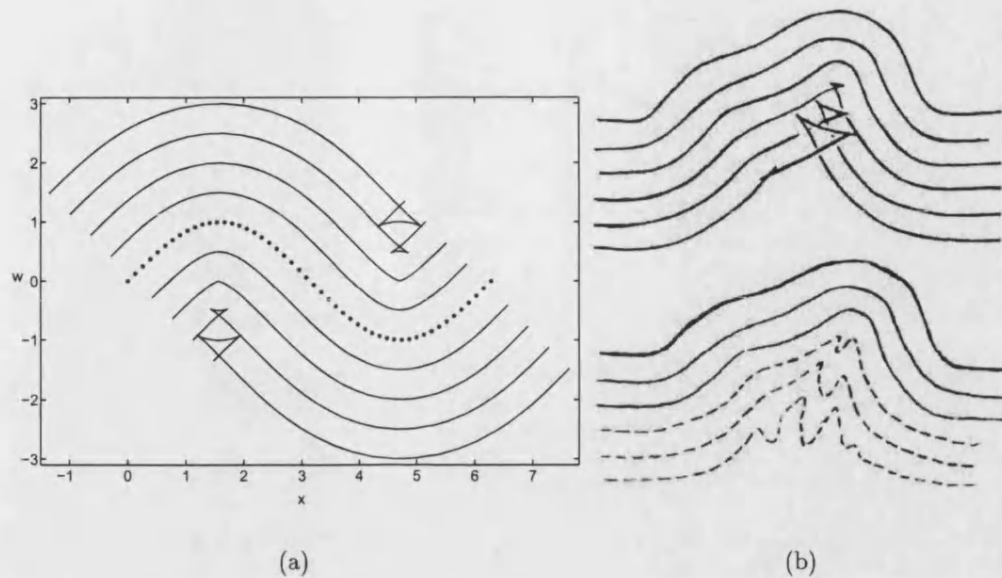


Figure 7.1: (a) Tracing envelopes of constant thickness of a sinewave, (b) Crumpling at the base of a fold. (After Goguel 1962)

favourable for a new hump to be formed then the stress is passed on to the undeformed material. Geometrical lockup, in general, may not happen until much further down the post-buckling path, if it occurs at all; especially if the matrix interferes with the cusps.

Finding solutions to the linearized multilayer differential equation and boundary conditions, given in Chapter 6, using a numerical package such as AUTO may also lead to better comparisons with the experiments, as this would not be restricted to purely sinusoidal deflections. Although the applicability is questionable due to the simplifications, the full nonlinear model could also be examined.

To aid in all of the above, some more experiments are needed, where the foundation is increased in thickness to stop the rigid boundaries interfering with the humps. Hopefully this would give better comparisons with the multilayer model and allow a more careful study of the propagation sequence.

The propagation process from the splines formulation should ideally be extended to more humps; however, the equations get increasingly complicated and the computational time increases rapidly. It would be easier and more productive to assume that $n - 1$ humps have already formed and model the process of devel-

opment of the n th cell. This should be possible with just a slight modification of boundary conditions at one end of one of the splines, from homoclinic to periodic boundary conditions.

Finally, having studied kink banding (Wadee & Edmunds, 2005; Edmunds & Wadee, 2005) and parallel folding, it would be of interest to see if a process exists that would take one from the former to latter. The overburden pressure is certainly involved as it is considerably higher in the former case and is related to the foundation. There are also similarities between kink bands and parallel fold limbs and it may be that in the limbs, like a kink band, in order for friction to be released, the orientation and rotation angles must be the same.

A study of chevron folding is also a possibility as, in the author's opinion, this might be considered as a middle ground between kink bands and concentric folds. Chevron folds have small sharp hinges and long limbs almost forming a corner. If a wavefront is extended outward from a corner, it becomes more rounded, as seen in Fig. 7.1; if extended inwards the confinement means that kink bands appear. In preliminary experiments by Hunt *et al.* (2000b), it was shown that chevron folding could be obtained from kink banding (Fig. 7.2), by making certain adjustments. Whether the same could be done from parallel folding remains to be seen and experiments altering different parameters would be needed.

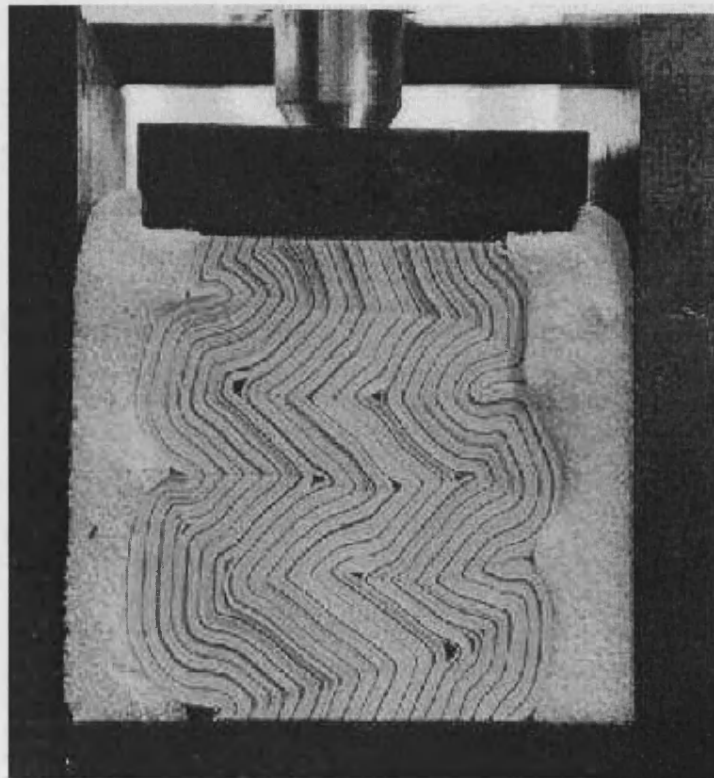


Figure 7.2: Chevron folds obtained from kink bands. (After Hunt *et al.* 2000b)

References

- Amazigo, J. C., & Fraser, W. B. 1971. Buckling under external pressure of cylindrical shells with dimple shaped initial imperfections. *Int. J. Solids Struct.*, **7**, 883–900.
- Amazigo, J. C., Budiansky, B., & Carrier, G. F. 1970. Asymptotic analyses of the bucking of imperfect columns on nonlinear elastic foundations. *Int. J. Solids Struct.*, **6**, 1341–1356.
- Arnell, R. D., Davies, P. B., Halling, J., & Whomes, T. L. 1991. *Tribology, Principles and Design Applications*. Basingstoke: Macmillan.
- Bay, N. 1976. *Friction and adhesion in metal forming and cold welding*. Ph.D. thesis, Tech. Univ. of Denmark.
- Bayly, B. 1992. *Mechanics in structural geology*. New York: Springer-Verlag.
- Bayly, M. B. 1974. An energy calculation concerning the roundness of folds. *Tectonophysics*, **24**, 291–316.
- Beardmore, R. E., Peletier, M. A., Budd, C. J., & Wadee, M. Ahmer. 2005. Bifurcations of periodic solutions satisfying the zero-Hamiltonian constraint in fourth order differential equations. *SIAM J. Appl. Math.* (To be published).
- Bensimon, D., Shraiman, B. I., & Croquette, V. 1988. Nonadiabatic effects in convection. *Physical Review A*, **38**(10), 5461–5464.
- Biot, M. A. 1937. Bending of an infinite beam on an elastic foundation. *ASME Jour. Appl. Mech.*, **4**, A1–A7.
- Biot, M. A. 1938. Theory of elasticity with large displacements and rotations. *Pages 117–122 of: Proc. 5th Internat. Cong. Applied Mech.*

- Biot, M. A. 1957. Folding instability of a layered viscoelastic medium under compression. *Proc. R. Soc. Lond.*, A **242**, 444–454.
- Biot, M. A. 1961. Theory of folding of stratified viscoelastic media and its implication in tectonics and orogenesis. *Bull. Geol. Soc. Amer.*, **72**, 1595–1620.
- Biot, M. A. 1963a. Internal buckling under initial stress in finite elasticity. *Proc. R. Soc. Lond.*, A **273**, 306–328.
- Biot, M. A. 1963b. Stability of multilayered continua including the effect of gravity and viscoelasticity. *J. Franklin Inst.*, **276**, 231–252.
- Biot, M. A. 1963c. Theory of stability of multilayer continua in finite anisotropic elasticity. *J. Franklin Inst.*, **276**, 128–153.
- Biot, M. A. 1964. Theory of internal buckling of a confined multilayered structure. *Bull. Geol. Soc. Amer.*, **75**, 563–568.
- Biot, M. A. 1965a. *Mechanics of Incremental Deformations*. New York: Wiley.
- Biot, M. A. 1965b. Theory of similar folding of the first and second kind. *Bull. Geol. Soc. Amer.*, **76**, 251–258.
- Blay, P., Cosgrove, J. W., & Summers, J. M. 1977. An experimental investigation of the development of structures in multilayers under the influence of gravity. *Jl. geol. Soc. Lond.*, **133**, 329–342.
- Bolt, H. M. 1989. *Secondary bifurcation and localization phenomena in nonlinear structural mechanics*. Ph.D. thesis, Imperial College, London.
- Bowden, F. P., & Tabor, D. 1973. *Friction, An Introduction to Tribology*. New York: Anchor.
- Brogliato, B. 1999. *Nonsmooth mechanics (2nd edition)*. London: Springer-Verlag.
- Budd, C. J., & Peletier, M. A. 2000. Approximate self-similarity in models of geological folding. *SIAM J. Appl. Math.*, **60**(3), 990–1016.
- Budd, C. J., Hunt, G. W., & Peletier, M. A. 1999. Self-similar fold evolution under prescribed end-shortening. *Math. Geol.*, **31**(8), 989–1005.
- Budd, C. J., Hunt, G. W., & Kuske, R. 2001. Asymptotics of cellular buckling close to the Maxwell load. *Proc. R. Soc. Lond.*, A **457**, 2935–2964.

- Budd, C. J., Edmunds, R., & Hunt, G. W. 2003. A nonlinear model for parallel folding with friction. *Proc. R. Soc. Lond., A* **459**, 2097–2119. ISSN 1364-5021.
- Champneys, A. R., Hunt, G. W., & Thompson, J. M. T. 1999. *Localization and solitary waves in solid mechanics*. Singapore: World Scientific Publishing.
- Chapple, W. M. 1968. A mathematical theory of finite-amplitude rock-folding. *Bull. Geol. Soc. Amer.*, **79**, 47–68.
- Chater, E., Hutchinson, J. W., & Neale, K. W. 1983. Buckle propagation on a beam on a nonlinear elastic foundation. *In*: Thompson, J. M. T., & Hunt, G. W. (eds), *Collapse: the buckling of structures in theory and practice. IUTAM symposium*. Cambridge: Cambridge University Press.
- Cobbold, P. R. 1975. Fold propagation in single embedded layers. *Tectonophysics*, **27**, 333–351.
- Crisfield, M. A., & Will, J. 1986. Solution strategies and softening materials. *Comput. Meth. Appl. Mech. Eng.*, **66**(3), 267–289.
- Currie, J. B., Patnode, H. W., & Trump, R. P. 1962. Development of folds in sedimentary strata. *Bull. Geol. Soc. Amer.*, **73**, 655–674.
- de Boor, C., & Swartz, B. 1973. Collocation at Gaussian points. *SIAM J. Numer. Anal.*, **10**, 582–606.
- de Sitter, L. U. 1964. *Structural Geology*. New York: McGraw–Hill.
- Doedel, E. J. 1997. Nonlinear numerics. *J. Franklin Inst.*, **334B**(5–6), 1049–1073.
- Doedel, E. J., Champneys, A. R., Fairgrieve, T. F., Kuznetsov, Y. A., Sandstede, B., & Wang, X. J. 1997. *AUTO97: Continuation and bifurcation software for ordinary differential equations*. Tech. rept. Department of Computer Science, Concordia University, Montreal, Canada. Available by FTP from ftp.cs.concordia.ca in /pub/doedel/auto.
- Domokos, G., Holmes, P., & Royce, B. 1997. Constrained Euler buckling. *J. Nonlinear Sci.*, **7**, 281–314.
- Donath, F. A. 1962. Role of layering in geological deformation. *Trans. N. Y. Acad. Sci Series 2*, **24**, 236–249.

- Donath, F. A., & Parker, R. B. 1964. Folds and folding. *Bull. Geol. Soc. Amer.*, **75**, 45–62.
- Edmunds, R., & Wadee, M. Ahmer. 2005. On kink banding in individual PPTA fibres. *Compos. Sci. Tech.* (To be published).
- Edmunds, R., Hunt, G. W., & Wadee, M. Ahmer. 2005. Parallel folding in multilayered structures. *J. Mech. Phys. Solids*. (Submitted 03/2005).
- Euler, L. 1744. *Methodus inveniendi lineas curvas maximi minimive proprietate gradientes*. Lausanne and Geneva. Appendix: De cuvis elasticis.
- Everall, P. R. 1999. *Mode jumping and quasi-periodicity in nonlinear elastic structures*. Ph.D. thesis, Univ. of Bath.
- Glendinning, P. 1994. *Stability, Instability & Chaos: An introduction to the theory of nonlinear differential equations*. Cambridge: Cambridge University Press.
- Goguel, J. 1943. *Introduction a l'étude mécanique des déformations de l'écorce terrestre*. Paris: Mémoire, Ministère de la Production Industrielle et des Communications, Imprimerie Nationale.
- Goguel, J. 1962. *Tectonics*. San Francisco: Freeman.
- Goldstein, S. 1926. The stability of a strut under thrust, when buckling is resisted by a force proportional to the displacement. *Cambridge Philos. Soc. Proc.*, **23**, 120–129.
- Griffiths, H. B. 1981. *Surfaces*. Cambridge: Cambridge University Press.
- Gunn, R. 1937. A qualitative study of mountain building. *J. Franklin Inst.*, **224**(1), 19–53.
- Heck, A. 1996. *Introduction to Maple*. New York: Springer.
- Hirsch, M. W. 1976. *Differential Topology*. New York: Springer-Verlag.
- Hobbs, B. E., Means, W. D., & Williams, P. F. 1976. *An Outline of Structural Geology*. Brisbane: Wiley.
- Holmes, P., Domokos, G., & Hek, G. 2000. Euler buckling in a potential field. *J. Nonlinear Sci.*, **10**, 477–505.

- Honea, E., & Johnson, A. M. 1976. A theory of concentric, kink and sinusoidal folding and of monoclinical flexuring of compressible, elastic multilayers. IV. Development of sinusoidal and kink folds in multilayers confined by rigid boundaries. *Tectonophysics*, **30**, 197–239.
- Hunt, G. W. 1983. Elastic stability: in structural mechanics and applied mathematics. In: Thompson, J. M. T., & Hunt, G. W. (eds), *Collapse: the buckling of structures in theory and practice. IUTAM symposium*. Cambridge: Cambridge University Press.
- Hunt, G. W. 1986. Hidden (a)symmetries of elastic and plastic bifurcation. *Appl. Mech. Rev.*, **39**(8), 1165–1186.
- Hunt, G. W. 1989. Bifurcation of structural components. *Proc. Instn. Civ. Engrs. Part 2*, **87**, 443–467.
- Hunt, G. W. 2005. Buckling in space and time. *Nonlinear Dynamics*. (To be published).
- Hunt, G. W., & Bolt, H. M. 1986. Elastic mimicry of elasto-plastic responses. *Civ. Engng Syst.*, **3**, 100–108.
- Hunt, G. W., & Everall, P. R. 1999. Arnold tongues and mode-jumping in the supercritical post-buckling of an archetypical elastic structure. *Proc. R. Soc. Lond., A* **455**, 125–140.
- Hunt, G. W., & Wadee, M. Ahmer. 1998. Localization and mode interaction in sandwich structures. *Proc. R. Soc. Lond., A* **454**, 1197–1216.
- Hunt, G. W., & Wadee, M. K. 1991. Comparative lagrangian formulations for localized buckling. *Proc. R. Soc. Lond., A* **434**, 458–502.
- Hunt, G. W., Bolt, H. M., & Thompson, J. M. T. 1989. Structural localization phenomena and the dynamical phase-space analogy. *Proc. R. Soc. Lond., A* **425**, 245–267.
- Hunt, G. W., Wadee, M. K., & Shiacolas, N. 1993. Localized elasticae for the strut on the linear foundation. *ASME J. Appl. Mech.*, **60**, 1033–1038.
- Hunt, G. W., Mühlhaus, H. B., & Whiting, A. I. M. 1997. Folding processes and solitary waves in structural geology. *Phil. Trans. R. Soc. Lond., A* **355**, 2197–2213.

- Hunt, G. W., Peletier, M. A., Champneys, A. R., Woods, P. D., Wadee, M. Ahmer, Budd, C. J., & Lord, G. J. 2000a. Cellular buckling in long structures. *Nonlinear Dynamics*, **21**(1), 3–29.
- Hunt, G. W., Peletier, M. A., & Wadee, M. Ahmer. 2000b. The Maxwell stability criterion in pseudo-energy models of kink banding. *J. Struct. Geol.*, **22**(5), 669–681.
- Hunt, G. W., Wadee, M. Ahmer, & Peletier, M. A. 2001. Friction models of kink banding in compressed layered structures. *Pages 249–256 of: Mühlhaus, H-B., Dyskin, A. V., & Pasternak, E. (eds), Proceedings of the 5th International Workshop on Bifurcation and Localization in Geomechanics (IWBL99)*. Lisse: Swets & Zeitlinger.
- Hunt, G. W., Hu, B., Butler, R., Almond, D. P., & Wright, J. E. 2004. Nonlinear modeling of delaminated struts. *AIAA Journal*, **42**(11), 2364–2372.
- Hunt, G. W., Edmunds, R., & Budd, C. J. 2005. Serial parallel folding with friction: a primitive model using cubic B-splines. *J. Struct. Geol.* (Submitted 07/2004).
- Hutchinson, J. W., & Koiter, W. T. 1970. Postbuckling theory. *Appl. Mech. Rev.*, **23**, 1353–1366.
- Johnson, A. M. 1977. *Styles of Folding*. Amsterdam: Elsevier.
- Johnson, A. M., & Ellen, S. D. 1974. A theory of concentric, kink and sinusoidal folding and of monoclinical flexuring of compressible, elastic multilayers. I. Introduction. *Tectonophysics*, **21**, 301–339.
- Johnson, A. M., & Honea, E. 1975b. A theory of concentric, kink and sinusoidal folding and of monoclinical flexuring of compressible, elastic multilayers. II. Initial stress and nonlinear equations of equilibrium. *Tectonophysics*, **25**, 261–280.
- Johnson, A. M., & Honea, E. 1975a. A theory of concentric, kink and sinusoidal folding and of monoclinical flexuring of compressible, elastic multilayers. III. Transition from sinusoidal to concentric-like to chevron folds. *Tectonophysics*, **27**, 1–38.
- Jordan, D. W., & Smith, P. 1977. *Nonlinear Ordinary Differential Equations (2nd Edition)*. Oxford: Oxford University Press.

- Kerr, A. D. 1964. Elastic and viscoelastic foundation models. *ASME J. Appl. Mech.*, **31**, 491–498.
- Kryiakides, S., & Babcock, C. D. 1983. Buckle propagation phenomena in pipelines. In: Thompson, J. M. T., & Hunt, G. W. (eds), *Collapse: the buckling of structures in theory and practice. IUTAM symposium*. Cambridge: Cambridge University Press.
- Kuenen, P. H., & de Sitter, L. U. 1938. Experimental investigation into the mechanisms of folding. *Leidsche Geol. Med.*, **XII**, 219–239.
- Lancaster, P., & Šalkausas, K. 1987. *Curve and Surface Fitting An Introduction*. London: Academic.
- Maier, G., & Hueckel, T. 1979. Nonassociated and coupled flow rules of elastoplasticity for rock-like materials. *Int. J. Rock Mech. Min. Sci. & Geomech. Abstr.*, **16**, 77–92.
- Marti, J. T. 1986. *Introduction to Sobolev Spaces and Finite Element Solution of Elliptic Boundary Value Problems*. London: Academic.
- McClintock, F. A., & Walsh, J. B. 1962. Friction in Griffiths cracks in rock under pressure. *Pages 1015–1021 of: Proc. 4th U. S. National Congr. on Appl. Mech.*
- Nash, C., & Sen, S. 1983. *Topology & Geometry for Physicists*. London: Academic.
- Nellemann, T., Bay, N., & Wanheim, T. 1977. Real area of contact and friction stress—The role of trapped lubricant. *Wear*, **43**, 45–53.
- Nepomnyashchy, A. A., Tribelsky, M. I., & Velarde, M. G. 1994. Wave number selection in convection and related problems. *Physical Review E*, **50**(2), 1194–1197.
- Peletier, M. A. 2001a. Generalized monotonicity from global minimization in fourth-order ordinary differential equations. *Nonlinearity*, **14**(5), 1221–1238.
- Peletier, M. A. 2001b. Sequential buckling: a variational analysis. *SIAM J. Math. Anal.*, **32**(5), 1142–1168.

- Poiter-Ferry, M. 1983. Amplitude modulation, phase modulation and localization of buckling patterns. *In: Thompson, J. M. T., & Hunt, G. W. (eds), Collapse: the buckling of structures in theory and practice. IUTAM symposium.* Cambridge: Cambridge University Press.
- Press, W. H., Flannery, B. P., Teukolsky, S. A., & Vetterling, W. T. 1986. *Numerical Recipes: The Art of Scientific Computing.* Cambridge: Cambridge University Press.
- Price, N. J. 1970. Laws of rock behaviour in the Earth's crust. *Chap. 1, pages 3–23 of: Sommerton, W. H. (ed), Rock Mechanics-theory and practice. Proceeding of 11th Symposium of Rock Mechanics.* A. I. M. M.
- Price, N. J. 1975. Rates of deformation. *Jl. geol. Soc. Lond.*, **131**, 553–575.
- Price, N. J., & Cosgrove, J. W. 1990. *Analysis of Geological Structures.* Cambridge: Cambridge University Press.
- Ramberg, H. 1959. Theoretical and experimental studies of ptygmatic folding. *Norsk. Geol. Tidsskr.*, **39**, 99–151.
- Ramberg, H. 1960. Relationship between length of arc and thickness of ptygmatically folded veins. *Am. Jour. Sci.*, **258**, 36–46.
- Ramberg, H. 1961. Contact strain and folding instability of a multilayered body under compression. *Geol. Rundsch.*, **51**, 405–439.
- Ramberg, H., & Strömgård, K.-E. 1971. Experimental tests of modern buckling theory applied on multilayered media. *Tectonophysics*, **11**, 461–472.
- Ramsey, J. G. 1967. *Folding and Fracturing of Rocks.* London: McGraw Hill.
- Riks, E. 1972. The application of Newton's method to the problem of elastic stability. *ASME J. Appl. Mech.*, **39**(4), 1060–1065.
- Rivierre, L., Polit, O., & Billoët, J. L. 2001. Analytical and experimental post-buckling of conditioned cables. *Strut. Eng. Mech.*, **12**(6), 595–614.
- Rudnicki, J. W., & Rice, J. R. 1975. Conditions for the localization of deformation in pressure-sensitive dilatant materials. *Mech. Phys. Solids*, **23**, 371–394.
- Russell, R. D., & Christiansen, J. 1978. Adaptive mesh selection strategies for solving boundary value problems. *SIAM J. Numer. Anal.*, **15**(1), 59–80.

- Smith, R. B. 1975. Unified theory of the onset of folding, boudinage, and mullion structure. *Bull. Geol. Soc. Amer.*, **86**, 1601–1609.
- Smith, R. B. 1977. Formation of folds, boudinage, and mullions in non-Newtonian materials. *Bull. Geol. Soc. Amer.*, **88**, 213–320.
- Smoller, J. 1983. *Shock Waves and Reaction–Diffusion Equations*. New York: Springer-Verlag.
- Smoluchowski, M. 1909. Über ein gewisse stabilitätsproblem. *Akad. Wiss. Krakau Math. Kl.*, 3–20.
- Solymar, L. 1988. *Lectures on Fourier Series*. Oxford: Oxford University Press.
- Strogatz, S. H. 1994. *Nonlinear Dynamics and Chaos*. Massachusetts: Addison-Wesley.
- The Math Works, Inc. 2001. *MATLAB: High-performance numeric computation and visualization software*. Natick, Massachusetts, USA: The Math Works Inc. Version 6.1 Release 12.1.
- Thompson, J. M. T., & Hunt, G. W. 1973. *A General Theory of Elastic Stability*. London: Wiley.
- Thompson, J. M. T., & Hunt, G. W. 1983. On the buckling and imperfection-sensitivity of arches with and without prestress. *Int. J. Solids Struct.*, **19**(5), 445–459.
- Thompson, J. M. T., & Stewart, H. B. 1986. *Nonlinear Dynamics and Chaos*. London: Wiley.
- Thompson, J. M. T., & Virgin, L. N. 1988. Spatial chaos and localization phenomena in nonlinear elasticity. *Phys. Lett. A*, **126**(8–9), 491–496.
- Timoshenko, S. P., & Gere, J. M. 1961. *Theory of Elastic Stability*. New York: McGraw-Hill.
- Timoshenko, S. P., & Gere, J. M. 1973. *Mechanics of Materials*. New York: Van Nostrand Reinhold.
- Tvergaard, V., & Needleman, A. 1980. On the localization of buckling patterns. *ASME J. Appl. Mech.*, **47**, 613–619.

- Tvergaard, V., & Needleman, A. 1983. On the development of localized buckle patterns. *In: Thompson, J. M. T., & Hunt, G. W. (eds), Collapse: the buckling of structures in theory and practice. IUTAM symposium.* Cambridge: Cambridge University Press.
- Van Hise, C. R. 1894. Principles of North American pre-Cambrian geology. *US Geol. Surv. 16th Ann. Report*, 571–843.
- Wadee, M. Ahmer. 1998. *Localized buckling in sandwich structures.* Ph.D. thesis, Univ. of Bath.
- Wadee, M. Ahmer. 1999. Experimental evaluation of interactive buckle localization in compression sandwich panels. *J. Sandwich Structures & Materials*, **1**(3), 230–254.
- Wadee, M. Ahmer. 2000. Effects of periodic and localized imperfections on struts on nonlinear foundations and compression sandwich panels. *Int. J. Solids Struct.*, **37**, 1191–1209.
- Wadee, M. Ahmer, & Edmunds, R. 2005. Kink band propagation in layered structures. *J. Mech. Phys. Solids.* (Submitted 08/2004).
- Wadee, M. Ahmer, Hunt, G. W., & Peletier, M. A. 2004. Kink band instability in layered structures. *J. Mech. Phys. Solids*, **52**(5), 1071–1091.
- Wadee, M. K., Coman, C. D., & Bassom, A. P. 2002. Solitary wave interaction phenomena in a strut buckling model incorporating restabilization. *Physica D*, **163**(1–2), 26–48.
- Wait, R., & Mitchell, A. R. 1985. *Finite Element Analysis and Applications.* London: Wiley.
- Waltham, D. 1997. Why does salt start to move? *Tectonophysics*, **282**, 117–128.
- Wanheim, T., & Bay, N. 1978. A model for friction in metal forming processes. *Annals of the CIRP*, **27**(1), 1–6.
- Whiting, A. I. M. 1997. A Galerkin procedure for localized buckling of a strut on a nonlinear elastic foundation. *Int. J. Solids Struct.*, **34**(6), 727–739.
- Whiting, A. I. M., & Hunt, G. W. 1997. Evolution of nonperiodic forms in geological folds. *J. Math. Geol.*, **29**(5), 705–723.